

# **On the nonlinear elastodynamics of skeletal muscle**

by

**Javier Alejandro Almonacid Paredes**

M.Sc., Simon Fraser University, 2020

B.Sc., Universidad de Concepción, 2015

Thesis Submitted in Partial Fulfillment of the  
Requirements for the Degree of  
Doctor of Philosophy

in the  
Department of Mathematics  
Faculty of Science

**© Javier Alejandro Almonacid Paredes 2025**  
**SIMON FRASER UNIVERSITY**  
**Summer 2025**

Copyright in this work is held by the author. Please ensure that any reproduction  
or re-use is done in accordance with the relevant national copyright legislation.

# Declaration of Committee

Name: **Javier Alejandro Almonacid Paredes**

Degree: **Doctor of Philosophy**

Thesis title: **On the nonlinear elastodynamics of skeletal muscle**

Committee:

Chair:	Amarpreet Rattan Associate Professor Department of Mathematics
	<b>Nilima Nigam</b> Supervisor Professor Department of Mathematics
	<b>James Wakeling</b> Co-Supervisor Professor Department of Biomedical Physiology and Kinesiology
	<b>Ben Adcock</b> Internal Examiner Professor Department of Mathematics
	<b>TBD</b> External Examiner TBD Professor Department of TBD TBD University

# Abstract

In this thesis, we investigate the nonlinear elastodynamics of skeletal muscle tissue. We begin the discussion with one-dimensional models. First, we study the inertial effects in a multibody model of the muscle-tendon unit using experimentally obtained data. Then, we study the unphysical lack of stability in these multibody models and propose a new continuum model that provides stability throughout the range of motion of a muscle. Next, as groundwork for studying dynamic models, we examine time discretization options for Neo-Hookean deformation in the presence of a highly stiff material, as is the case for active muscle tissue. Moving on to three-dimensional (3D) models, we begin with a new Lagrangian framework for a 3D model of skeletal muscle tissue. This is discretized using a three-field variational formulation and a new implicit time discretization strategy. Furthermore, we formalize several key concepts in physiology in precise mathematical terms, including *isometric* vs. *dynamic* contractions, as well as *muscle gearing*. In physiology, isometric contractions are those in which the total length of the muscle belly is fixed; in most existing simulation experiments, the dynamics of the muscle with fixed Dirichlet boundary conditions are conflated with a zero-velocity system. We discuss the appropriateness of using dynamic and quasi-static simulations, demonstrating (a) the importance of inertial terms and (b) that muscle deformation is a truly 3D phenomenon. We then show the applicability of the finite element formulation to a scenario in which we combine magnetic resonance imaging (MRI) data with motion capture and electromyography (EMG) data. We also use these ideas to study gearing in skeletal muscle tissue, making the first use of a continuum mechanics model for these purposes. Developed as part of this project, we introduce **Flexodeal**, a new finite-element framework for studying musculoskeletal dynamics. **Flexodeal** is an open-source computational library designed to perform three-dimensional dynamic or quasi-static deformations of skeletal muscle tissue using a Hill-type model and the finite element library deal.II. We have also developed **Flexodeal Lite** as a simpler version of **Flexodeal** that can be used as a basis to advance numerical methods in continuum biomechanics.

**Keywords:** skeletal muscle; continuum mechanics; finite element method; time stepping schemes; musculoskeletal simulation; gearing

# Table of Contents

<b>Declaration of Committee</b>	<b>ii</b>
<b>Abstract</b>	<b>iii</b>
<b>Table of Contents</b>	<b>iv</b>
<b>List of Tables</b>	<b>ix</b>
<b>List of Figures</b>	<b>xi</b>
<b>1 Introduction</b>	<b>1</b>
1.1 Muscle anatomy . . . . .	1
1.2 Muscle architecture . . . . .	3
1.3 Fundamental models of skeletal muscle . . . . .	4
1.4 Computational models . . . . .	6
1.4.1 One-dimensional models . . . . .	7
1.4.2 Three-dimensional models . . . . .	8
1.5 Stability of computational models . . . . .	10
1.6 Main contributions and outline of this thesis . . . . .	11
<b>I One-dimensional elastodynamics</b>	<b>14</b>
<b>2 Inertial effects in a multibody mass-spring model of the muscle-tendon unit</b>	<b>15</b>
2.1 Background . . . . .	15
2.2 Mathematical models . . . . .	16
2.2.1 Main concepts . . . . .	16
2.2.2 Hill's muscle model . . . . .	17
2.2.3 Massless and mass-enhanced models of the MTU . . . . .	18
2.2.4 Optimal muscle and tendon length . . . . .	20
2.2.5 Initial muscle length . . . . .	22
2.2.6 Scaling . . . . .	22

2.3	Experimental data: muscles and tasks in consideration . . . . .	23
2.4	Computational implementation . . . . .	24
2.5	Main results . . . . .	26
2.5.1	Overall behaviour for different muscles and tasks . . . . .	26
2.5.2	Dynamics of the ST during running . . . . .	28
2.5.3	Influence of the number of masses in the computation . . . . .	28
<b>3</b>	<b>Dynamical stability and the continuum limit of multibody models</b>	<b>31</b>
3.1	Background . . . . .	31
3.2	Mathematical description of the descending limb instability . . . . .	33
3.2.1	The model for an isometric contraction . . . . .	33
3.2.2	Stability of the zero solution . . . . .	34
3.2.3	A numerical example . . . . .	37
3.3	Stabilizing the model . . . . .	37
3.3.1	The continuum limit of the mass-enhanced model . . . . .	38
3.3.2	Convexifying the FL relationship . . . . .	40
3.3.3	A stabilized mass-enhanced muscle model . . . . .	41
3.4	Nondimensionalization of the continuum system and the influence of mass .	43
<b>4</b>	<b>First order is enough: time discretization alternatives for dynamic Neo-Hookean deformation</b>	<b>45</b>
4.1	Background . . . . .	46
4.1.1	Time stepping schemes in engineering elastodynamics . . . . .	46
4.1.2	Time or space first? Rothe's method versus method of lines . . . . .	47
4.2	Model problem for nonlinear elasticity . . . . .	48
4.3	A first order time stepping scheme . . . . .	48
4.3.1	Rothe's method and finite element formulation . . . . .	48
4.3.2	Method of lines . . . . .	54
4.4	Newmark schemes . . . . .	56
4.4.1	Newmark in the context of Rothe's method . . . . .	57
4.4.2	Newmark in the context of the MOL . . . . .	58
4.5	HHT- $\alpha$ method . . . . .	59
4.5.1	HHT- $\alpha$ in the context of Rothe's method . . . . .	60
4.5.2	HHT- $\alpha$ in the context of the MOL . . . . .	60
4.6	Convergence studies: linear elasticity . . . . .	61
4.7	Neo-Hookean experiments, overshooting, and velocity approximations . . .	62
4.8	Discussion . . . . .	74
4.9	Conclusion . . . . .	74

<b>II Three-dimensional elastodynamics</b>	<b>76</b>
<b>5 A Lagrangian framework for a model of skeletal muscle tissue</b>	<b>77</b>
5.1 Elements of continuum mechanics . . . . .	77
5.1.1 Kinematics . . . . .	78
5.1.2 Material and spatial derivatives . . . . .	79
5.1.3 Deformation gradient . . . . .	81
5.1.4 Rates of deformation tensors . . . . .	82
5.1.5 Fundamental strain tensors, fibre stretch, and fibre strain rate . . . . .	83
5.1.6 Stress tensors . . . . .	84
5.1.7 Volumetric-isochoric decomposition for compressible hyperelastic materials . . . . .	85
5.1.8 A strain-energy function for compressible, transversely isotropic materials . . . . .	90
5.2 Constitutive laws for skeletal muscle . . . . .	90
5.2.1 Muscle fibres . . . . .	91
5.2.2 Base material . . . . .	92
5.2.3 Intramuscular fat . . . . .	94
5.3 Extending the SEF to the muscle-tendon unit . . . . .	94
5.4 Lagrangian formulation of the elastodynamic problem . . . . .	96
5.5 A first order, fully implicit time discretization . . . . .	98
5.6 Linearization . . . . .	101
5.6.1 Newton's method . . . . .	102
5.6.2 Construction of the block-matrix system . . . . .	103
5.7 Fourth-order elasticity tensors . . . . .	105
5.7.1 Along-fibre contribution . . . . .	105
5.7.2 Base material and other components of the MTU . . . . .	108
5.8 Finite element approximation . . . . .	108
5.8.1 Approximation properties . . . . .	109
5.8.2 On polyconvexity and well-posedness of the mixed formulation . . . . .	110
5.8.3 Solution of the discretized linear system . . . . .	113
<b>6 Flexodeal: a new finite-element framework for studying musculoskeletal dynamics</b>	<b>114</b>
6.1 Motivation . . . . .	115
6.2 Implementation details . . . . .	116
6.2.1 Inputs . . . . .	116
6.2.1.1 Parameter file . . . . .	116
6.2.1.2 Prescribed strain and activation profiles . . . . .	118
6.2.1.3 Markers . . . . .	118

6.2.1.4	Quadrature point data (not implemented in Flexodeal Lite)	118
6.2.2	Outputs	120
6.2.2.1	Activation and muscle length	120
6.2.2.2	Displacements at predefined markers	120
6.2.2.3	Energies	120
6.2.2.4	Forces	122
6.2.2.5	Gearing-related information	123
6.2.2.6	Mean fibre stretch and pennation	124
6.2.2.7	Mechanical variables at all QPs (binary files)	125
6.2.2.8	VTU files	125
6.2.2.9	Other outputs	127
6.3	Convergence studies	127
6.3.1	Error computation	128
6.3.2	Isometric contractions	129
6.3.3	Setup	129
6.3.4	Main results	131
6.4	The force-length relationship of whole muscle	134
6.4.1	An idealized muscle	135
6.4.2	Setup	135
6.4.3	Results	138
6.4.4	Numerical implications of a different protocol involving active lengthening	141
6.5	The effect of mass and the force-velocity relationship in isometric contractions	142
6.5.1	Setup	142
6.5.2	Main results	143
6.6	Deformation of a human medial gastrocnemius during locomotion	146
6.6.1	Setup	146
6.6.2	Results	147
<b>7</b>	<b>Gearing in muscle tissues: a first-of-its-kind computational study</b>	<b>150</b>
7.1	Introduction	150
7.2	Computational setup and main definitions	152
7.2.1	Computational domain and architecture	152
7.2.2	Muscle model	153
7.2.3	Testing protocol	154
7.2.4	Gearing in the Flexodeal framework	155
7.3	Results	157
<b>8</b>	<b>Conclusions and future work</b>	<b>162</b>
8.1	Summary of contributions	162

8.2 Future work . . . . .	165
8.2.1 Mass-enhanced muscle models in 1D . . . . .	165
8.2.2 Hu-Washizu formulations for skeletal muscle . . . . .	165
8.2.3 A posteriori error estimator . . . . .	166
8.2.4 Nonlinear solvers, preconditioners, and parallel computing . . . .	166
8.2.5 Validation, modifications, and further applications of Flexodeal . . .	167
8.3 Conclusions . . . . .	167
<b>Bibliography</b>	<b>168</b>
<b>Appendix A Force relationships</b>	<b>184</b>
A.1 Forces used in 1D experiments . . . . .	184
A.2 Forces used in 3D experiments . . . . .	184

# List of Tables

Table 2.1	List of parameters for the mass-enhanced and massless models. The muscles listed in the table are the <i>medial gastrocnemius</i> (MG), <i>semi-tendinosus</i> (ST), and <i>vastus medialis</i> (VM). . . . .	21
Table 2.2	List of MATLAB <sup>®</sup> built-in solvers in use. . . . .	24
Table 2.3	Computation times (in hours) for each muscle-task combination at scales 1 and 10 for the full 25 seconds of available data using the mass-enhanced model. . . . .	26
Table 3.1	Variation in the musculoskeletal Reynolds number $\text{Re}_{MSK}$ when a scaling factor $s$ is introduced for two different maximum (unloaded) strain rates ( $5 \text{ s}^{-1}$ and $10 \text{ s}^{-1}$ ). Here, $\rho_0 = 1.060 \text{ kg m}^{-3}$ , $\sigma_0 = 200 \text{ kPa}$ , $L_{\text{mus}}^{\text{opt}} = 0.3 \text{ m}$ . . . . .	44
Table 4.1	Error behaviour for each of the proposed methods. Left three columns: convergence in time ( $L^\infty$ norm) with fixed space mesh size ( $\Delta x = L/8 = 62.5 \text{ mm}$ ). Right three columns: convergence in space ( $L^2$ norm) with fixed time step size $\Delta t = 10^{-5} \text{ s}$ . . . . .	63
Table 4.2	Performance of Matlab's adaptive solvers for the MOL system (4.3.32) and the lengthening experiment using the sinusoidal profile (4.7.5) as boundary condition ( $\Delta x = L/64$ ). For <code>ode23s</code> , the Jacobian was (numerically) computed at each time step by the solver. . . . .	72
Table 5.1	Constants in the SEFs defining the base material component of muscle tissue. . . . .	94
Table 5.2	Constants in the SEF defining intramuscular fat. . . . .	94
Table 5.3	Constants in the SEF defining tendon and aponeurosis. . . . .	95
Table 6.1	Minimum quadrature order required depending on the type of simulation (dynamic or quasi-static) and finite element polynomial degree. .	120
Table 6.2	Contents of the file <code>cell_data_main-3d-N.data</code> . . . . .	126
Table 6.3	Contents of the file <code>cell_data_tensors-3d-N.data</code> . Each tensor is stored in row order, that is, the 9 columns contain information of the (1,1), (1,2), (1,3), (2,1), ..., (3,2), and (3,3) components. . . . .	127

Table 6.4	Errors and convergence rates for $\mathbf{U}$ , $p$ , and $D$ measured at time $t = T$ for different time step sizes $\Delta t$ using a dynamic simulation. . . . .	133
Table 6.5	Errors and convergence rates for $\mathbf{U}$ , $p$ , and $D$ measured at time $t = T$ for different grid refinement levels (GRL) using a dynamic simulation. . . . .	133
Table 6.6	Errors and convergence rates for $\mathbf{U}$ , $p$ , and $D$ at different grid refinement levels (GRL) using a quasi-static simulation. . . . .	134
Table 7.1	Range of prescribed strain rates (PSR) $\dot{\varepsilon}_M^*$ at the $+x$ end of the domain for the shortening phase of the experiment. Each PSR can be multiplied by the initial length of the muscle $L_{mus}$ to obtain a prescribed (shortening) velocity (PV). Furthermore, we compare these values with the computed mean muscle velocity (MMV), where we observe $MMV \approx \frac{1}{2}PV$ . . . . .	158
Table A.1	Cubic spline coefficients for the active force-length relationship $\hat{F}_A$ used for 1D experiments. . . . .	185
Table A.2	Cubic spline coefficients for the passive force-length relationship $\hat{F}_P$ used for 1D experiments. . . . .	185
Table A.3	Cubic spline coefficients for the force-velocity $\hat{F}_V$ relationship used for 1D experiments. . . . .	186
Table A.4	Cubic spline coefficients for the tendon force-length relationship $\hat{F}_T$ used for 1D experiments. . . . .	186
Table A.5	Parameters describing the muscle active stress-stretch relationship $\hat{\sigma}_A$ used for 3D experiments. . . . .	187
Table A.6	Parameters describing the muscle passive stress-stretch relationship $\hat{\sigma}_P$ used for 3D experiments. . . . .	188
Table A.7	Parameters describing the muscle passive stress-strain-rate relationship $\hat{\sigma}_V$ used for 3D experiments. . . . .	188
Table A.8	Parameters describing the aponeurosis stress-stretch relationship $\hat{\sigma}_{apo}$ used for 3D experiments. . . . .	188

# List of Figures

Figure 1.1	The structure of skeletal muscle at different length scales [36]. . . . .	2
Figure 1.2	Different types of muscle architectures. Source: [21] (Access for free at <a href="https://openstax.org">openstax.org</a> ). . . . .	4
Figure 1.3	Huxley-type muscle model. The myosin binding site (M) oscillates around the origin (O) and can bind to the actin head (A) for $x > 0$ . . . . .	5
Figure 1.4	Hill-type muscle model, showing the active contractile element (CE), the passive parallel element (PEE), and the series elastic element (SEE). The force $F_T$ exerted by the SEE is balanced by the horizontal component of $\vec{F}_M$ , i.e. $F_m \cos(\beta)$ , where $\beta$ is the pennation angle of the muscle. . . . .	6
Figure 1.5	Force relationships for different muscles in a frog. A: active force $\hat{F}_L$ (thin dashed line). P: passive force $\hat{F}_P$ (thin solid line), T: total force $\hat{F}_L + \hat{F}_P$ (thick line). Adapted from [159]. . . . .	7
Figure 2.1	Sketch of an MTU with dimensions characterized by the muscle and tendon lengths, respectively $L_M$ and $L_T$ . Left: initial state ( $t = 0$ ). Right: deformed state after shortening ( $t > 0$ ). . . . .	16
Figure 2.2	Force-length (FL) and force-velocity (FV) relationships that are part of Hill's muscle model (2.2.3). . . . .	17
Figure 2.3	(A) A simple Hill-type model of the MTU (muscle region in pink, tendon region in grey) using massless springs. Depicted here are the (active) contractile element (CE), the passive elastic element (PEE), and the series elastic element (SEE) representing the tendon. (B) A multibody model of the MTU that does not neglect the mass of the muscle, which is equally distributed throughout the muscle segment. . . . .	18
Figure 2.4	Tendon FL relationship (left) with its toe region shown in detail (right). . . . .	19
Figure 2.5	Example traces of the data (muscle: ST, task: running) used as input for the one-dimensional massless and mass-enhanced models. In this case, the activation $\hat{a}$ has been computed from the excitation $\hat{u}$ using Zajac's ODE (2.2.5). . . . .	23

Figure 2.6	Traces of muscle strains ( $\lambda_M$ ) and strain rates ( $\dot{\varepsilon}_M$ ) as the relative tolerance in the ODE solver is varied while the absolute tolerance is fixed to $10^{-10}$ . . . . .	25
Figure 2.7	Average time step size $\Delta t$ in the mass-enhanced model as the relative tolerance decreases while the absolute tolerance is fixed to $10^{-10}$ . . . . .	25
Figure 2.8	Predicted (normalized) forces when the scaling parameter is unchanged (i.e. $s = 1$ ; A) and when $s = 10$ (B) for 9 different muscle-task combinations. RMSE computed using the data range shown in the figures. . . . .	27
Figure 2.9	Predicted dynamics using the massless (dashed black lines) and mass-enhanced (solid blue line) models for the ST muscle during running. From top to bottom, the first row shows the (given) muscle excitation and (computed) activation, then the (computed) muscle strain $\varepsilon_M$ , muscle strain rate $\dot{\varepsilon}_M$ , tendon strain $\varepsilon_T$ , and normalized muscle force $\hat{F}_M = F_M/F_0$ . . . . .	29
Figure 2.10	Traces of muscle strains ( $\lambda_M$ ), strain rates ( $\dot{\varepsilon}_M$ ), and (normalized) muscle force $\hat{F}_M$ as the number of masses vary in the mass-enhanced model: from $N = 0$ (second row, i.e. massless model), $N = 2$ (third row), up to $N = 128$ (last row). For reference we have added the computed activation in the first row. . . . .	30
Figure 3.1	(A) Active and passive FL relationships. The region $\lambda_M < 1$ corresponds to the ascending limb (in blue) since the curve has a positive slope. In turn, the region $\lambda_M > 1$ corresponds to the descending limb (in ochre) which has a distinctive negative slope. (B) When active and passive forces are added, they form the <i>total</i> FL relationship, which typically has a dip region (i.e. a region with negative slope) around $1 < \lambda_M < 1.35$ . . . . .	32
Figure 3.2	Mass-enhanced muscle model adapted for an isometric contraction. Here, the sum of all element lengths (i.e. $\sum_{i=1}^N l_i = L_M$ ) is fixed. . . . .	34
Figure 3.3	Stability of an isometric contraction according to the system of ODEs (3.2.1). The elements (as well as the muscle) are stretched initially at around 85% (left), 115% (middle), and 145% (right) of the muscle's optimal length. At an initial stretch of 115%, the descending limb instability causes the segments to bifurcate to two different lengths. . . . .	37
Figure 3.4	Forces in the stabilized model (3.3.12). When the base material component (yellow) is added to the active (blue) and passive (red) forces, the total force (black) is a monotonically increasing function. . . . .	42

Figure 3.5	Stability of an isometric contraction according to the system of ODEs (3.3.12). As before, the elements (as well as the muscle) are stretched initially at around 85% (left), 115% (middle), and 145% (right) of the muscle's optimal length. In all cases, the contractions are stable since the derivative of the total force (made of active, passive, and base material components) is always positive. . . . .	42
Figure 4.1	Example of overshooting in the velocity variable, which causes even higher oscillations in the acceleration. . . . .	47
Figure 4.2	Mesh for the interval $[0, L]$ . . . . .	50
Figure 4.3	Strains (top half) and strain rates (bottom half) for the lengthening experiment using the $C^\infty$ boundary condition (4.7.3) at four different locations: $x = 0.25L$ , $x = 0.5L$ , $x = 0.9L$ , and $x = L$ . . . . .	66
Figure 4.4	Strains over $t \in [0, 2]$ (top half) and a zoomed version to $t \in [0, 0.2]$ (bottom half) at four different locations: $x = 0.25L$ , $x = 0.5L$ , $x = 0.9L$ , and $x = L$ . Lengthening experiment performed using the linear profile (4.7.4). . . . .	67
Figure 4.5	Strains over $t \in [0, 1]$ (top half) and a zoomed version to $t \in [0, 0.25]$ (bottom half) at four different locations: $x = 0.25L$ , $x = 0.5L$ , $x = 0.9L$ , and $x = L$ . Lengthening experiment performed using the sinusoidal profile (4.7.5). . . . .	68
Figure 4.6	Strain rates over $t \in [0, 2]$ (top half) and a zoomed version to $t \in [0.58, 0.65]$ where the (prescribed) strain rate jumps from $0.2 \text{ s}^{-1}$ to $0 \text{ s}^{-1}$ (bottom half) at four different locations: $x = 0.25L$ , $x = 0.5L$ , $x = 0.9L$ , and $x = L$ . Lengthening experiment performed using the linear profile (4.7.4). . . . .	69
Figure 4.7	Strain rates over $t \in [0, 1]$ (top half) and a zoomed version to $t \in [0, 0.25]$ showcasing the nonzero velocity at the beginning (bottom half) at four different locations: $x = 0.25L$ , $x = 0.5L$ , $x = 0.9L$ , and $x = L$ . Lengthening experiment performed using the sinusoidal profile (4.7.4). . . . .	70
Figure 4.8	Strain (left) and strain rate (right) profiles at four different locations ( $x = 0.25L$ , $x = 0.5L$ , $x = 0.9L$ , and $x = L$ ) for the lengthening experiment using the linear profile (4.7.4) and an IMEX time stepping scheme ( $\Delta x = L/64$ , $\Delta t = 0.5 \cdot 10^{-6}$ ). . . . .	71
Figure 4.9	Strain rates (left column) and time step sizes (right column) for the Matlab solvers that finished solving the lengthening experiment (see Table 4.2). . . . .	73

Figure 5.1	Deformation of a body from its reference configuration $\mathcal{B}_0$ to a current configuration $\mathcal{B}_t = \varphi(\mathcal{B}_0, t)$ , showing also the displacement $\mathbf{U}(\mathbf{X}, t)$ of a typical particle from $\mathbf{X} \in \mathcal{B}_0$ to $\mathbf{x} \in \mathcal{B}_t$ . The motion $\varphi$ also maps the Dirichlet boundary $\Gamma_{D,0}$ to $\Gamma_{D,t}$ (solid curves), as well as the Neumann boundary $\Gamma_{N,0}$ to $\Gamma_{N,t}$ (dashed curves). . . . .	78
Figure 5.2	Transformation of surface elements. In the reference configuration $\mathcal{B}_0$ , we observe a surface element $dS$ (with unit normal $\mathbf{N}$ ) and a traction vector $\mathbf{T}$ . Similarly, in the current configuration $\mathcal{B}_t$ , we have a surface element $ds$ (with unit normal $\mathbf{n}$ ) and a traction vector $\mathbf{t}$ . . . . .	82
Figure 5.3	Fibre orientations fields $\mathbf{a}_0$ in the reference configuration and $\mathbf{a} = \mathbf{F}\mathbf{a}_0$ in the deformed configuration. A fibre can be represented as an infinitely small line element $dl$ with orientation $\mathbf{a}_0$ that passes through $\mathbf{X} \in \mathcal{B}_0$ and deforms to an element of length $\lambda dl$ with orientation $\mathbf{a}$ , where $\lambda$ is the fibre stretch field. The angle between the orientation $\mathbf{a}$ and the line of action vector $\hat{\ell}$ is called the <i>pennation</i> angle and is denoted by $\beta$ . The initial pennation angle $\beta_0$ is simply the angle between $\mathbf{a}_0$ and $\hat{\ell}$ . . . . .	83
Figure 5.4	Hill's model depicted as a manifold in which the fibre stretch $\lambda$ and the fibre strain rate $\dot{\varepsilon}$ can vary simultaneously according to (5.2.5). We also show the curves $\sigma_{Hill}(\lambda, 0)/\sigma_0$ (red) and $\sigma_{Hill}(0, \dot{\varepsilon})/\sigma_0$ (black), which correspond to the total force-length (FL) and force-velocity (FV) relationships in Figure 2.2. . . . .	91
Figure 5.5	Three-dimensional continuum representation of the muscle-tendon unit showing its main three components: muscle tissue, aponeurosis, and tendon. . . . .	96
Figure 6.1	Fibre force relationships implemented in <b>Flexodeal</b> (muscle and aponeurosis) and <b>Flexodeal Lite</b> (muscle only). The code allows for continuously varying activation profiles, but for reference, we choose 6 different choices of activation level (from 0% to 100%) to represent the influence of the activation level on the fibre force. . . . .	117
Figure 6.2	An example of the <code>.dat</code> files containing the necessary control points to define time-dependent curve. These particular boundary strain and activation profiles are part of the default experiment in <b>Flexodeal Lite v1.5.4</b> . . . . .	119

Figure 6.3	Muscle block geometry, including a 3D view (top) and the main quantities that describe the muscle architecture (bottom). In particular, the fibres are parallel to each other and oriented with an initial pennation angle $\beta_0$ in the $xz$ plane, which results in an initial orientation field $\mathbf{a}_0(\mathbf{X}) = \langle \cos(\beta_0), 0, \sin(\beta_0) \rangle$ for any $\mathbf{X} \in \mathcal{B}_0$ . . . . .	130
Figure 6.4	Visualization of the displacement $\mathbf{U}$ , pressure $p$ , dilatation $D$ , and fibre stretch $\lambda$ fields for the convergence study described in Section 6.3. Left column: initial state ( $t = 0.0$ s) showing $(\mathbf{U}, p, D) = (\mathbf{0}, 0, 1)$ and $\lambda = 1$ . Right column: end state ( $t = 0.2$ s). . . . .	132
Figure 6.5	Relative $L^2$ error in the displacement, pressure, and dilatation variables, measured at the end of the simulation time, using a dynamic computation. Left: error as $\Delta t$ decreases while the grid refinement level is fixed to 3. Right: error as the grid refinement level increases while keeping $\Delta t = 0.01$ s. . . . .	133
Figure 6.6	Relative $L^2$ error in the displacement, pressure, and dilatation variables, measured at the end of the simulation time, using a quasi-static computation. Error computed using a fixed time step size $\Delta t = 0.01$ s. . . . .	134
Figure 6.7	Idealization of a medial gastrocnemius muscle according to Ross et al. [164]. Top row: main dimensions describing the muscle architecture. Bottom row: (computational) boundary IDs for each face. The muscle fibres (grey region) run parallel to each other at an angle $\beta_0$ with respect to the line of action $\hat{\ell}$ . In turn, the aponeurosis fibres (white regions) run parallel to the longitudinal direction of the aponeurosis. The parameters that define this domain are the muscle length $L_{mus}$ , aponeurosis length $L_{apo}$ , aponeurosis height $H_{apo}$ , muscle width $W_{mus}$ , and the pennation angle $\beta_0$ . The muscle fibre length $L_f$ and angle $\alpha_0$ can be computed as in Equation (6.4.1). . . . .	136
Figure 6.8	3D view of the meshes used to compute the force-length curves in Figures 6.9 (left) and 6.10 (right). The mesh on the left only contains voxels with muscle tissue. In turn, the mesh on the right, contains voxels of muscle tissue, along with a pair of thin aponeurosis layers on the $+z$ and $-z$ faces of this domain. . . . .	137
Figure 6.9	Force-length curves of whole muscle computed using <b>Flexodeal Lite</b> using a parallel-fibred muscle block geometry and different base material factors: $s_{base} = 1$ (top row), $s_{base} = 1.5$ (middle row), $s_{base} = 10$ (bottom row). Force measured at the $+x$ end of the domain. . . . .	139

Figure 6.10	Force-length curve of whole muscle computed in <b>Flexodeal</b> using the idealized MG described in Figure 6.7 (initial pennation angle $\beta_0 = 15.3^\circ$ ). Force measured at the face where the moving Dirichlet condition was applied, which also is a face where there is only aponeurosis tissue. . . . .	140
Figure 6.11	Stress-stretch relationships for the base material components of muscle (left) and aponeurosis (right), normalized by their maximum isometric stress $\sigma_0$ , for the particular case of uniaxial extension. . . . .	140
Figure 6.12	Evolution of the active fibre stress when the muscle is passively lengthened and then activated to 100% (blue path) and when the muscle is activated to 100% then lengthened (red path). . . . .	141
Figure 6.13	Computed force ( $+x$ component on the fixed $+x$ end) using the quasi-static code (left) and the dynamic code (middle) for different initial pennation angles $\beta_0$ , and the relative difference between them (right). . . . .	143
Figure 6.14	Computed mean pennation angle $\text{avg}_S(\beta)$ using the quasi-static code (left) and the dynamic code (middle) for different initial pennation angles $\beta_0$ , and the relative difference between them (right). . . . .	144
Figure 6.15	Computed mean fibre stretch $\text{avg}_S(\lambda)$ using the quasi-static code (left) and the dynamic code (middle) for different initial pennation angles $\beta_0$ , and the relative difference between them (right). . . . .	145
Figure 6.16	Post-processed mean fibre strain rate $\text{avg}_S(\dot{\varepsilon})$ obtained from a quasi-static computation using mean fibre stretch data (left) and computed mean fibre strain rate using the dynamic code (middle) for different initial pennation angles $\beta_0$ , and the relative difference between them (right). . . . .	145
Figure 6.17	Computational representation of the human MG used in Section 6.6 derived from MRI shown in the XZ plane (top) and in the XY plane (bottom). . . . .	146
Figure 6.18	Top to bottom: traces of activation, boundary strain, average fibre stretch, average normalized fibre strain rate, average pennation angle, force (x component at the $+x$ end of the domain) and volume ratio, for the experiment described in Section 6.6. . . . .	148
Figure 6.19	Snapshots of the displacement field (magnitude, in m) at five different points of the simulation described in Section 6.6. . . . .	149

Figure 7.1	(A) Computational domain in its reference configuration $\mathcal{B}_0$ , which corresponds to a muscle block of dimensions $L_{mus} \times H_{mus} \times W_{mus}$ , including the line of action vector $\hat{\ell} = \langle 1, 0, 0 \rangle$ and the region slab( $\mathcal{B}_0$ ) $\subset \mathcal{B}_0$ (in orange) used to compute average quantities in Section 7.2.4. (B) Sagittal ( $xz$ ) plane showing a representative fibre (red line), and the initial pennation angle $\beta_0$ . . . . .	152
Figure 7.2	Midsection of the muscle block perpendicular to the $x$ -axis (i.e. the plane that slices the domain at $x_1 = L_{mus}/2$ ) in the reference configuration $\mathcal{B}_0$ (left) and in the deformed configuration $\mathcal{B}_T$ at time $t = T$ (right). The figure also shows the location of the markers $\mathbf{X}_L$ , $\mathbf{X}_R$ , $\mathbf{X}_T$ , and $\mathbf{X}_B$ in the reference configuration (with their counterparts $\mathbf{x}_L$ , $\mathbf{x}_R$ , $\mathbf{x}_T$ , and $\mathbf{x}_B$ in the deformed configuration) used to compute the muscle thickness and width ( $H_{mus}^T$ and $W_{mus}^T$ ) at the end of the simulation. . . . .	155
Figure 7.3	Representative computational experiment used to compute muscle gearing ( $\dot{\varepsilon}_M^* = 2 \text{ s}^{-1}$ , $a_{max} = 1.0$ ). Left column: Evolution of the activation, muscle force (x component, computed at the $+x$ face), mean muscle and fibre velocities (averaged over slab( $\mathcal{B}_0$ )), muscle thickness and width, and pennation angle throughout the experiment. Right column: Evolution of the fibre stretch $\lambda(\mathbf{X}, t)$ at four different times: initial state at $t = 0 \text{ s}$ (A), end of the passive stretch phase at $t = 0.1 \text{ s}$ (B), end of activation ramp at $t = 0.2 \text{ s}$ (C), and end state at $t = 0.2 + 0.1/\dot{\varepsilon}_M^*$ . . . . .	156
Figure 7.4	Mean fibre velocity (left) and normalized muscle force (right) as functions of MMV and maximum activation (measured at the end of each simulation, i.e. when the muscle block returned to its initial length). . . . .	158
Figure 7.5	Mean pennation angle (left) and its rate of change (right) as functions of MMV and maximum activation (measured at the end of each simulation, i.e. when the muscle block returned to its initial length). . . . .	159
Figure 7.6	Muscle gearing as a function of (normalized) muscle force and MMV. . . . .	160
Figure 7.7	Muscle gearing as a function of (normalized) muscle force for different maximum activation levels. . . . .	160
Figure 7.8	Muscle width and thickness at the end of the active shortening phase, shown here as a function of maximum activation level and MMV. . . . .	161

# Chapter 1

## Introduction

The musculoskeletal system can only be described as a marvel of nature. Its components are not only capable of producing force and sustaining loads but can also adapt to changing environments in remarkable ways. At the core of this system is skeletal muscle: a material that can actively contract, deform nonlinearly, and respond to complex mechanical demands. This makes the elastodynamics of this biological tissue a fascinating area of research at the intersection of applied mathematics, physiology, and scientific computing.

Most of what we know so far about how and why muscles deform comes from tensile experiments using single muscle fibres [85] and small muscles, such as those from frogs [72, 93], rats [69], and cats [153]. But as computational power increases, researchers have started to use computational models to conduct experiments that may not be feasible to perform *in vivo*. Nowadays, these models are used in a variety of settings, such as to predict the outcome of surgical procedures [188], to study the stiffness of muscle affected by cerebral palsy [103], to study muscle energetics [196], to explore motor control [197], among others.

By model, we refer to the set of mathematical elements that describe the elastodynamics of skeletal muscle tissue. This rather generic description contrasts with approaches that are more limited in scope, such as “animal models” (e.g. “rat models” [143, 205]) in which a different animal yields a different model, or computational models that are tied to the particular experimental setup they wish to explain (in this case, two different muscles cannot be described by the same model [38, 191]).

Before exploring the different approaches used to model skeletal muscle tissue and the main contributions of this thesis, let us discuss the main reasons that make skeletal muscle tissue behave uniquely from a solid mechanics perspective.

### 1.1 Muscle anatomy

Skeletal muscle is a highly-complex biological tissue that is capable of generating work and power for different tasks, such as postural control, locomotion, stabilization of bones and joints, and heat generation [86, 111]. The mechanics of its deformation involve several

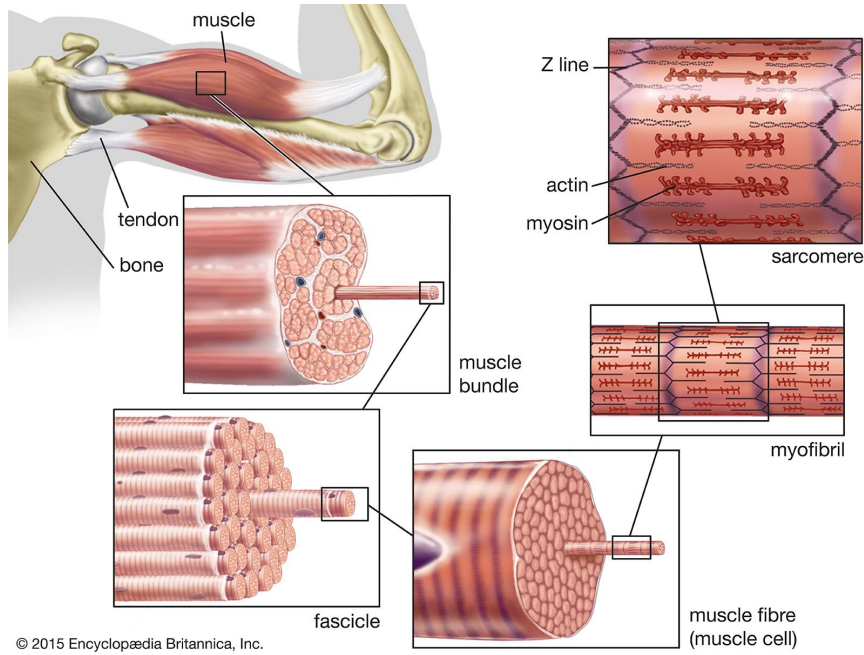


Figure 1.1: The structure of skeletal muscle at different length scales [36].

length scales (see Figure 1.1), from sarcomeres in the scale of micrometres to the size of whole skeletal muscles in the scale of cm, or even metres for larger mammals [111].

At its core, skeletal muscle tissue is made of tubular muscle cells called *muscle fibres*. These fibres are embedded in a matrix of connective tissue known as the *extracellular matrix* (ECM). This connective tissue matrix not only provides mechanical continuity for force transmission but also plays vital roles in structural integrity and mechanotransduction. Interwoven within this matrix are vascular networks that ensure metabolic support, along with neural components that facilitate activation through motor innervation [70, 111, 119].

Muscle fibres contain many *myofibrils* which are rod-like structures composed by repeating units called *sarcomeres* (see Figure 1.1). At about  $2.2 \mu\text{m}$  in length [37], the sarcomere is the fundamental unit in muscle. Fibrous proteins in its interior (most notably *actin* and *myosin*, respectively the thin and thick filaments) slide past each other (this is the sliding filament theory) to form *cross-bridges* that generate *active force* (this is the cross-bridge theory) [76, 94].

Muscle contraction begins with an *activation* phase. It starts with a nerve signal, or action potential, reaching the end of a motor neuron, which causes the depolarization of the cell membrane of the muscle fibre. This chemical signal triggers another action potential in the muscle fibre, which travels along the surface and down into T-tubules. The signal then reaches the sarcoplasmic reticulum, causing it to release calcium ions into the muscle cell. Calcium binds to troponin, a protein on the thin filament, which causes a shift in the troponin-tropomyosin complex and exposes binding sites on actin. With these sites

exposed, the myosin hydrolyzes adenosine triphosphate (ATP), which causes its globular head to attach to the actin to form a cross-bridge that ultimately generates active force [171].

Whether muscle fibres are activated or not, stretching them beyond their resting length generates a *passive* response largely attributed to two additional proteins: titin and nebulin, which contribute to the overall structure and stability of the muscle. Titin is the largest known protein in the human body and spans half the length of the sarcomere, connecting the myosin to the Z-disks (or Z lines in Figure 1.1) [137, 138]. Functionally, titin acts as a molecular spring, generating passive force when the muscle is stretched, resisting overstretch and helping in the restoration of the original length of sarcomeres following extension.

## 1.2 Muscle architecture

Macroscopically, muscle fibres are organized in a way that optimizes muscle function. This structure, known as *muscle architecture*, is defined by Lieber as “the arrangement of muscle fibres within a muscle relative to the axis of force generation” [111]. In this definition, it is implicitly assumed that the axis of force generation refers to the *principal* component of the force vector and that it coincides with the muscle’s line of action. The latter is often defined as direction vector of the line between origin and tendon insertion (although more intricate characterizations might be needed) [107].

There exist several types of muscle architectures (see Figure 1.2). Lieber & Fridén [113] in particular mention three groups: (a) parallel, in which the fibres extend parallel to the muscle’s axis of force generation, (b) pennate, in which fibres run mostly at a single angle relative to axis of force generation, and (c) multipennate, in which fibres run at different angles relative to the axis of force generation. Muscle architecture is determined experimentally, usually through four parameters [113]:

1. Muscle length, which is defined as “the distance from the origin of the most proximal muscle fibres to the insertion of the most distal fibres” [111],
2. Fibre length, which is obtained from the length of small fibre bundles (given how hard it is to extract a single fibre),
3. Pennation angle, which is the angle between the fibres and the axis of force generation,
4. Physiological cross-sectional area (PCSA), which represents the sum of the cross-sectional areas of all muscle fibres. It can be computed as:

$$\text{PCSA} = \frac{\text{muscle mass}}{\text{muscle density} \times \text{fibre length}}.$$

These descriptors can vary significantly during contraction. For instance, the human medial gastrocnemius has a pennation angle of about  $20^\circ$  at rest, but this angle can go

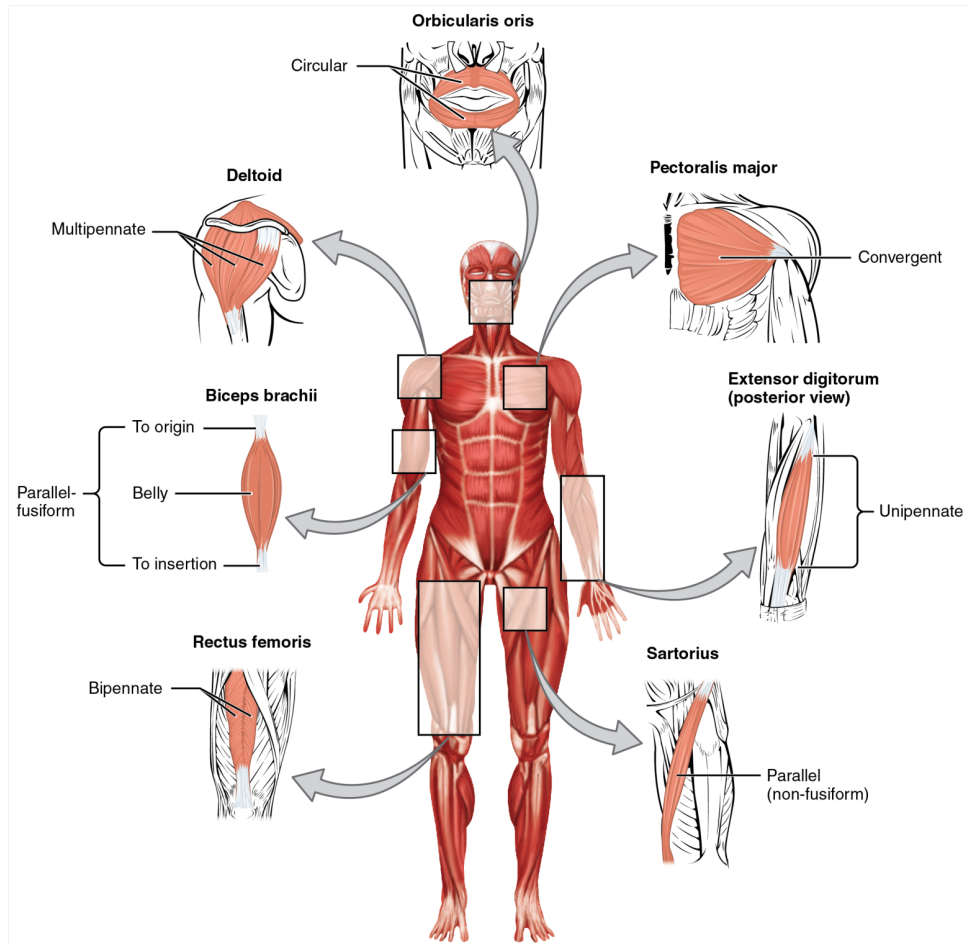


Figure 1.2: Different types of muscle architectures. Source: [21] (Access for free at [openstax.org](https://openstax.org)).

up to  $45^\circ$  upon contraction [113]. Such dynamic architectural changes profoundly influence muscle function, yet their effects they are difficult to quantify *in vivo* due to experimental and ethical constraints. This leads us to the necessity of mathematical models of muscle that can be studied with *in silico* experiments. We discuss two fundamental models first, to then dive deeper into computational models.

### 1.3 Fundamental models of skeletal muscle

Muscles generate force to perform mechanical functions essential for movement, stability, and interaction with the environment. Thus, force is one of the most important physiological quantities used to characterize muscle function. Measuring force *in vivo*, however, is virtually impossible, as it often involves surgical procedures that implant buckles or transducers in a subject's tendon [22, 101]. Therefore, muscle force is instead *estimated* using non-invasive methods such as joint torque measurements via dynamometry, fibre kinematics

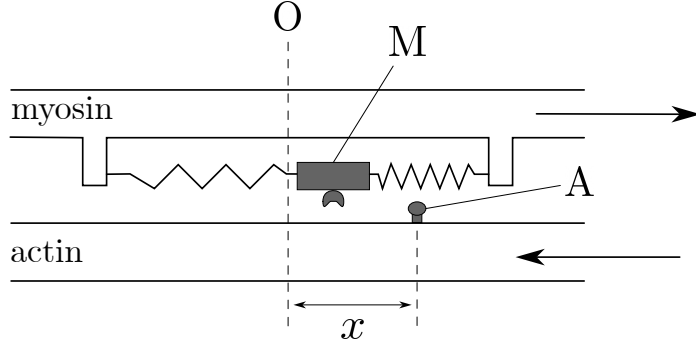


Figure 1.3: Huxley-type muscle model. The myosin binding site (M) oscillates around the origin (O) and can bind to the actin head (A) for  $x > 0$ .

obtained from ultrasonography, and muscle activation signals from surface electromyography (EMG). The collected data are then used as input for muscle models, which can be broadly categorized into: (a) mechanistic models, which are based on the interaction between actins and myosins, and (b) phenomenological models, which are based on the mesoscopic and macroscopic muscle behaviour.

Mechanistic models are rooted in the work by H. F. Huxley [93] in 1957, and therefore they are known as *Huxley-type models*. Here, it is of interest to first find the distribution of the fraction of cross-bridges that could be attached in a sarcomere [72, 93]. Denoting the latter by  $n(x, t)$ , the goal is to solve the first-order, hyperbolic partial differential equation (PDE):

$$\frac{\partial n}{\partial t} - v(t) \frac{\partial n}{\partial x} = (1 - n)\mathfrak{f}(x, a) - n\mathfrak{g}(x),$$

where  $v = \frac{dx}{dt}$  is the speed at which actin and myosin filaments pass each other (see Figure 1.3),  $\mathfrak{f}(x, a)$  and  $\mathfrak{g}(x)$  are respectively the attachment and detachment rates of the cross-bridges, and  $a = a(t)$  is a function describing the activation of muscle [127]. The active force  $F_{CE}$  is then computed as the first moment of the distribution  $n$ , that is,

$$F_{CE}(t) = k \int_{-\infty}^{\infty} n(x, t) x dx,$$

where the constant  $k > 0$  is the stiffness of the cross-bridges.

In turn, phenomenological models (the main focus of this thesis) are based on the work by F. E. Zajac [208] in 1989, which is further based on the developments by A. V. Hill, primarily from his 1938 article [85]. Here, the muscle-tendon unit (MTU) is described as an actuator that contains a contractile element (CE) that generates a force  $F_{CE}$  and a passive elastic element (PEE) that generates a force  $F_{PEE}$ . These two elements are connected in parallel, and the combination of them—representing the muscle part of the MTU—is connected to a series elastic element (SEE) which represents the tendon part of the MTU. We show this arrangement in Figure 1.4. These models are commonly known as *Hill-type*

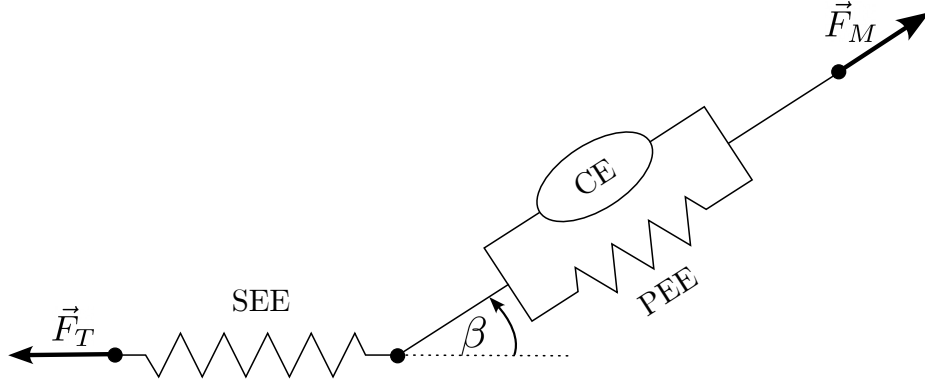


Figure 1.4: Hill-type muscle model, showing the active contractile element (CE), the passive parallel element (PEE), and the series elastic element (SEE). The force  $F_T$  exerted by the SEE is balanced by the horizontal component of  $\vec{F}_M$ , i.e.  $F_m \cos(\beta)$ , where  $\beta$  is the pennation angle of the muscle.

*muscle models* because, in this case, the force a muscle generates follows the equation:

$$F_M(a, \lambda, \dot{\lambda}) = F_{CE} + F_{PEE} = F_0 \left[ a(t) \hat{F}_A(\lambda) \hat{F}_V(\dot{\lambda}) + \hat{F}_P(\lambda) \right], \quad (1.3.1)$$

where  $0 \leq a(t) \leq 1$  represents the activation level of the muscle,  $\lambda$  is the normalized muscle length, and  $\dot{\lambda}$  is the normalized muscle velocity. Furthermore,  $\hat{F}_A$ ,  $\hat{F}_V$ ,  $\hat{F}_P$  are known respectively as the active force-length, force-velocity, and passive force-length relationships, which describe how the muscle force changes with muscle length and muscle velocity. In particular, the region of the total force-length relationship that has a negative slope (when it is present) is called *descending limb*. In this expression,  $F_0$  is called the maximum isometric force and is defined as the greatest force a muscle can generate while contracting without changing its length. The length at which this occurs is known as the optimal length. In these models, muscle is assumed to behave like a scaled up muscle fibre, and therefore, the force curves needed for this model can be obtained from either bundles of fibres or from whole muscles. Furthermore, each muscle can have its own set of force relationships, which for instance, may or may not have a descending limb (see Figure 1.5).

## 1.4 Computational models

In silico modelling of skeletal muscle provides a powerful framework for investigating muscle mechanics beyond the limits of experimental observation. By simulating muscle behaviour computationally, these models enable the analysis of important physiological variables (such as fibre stretch, fibre strain rates, and whole muscle forces) that are otherwise difficult to measure *in vivo* (and even in controlled *in situ* or *in vitro* experiments). In addition, computational models can be used to analyze “what-if” scenarios in which either the (resting) muscle architecture or its constitutive elements are directly modified.

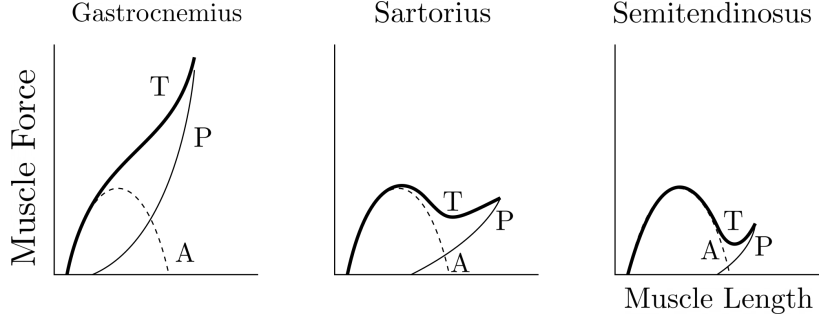


Figure 1.5: Force relationships for different muscles in a frog. A: active force  $\hat{F}_L$  (thin dashed line). P: passive force  $\hat{F}_P$  (thin solid line), T: total force  $\hat{F}_L + \hat{F}_P$  (thick line). Adapted from [159].

From the definition of muscle architecture in Section 1.2 (and by simply looking at our muscles) we observe that muscle deformation occurs across all three dimensions of Euclidean space. However, neither Huxley nor Hill-type models (as presented in the previous section) account for this behaviour. While there exist geometric models that can explain some of these shape changes (see, e.g., [49, 179]), the focus of this discussion (and this thesis) will be on computational models based on differential equations. Here, two main categories can be distinguished: 1D models based on ordinary differential equations (ODEs) where the focus is on simplicity and macroscopic behaviour, and 3D PDE-based models where the focus is on detailed spatio-temporal information.

Two-dimensional (2D) PDE-based models can be seen as simplifications of 3D models in which deformation in the out-of-plane direction is simply neglected. However, during contraction, muscles bulge in thickness *and* width in an attempt to conserve volume [19]. This translates into a “constant area” assumption [59] that brings almost no meaningful advantage over 1D representations, which already encapsulate the primary axial dynamics without excessive computational cost. Hence, they will not be discussed any further in this work.

#### 1.4.1 One-dimensional models

Hill-type models can be implemented in a computational setup directly, that is, the force a muscle generates can be estimated using (1.3.1), a given activation profile  $a(t)$ , and time traces of muscle length and velocity (unlike Huxley-type models, where an appropriate PDE solver must be considered). This is the basis of OpenSim: an open-source musculoskeletal modelling and simulation platform that enables the analysis of movement dynamics and estimation of muscle and joint forces using experimental kinematics, kinetics, and electromyography data [45]. Here, each muscle is modelled as a 1D spring that generates force according to (1.3.1), and therefore it is simple enough that allows for simulations involving multiple muscles and joints [23, 151, 157, 182]. OpenSim, along with AnyBody Modeling

System<sup>TM</sup>, are the prominent software choices for the analysis of skeletal muscle function and animal locomotion [67].

Nevertheless, the accuracy of these simulations decreases as the experiments drift away from the ideal conditions in which the force relationships in (1.3.1) were obtained, namely isokinetic or isometric contractions with maximal activation [47, 108, 129, 147]. Therefore, researchers continue to modify these 1D models to include many of the missing features from the original model, such as fatigue [146], history dependence [122, 166], mass, and inertial effects [73, 166, 167, 168].

In particular, mass effects were first studied computationally by Günther et al. [73] in which the mass of the muscle was spread out within a system of interconnected springs with linear dynamics, finding that larger mass slows down contraction times. Then, Ross et al. [166] developed a muscle model based on a damped harmonic oscillator whose dynamics counteract the action of an actuator that generates force according to (1.3.1). This idea was later applied by Ross & Wakeling [167] to a multibody system in which, similar to the work by Günther et al. [73], the mass is spread over many individual masses, interconnected by Hill-type actuators. Here, it was shown that the addition of mass affects the speed of contraction, specially during submaximal activation. This multibody model was also applied to a muscle-tendon unit by Ross & Wakeling [168] and Chen [41]. In particular, Chen evaluated the differences in force prediction between this multibody model (also known as the “mass-enhanced” model) and a massless model similar to that of Millard et al. [129] (without damping) for a set of human locomotion experiments, finding differences of up to 8% when the mass of the system is scaled by a factor of 10 and more pronounced differences for faster locomotion. In all the multibody systems mentioned so far, the number of masses in the system has been kept fixed to 16, given that Günther et al. [73] reported that for their case (linear dynamics) there was not a significant difference in the outputs when either 16 or 32 masses were considered.

#### 1.4.2 Three-dimensional models

From the point of view of solid mechanics, skeletal muscle is a fibre-reinforced, visco-hyperelastic, composite biomaterial that can sustain active and passive large deformations that are dynamic in nature [4, 164, 196]. Thus, physiologically-relevant computational models in 3D can be remarkably complex, and a universally accepted framework has yet to be established. While many existing models incorporate a Hill-type contractile component, others adopt alternative approaches, such as including a Huxley-type component [140] or omitting both paradigms all together [68, 139]. This section, however, is restricted to 3D models that explicitly include a Hill-type component.

The main idea is to use the principles of continuum mechanics to describe the deformation of skeletal muscle. A first approach consists of solving the so called *quasi-static*

problem: find a material displacement  $\mathbf{U}$  such that:

$$\mathbf{0} = \mathbf{Div} \mathbf{P}(\mathbf{U}), \quad (1.4.1)$$

Here,  $\mathbf{P}$  is the first Piola-Kirchhoff stress tensor which, in this case, is only assumed to depend on the displacement  $\mathbf{U}$ . In particular,  $\mathbf{P}$  is described using a strain-energy function (SEF)  $\Psi$ , which is further decomposed into volumetric and isochoric parts:

$$\Psi = \Psi_{iso} + \Psi_{vol}, \quad (1.4.2)$$

where the volumetric part  $\Psi_{vol}$  represents the near-incompressible behaviour of muscle [19]. In turn, the isochoric part  $\Psi_{iso}$  represents the constitutive elements of muscle, such as muscle fibres (whose response varies according to (1.3.1)) and the base material around them (assumed to be hyperelastic).

This approach can be first found for active muscle tissue in the works by Blemker [24, 25, 26] in 2004. It differs from previous finite element approaches (such as the one put forth by Johansson [96]) in the sense that muscle in 3D is no longer a scaled-up fibre (i.e. the entire volume has fibre properties with no base material around). In this way, muscle models that follow this approach can differ in the choice of force relationships, as well as what type of hyperelastic material (Neo-Hookean, Ogden, Mooney-Rivlin, Yeoh, etc.) should be used to represent the base material component (see, e.g., [80, 186]). Furthermore, Blemker's model is one of the default choices in 3D biomechanical modelling software ArtiSynth [116] and FEBio [117]. Following a similar approach as Blemker, Rahemi et al. [155, 156], Dominguez [54], and Wakeling et al. [196] implemented a quasi-static model of skeletal muscle deformation but this time using a three-field variational formulation by Simo et al. [180] that increases the robustness of the numerical method.

However, (1.4.1) does not include a velocity term, meaning that force-velocity effects are completely neglected. While it is possible to solve the problem:

$$\mathbf{0} = \mathbf{Div} \mathbf{P}(\mathbf{U}; \mathbf{V}), \quad (1.4.3)$$

where  $\mathbf{V} = \dot{\mathbf{U}}$  is the material velocity (see, for instance, [52, 80, 81, 120, 187]), the true effects of mass and inertia can only be seen in *fully dynamic* models, i.e. those that attempt to solve:

$$\rho_0 \ddot{\mathbf{U}} = \mathbf{Div} \mathbf{P}(\mathbf{U}, \mathbf{V}), \quad (1.4.4)$$

where  $\rho_0$  is the density of muscle (at rest). Despite its completeness in describing the 3D active deformation of skeletal muscle, this problem has received much less attention.

One of the first attempts at a fully dynamic 3D model was put forth by Johansson et al. [96] and Meier & Blickhan [124] in 2000. Here, although muscle is considered to have active

and passive properties (including force-velocity effects) as those of a fibre, the material is completely isotropic. In particular, [96] uses a two-field displacement-pressure formulation.

Then, Böll & Reese [30] in 2008 proposed a model of muscle in which fibres are rigid 1D trusses embedded in a 3D material. Furthermore, only a proportion of the body can be fully activated. A dynamic extension to the (now celebrated) work by Blemker et al. [26] from 2005 only appeared nearly 13 years later, in the works of Ross et al. [166], Dominguez [54], and Ross et al. [164]. Here, the three-field formulation from Wakeling et al. [196] is extended to include mass, inertial, and force-velocity effects. However, the numerical methods were not sufficiently robust to cover multiple cases of 100% activation (as noted by Tam [185]).

Unaware of the developments by Blemker in the early 2000s, Vavourakis et al. [192] in 2014 implemented a dynamic 3D finite element muscle model similar to that of Dominguez [54] but using a displacement-only formulation (as opposed to a three-field formulation). The numerical experiments in [192] reflect the challenging scenario when attempting realistic simulations of skeletal muscle. To model the active deformation of a quarter of a squid's tentacle with 477 voxels (including 371 hexahedral voxels) over 0.07 seconds of simulation time, a time step size of  $\Delta t = 0.25 \times 10^{-6}$  s were required with an implicit time stepping scheme (Newmark's average acceleration method [91]), and  $\Delta t = 0.5 \times 10^{-8}$  s when using an explicit time stepping scheme.

## 1.5 Stability of computational models

The *dynamical* stability of Hill-type muscle models has been recently criticized by Yeo et al. [206]. Using a 1D model with actuators connecting multiple masses in series (similar to that of Ross et al. [165]) the authors show that, the isometric contraction of fully active muscle can lead muscle segments to diverge to two completely different lengths when the contraction is performed along the descending limb of the force-length curve. The idea is not new, and a mathematical treatment of the problem can be found in the work by Zahalak [207] in 1997. However, because the authors in [206] incorrectly named this phenomenon as “numerical”, the idea that Hill-type muscle models can be “numerically unstable” has unfortunately gained traction (see, for example, [126, 174]).

Nevertheless, the fact that some force-length curves do have a descending limb is an interesting fact in itself, especially when it has been shown that active stretching can lead to muscle forces larger than its maximum isometric force (i.e., no descending limb). This phenomenon is known as *residual force enhancement* (RFE) [83] and it has been attributed to the protein titin [82]. Thus, many muscle models that include titin (as a separate, activation-dependent element) are considered “stable” (see, for example, [79, 128, 174]). However, the significance of titin is a matter of discussion [112], and other factors, such as the extracellular matrix (ECM), are also thought to bring stability to muscles [70].

The question of stability in 3D is much more difficult to answer. For instance, the dynamical stability of models such as Blemker's [26], as well as the development of an eigenvalue solver for active muscle deformation are still open problems. In turn, the numerical stability of 3D finite element models is associated to the polyconvexity of the strain-energy function that models the system [175]. In particular, Heidlauf et al. [79] developed a 3D muscle model that includes actin-titin interactions, and which therefore is stable given that the condition of polyconvexity is satisfied (see also [174]).

## 1.6 Main contributions and outline of this thesis

In this highly interdisciplinary work, a recurring challenge has been to mathematically formalize physiological concepts in order to obtain experimental data consistently and to integrate these into models. What do physiologists mean by concepts such as stability, gearing, isometric contractions? Precise definitions had to be made.

In this thesis, we develop a rigorous mathematical and scientific computing framework to study the nonlinear elastodynamics of 1D and 3D Hill-type muscle models, with an emphasis on adapting our mathematical definitions and numerical methods to the commonly-accepted physiological principles in this area.

In **Chapter 2**, we study the inertial effects due to the addition of mass in multibody 1D models of the muscle-tendon unit, especially when compared to a model that does not have mass. We first provide a mathematical description of the models, to then implement them in Matlab. Then, using experimentally-obtained data by Chen [41] and Dick et al. [46] from multiple muscles of the lower limb and multiple tasks of common human locomotion, such as walking, running, and cycling, we perform dynamic simulations that show not only the influence of mass for muscles of larger sizes, but also how the number of masses in the system affects the quality of the solutions, which may not necessarily follow the guidelines by Günther et al. [73].

In **Chapter 3**, we study the dynamical stability of the multibody muscle model discussed in Chapter 2, in particular, the so-called descending limb instability. We first show that the multibody model (which does show this instability) corresponds to a particular discretization of a 1D wave equation, which can be seen as a 1D reduction of 3D elasticity. Based on this fact, we consider a novel 1D continuum model of muscle that includes a base material contribution to stabilize the dynamical system, showing that there could be other muscle components (not necessarily titin as an activation-dependent element, for instance), that can provide dynamical stability to Hill-type muscle models.

In **Chapter 4**, we study different time stepping schemes for 1D Neo-Hookean deformation. Here, the main goal is to gather information about the performance of these methods on a stiff material similar to skeletal muscle tissue, with the intention of making an informed choice when choosing the time discretization for the fully dynamic 3D model. We performed

a systematic study of Newmark-type methods and we analyze the performance of first and second order implicit time stepping schemes in the presence of nonsmooth boundary conditions, with a focus on potential overshooting.

In **Chapter 5**, we develop a new Lagrangian framework for a fully dynamic 3D muscle model previously studied by Dominguez [54] (see also, [164]). We discuss the main continuum mechanics concepts needed to understand this model. In addition, we introduce mathematical definitions for important concepts, such as fibre stretch and fibre strain rate (both in isochoric and non-isochoric versions). We use a three-field variational approach due to Simo et al. [180] and provide a novel time-stepping scheme to allow for strain-rate-dependent dynamics. The introduction of the fibre strain rate in the system is one of the most challenging parts of this framework, as it requires a proper definition *and* a proper discretization. We linearize the system in the dynamic regime, providing explicit expressions for the fourth-order elasticity tensor that are suitable for fully active contraction. We also discuss the impact of the descending limb instability in the polyconvexity of the strain-energy function that describes the system.

In **Chapter 6**, we introduce **Flexodeal**: a new finite element framework for studying musculoskeletal dynamics. This is an open-source project born from the advances in Chapter 5, available to the public from the Neuromuscular Mechanics Laboratory's GitHub site: <https://github.com/sfu-nml>. Consistent with software engineering principles, we provide in this chapter documentation of this software, showing the main characteristics of its implementation, which is based on the finite element library deal.II [7]. This also shows how primary quantities of interest (such as forces, energies, pennation, muscle and fibre velocities, among others) are computed. We also perform a spatio-temporal convergence study on a particular case of isometric contraction of a pennate block of muscle tissue. Then, we present several applications of **Flexodeal** to study the force-length relationship of whole muscle (that may include aponeurosis tissue), to analyze the impact mass and force-velocity effects in dynamic simulations, and to present the applicability of the software to a more involved scenario that couples a computational domain obtained from magnetic resonance imaging (MRI) and experimental locomotion data.

In **Chapter 7**, we use **Flexodeal** to study muscle gearing, the first time a continuum mechanics model is used to study this phenomenon. Muscle gearing is the mechanism by which dynamic changes in muscle architecture cause a decoupling of muscle and fibre velocities, which optimize muscle performance under varying mechanical demands. First, we develop a computational setup that is suitable for the **Flexodeal** framework, which includes a careful mathematical redefinition of the concept of gearing from traditional 1D approaches to 3D. Furthermore, we adapt our setup to that of an experimental study by Holt et al. [89]. We discuss the validity of the results and the implications on the physiological elements that contribute to gearing.

Some of the results of Chapter 5 were published in:

J. A. ALMONACID, S. A. DOMÍNGUEZ-RIVERA, R. N. KONNO, N. NIGAM, S. A. ROSS,  
C. TAM, AND J. M. WAKELING, *A three-dimensional model of skeletal muscle tissues*,  
SIAM Journal on Applied Mathematics, 84 (2024), pp. S538–S566

In turn, some of the results in Chapter 7 are available in:

M. PINTO, J. WAKELING, J. ALMONACID, AND A. BLAZEVICH, *From muscle fibres to gears: How fibre rotation and shape change impact muscle function*, bioRxiv, (2025), pp. 2025–06

and have been submitted for publication.

# Part I

## One-dimensional elastodynamics

## Chapter 2

# Inertial effects in a multibody mass-spring model of the muscle-tendon unit

In this chapter, we study the inertial effects due to added mass in a particular set of forward dynamics simulations of muscle-tendon units (MTUs). More precisely, using locomotion data collected in studies by Chen [41] and Dick et al. [46], we compare the predictions of a multibody mass-spring model of the MTU against those of a simpler model widely used in biomechanical simulations. In addition, we investigate the influence of the input data in the numerical aspects of the problem. We show that they are not only influenced by the stiffness of the system, but also by the muscle in consideration and the task is asked to perform.

First, we mathematically describe the ordinary differential equations (ODEs) and the different concepts behind MTU models. Next, we describe the data and parameters in use for this study. Then, we describe the computational implementation of the different solvers required to perform these simulations. Here, we aim to compute lengths and velocities for muscle and tendon, as well as muscle force. Finally, we present a series of tests which show that both models (with and without added mass) show different dynamics, reiterating the importance of considering mass in muscle models for certain experimental scenarios.

### 2.1 Background

One-dimensional models of skeletal muscle are effective in capturing the overall dynamics of skeletal muscle. Their relative simplicity allows physiologists to perform cheap forward dynamics simulations on a range of subjects, muscles, and tasks.

Consider, for instance, the protocol developed by Chen [41] to record data from a human subject during locomotion tasks. Here, 24 LED motion-capture markers were secured to the skin over the pelvis and lower extremities of each participant to capture kinematic and kinetic data. Furthermore, bipolar Ag/AgCl surface electromyography (EMG) electrodes

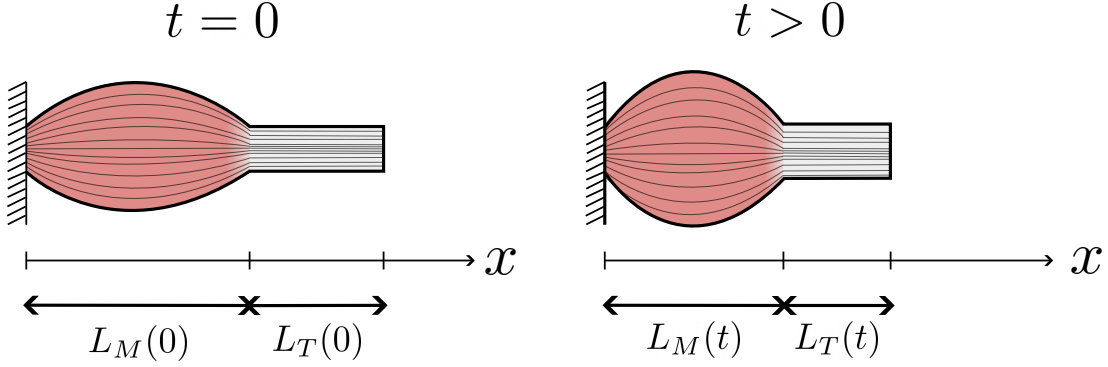


Figure 2.1: Sketch of an MTU with dimensions characterized by the muscle and tendon lengths, respectively  $L_M$  and  $L_T$ . Left: initial state ( $t = 0$ ). Right: deformed state after shortening ( $t > 0$ ).

were positioned over the bellies of 10 different muscles to capture EMG data. After this setup is complete, the subjects were asked to perform 4 different tasks (walking and running on a treadmill, hopping, and sit-to-stand from a chair) with appropriate breaks in between. The data was recorded for about 30 seconds per task and each task was repeated twice. Assuming that data was collected for 20 subjects, this means that up to  $20 \times 10 \times 8 = 1600$  different simulations could be performed. Thus, accurate and efficient models and numerical algorithms are required to analyze the data in a feasible timeframe.

## 2.2 Mathematical models

Let us develop a mathematical model of a dynamically contracting one-dimensional muscle tendon unit, such as the one depicted in Figure 2.1. Denote by  $L_M = L_M(t)$  and  $L_T = L_T(t)$  the muscle and tendon lengths, respectively, at time  $t \geq 0$ . Moreover, denote by  $L = L(t)$  the total length of the MTU which satisfies  $L_M(t) + L_T(t) = L(t)$  for any time  $t \geq 0$ .

### 2.2.1 Main concepts

We define the *muscle stretch*  $\lambda_M$ , the *muscle strain*  $\varepsilon_M$ , and the *muscle strain rate*  $\dot{\varepsilon}_M$  as

$$\lambda_M := \frac{L_M}{l_M^{opt}}, \quad \varepsilon_M := \lambda_M - 1, \quad \dot{\varepsilon}_M = \frac{1}{\dot{\varepsilon}_0} \frac{d\lambda_M}{dt} = \frac{1}{l_M^{opt} \dot{\varepsilon}_0} \frac{dL_M}{dt}, \quad (2.2.1)$$

where  $l_M^{opt}$  is the *optimal muscle length* and  $\dot{\varepsilon}_0$  is the maximum unloaded shortening strain rate. Similarly, we can define the *tendon stretch*  $\lambda_T$  and *tendon strain*  $\varepsilon_T$  as

$$\lambda_T := \frac{L_T}{l_T^{opt}}, \quad \varepsilon_T := \lambda_T - 1. \quad (2.2.2)$$

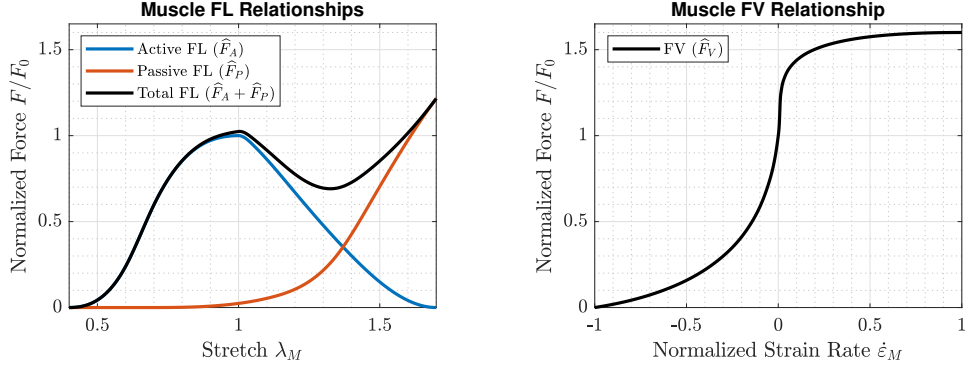


Figure 2.2: Force-length (FL) and force-velocity (FV) relationships that are part of Hill's muscle model (2.2.3).

The *optimal tendon length*  $l_T^{opt}$  can be computed from the *optimal MTU length*  $l_{MTU}^{ten}$  as  $l_T^{opt} = l_{MTU}^{opt} - l_M^{opt}$ . For now, the reader can consider these quantities as given, however, they will be discussed more in detail in Section 2.2.4.

### 2.2.2 Hill's muscle model

In a simple model, such as the one shown in Figure 2.3A, muscle can be thought as a one-dimensional spring containing a contractile element (CE) and a parallel elastic element (PEE). The first one is related to the force produced by actin-myosin interactions during activation, whereas the latter is related to passive components of the muscle fibre (such as titin), which act to prevent overstretching of the sarcomeres that form the muscle fibre. The muscle force  $F_M$  in this case is given by (cf. [208]):

$$F_{Hill}(\lambda_M, \dot{\varepsilon}_M) = F_0 \left\{ a(t) \hat{F}_A(\lambda_M) \hat{F}_V(\dot{\varepsilon}_M) + \hat{F}_P(\lambda_M) \right\}. \quad (2.2.3)$$

In this expression, known as the standard *Hill's muscle model*:

1. The maximum isometric force,  $F_0$ , is the maximum force that a muscle can produce during an isometric contraction (that is, a *fixed-length* contraction). This force is achieved when the length of the muscle  $L_M$  is exactly the optimal muscle length  $l_M^{opt}$ . Therefore, assuming no pennation, it can be computed as:

$$F_0 = \sigma_0 \cdot PCSA_0 = \sigma_0 \cdot \frac{V_{0,M}}{l_M^{opt}}, \quad (2.2.4)$$

where  $\sigma_0$  is the maximum isometric stress of muscle tissue,  $PCSA_0$  is the optimal physiological cross-sectional area (PCSA), and  $V_{0,M}$  is the muscle volume.

2. The time-dependent activation function,  $a = a(t)$ , characterizes the influx of  $\text{Ca}_2^+$  ions that trigger the formation of cross-bridges between actins and myosins within

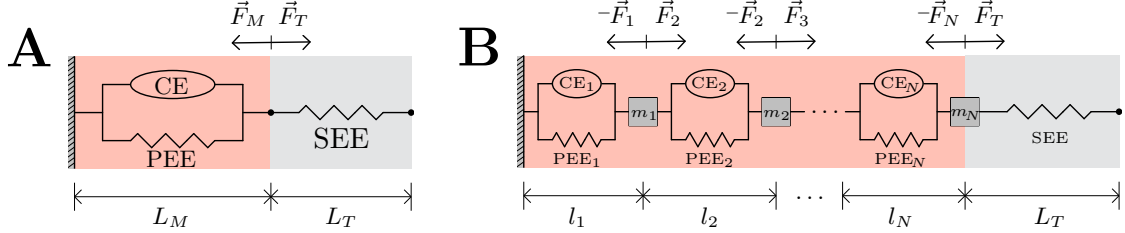


Figure 2.3: (A) A simple Hill-type model of the MTU (muscle region in pink, tendon region in grey) using massless springs. Depicted here are the (active) contractile element (CE), the passive elastic element (PEE), and the series elastic element (SEE) representing the tendon. (B) A multibody model of the MTU that does not neglect the mass of the muscle, which is equally distributed throughout the muscle segment.

sarcomeres. This function can be computed given an excitation  $u(t)$  using Zajac's equation [208]:

$$\frac{da}{dt} + \frac{a(t)}{\tau_{act}} (\beta + (1 - \beta)u(t)) = \frac{u(t)}{\tau_{act}}. \quad (2.2.5)$$

3. The functions  $\hat{F}_A = \hat{F}_A(\lambda_M)$  and  $\hat{F}_V = \hat{F}_V(\dot{\varepsilon})$  are known respectively as the active *force-length* (FL) and *force-velocity* (FV) relationships. They are related to the CE of the model and describe the force produced due to actin-myosin interactions during activation. These are normalized functions, meaning that  $\hat{F}_A(1) = 1$  and  $\hat{F}_V(0) = 1$ .
4. The function  $\hat{F}_P = \hat{F}_P(\lambda_M)$  is known as the passive FL relationship. It is related to the PEE and describes the force produced by passive components of the muscle fibre (such as titin), which act to prevent overstretching of the sarcomeres.

The force relationships  $\hat{F}_A$ ,  $\hat{F}_V$ , and  $\hat{F}_P$  are typically fit from experimental data obtained through tensile experiments, and therefore do not have a standard expression. For this particular set of experiments, we use least-squares fits of the Bézier curves used by Ross et al. [167]. This allows us to evaluate the force directly given a stretch  $\lambda_M$  without the need for solving a nonlinear equation, as is the case for Bézier curves (albeit with a minor loss of accuracy since the Bézier curves are already fit from experimental data). We show these curves in Figure 2.2 and give their exact definitions in Appendix A.

### 2.2.3 Massless and mass-enhanced models of the MTU

For the model in Figure 2.3A, the muscle force  $F_M \equiv F_{Hill}$  is balanced by the tendon force  $F_T$  (shown in Figure 2.4) at all times, that is:

$$F_M(\lambda_M, \dot{\varepsilon}_M) = F_T(\lambda_T), \quad t > 0. \quad (2.2.6)$$

This first-order implicit ODE, which we refer to as the *massless* model, represents a model of the MTU in which the mass of the muscle is not taken into consideration. While this may

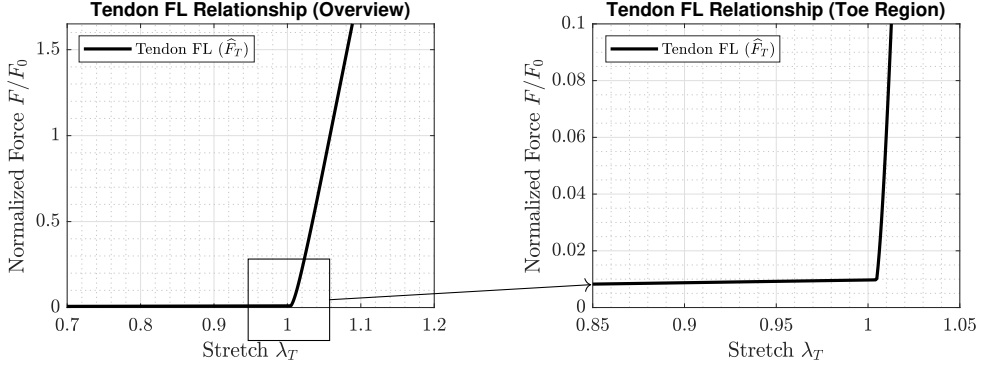


Figure 2.4: Tendon FL relationship (left) with its toe region shown in detail (right).

seem like an outrageous simplification of the problem, it is actually what is being solved in the backend of many popular biomechanics software, such as OpenSim [45]. Hence, **this model's absence of mass raises the question of whether including mass has any effect in the prediction of the dynamics of the system.**

In an attempt to answer the previous question, based on the work by Günther et al. [73], Ross et al. [166], and Ross & Wakeling [167, 168], Chen [41] has put forward a muscle model in which the mass of the muscle is equally distributed into  $N$  segments (see Figure 2.3B), forming a multibody system with  $N$  bodies. The dynamics in this model, which we refer to as the *mass-enhanced* model, are given by the set of second-order ODEs:

$$m_1 \ddot{u}_1 = F_2(\lambda_2, \dot{\varepsilon}_2) - F_1(\lambda_1, \dot{\varepsilon}_1), \quad (2.2.7a)$$

$$m_2 \ddot{u}_2 = F_3(\lambda_3, \dot{\varepsilon}_3) - F_2(\lambda_2, \dot{\varepsilon}_2), \quad (2.2.7b)$$

⋮

$$m_N \ddot{u}_N = F_T(\lambda_T) - F_N(\lambda_N, \dot{\varepsilon}_N). \quad (2.2.7c)$$

Here,  $m_1 = m_2 = \dots = m_N = m_{mus}/N$ , where the mass of the muscle  $m_{mus}$  depends on its (initial) volume  $V_{0,M}$  through the (initial) density of muscle tissue  $\rho_0$ , which is assumed to be constant across mammalian species [125]:

$$\rho_0 = \frac{m_{mus}}{V_{0,M}} = 1,060 \frac{\text{kg}}{\text{m}^3}. \quad (2.2.8)$$

Moreover, the muscle volume  $V_{0,M}$  is estimated using a formula depending on the subject's height  $H$  and mass  $W$  [75]:

$$V_{0,M} = V_0 \cdot \chi_M, \quad V_0 = (47WH + 1285) \cdot 10^{-6}, \quad (2.2.9)$$

where  $\chi_M$  is the fraction of individual muscle relative to the volume of one lower leg  $V_0$  (see Table 2.1).

In turn,  $u_i$  denotes the displacement of the  $i$ -th segment, that is,

$$u_i = x_i - x_i^0, \quad i = 1, \dots, N, \quad (2.2.10)$$

where  $x_i$  is the position of the  $i$ -th segment and  $x_i^0$  denotes its initial position. Furthermore,  $\lambda_i$  and  $\dot{\varepsilon}_i$  denote the segment stretch and strain rate of the  $i$ -th segment, respectively

$$\lambda_i = \frac{l_i}{l_s^{opt}} = \frac{l_i}{l_M^{opt}/N}, \quad \dot{\varepsilon}_i = \frac{\dot{\lambda}_i}{\dot{\varepsilon}_0}, \quad i = 1, \dots, N.$$

These stretches and strain rates can be written in terms of the displacements  $u_i$  as:

$$\lambda_1 = \frac{u_1 + l_s^0}{l_s^{opt}}, \quad \lambda_2 = \frac{u_2 - u_1 + l_s^0}{l_s^{opt}}, \quad \dots, \quad \lambda_N = \frac{u_N - u_{N-1} + l_s^0}{l_s^{opt}}, \quad (2.2.11)$$

and

$$\dot{\varepsilon}_1 = \frac{\dot{u}_1}{l_s^{opt}\dot{\varepsilon}_0}, \quad \dot{\varepsilon}_2 = \frac{\dot{u}_2 - \dot{u}_1}{l_s^{opt}\dot{\varepsilon}_0}, \quad \dots, \quad \dot{\varepsilon}_N = \frac{\dot{u}_N - \dot{u}_{N-1}}{l_s^{opt}\dot{\varepsilon}_0}, \quad (2.2.12)$$

with  $l_s^0 := L_M(0)/N$  is the initial length of each segment and  $l_s^{opt} = l_M^{opt}/N$ . In particular, the muscle length can be computed directly from the position of the last mass, i.e.  $L_M = x_N$ .

To complete the description of the massless and mass-enhanced models (equations (2.2.6) and (2.2.7), respectively), we have to provide the optimal muscle length  $l_M^{opt}$ , as well as the initial muscle length  $L_M(0)$ . The latter is sufficient to provide initial conditions for the system (2.2.7) (assuming that the system of  $N$  bodies is initially at rest, i.e.  $\dot{u}_i(0) = 0$ ). Because we will be working with experimentally-obtained data and force relationships that are particular to this study,  $l_M^{opt}$  and  $L_M(0)$  can only be *estimated* from the literature, so an optimized value must be computed to ensure simulations start from static equilibrium. This topic will be discussed in the next section.

## 2.2.4 Optimal muscle and tendon length

The optimal muscle length,  $l_M^{opt}$ , is the length at which myofilament overlap is optimal<sup>1</sup> and force production is maximal [63], that is, when  $F_M = F_0$  at  $L_M = l_M^{opt}$ . When the MTU is fixed at this length (that is,  $L = l_{MTU}^{opt}$ ), muscle and tendon forces balance:  $F_M(1) = F_0 = F_T(1)$ . This means that the definition of  $l_M^{opt}$  depends on the FL relationship, which is particular to the muscle in study. Therefore, any quantity obtained from the literature can only be considered an *estimate*. Denote the estimated optimal muscle and tendon lengths

<sup>1</sup>This happens at sarcomere lengths of about 2.6-2.8  $\mu\text{m}$  in human muscle and 2.0-2.2  $\mu\text{m}$  in frog muscle [63].

Description		Value	References
$\sigma_0$	Muscle maximum isometric stress	225 kPa	[123, 152]
$\dot{\varepsilon}_0$	Muscle maximum unloaded shortening strain rate	$5 \text{ s}^{-1}$ (walking, running) $10 \text{ s}^{-1}$ (cycling)	[195]
$\tau_{act}$	Time constant for activation	0.045 s (walking, running) 0.025 s (cycling)	[47]
$\beta$	Ratio of $\tau_{act}$ to deactivation time constant	0.6	[47]
$\chi_M$	Volume fraction of muscle with respect to that of one lower leg	MG: 0.0362 VM: 0.0606 ST: 0.026	[75]
$r_M$	Muscle-to-MTU length ratio	MG: 0.54 VM: 0.84 ST: 0.70	[104, 142]
$l_{MTU}^{opt}$	Optimal MTU length	Subject 1 (walking, running): MG: 0.3910 m VM: 0.2770 m ST: 0.4122 m Subject 2 (cycling): MG: 0.3952 m VM: 0.2171 m ST: 0.4381 m	[41]

Table 2.1: List of parameters for the mass-enhanced and massless models. The muscles listed in the table are the *medial gastrocnemius* (MG), *semitendinosus* (ST), and *vastus medialis* (VM).

respectively by  $\widetilde{l}_M^{opt}$  and  $\widetilde{l}_T^{opt}$ , which are given by:

$$\widetilde{l}_M^{opt} := l_{MTU}^{opt} r_M, \quad \widetilde{l}_T^{opt} := l_{MTU}^{opt} (1 - r_M). \quad (2.2.13)$$

Here,  $l_{MTU}^{opt}$  is the optimal MTU length (given) and  $r_M$  is the muscle-to-MTU-length ratio (see Table 2.1). Furthermore, assume that this estimate as a deviation  $\Delta l_M^{opt}$  from the true value  $l_M^{opt}$ , i.e.

$$l_M^{opt} = \widetilde{l}_M^{opt} + \Delta l_M^{opt}, \quad l_T^{opt} = \widetilde{l}_T^{opt} - \Delta l_T^{opt}. \quad (2.2.14)$$

Since muscle and tendon force balance at optimal MTU length, and assuming that the muscle is inactive ( $a = 0$ ) and  $F_T = F_0 \widehat{F}_T$ , the true values  $l_M^{opt}$  and  $l_T^{opt}$  can be obtained by solving the following equation for the error  $\Delta l_M^{opt}$ :

$$\widehat{F}_P \left( \frac{\widetilde{l}_M^{opt}}{\widetilde{l}_M^{opt} + \Delta l_M^{opt}} \right) = \widehat{F}_T \left( \frac{\widetilde{l}_T^{opt}}{\widetilde{l}_T^{opt} - \Delta l_T^{opt}} \right). \quad (2.2.15)$$

### 2.2.5 Initial muscle length

Similar to the computation of optimal muscle and tendon lengths, to ensure the simulation begins from static equilibrium, we assume that the given initial MTU length  $L(0)$  only provides estimates for the initial muscle and tendon lengths, that is:

$$\widetilde{L}_M(0) = L(0) \cdot r_M, \quad \widetilde{L}_T(0) = L(0) \cdot (1 - r_M). \quad (2.2.16)$$

Furthermore, we assume that the true values for  $L_M(0)$  and  $L_T(0)$  are off by a factor of  $\Delta L_M(0)$ , that is,

$$L_M(0) = \widetilde{L}_M(0) + \Delta L_M(0), \quad L_T(0) = \widetilde{L}_T(0) - \Delta L_T(0). \quad (2.2.17)$$

Then, we can find the value of this correction by solving the equation

$$F_P \left( \frac{\widetilde{L}_M(0) - \Delta L_M(0)}{l_M^{opt}} \right) = F_T \left( \frac{\widetilde{L}_T(0) + \Delta L_T(0)}{l_T^{opt}} \right). \quad (2.2.18)$$

The corrections  $\Delta l_M^{opt}$  and  $\Delta L_M(0)$  are typically small and represent the correct setup of the locomotion experiment at the time of data collection.

### 2.2.6 Scaling

As mentioned in the introduction to this thesis, most of our knowledge in human biomechanics comes from experiments performed in small animals, such as frogs, rats, and cats. However, it is known that larger (thus heavier) muscles will yield more inertial effects than

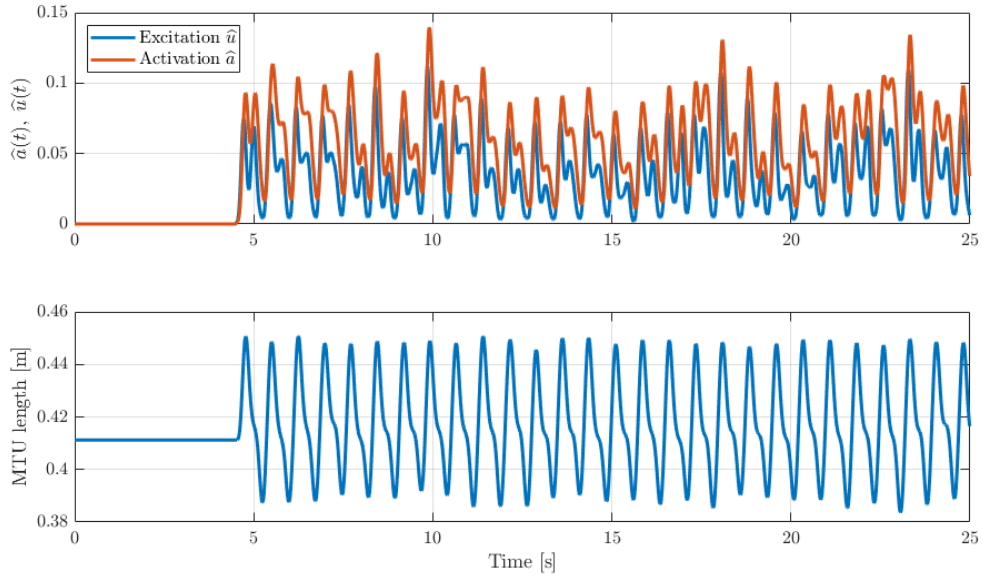


Figure 2.5: Example traces of the data (muscle: ST, task: running) used as input for the one-dimensional massless and mass-enhanced models. In this case, the activation  $\hat{a}$  has been computed from the excitation  $\hat{u}$  using Zajac's ODE (2.2.5).

smaller ones, so the size difference should not always be neglected [41, 166]. This motivates the consideration of scaled up versions of the muscles in study. In this way, a scaling factor of  $s$  means that the MTU length will be scaled up by a factor of  $s$ , the physiological cross sectional area of muscle by a factor of  $s^2$ , the muscle volume by a factor of  $s^3$ , and so on. For example, in studies of gearing, the MG from young rats considered by Holt et al. [89] had an average volume of  $8.4906 \cdot 10^{-7} \text{ m}^3$ . In turn, the subject used in this study for walking and running tasks had a MG volume of about  $2.3348 \cdot 10^{-4} \text{ m}^3$ . That is about 275 times the volume of the rat MG, equivalent to a scaling factor of about 6.5. In this study, we will use scales of 1 and 10.

## 2.3 Experimental data: muscles and tasks in consideration

We consider two subjects of equal mass (68 kg) and height (1.67 m) who were asked to perform a set of locomotion tasks: walking and running at their own pace [41], and cycling at a cadence of  $80 \text{ s}^{-1}$  and a crank load of 26 Nm [46]. Moreover, we consider the muscle excitation  $\hat{u}(t)$  and MTU length  $L(t)$  from three different muscles: medial gastrocnemius (MG), vastus medialis (VM), and semitendinosus (ST). Thus, nine different muscle-task combinations can be formed. An example of these data are shown in Figure 2.5 for the ST during running. All data were recorded for a time span of 25 seconds. For more precise details on the experiment setup and data collection, we refer the reader to [41].

Description	MATLAB <sup>®</sup> solver	AbsTol	RelTol	N
Zajac ODE (2.2.5)	<code>ode45</code>	1e-6	1e-3	-
Parameter calibration (2.2.15), (2.2.18)	<code>fzero</code>	-	-	-
Massless model (2.2.6)	<code>ode15i</code>	1e-6	1e-6	-
Mass-enhanced model (2.2.7)	<code>ode15s</code>	1e-10	1e-6	64

Table 2.2: List of MATLAB<sup>®</sup> built-in solvers in use.

## 2.4 Computational implementation

Solvers for the massless (2.2.6) and mass-enhanced model (2.2.7), as well as for the Zajac ODE (2.2.5) and the calibration steps (2.2.15) and (2.2.18) were implemented in MATLAB<sup>®</sup> using built-in routines. See Table 2.2 for a list of these solvers and the default parameters that were used. In particular, the ODE solvers are *adaptive*, meaning that the time step size is controlled by absolute and relative tolerance requirements [178]. First, `ode45` is a single-step solver based on an explicit Runge-Kutta (4,5) formula (the Dormand-Prince pair [55]). It is typically used for non-stiff ODEs, such as Zajac’s ODE (2.2.5). Next, `ode15s` is a variable-order, variable-step solver based on differentiation formulas of order 1 to 5 [178]. It is a multistep solver used for solving stiff ODEs, such as the mass-enhanced model (2.2.7). Finally, `ode15i` is similar to `ode15s`, but it is designed to solve fully implicit differential equations [177], such as the massless model (2.2.6).

### A convergence test

To have an idea on what to expect for the general results, and to evaluate the convergence of the solvers, let us perform an experiment using the MTU length and activation data from the ST muscle during running. Here, we fix the scale to  $s = 10$ , the number of masses to  $N = 16$  (as used in [41, 167, 168]), the absolute tolerance to  $10^{-10}$ , and vary the relative tolerance from  $10^{-2}, 10^{-4}, \dots$  down to  $10^{-10}$ . We show the results in Figure 2.6 for three representative seconds of output. Recall that no exact solution is available for this problem.

First, we observe that the muscle stretch  $\lambda_M$  and the muscle strain rate  $\dot{\varepsilon}_M$  are within the (generally accepted) operating ranges of human muscle, that is  $\lambda_M \in [0.85, 1.15]$  and  $\dot{\varepsilon}_M \in [-0.3, 0.3]$ . Next, we notice that the muscle stretch contains minor oscillations when  $\lambda_M < 1$ . These are then amplified in the muscle strain rate as it varies from  $\dot{\varepsilon}_M < 0$  to  $\dot{\varepsilon}_M > 0$ . Moreover, reducing the relative tolerance does not yield a better approximation (qualitatively speaking), even though the average time step size is indeed decreasing (see Figure 2.7). This is a sign that the solver is correctly resolving the primary unknowns, and that the apparent stiffness in the system is not tied to the time discretization, as we will see in the next section.

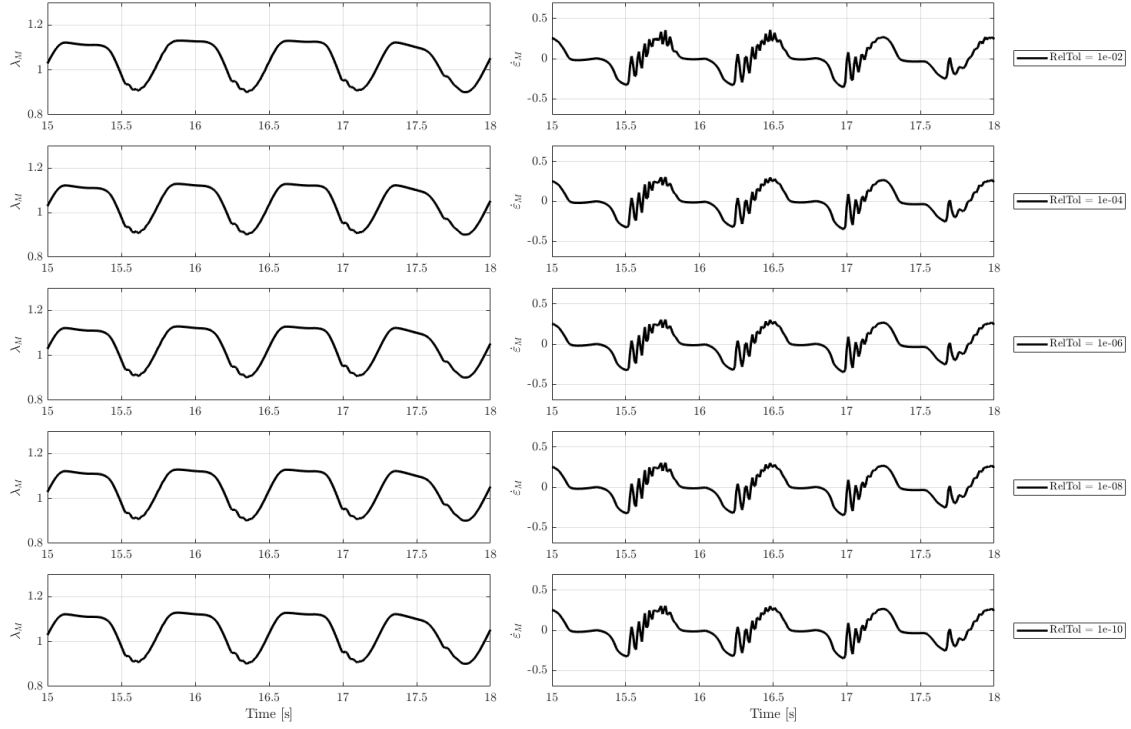


Figure 2.6: Traces of muscle strains ( $\lambda_M$ ) and strain rates ( $\dot{\varepsilon}_M$ ) as the relative tolerance in the ODE solver is varied while the absolute tolerance is fixed to  $10^{-10}$ .

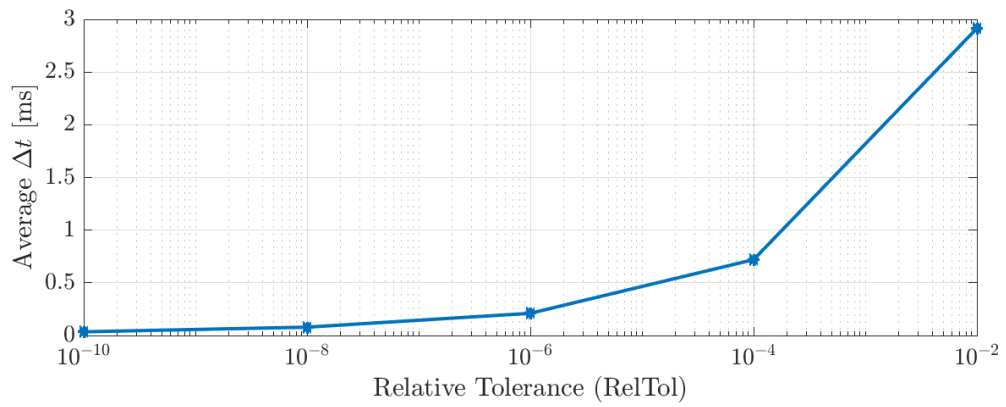


Figure 2.7: Average time step size  $\Delta t$  in the mass-enhanced model as the relative tolerance decreases while the absolute tolerance is fixed to  $10^{-10}$ .

scale = 1			
Muscle \ Task	Walking	Cycling	Running
MG	1.01	0.80	1.19
VM	2.28	1.33	2.79
ST	1.28	0.83	1.54
scale = 10			
Muscle \ Task	Walking	Cycling	Running
MG	1.15	0.99	1.79
VM	2.07	3.29	3.70
ST	2.54	0.90	5.10

Table 2.3: Computation times (in hours) for each muscle-task combination at scales 1 and 10 for the full 25 seconds of available data using the mass-enhanced model.

## 2.5 Main results

We perform simulations for all 9 muscle-task pairs at scales  $s = 1$  and  $s = 10$  using the solvers described in the previous section. Moreover, we focus on the behaviour of the ST during running. Finally, we analyze the impact of the number of the masses on the system in the quality of the output.

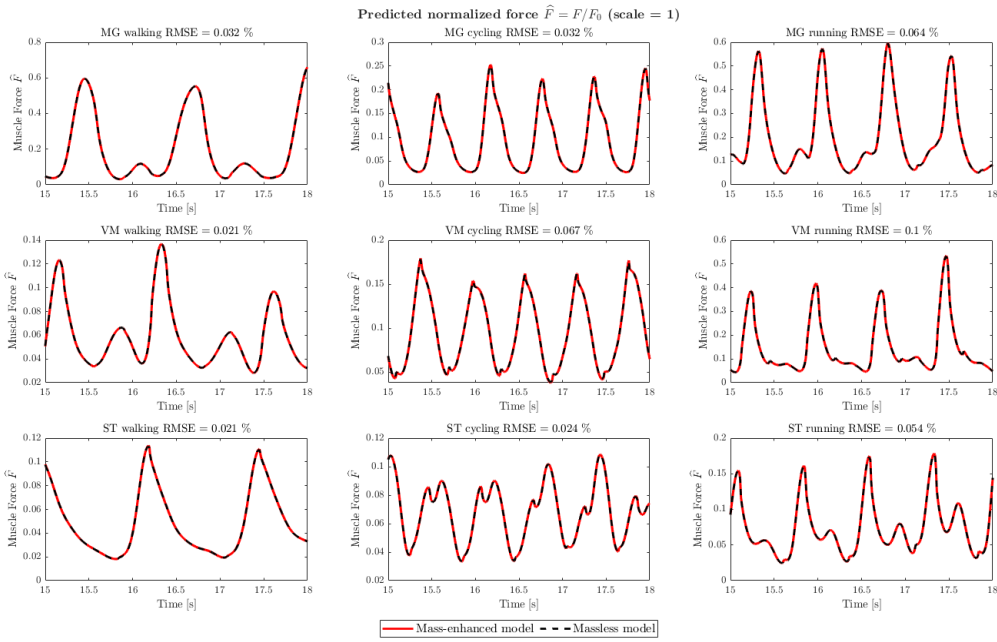
### 2.5.1 Overall behaviour for different muscles and tasks

In Figure 2.8 we show the predicted normalized muscle force (i.e.  $F_M/F_0$ , see (2.2.3)) using the massless and mass-enhanced ( $N = 64$ ) models for three representative seconds of data. The input data in this case are MTU lengths and activation patterns from the three different muscles and the three different tasks specified in Section 2.3. In line with the findings by Chen [41], we observe negligible differences when  $s = 1$  (see Figure 2.8A) and significant differences when  $s = 10$  (up to 14% RMSE difference for ST-running, see Figure 2.8B).

In general, when we scale the muscle 10 times its size (i.e.  $s = 10$ ), the mass-enhanced model can capture much sharper dynamics than the massless model. Moreover, the inertial effects can cause faster variations of muscle force (ST-walking), shifts in phase (VM-cycling), and differences of peak (local) force of above 100% (ST-running).

Computationally speaking, even though the dynamics of the MTU are, in general, smooth for all muscle-task pairs (see, for instance, Figure 2.5), the time that it takes to simulate the full 25 seconds of data varies significantly, not only depending on the model but also on the muscle and the task of choice. While the massless model finishes computation in about 1 to 5 seconds, the mass-enhanced model can easily take hours to compute a result (up to 5 hours for the ST muscle during running, see Table 2.3).

**A**



**B**

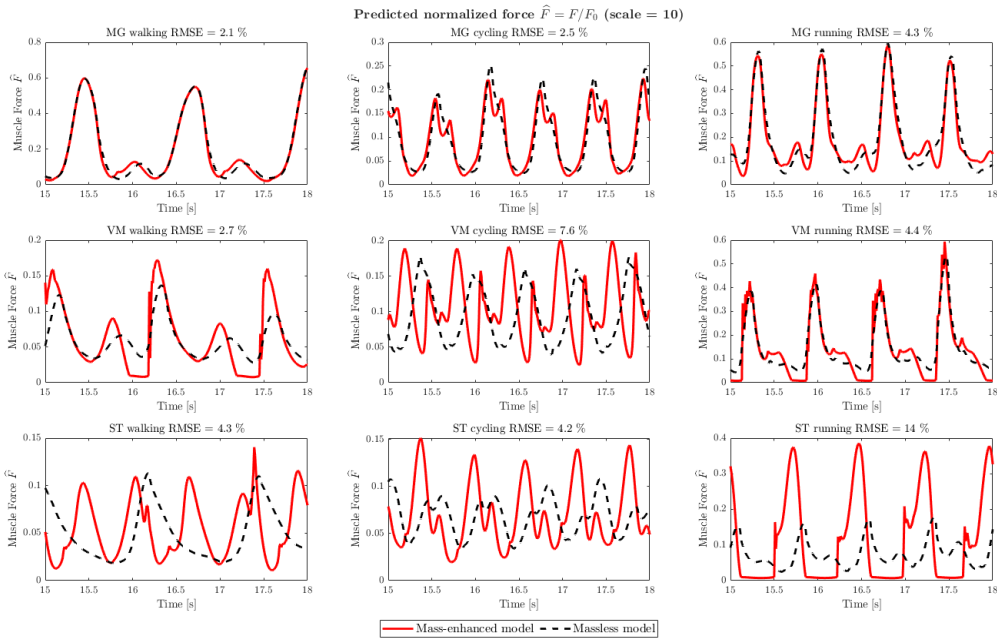


Figure 2.8: Predicted (normalized) forces when the scaling parameter is unchanged (i.e.  $s = 1$ ; A) and when  $s = 10$  (B) for 9 different muscle-task combinations. RMSE computed using the data range shown in the figures.

### 2.5.2 Dynamics of the ST during running

In view of the previous results, we decide to have a closer look at the behaviour of the ST muscle during running. In particular, we show traces of excitation, activation, muscle length, tendon length, muscle strain rate, and normalized muscle force for  $s = 1$  and  $s = 10$  in Figure 2.9. Here, the excitation is given from the experimental data, the activation is computed based on this excitation using (2.2.5), and the rest of the variables are computed by the solver. In particular, the muscle force is equal to the computed tendon force, since we are assuming that the tendon transmits the entirety of the force generated by muscle.

These results show that the tendon acts as a strut when  $s = 1$ , but it is no longer the case for  $s = 10$ . Indeed, tendon strains of up to -20% are observed, and they produce sharp variations of strain rate (and ultimately force) that the massless model cannot capture. Another important feature is that, when  $s = 10$ , we observe a development of impulsive forces when transitioning from  $\dot{\varepsilon}_M < 0$  to  $\dot{\varepsilon}_M > 0$ . This is something that has not been described previously (cf. [41, 166]) because the dynamics in these works are much smoother. We also note that the results in Figure 2.9 were computed using  $N = 64$  masses (see Table 2.2) because the simulation was not fully resolved when  $N = 16$  masses were used.

### 2.5.3 Influence of the number of masses in the computation

The phenomenon in the previous subsection is a strong indication that, in certain scenarios, the number of masses in the model might need to be modified from the standard  $N = 16$  suggested by Ross et al. [165]. To view this in more detail, we performed a homogenization study by varying the number of masses from 0 (i.e., a simulation using the massless model) to 128 masses. We portray these results in Figure 2.10. Here, we observe how it is only when using  $N = 128$  masses that we do not observe any unphysical oscillations. However, simulating 18 seconds of data took about 42 hours of computational time and a significant amount of memory, so this is not a feasible approach for studying multiple muscle-task combinations.

In general, we observed that the number of masses needed to fully resolve the traces depended on the scale, task, and muscle in study. This effect can be seen from Figure 2.8B. In particular, for scale  $s = 10$ , the traces for the VM-running and ST-running combination show some spurious oscillations that are not present in the traces for the MG. This also suggests that the problem could be better approached using a one-dimensional *continuum* model (see next chapter), that is, a model derived from an infinitely large number of masses (i.e.  $N \rightarrow \infty$ ). This would open the door to the development of efficient numerical solvers using techniques such as the finite element method.

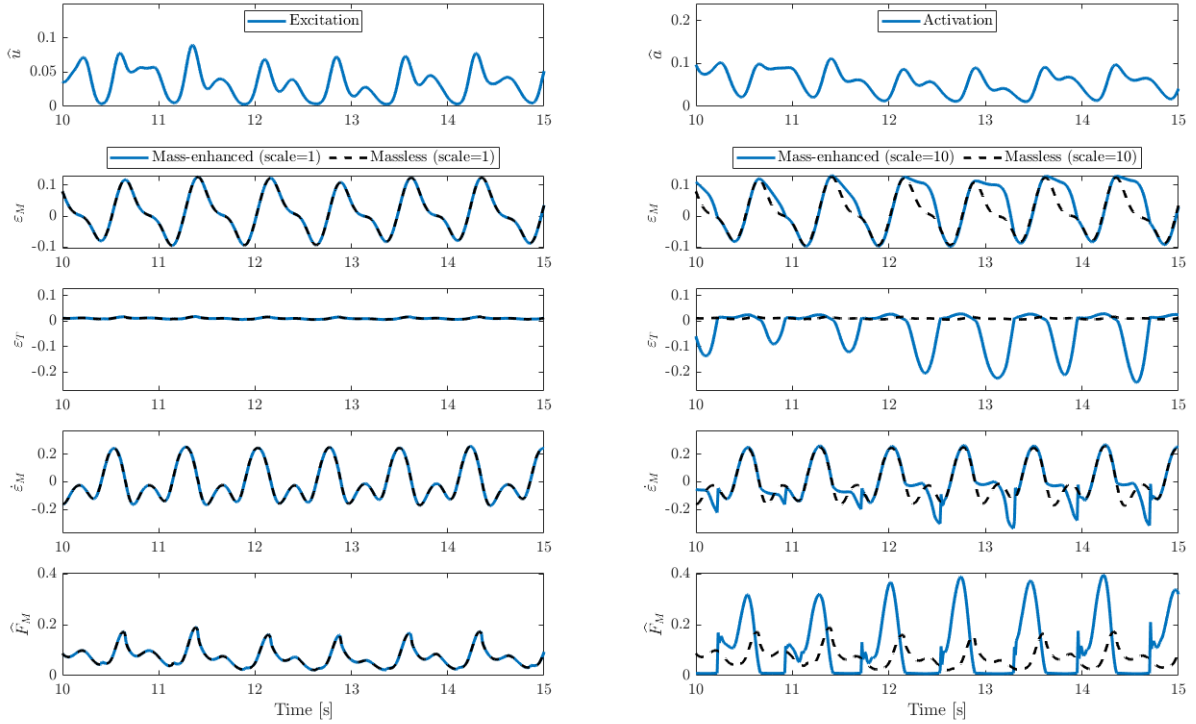


Figure 2.9: Predicted dynamics using the massless (dashed black lines) and mass-enhanced (solid blue line) models for the ST muscle during running. From top to bottom, the first row shows the (given) muscle excitation and (computed) activation, then the (computed) muscle strain  $\varepsilon_M$ , muscle strain rate  $\dot{\varepsilon}_M$ , tendon strain  $\varepsilon_T$ , and normalized muscle force  $\hat{F}_M = F_M/F_0$ .

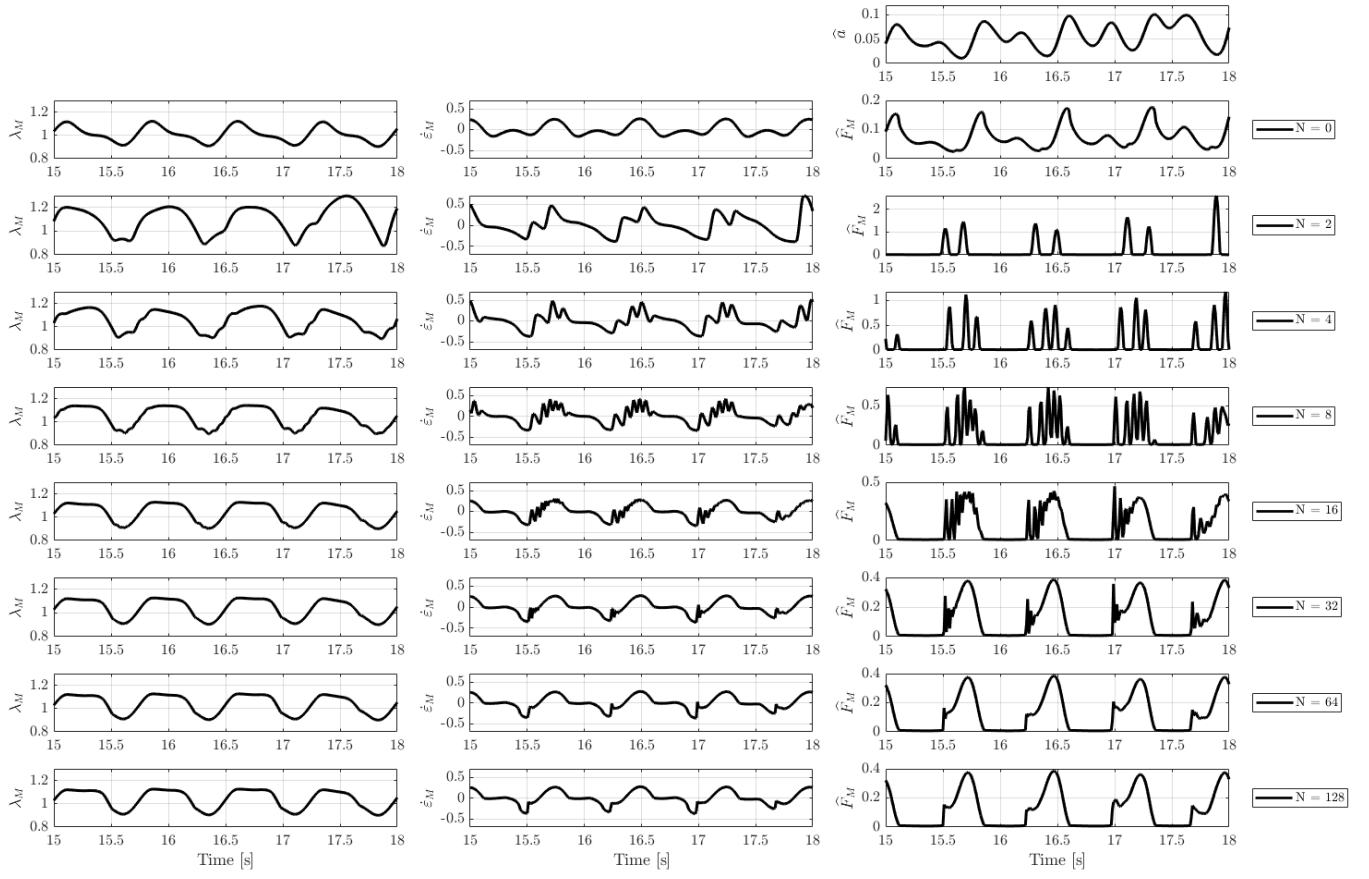


Figure 2.10: Traces of muscle strains ( $\lambda_M$ ), strain rates ( $\dot{\lambda}_M$ ), and (normalized) muscle force  $\hat{F}_M$  as the number of masses vary in the mass-enhanced model: from  $N = 0$  (second row, i.e. massless model),  $N = 2$  (third row), up to  $N = 128$  (last row). For reference we have added the computed activation in the first row.

## Chapter 3

# Dynamical stability and the continuum limit of multibody models

We now turn our attention to the issue of stability in muscle models. In particular, we refer to a dynamical system (such as the mass-enhanced model (2.2.7)) being *dynamically* stable if small perturbations or deviations from an equilibrium state result in the system eventually remaining near or returning to that equilibrium state over time (see, e.g., [184]). This is in contrast to the concept of *numerical* stability, which is tied to the numerical scheme used to approximate the solution to a dynamical system. We remark that these terms are *not* interchangeable and that the present chapter will focus entirely on the dynamical stability of models such as (2.2.7).

First, we introduce the context in which multibody models are unstable and the mathematical reasons behind. We present some numerical experiments to visualize the effects of this instability. Next, we propose a simple method to stabilize the system based on previously-validated three-dimensional models. This will require us to explore the continuum limit of the mass-enhanced model, that is, as the number of masses in the system grows infinitely. Finally, we visualize the dynamics on this updated system and the implications when analyzing the mass effects in a one-dimensional context.

### 3.1 Background

The force-length (FL) relationship, which was described for the first time in 1966 for the semitendinosus muscle in frogs [72], is an important component of Hill-type muscle models. It describes the contractile forces generated by the active and passive elements in a muscle fibre.

The active force-length curve is a “bell”-shaped curve that characterizes the actin-myosin interactions formed upon activation. At a sarcomere level, an increasing level of activation leads to a greater overlap between actins and myosins, but only until the sarcomere has

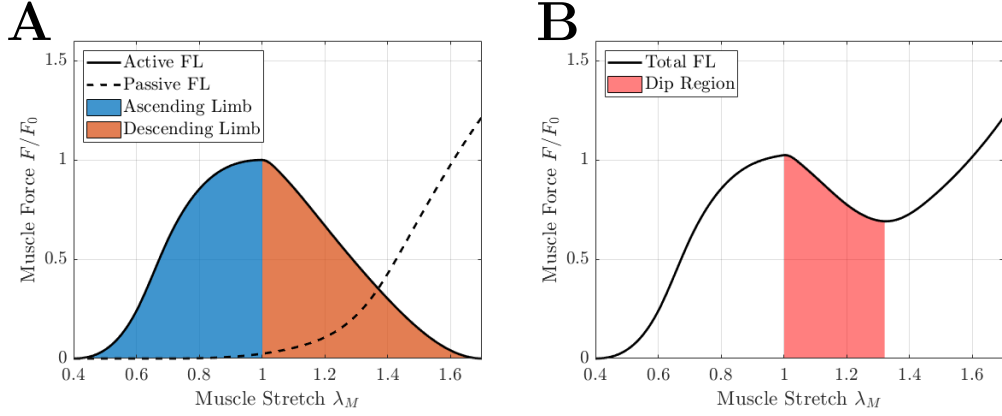


Figure 3.1: (A) Active and passive FL relationships. The region  $\lambda_M < 1$  corresponds to the ascending limb (in blue) since the curve has a positive slope. In turn, the region  $\lambda_M > 1$  corresponds to the descending limb (in ochre) which has a distinctive negative slope. (B) When active and passive forces are added, they form the *total* FL relationship, which typically has a dip region (i.e. a region with negative slope) around  $1 < \lambda_M < 1.35$ .

reached its optimal length. Beyond this, the overlap between actin and myosin decreases. This reduction means fewer cross-bridges can form, thereby decreasing the ability of the sarcomere to generate active force. Because a muscle fibre can be seen as a bundle of serially-connected sarcomeres, the active force that a muscle fibre generates is assumed to follow this same logic (see Figure 3.1A). In turn, the passive force combines the force-generating effects of extracellular components (such as the endomysium, perimysium, epimysium, and sarcolemma) and intracellular components (such as titin) that act to prevent overstretching.

The region on which the active force is increasing (that is,  $\lambda_M < 1$ ) is known as the *ascending limb*, whereas the region where the force is decreasing (that is,  $\lambda_M > 1$ ) is known as the *descending limb*. When active and passive forces are combined, the resulting curve may have a “dip” region because the passive curve has a slope that is not positive enough to overtake the negative slope of the active curve (see Figure 3.1B). This is particularly problematic if the goal is to simulate isometric contractions in this dip region using a multibody model such as the mass-enhanced model (2.2.7). A small perturbation of the system in this region can generate dynamics that do not reflect the behaviour of skeletal muscle. This phenomenon is known as the *descending limb instability* and has been a subject of discussion for almost 20 years [3, 206, 207]. We remark that this is an instability of *dynamical* type, not numerical (as sometimes is referred to, see [206]). A more precise description of this phenomenon can be made using tools from dynamical systems, which will be the goal of the next section.

## 3.2 Mathematical description of the descending limb instability

Let us dive into the reasons behind the descending limb instability (DLI) in the context of the mass-enhanced model (2.2.7). This will be useful to understand what originates this instability and what can be done to remediate it. We begin this section by establishing what an isometric contraction means for our purposes.

**Definition 3.1** (Isometric contraction). Consider a muscle modelled as a series of one-dimensional elastic elements (i.e. as in the mass-enhanced model). We say that a muscle is contracted *isometrically* if the total muscle length  $L_M$  remains constant at all times, independent of the activation level. For the case of a muscle-tendon unit (MTU), we say the MTU is contracted isometrically if the combined length of muscle and tendon remains constant throughout the experiment,

The definition above implies that, although the length of the muscle (or an MTU) remains fixed during an isometric contraction, the length of its constitutive elements (i.e., each segment in the mass-enhanced model, or the muscle and tendon lengths in an MTU) may experience individual variations.

### 3.2.1 The model for an isometric contraction

Consider a muscle modelled as a series of  $N$  contractile elements with  $N - 1$  masses distributed in the same fashion as the mass-enhanced model (2.2.7) (see Figure 3.2). Moreover, assume that the length is given by  $\lambda_M L_M$ , where  $L_M$  is the optimal muscle length and  $\lambda_M$  is a given stretch. Then, the system (2.2.7) now reads:

$$m_1 \ddot{u}_1 = F_2(\lambda_2, \dot{\varepsilon}_2) - F_1(\lambda_1, \dot{\varepsilon}_1), \quad (3.2.1a)$$

$$m_2 \ddot{u}_2 = F_3(\lambda_3, \dot{\varepsilon}_3) - F_2(\lambda_2, \dot{\varepsilon}_2), \quad (3.2.1b)$$

⋮

$$m_{N-1} \ddot{u}_{N-1} = F_N(\lambda_N, \dot{\varepsilon}_N) - F_{N-1}(\lambda_{N-1}, \dot{\varepsilon}_{N-1}). \quad (3.2.1c)$$

Here, for  $i = 1, \dots, N - 1$ ,  $u_i$  is the displacement of the  $i$ -th segment,  $m_i = m_{mus}/(N - 1)$  with  $m_{mus}$  being the mass of the muscle, and the forces  $F_i$  are given by Hill's force:

$$F_i(\lambda_i, \dot{\varepsilon}_i) = F_{Hill}(\lambda_i, \dot{\varepsilon}_i) = F_0 \{ F_A(\lambda_i) F_V(\dot{\varepsilon}_i) + F_P(\lambda_i) \}. \quad (3.2.2)$$

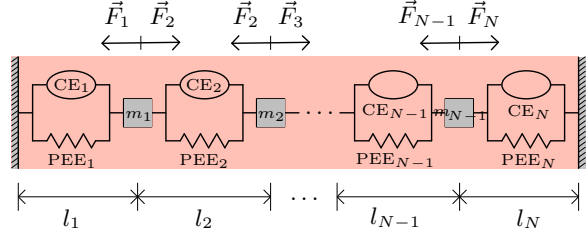


Figure 3.2: Mass-enhanced muscle model adapted for an isometric contraction. Here, the sum of all element lengths (i.e.  $\sum_{i=1}^N l_i = L_M$ ) is fixed.

Note that, unlike the expression in (2.2.3), we are assuming a fully active muscle (i.e.  $a(t) = 1$ ). As before, the segment stretches  $\lambda_i$  are given by:

$$\lambda_1 = \frac{u_1}{l_s^{opt}} + \lambda_M, \quad (3.2.3a)$$

$$\lambda_i = \frac{u_i - u_{i-1}}{l_s^{opt}} + \lambda_M, \quad i = 2, \dots, N-1, \quad (3.2.3b)$$

$$\lambda_N = \frac{-u_{N-1}}{l_s^{opt}} + \lambda_M, \quad (3.2.3c)$$

with  $l_s^{opt} = L_M/N$ , whereas the strain rates  $\dot{\varepsilon}_i$  are just:

$$\dot{\varepsilon}_i = \frac{1}{\dot{\varepsilon}_0} \frac{d\dot{\lambda}_i}{dt}, \quad i = 1, \dots, N. \quad (3.2.4)$$

We remark that, because we are modelling an isometric contraction, these strain rates will be near zero, and thus the contribution from the FV relationship is negligible since  $F_V(0) = 1$ . However, we decide to leave this dependence in the definition of Hill's force (3.2.2) and in the right-hand side of (3.2.1) not only to preserve the structure of the muscle model but also to reuse the computational tools developed in the previous chapter.

### 3.2.2 Stability of the zero solution

First, we rewrite the system (3.2.1) as a system of first order ODEs, which we can compactly express as:

$$\frac{d}{dt} \begin{pmatrix} \vec{u} \\ \vec{v} \end{pmatrix} = \frac{N-1}{m_{mus}} \begin{bmatrix} \mathbf{0} & \mathbf{I} \\ \mathbf{0} & \mathbf{0} \end{bmatrix} \begin{pmatrix} \vec{u} \\ \vec{v} \end{pmatrix} + \mathcal{F}(\vec{u}, \vec{v}), \quad (3.2.5)$$

where  $\vec{u} = (u_1, \dots, u_{N-1})^\top$  is the vector of displacements,  $\vec{v} = (v_1, \dots, v_{N-1})^\top$  is the vector of velocities (not to be confused with strain rates, see Equation (3.2.4)), and the nonlinear

term  $\mathcal{F}(\vec{u}, \vec{v})$  is given by

$$\mathcal{F}(\vec{u}, \vec{v}) = \begin{pmatrix} \vec{0} \\ \vec{F}(\vec{u}, \vec{v}) \end{pmatrix}, \quad \vec{F}(\vec{u}, \vec{v}) = \begin{pmatrix} F(\lambda_2, \dot{\varepsilon}_2) - F(\lambda_1, \dot{\varepsilon}_1) \\ \vdots \\ F(\lambda_N, \dot{\varepsilon}_N) - F(\lambda_{N-1}, \dot{\varepsilon}_{N-1}), \end{pmatrix} \quad (3.2.6)$$

with the force  $F$  corresponding to Hill's force with maximal activation ( $a = 1$ ), that is

$$F(\lambda, \dot{\varepsilon}) = F_0 \left\{ F_A(\lambda) F_V(\dot{\varepsilon}) + F_P(\lambda) \right\}. \quad (3.2.7)$$

Notice that the zero solution, that is  $(\vec{u}, \vec{v}) = (\vec{0}, \vec{0})$  is an equilibrium point of the system (3.2.5). From the definition of the segment stretches  $\lambda_i$  in (3.2.3), we observe that

$$u_i = 0 \quad \Rightarrow \quad \lambda_i = \lambda_M, \quad \forall i = 1, \dots, N-1.$$

Furthermore, from the definition of the strain rates in (3.2.4) and the velocities in (3.2.5), we have

$$v_i = 0 \quad \Rightarrow \quad \dot{u}_i = 0 \quad \Rightarrow \quad \dot{\varepsilon}_i = \frac{1}{\dot{\varepsilon}_0} \frac{d}{dt} \left( \frac{u_i - u_{i-1}}{l_s^{opt}} \right) = \frac{1}{\dot{\varepsilon}_0} \left( \frac{\dot{u}_i - \dot{u}_{i-1}}{l_s^{opt}} \right) = 0,$$

for all  $i = 1, \dots, N-1$ . Therefore, the segment forces that define  $\vec{F}$  in (3.2.6) cancel each other, so the right-hand side of (3.2.5) vanishes.

According to the theorem of Hartman-Grobman [44], we may linearize (3.2.5) around  $(\vec{0}, \vec{0})$  to analyze the stability of this equilibrium point. Furthermore, because the changes in stretch are will be small relative to the time it takes the system to stabilize, we can assume that  $\dot{\varepsilon}_i \approx 0$ . Thus, it suffices to analyze the linear system:

$$\frac{d}{dt} \begin{pmatrix} \vec{u} \\ \vec{v} \end{pmatrix} = J(\vec{0}, \vec{0}) \begin{pmatrix} \vec{u} \\ \vec{v} \end{pmatrix}, \quad (3.2.8)$$

where the Jacobian  $J(\vec{u}, \vec{v})$ , for arbitrary  $(\vec{u}, \vec{v})$ , is given by

$$J(\vec{u}, \vec{v}) = \begin{bmatrix} \mathbf{0} & \frac{N-1}{m_{mus}} \mathbf{I}_{N-1} \\ \frac{\partial \vec{F}}{\partial \vec{u}} & \mathbf{0} \end{bmatrix}, \quad (3.2.9)$$

with  $\mathbf{I}_{N-1} \in \mathbb{R}^{N-1 \times N-1}$  being the identity matrix and  $\frac{\partial \vec{F}}{\partial \vec{u}}$  the tridiagonal matrix of entries

$$\left( \frac{\partial \vec{F}}{\partial \vec{u}} \right)_{i,i} = -\frac{1}{l_s^{opt}} \left[ \frac{\partial F}{\partial \lambda}(\lambda_{i+1}, 0) + \frac{\partial F}{\partial \lambda}(\lambda_i, 0) \right] \quad (3.2.10)$$

and

$$\left( \frac{\partial \vec{F}}{\partial \vec{u}} \right)_{i+1,i} = \left( \frac{\partial \vec{F}}{\partial \vec{u}} \right)_{i,i+1} = \frac{1}{l_s^{opt}} \frac{\partial F}{\partial \lambda}(\lambda_i, 0). \quad (3.2.11)$$

In particular, when  $(\vec{u}, \vec{v}) = (\vec{0}, \vec{0})$ , we have

$$J(\vec{0}, \vec{0}) = \begin{bmatrix} \mathbf{0} & \frac{N-1}{m_{mus}} \mathbf{I}_{N-1} \\ \frac{1}{l_s^{opt}} \frac{\partial F}{\partial \lambda}(\lambda_M, 0) \mathbf{D}_0 & \mathbf{0} \end{bmatrix}, \quad (3.2.12)$$

where  $\mathbf{D}_0 \in \mathbb{R}^{N-1 \times N-1}$  is the matrix

$$\mathbf{D}_0 = \begin{bmatrix} -2 & 1 & 0 & \cdots & 0 \\ 1 & -2 & 1 & \cdots & 0 \\ \ddots & \ddots & \ddots & & \\ 0 & \cdots & 0 & 1 & -2 \end{bmatrix}. \quad (3.2.13)$$

The latter is a matrix typically found in finite difference schemes for ODEs and PDEs (see, e.g., [183]). Its eigenvalues are:

$$\nu_k = -4 \sin^2 \left( \frac{k\pi}{2N} \right), \quad k = 1, \dots, N-1. \quad (3.2.14)$$

Therefore, to find the eigenvalues  $\omega_k$  of  $J(\vec{0}, \vec{0})$ , we may use the following identity:

$$\det \left( \omega \mathbf{I}_{2(N-1)} - J(\vec{0}, \vec{0}) \right) = \det \left( \omega^2 \mathbf{I}_{N-1} - \frac{N-1}{l_s^{opt} m_{mus}} \frac{\partial F}{\partial \lambda}(\lambda_M, 0) \mathbf{D}_0 \right),$$

which gives rise to two cases, depending on the sign of  $\frac{\partial F}{\partial \lambda}(\lambda_M, 0)$ .

First, if  $\frac{\partial F}{\partial \lambda}(\lambda_M, 0) > 0$  (that is, the muscle is contracted on the *ascending* limb of the FL relationship), then the eigenvalues of the Jacobian are:

$$\omega_k = \pm 2 \frac{N-1}{l_s^{opt} m_{mus}} \frac{\partial F}{\partial \lambda}(\lambda_M, 0) \sin \left( \frac{k\pi}{2N} \right) i, \quad k = 1, \dots, N-1, \quad (3.2.15)$$

with  $i = \sqrt{-1}$ . Although all the eigenvalues are purely complex, they are distinct, and therefore the system (3.2.5) is stable according to [74, Theorem 13.1].

In contrast, if  $\frac{\partial F}{\partial \lambda}(\lambda_M, 0) < 0$  (that is, the muscle is contracted on the *descending* limb of the FL relationship), then the eigenvalues are purely real:

$$\omega_k = \pm 2 \frac{N-1}{l_s^{opt} m_{mus}} \frac{\partial F}{\partial \lambda}(\lambda_M, 0) \sin \left( \frac{k\pi}{2N} \right), \quad k = 1, \dots, N-1. \quad (3.2.16)$$

Therefore, because of the presence of positive eigenvalues, the system (3.2.5) is unstable. This is a mathematical characterization of the descending limb instability (DLI).

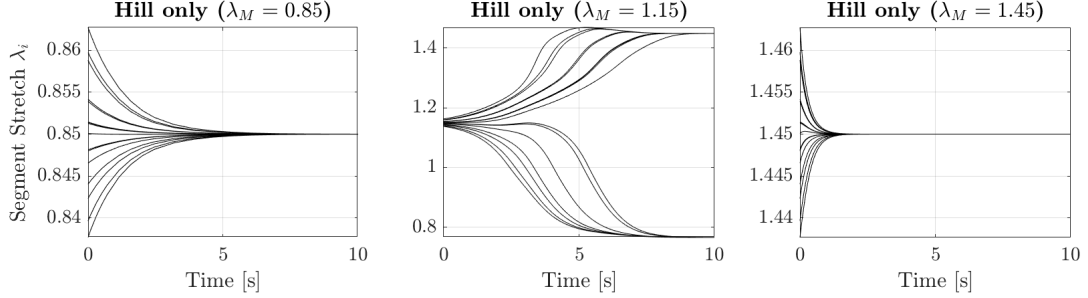


Figure 3.3: Stability of an isometric contraction according to the system of ODEs (3.2.1). The elements (as well as the muscle) are stretched initially at around 85% (left), 115% (middle), and 145% (right) of the muscle’s optimal length. At an initial stretch of 115%, the descending limb instability causes the segments to bifurcate to two different lengths.

### 3.2.3 A numerical example

Consider as in [206] a muscle of length  $L_M = 0.3$  m with maximum isometric force  $F_0 = 525$  N. Without loss of generality, we set the maximum strain rate to  $\dot{\varepsilon}_0 = 5 \text{ s}^{-1}$ . We also take  $N = 17$  masses and an initial condition  $u_i = \eta_i$ ,  $\dot{u}_i = 0$ , for  $i = 1, \dots, N - 1$ , with  $\eta_i$  being a random variable drawn from a uniform distribution on  $[-0.01, 0.01]$ .

To observe the DLI, we perform three isometric contractions in different parts of the FL curve:

1. On the ascending limb at  $\lambda_M = 0.85$ ,
2. On the descending limb at  $\lambda_M = 1.15$ ,
3. On the descending limb but at a point where the derivative of the total FL curve is positive, say  $\lambda_M = 1.45$ .

We show these results in Figure 3.3. Here, we see that when  $\lambda_M = 0.85$  or  $\lambda_M = 1.45$ , we have that  $\frac{\partial F}{\partial \lambda}(\lambda_M, 0) > 0$  and therefore the system eventually returns to a static equilibrium where all the segments have the same length. However, when  $\lambda_M = 1.15$ , we have that  $\frac{\partial F}{\partial \lambda}(\lambda_M, 0) < 0$  and a bifurcation is produced: muscle segments diverge to two different lengths that produce the same force.

## 3.3 Stabilizing the model

The model (3.2.1) allows for an arbitrary number of contractile units. Therefore, it is perfectly reasonable to assume a large enough  $N$  can reduce each contractile unit into the representation of a sarcomere. In this scenario, the DLI would tell us that sarcomeres may undergo sudden overstretching or “popping” when the muscle is isometrically contracted at a length beyond optimal. And while this *is* a physiological phenomenon known as *sarcomere*

*popping* [131, 132, 133], experiments on single myofibrils show a rather stable behaviour of sarcomeres, i.e. no “popping” on the scale of a myofibril [97].

Deriving an accurate, stable, and physiologically-informed muscle model is then an almost Sisyphean task. The properties of skeletal muscle tissue are so heterogeneous that the behaviour of a first-stretched-then-activated muscle fibre (which is how the active force curve is constructed) is completely different compared to one which is first activated and then stretched. At the sarcomere level, this active stretching typically yields FL curves that do not have a dip region, leading to forces that are above the maximum isometric force. This phenomenon is known as *residual force enhancement* (RFE) and, at least mathematically, explains why sarcomeres are stable in both ascending and descending limbs of the active FL curve [98].

History-dependent effects, such as RFE, are typically attributed to *titin*, the largest protein in the human body and a component of the parallel elastic element in sarcomeres. Upon active stretch, titin binds to actin to increase its stiffness [137], with a large enough increase that the total FL curve no longer has a dip region (if it had one), thus *convexifying* the curve. In this way, it is no surprise that muscle models that do include titin as an activation-dependent elastic element are stable [78, 79, 109, 128, 174].

RFE has always been observed in single muscle fibres from humans and animals [98, 148, 160]. However, RFE may not always be observed *in vivo* at the whole muscle level [14, 40, 87], yet the contractions are still stable. Could there be components different than titin that bring stability to a muscle fibre?

In mathematical terms, the DLI can be overcome by adding *any* stiff-enough elastic element (not necessarily titin) to Hill’s model (3.2.2). Therefore, it is also not surprising that three-dimensional models are, more often than not, stable given the addition of a passive, base material contribution [4]. Hence, we can draw inspiration from these models to add a hyperelastic component to the system (3.2.1) and show that the resulting model is stable on both limbs of the active FL curve. Given that this is performed at the continuum level, we must first introduce a continuum version of the mass-enhanced model by taking the limit as the number of masses  $N \rightarrow \infty$ .

### 3.3.1 The continuum limit of the mass-enhanced model

Consider the model (3.2.1) but with an additional mass at the right end that is pulled with a constant force  $F_{ext}$ . Furthermore, assume that  $m_i = m_{mus}/N$  and the muscle is not pre-stretched, i.e.  $\lambda_M = 1$ . In addition, define  $l_s^{opt} = L_{mus}^{opt}/N =: \Delta x$ . After some algebraic

manipulations, the system (3.2.1) becomes:

$$\frac{m_{mus}}{L_{mus}^{opt}} \ddot{u}_1 = \frac{F(\lambda_2, \dot{\varepsilon}_2) - F(\lambda_1, \dot{\varepsilon}_1)}{\Delta x}, \quad (3.3.1a)$$

$$\frac{m_{mus}}{L_{mus}^{opt}} \ddot{u}_2 = \frac{F(\lambda_3, \dot{\varepsilon}_3) - F(\lambda_2, \dot{\varepsilon}_2)}{\Delta x}, \quad (3.3.1b)$$

⋮

$$\frac{m_{mus}}{L_{mus}^{opt}} \ddot{u}_N = \frac{F_{ext} - F(\lambda_N, \dot{\varepsilon}_N)}{\Delta x}. \quad (3.3.1c)$$

In particular, the segment stretches  $\lambda_i$  and strain rates  $\dot{\varepsilon}_i$  now read:

$$\lambda_i = 1 + \frac{u_i - u_{i-1}}{\Delta x}, \quad (3.3.2)$$

and

$$\dot{\varepsilon}_i = \frac{1}{\dot{\varepsilon}_0} \frac{d}{dt} \left( \frac{u_i - u_{i-1}}{\Delta x} \right). \quad (3.3.3)$$

We are interested in studying the behaviour of the system (3.3.1)-(3.3.3) as  $N \rightarrow \infty$ , or equivalently, as  $\Delta x \rightarrow 0$ . This is the *continuum limit*. In this case, equations (3.3.2) and (3.3.3) define the following the quantities:

$$\lambda(x, t) := \lim_{\Delta x \rightarrow 0} \lambda_i = 1 + \frac{\partial u}{\partial x}, \quad (3.3.4)$$

and

$$\dot{\varepsilon}(x, t) = \lim_{\Delta x \rightarrow 0} \dot{\varepsilon}_i = \frac{1}{\dot{\varepsilon}_0} \frac{\partial}{\partial t} \left( \frac{\partial u}{\partial x} \right) = \frac{1}{\dot{\varepsilon}_0} \frac{\partial \lambda}{\partial t}. \quad (3.3.5)$$

That is, we have recovered the one-dimensional version of the stretch and strain rate variables that are commonly considered in solid mechanics. Moreover, we can make the following claim with respect to the system (3.3.1).

**Claim 3.1.** *The system of ODEs (3.3.1) corresponds to a first-order method of lines discretization of the partial differential equation (PDE):*

$$\rho_{0,L} \frac{\partial^2 u(x, t)}{\partial t^2} = \frac{\partial F(\lambda(x, t), \dot{\varepsilon}(x, t))}{\partial x}, \quad 0 < x < L_{mus}^{opt}, \quad 0 < t < \infty, \quad (3.3.6)$$

subject to boundary conditions

$$u(0, t) = 0, \quad (3.3.7a)$$

$$F(\lambda(\cdot, t), \dot{\varepsilon}(\cdot, t)) \Big|_{x=L_{mus}^{opt}} = F_{ext}(t), \quad (3.3.7b)$$

and initial conditions

$$u(x, 0) = \frac{\partial u}{\partial t} = 0. \quad (3.3.8)$$

Here,  $F$  corresponds to Hill's force defined in (3.2.2) and  $\rho_{0,L} := m_{mus}/L_{mus}^{opt}$  is a linear density.

Note that the Neumann condition (3.3.7b) to a nonlinear type of boundary condition depending on  $\frac{\partial u}{\partial x}$ . Thus, the problem (3.3.6)-(3.3.8) is at least well-defined. Whether it is *well-posed* (that is, given a smooth  $F_{ext}$ , the problem has a unique regular solution depending continuously on  $F_{ext}$ ) is a different story and will not be discussed here. As it is known, this can only be done in limited scenarios (for instance, when  $F$  is linear, see [190]), so a general result cannot be stated for arbitrary  $F$  and  $F_{ext}$ .

*Proof.* Consider a discretization  $\{x_0, x_1, \dots, x_N\}$  with constant spacing  $\Delta x := L_{mus}^{opt}/N$  of the interval  $[0, L_{mus}^{opt}]$  where  $x_0 = 0$  and  $x_N = L_{mus}^{opt}$ , then, define  $u_i := u(x_i, t)$  for  $t \geq 0$ ,  $i = 1, \dots, N$ . Furthermore, consider a backwards first-order formula for the stretch and strain rates, that is,

$$\lambda_i = \lambda(x_i, t) = 1 + \frac{u_i - u_{i-1}}{\Delta x},$$

and

$$\dot{\varepsilon}_i = \dot{\varepsilon}(x_i, t) = \frac{1}{\dot{\varepsilon}_0} \frac{d\lambda_i}{dt}.$$

These are precisely (3.3.2) and (3.3.3). Now, to discretize the gradient on the right-hand side of (3.3.6), consider a forwards first-order difference:

$$\rho_{0,L} \frac{d^2 u_i}{dt^2} = \frac{F(\lambda_{i+1}, \dot{\varepsilon}_{i+1}) - F(\lambda_i, \dot{\varepsilon}_i)}{\Delta x}, \quad i = 1, \dots, N.$$

Given that there is not an  $x_{N+1}$  mass, the force required at this "ghost" node can be taken precisely as  $F_{ext}$  according to the boundary condition (3.3.7b). Hence, the previous expression is just (3.3.1).  $\square$

### 3.3.2 Convexifying the FL relationship

Let us introduce a base material component to Hill's force (3.2.2) assuming that it behaves as Neo-Hookean material:

$$F_{NH}(\lambda) = \begin{cases} F_0 \frac{\kappa}{\sigma_0} \left( \hat{\mathcal{L}}_\mu \lambda + \frac{\hat{\mathcal{L}}_\lambda \log(\lambda) - \hat{\mathcal{L}}_\mu}{\lambda} \right), & \lambda \geq 1, \\ 0, & \text{otherwise.} \end{cases} \quad (3.3.9)$$

Here,  $\kappa$  is the bulk modulus of muscle,  $\sigma_0$  is the maximum isometric stress, and the (non-dimensional) Lamé parameters are given by

$$\hat{\mathcal{L}}_\lambda = \frac{\nu}{(1-\nu)(1-2\nu)}, \quad \hat{\mathcal{L}}_\mu = \frac{1}{2(1+\nu)}, \quad (3.3.10)$$

with  $\nu$  being the Poisson's ratio of muscle tissue, which can be set to  $\nu = 0.499$  owing to the (near-)incompressibility of muscle [105].

In principle, the PDE (3.3.6) can be seen as a model for the one-dimensional deformation of a muscle fibre in which every point inside is subjected to Hill's force. Therefore, if we think of a fibre as a bundle of myofibrils, then we can consider the components that are in between to be part of the base material of a fibre. These components include (but are not limited to) the sarcoplasmic reticulum and the T-tubules. In this way, we consider the following expression for the muscle force in (3.3.6):

$$F(\lambda, \dot{\varepsilon}) = (1 - \chi_{BM}) F_{Hill}(\lambda, \dot{\varepsilon}) + \chi_{BM} F_{NH}(\lambda), \quad (3.3.11)$$

where  $\chi_{BM}$  denotes the fraction of base material that could be present in a muscle fibre. Thus, the more base material we introduce in the model, the more we can convexify the FL curve. Luckily,  $\chi_{BM}$  does not have to be large to bring stability to the system, as we will see in the experiment below.

### 3.3.3 A stabilized mass-enhanced muscle model

Following the result in Claim 3.1, we can write a stabilized version of (3.2.1) using the force expression (3.3.11):

$$\begin{aligned} m_{i-1} \ddot{u}_{i-1} &= (1 - \chi_{BM}) [F_{Hill}(\lambda_i, \dot{\varepsilon}_i) - F_{Hill}(\lambda_{i-1}, \dot{\varepsilon}_{i-1})] \\ &\quad + \chi_{BM} [F_{BM}(\lambda_i) - F_{BM}(\lambda_{i-1})], \quad i = 1, \dots, N-1, \end{aligned} \quad (3.3.12)$$

with the stretches  $\lambda_i$  and strain rates  $\dot{\varepsilon}_i$  as in (3.2.3) and (3.2.4), respectively. Then, we can repeat the experiment from Section 3.2.2 to test the stability of the zero solution. In particular, we take in equation (3.3.11) a bulk modulus  $\kappa = 10^6$  Pa and a maximum isometric stress  $\sigma_0 = 200$  kPa [4]. Furthermore, we consider  $\chi_{BM} = 0.0015$ , that is, we assume that 99.85% of the force that a muscle fibre produces is due to Hill's force and 0.15% from a base material contribution.

First, we portray the resulting forces in Figure 3.4 where the total force (3.3.11) shows RFE for muscle lengths above optimal (i.e.  $\lambda_M > 1$ ). Then, in Figure 3.5 we show the results for the same three isometric contractions as in Section 3.2.3 which show (1): no difference for  $\lambda_0 = 0.85$  since the Neo-Hookean term does not act for stretches below 1, (2): stabilization on the descending limb of the active FL curve, shown in the figure for  $\lambda_0 = 1.15$ , and (3): rapid stabilization due to a stiffer passive element. Therefore, it is clear that the base material component has a stabilizing effect in isometric contractions.

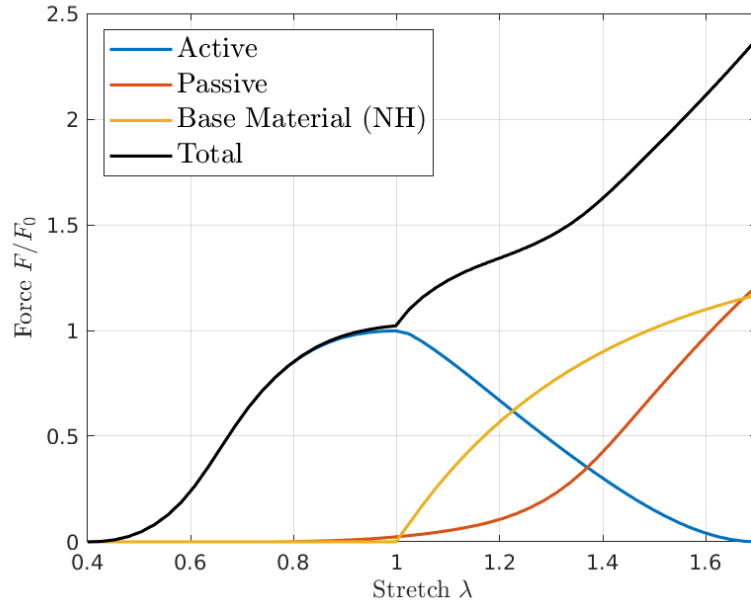


Figure 3.4: Forces in the stabilized model (3.3.12). When the base material component (yellow) is added to the active (blue) and passive (red) forces, the total force (black) is a monotonically increasing function.

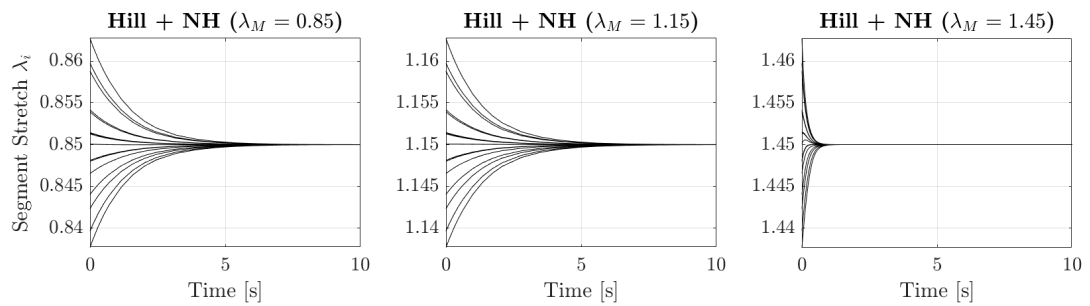


Figure 3.5: Stability of an isometric contraction according to the system of ODEs (3.3.12). As before, the elements (as well as the muscle) are stretched initially at around 85% (left), 115% (middle), and 145% (right) of the muscle's optimal length. In all cases, the contractions are stable since the derivative of the total force (made of active, passive, and base material components) is always positive.

### 3.4 Nondimensionalization of the continuum system and the influence of mass

The elastic model (3.3.6) with the force  $F$  given by (3.3.11) can be used to explain the mass effects discussed in Chapter 2 in a succinct way. First, let

$$\hat{F}_{Hill} = \frac{F_{Hill}}{F_0}, \quad \hat{F}_{NH} = \frac{F_{NH}}{F_0}, \quad (3.4.1)$$

denote the nondimensional versions of the Hill and Neo-Hookean force terms. Moreover, consider the following nondimensional variants of the displacement, space, and time variables:

$$\hat{u} = \frac{u}{L_{mus}^{opt}}, \quad \hat{x} = \frac{x}{L_{mus}^{opt}}, \quad \hat{t} = \frac{t}{1/\dot{\varepsilon}_0}. \quad (3.4.2)$$

Plugging these quantities into (3.3.6) we obtain:

$$\frac{\rho_{0,L}(L_{mus}^{opt})^2\dot{\varepsilon}_0^2}{F_0} \frac{\partial^2 \hat{u}}{\partial \hat{t}^2} = (1 - \chi_{BM})\hat{F}_{Hill} + \chi_{BM} \frac{\kappa}{\sigma_0} \hat{F}_{BM}. \quad (3.4.3)$$

All terms in the previous equation are nondimensional, but we can further rearrange the terms in the left-hand side to obtain a more physically meaningful number.

Recall that  $\rho_{0,L}$  is a *linear* density (it has units of  $\text{kg m}^{-1}$ ). We can convert this quantity into the more common *volumetric* density  $\rho_0$  through the cross-sectional area (CSA) of a muscle fibre, that is,

$$\rho_{0,L} = \rho_0 \cdot CSA. \quad (3.4.4)$$

Moreover, because the maximum isometric force  $F_0$  can be written in terms of the maximum isometric stress as  $F_0 = \sigma_0 \cdot CSA$ , the number on the left-hand side of (3.4.3) can be written as

$$\frac{\rho_0(L_{mus}^{opt})^2\dot{\varepsilon}_0^2}{F_0} = \frac{\rho_0(L_{mus}^{opt})^2\dot{\varepsilon}_0}{\sigma_0/\dot{\varepsilon}_0}. \quad (3.4.5)$$

The nondimensional number in the previous expression can be viewed as a ratio between inertial forces (due to mass) and viscous forces. As such, we call this number the *musculoskeletal Reynolds number* ( $Re_{MSK}$ ), akin to the Reynolds number commonly found in fluid dynamics. In this way, we can rewrite (3.4.3) as:

$$Re_{MSK} \frac{\partial^2 \hat{u}}{\partial \hat{t}^2} = (1 - \chi_{BM})\hat{F}_{Hill} + \chi_{BM} \frac{\kappa}{\sigma_0} \hat{F}_{BM}. \quad (3.4.6)$$

Therefore, if the length of the muscle scales by a factor  $s$ , the rescaled musculoskeletal Reynolds number becomes:

$$Re_{MSK} = s^2 \frac{\rho_0(L_{mus}^{opt})^2\dot{\varepsilon}_0}{\sigma_0/\dot{\varepsilon}_0}. \quad (3.4.7)$$

$s$	$\dot{\varepsilon}_0$ [s $^{-1}$ ]	$\text{Re}_{MSK}$
1	5	$1.1925 \cdot 10^{-5}$
1	10	$4.77 \cdot 10^{-5}$
10	5	$1.1925 \cdot 10^{-3}$
10	10	$4.77 \cdot 10^{-3}$

Table 3.1: Variation in the musculoskeletal Reynolds number  $\text{Re}_{MSK}$  when a scaling factor  $s$  is introduced for two different maximum (unloaded) strain rates ( $5\text{ s}^{-1}$  and  $10\text{ s}^{-1}$ ). Here,  $\rho_0 = 1.060\text{ kg m}^{-3}$ ,  $\sigma_0 = 200\text{ kPa}$ ,  $L_{mus}^{opt} = 0.3\text{ m}$ .

This explains why one can expect, in this one-dimensional context, that mass effects are larger for larger scales, longer muscles (such as the semitendinosus), and muscles that contain a higher proportion of faster fibres (i.e., larger  $\dot{\varepsilon}_0$ ). See Table 3.1 for some values of this nondimensional number.

## Chapter 4

# First order is enough: time discretization alternatives for dynamic Neo-Hookean deformation

As a prelude to the development of computational tools for the study of dynamic 3D skeletal muscle deformation, we now face the task of finding an appropriate time stepping scheme for this problem. This is an effort to extend the developments of Rahemi [154] and Dominguez [54] regarding quasi-static models. To accomplish this, we study the performance of different time stepping schemes, from methods used in engineering finite element analysis to Matlab's built-in solvers. However, because the complexity of the full 3D nonlinear model obscures the main details of the numerical algorithms in use, we therefore focus on applying these methods to a simpler (yet representative) model of one-dimensional Neo-Hookean deformation.

First, we discuss time stepping methods that are commonly used in dynamic analysis of structures, as well as their advantages and disadvantages. Next, we state a model problem in 1D and present some of these methods in two different contexts, depending on which variable in the continuous problem is discretized first: time or space. This is a particularly important consideration for nonlinear problems with (potentially) nonsmooth boundary conditions. Then, we present convergence studies for a linear problem. We then perform numerical experiments of Neo-Hookean deformation in order to compare. In addition to classic time stepping methods used in engineering, we also study an implicit-explicit (IMEX) method and several of Matlab's built-in solvers for systems of ODEs. We finish the chapter with a discussion on the obtained results and what this means for the development of a 3D *dynamic* finite element code for skeletal muscle tissue.

## 4.1 Background

We start with two discussions that will, hopefully, help the reader understand our choices and results for this chapter: what type of time stepping should we choose and what variable (space or time) should be discretized first.

### 4.1.1 Time stepping schemes in engineering elastodynamics

The discretization of elastodynamic models is a well established research area in engineering. Tried-and-tested techniques are widely available in modern, commonly used finite element analysis software, such as Ansys Mechanical, Ansys LS-DYNA, COMSOL, and Abaqus. In particular, for linear elastodynamics, well-known time stepping schemes include Newmark- $\beta$  schemes [136], Wilson- $\theta$  schemes [200], HHT- $\alpha$  schemes [84], WBZ- $\alpha$  schemes [204], HP- $\theta_1$  methods [88], and more recently, structure-dependent schemes (i.e. numerical methods whose parameters depend on the material properties of the structure) such as those by Chang [39]. In general, studies in mechanical engineering will claim that a good time stepping scheme for the linear problem must have the following characteristics (see, e.g. [91, 100, 169]):

1. Unconditional stability,
2. Second-order accuracy,
3. Being single-step, that is, only one set of implicit equations needs to be solved per time step and the only information needed to do this is from the immediately previous time step,
4. Controllable numerical dissipation in the higher modes,
5. Self-starting,
6. Should not *overshoot* the solution.

*Overshooting* is a phenomenon in which the numerical method “overestimates” the solution in the first steps due to the excitation of high-frequency modes (see Figure 4.1). This is commonly observed in stiff problems where either non-zero or non-smooth boundary conditions are used. Moreover, all the time schemes mentioned at the beginning of this section, are prone to suffer this problem [121]. This means that overshooting is, albeit undesirable, a potentially manageable nuisance.

While numerical methods such as Newmark’s or HHT- $\alpha$  do verify characteristics 1-6 above in the context of linear problems, they may not for nonlinear problems. Consider the nonlinear second order ODE:

$$\ddot{y} = \varphi(y, \dot{y}) \quad \text{in } (0, \infty),$$

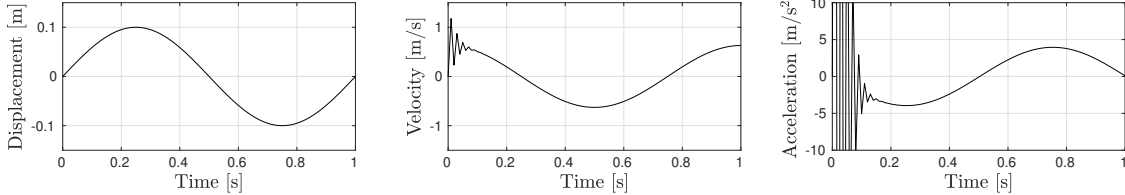


Figure 4.1: Example of overshooting in the velocity variable, which causes even higher oscillations in the acceleration.

where  $\varphi : \mathbb{R} \times \mathbb{R} \rightarrow \mathbb{R}$  is smooth function. If an implicit method is used to discretize this equation, then at each time step, the nonlinear problem must be linearized (using strategies such as Newton's method). Furthermore, if iterative solvers are used to solve the (discretized) linear problem, then multiple linear systems are solved at each Newton iteration, and multiple Newton iterations are needed for each time step. Therefore, second-order accuracy might not be achieved, or if it does, the numerical methods might still exhibit overshooting and oscillations beyond the high-frequency regime [60].

#### 4.1.2 Time or space first? Rothe's method versus method of lines

When it comes to numerical methods for spatio-temporal problems, at least two approaches arise depending on the order in which the variables (space and time) are discretized.

One alternative is to discretize the time variable first while keeping the space variable continuous. This is referred to as *Rothe's method* [170]. For second order parabolic and hyperbolic systems (the latter being the case for elastodynamics), this means that, at each time step, we are bound to solve an elliptic PDE in the space variable. For nonlinear PDEs, the linearization can be performed at a continuous level using, for instance, Gâteaux derivatives. One of the advantages of this method is that, in the context of finite element methods, updates to the mesh can easily be performed since they do not alter the variational formulation of the elliptic problem. However, one major disadvantage is that it is harder to test different time stepping strategies since they involve modifying the structure of the variational formulation itself, which may induce significant modifications to the computational solvers. We will see these differences throughout Sections 4.3 to 4.5.

A different approach is to discretize the space variable first, then the time variable. This leads to the *method of lines (MOL)* [110] and it is how Newmark-type methods are introduced in the engineering literature [91]. In this case, the parabolic or hyperbolic PDE is transformed into a system of ODEs. This is one of the major advantages of the MOL since it is relatively easy to test multiple time stepping schemes implemented as ODE solvers. However, this also means that the spatial mesh is fixed at all times, which is not amenable to a posteriori mesh refinements (especially at each time step).

## 4.2 Model problem for nonlinear elasticity

Consider a one-dimensional solid (which we may refer to as a “rod”) of linear density  $\rho_{0,L}$  and cross-sectional area  $A_0$  that occupies the region  $\Omega = [0, L]$ . Furthermore, let  $u = u(x, t)$  denote the displacement of a point  $x$  at time  $t$ . We consider the following model for the deformation of this rod subject to a prescribed displacement  $g = g(t)$  at one of its ends:

$$\rho_0 u_{tt} = P_x \quad \text{in } \Omega \times (0, \infty), \quad (4.2.1a)$$

$$u(x, 0) = 0, \quad u_t(x, 0) = 0 \quad \text{in } \Omega \times \{t = 0\} \quad (4.2.1b)$$

$$u(0, t) = 0, \quad u(L, t) = g(t) \quad \text{in } (0, \infty). \quad (4.2.1c)$$

Here,  $\rho_0 = \rho_{0,L}/A_0$  is a volumetric density and  $P = P(\lambda)$  is a constitutive equation for the stress of the material depending on the stretch  $\lambda := u_x + 1$ . The equation above is very similar to (3.3.6) but with a stress  $P$  instead of a force  $F$  to match the dimensions of the left-hand side of (4.2.1a).

## 4.3 A first order time stepping scheme

Let us consider a first order scheme inspired by previous works on skeletal muscle modelling (e.g. [54, 196]). To keep the focus on the time discretization, all methods will feature a spatial discretization based on second-order Lagrange finite elements.

### 4.3.1 Rothe’s method and finite element formulation

First, we convert the PDE (4.2.1a) into a system of first order PDEs. Then, we discretize the time derivatives using a first-order backwards formula. This yields the following semi-discrete problem for  $n \geq 0$ :

$$\frac{u^{n+1} - u^n}{\Delta t} = v^{n+1}, \quad (4.3.1a)$$

$$\rho_0 \left( \frac{v^{n+1} - v^n}{\Delta t} \right) = P(\lambda^{n+1})_x, \quad (4.3.1b)$$

where the stretch  $\lambda^{n+1} = \partial_x u^{n+1} + 1$ . Combining these two equations into a single one for  $u^{n+1}$  yields:

$$\rho_0 u^{n+1} - \Delta t^2 P(\lambda^{n+1})_x = \rho_0(u^n + \Delta t v^n), \quad n \geq 0. \quad (4.3.2)$$

Then, we take steps to discretize the spatial variable as specified at the beginning of this section. Multiplying (4.3.2) by a test function  $w \in H_0^1(\Omega)$  and integrating by part we obtain the nonlinear variational formulation: find  $u^{n+1} \in H^1(\Omega)$  such that  $u^{n+1}(0) = 0$ ,  $u^{n+1}(L) = g(t^{n+1})$ , and

$$R(u^{n+1}, w) = 0 \quad \forall w \in H_0^1(\Omega), \quad (4.3.3)$$

where  $R : H^1(\Omega) \times H_0^1(\Omega) \rightarrow \mathbb{R}$  is the functional defined by

$$R(u^{n+1}, w) := \rho_0 \int_0^L u^{n+1} w + \Delta t^2 \int_0^L P(\lambda^{n+1}) w_x - \rho_0 \int_0^L (u^n + \Delta t v^n) w. \quad (4.3.4)$$

### Linearization of the semi-discrete problem

We solve the nonlinear problem (4.3.3) using Newton's method. Suppose  $u^n \approx u(x, t^n)$ . Given  $u_0^{n+1} = u^n$ , the  $k$ -th iteration reads: find increments  $\delta u_k^{n+1}$  such that

$$\mathcal{D}R[u_k^{n+1}](\delta u_k^{n+1}, w) = -R(u_k^{n+1}, w) \quad \forall w \in H_0^1(\Omega), \quad (4.3.5)$$

where  $\mathcal{D}R$  is the Gâteaux derivative of  $R$  and can be computed as:

$$\mathcal{D}R[u](\delta u, w) = \lim_{\epsilon \rightarrow 0} \frac{d}{d\epsilon} R(u + \epsilon \delta u, w). \quad (4.3.6)$$

Therefore, the linear problem (4.3.5) becomes: find Newton increments  $\delta u_k^{n+1} \in H^1(\Omega)$  such that  $du_0^{n+1} = 0$  on  $x = 0$ ,  $du_0^{n+1} = g(t^{n+1}) - g(t^n)$  on  $x = L$ ,  $\delta u_k^{n+1} = 0$  on  $x = 0, L$  for  $k > 0$ , and:

$$\begin{aligned} \rho_0 \int_0^L \delta u_k^{n+1} w + \Delta t^2 \int_0^L \frac{dP}{d\lambda}(\lambda_k^{n+1}) \frac{d(\delta u_k^{n+1})}{dx} \frac{dw}{dx} = \\ - \rho_0 \int_0^L u_k^{n+1} w - \Delta t^2 \int_0^L P(\lambda_k^{n+1}) \frac{dw}{dx} + \rho_0 \int_0^L (u^n + \Delta t v^n) w, \end{aligned} \quad (4.3.7)$$

for any  $w \in H_0^1(\Omega)$ , where the stretch for the current Newton iteration is  $\lambda_k^{n+1} = \partial_x u_k^{n+1} + 1$ . Note that, unlike the nonlinear formulation (4.3.3), for  $k \geq 1$ , the linear formulation (4.3.7) is symmetric (i.e., test and trial spaces are the same).

The linear problem (4.3.7) is solved for each  $k \geq 0$  and the displacement is updated as  $u_{k+1}^{n+1} = u_k^{n+1} + \delta u_k^{n+1}$  until the following convergence criterion is satisfied:

$$\|\delta u_k^{n+1}\| \leq tol_u \quad \text{and} \quad \|R(u_k^{n+1})\| \leq tol_R, \quad (4.3.8)$$

where  $\|\cdot\|$  is a user-defined discrete norm (e.g. the Euclidean norm) arising from the discretized versions (see below) of the Newton update  $\delta u_k^{n+1}$  and the right-hand side of (4.3.5).

### Finite element formulation

In this subsection, we present the details of a finite element method (FEM) approach to deal with the spatial discretization. For the linear problem (4.3.7), we consider the following

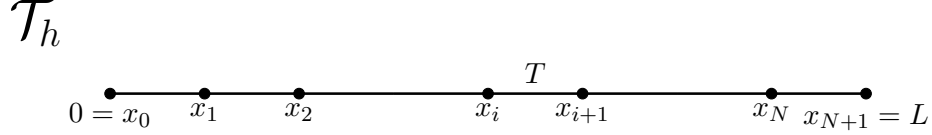


Figure 4.2: Mesh for the interval  $[0, L]$ .

Galerkin scheme for the Newton increment  $\delta u_k^{n+1}$ : given  $u_{h,k}^{n+1}$ , find  $\delta u_{h,k}^{n+1} \in V_h$  such that

$$\begin{aligned} \rho_0 \int_0^L \delta u_{h,k}^{n+1} w_h + \Delta t^2 \int_0^L \frac{dP}{d\lambda}(\lambda_{h,k}^{n+1}) \frac{d(\delta u_{h,k}^{n+1})}{dx} \frac{dw_h}{dx} = \\ - \rho_0 \int_0^L u_{h,k}^{n+1} w - \Delta t^2 \int_0^L P(\lambda_{h,k}^{n+1}) \frac{dw_h}{dx} + \rho_0 \int_0^L (u_h^n + \Delta t v_h^n) w_h, \end{aligned} \quad (4.3.9)$$

for any  $w_h \in V_h$ . Here,  $V_h$  is the space of second order Lagrange finite elements:

$$V_h = \left\{ v_h \in \mathcal{C}(\bar{\Omega}) : v_h|_T \in \mathbb{P}_2(T) \quad \forall T \in \mathcal{T}_h \right\}, \quad (4.3.10)$$

where  $\mathcal{C}(\bar{\Omega})$  is the space of continuous functions over  $\bar{\Omega} = [0, L]$ ,  $\mathbb{P}_2(T)$  is the space of quadratic polynomials over a segment  $T \subset [0, L]$ , and  $\mathcal{T}_h$  is a triangulation of the interval  $[0, L]$ . Therefore, if  $\{x_0, x_1, \dots, x_{N+1}\}$  is a discretization of the interval  $[0, L]$  with  $x_0 = 0$  and  $x_{N+1} = L$ , then,  $\mathcal{T}_h = \{[x_i, x_{i+1}]\}_{i=0}^N$  (see Figure 4.2).

### Notation for the local problems

The purpose of this subsection is to help establish both notation and details of the FEM applied to a local problem. This will be useful when comparing time stepping schemes.

First, let  $T \in \mathcal{T}_h$  be an arbitrary interval of the triangulation  $\mathcal{T}_h$  with endpoints  $x_i$  and  $x_{i+1}$ , that is,  $T = [x_i, x_{i+1}]$ . Then, consider the linear transformation  $\mathcal{F} : \hat{T} \rightarrow T$  that maps elements from the “reference” interval  $\hat{T} = [0, 1]$  to an arbitrary interval  $T$ :

$$\mathcal{F}(\hat{x}) := B\hat{x} + b = x, \quad (4.3.11)$$

where  $B := x_{i+1} - x_i$ ,  $b := x_i$ . Therefore, given a function  $u : T \rightarrow \mathbb{R}$ , we can define  $\hat{u} : \hat{T} \rightarrow \mathbb{R}$  as

$$\hat{u} = u \circ \mathcal{F},$$

from which we obtain the following identities that will help us move from an arbitrary interval  $T$  to the reference interval  $\hat{T}$ :

$$\frac{d\hat{u}}{d\hat{x}} = B \frac{du}{dx}, \quad (4.3.12a)$$

$$\int_T u \, dx = B \int_{\hat{T}} \hat{u} \, d\hat{x}, \quad (4.3.12b)$$

$$\int_T \frac{du}{dx} \frac{dw}{dx} \, dx = B^{-1} \int_{\hat{T}} \frac{d\hat{u}}{d\hat{x}} \frac{d\hat{w}}{d\hat{x}} \, d\hat{x}. \quad (4.3.12c)$$

Furthermore, any element in  $u \in \mathbb{P}_2(T)$  can be written as:

$$u(x) = \sum_{i=1}^3 p_i(x) u_i, \quad (4.3.13)$$

where

$$p_1(x) = \frac{(x - x_{i+1/2})(x - x_{i+1})}{(x_i - x_{i+1/2})(x_i - x_{i+1})}, \quad (4.3.14a)$$

$$p_2(x) = \frac{(x - x_i)(x - x_{i+1})}{(x_{i+1/2} - x_i)(x_{i+1/2} - x_{i+1})}, \quad (4.3.14b)$$

$$p_3(x) = \frac{(x - x_i)(x - x_{i+1/2})}{(x_{i+1} - x_i)(x_{i+1} - x_{i+1/2})}, \quad (4.3.14c)$$

with  $x_{i+1/2} = (x_i + x_{i+1})/2$ . Equation (4.3.13) can be compactly written as

$$u = [\mathbf{P}][\mathbf{u}], \quad (4.3.15)$$

where

$$[\mathbf{P}] := (p_1 \quad p_2 \quad p_3)_{1 \times 3}, \quad [\mathbf{u}] = \begin{pmatrix} u_1 \\ u_2 \\ u_3 \end{pmatrix}_{3 \times 1}.$$

Thus, the mapped expression  $\hat{u} = u \circ \mathcal{F}$  can be written as

$$\hat{u} = \sum_{i=1}^3 \hat{p}_i(\hat{x}) u_i = [\hat{\mathbf{P}}][\mathbf{u}], \quad (4.3.16)$$

where

$$[\hat{\mathbf{P}}] := (\hat{p}_1 \quad \hat{p}_2 \quad \hat{p}_3)_{1 \times 3}$$

and

$$\hat{p}_1(x) = (1 - 2\hat{x})(1 - \hat{x}), \quad (4.3.17a)$$

$$\hat{p}_2(x) = 4\hat{x}(1 - \hat{x}), \quad (4.3.17b)$$

$$\hat{p}_3(x) = \hat{x}(2\hat{x} - 1). \quad (4.3.17c)$$

These shape functions are meant to interpolate the nodes  $\hat{a}_1 = 0$ ,  $\hat{a}_2 = 1/2$ , and  $\hat{a}_3 = 1$ , that is,  $\hat{p}_i(\hat{a}_j) = \delta_{ij}$  for  $i, j = 1, 2, 3$ , with  $\delta_{ij}$  being the delta Kronecker. In addition, for the derivative of  $\hat{u}$ , we may write:

$$\frac{d\hat{u}}{d\hat{x}} = \sum_{i=1}^3 \frac{d\hat{p}_i}{d\hat{x}}(\hat{x}) u_i = [\hat{\mathbf{D}}\hat{\mathbf{P}}][\mathbf{u}], \quad (4.3.18)$$

where

$$[\hat{\mathbf{D}}\hat{\mathbf{P}}] = \begin{pmatrix} \frac{d\hat{p}_1}{d\hat{x}} & \frac{d\hat{p}_2}{d\hat{x}} & \frac{d\hat{p}_3}{d\hat{x}} \end{pmatrix}_{1 \times 3},$$

with an analogous expression for the derivative of  $u$  using the identity (4.3.12a).

### Local contributions and fully discrete system

Restricted to an element  $T = [x_i, x_{i+1}] \in \mathcal{T}_h$ , we can write (4.3.9) as:

$$\begin{aligned} \rho_0 \int_T \delta u_{h,k}^{n+1} w_h + \Delta t^2 \int_T \frac{dP}{d\lambda}(\lambda_{h,k}^{n+1}) \frac{d(\delta u_{h,k}^{n+1})}{dx} \frac{dw_h}{dx} = \\ - \rho_0 \int_T u_{h,k}^{n+1} w - \Delta t^2 \int_T P(\lambda_{h,k}^{n+1}) \frac{dw_h}{dx} + \rho_0 \int_T (u_h^n + \Delta t v_h^n) w_h, \end{aligned} \quad (4.3.19)$$

where each term can be fully computed following the ideas introduced above (we drop the  $h$  subscript for better readability). First, the terms on the left-hand side of (4.3.19) (recall that  $B = x_{i+1} - x_i$ ):

$$\begin{aligned} \rho_0 \int_T du_k^{n+1} w = \rho_0 B \int_{\hat{T}} \widehat{\delta u_k^{n+1}} \widehat{w} \\ = \rho_0 B \int_{\hat{T}} [\hat{\mathbf{P}}][\mathbf{d}\mathbf{u}_k^{n+1}][\hat{\mathbf{P}}][\mathbf{w}] \\ = [\mathbf{w}]^\top \left( \rho_0 B \int_{\hat{T}} [\hat{\mathbf{P}}]^\top [\hat{\mathbf{P}}] \right) [\mathbf{d}\mathbf{u}_k^{n+1}] \\ =: [\mathbf{w}]^\top \mathbf{M}_T [\mathbf{d}\mathbf{u}_k^{n+1}], \end{aligned} \quad (4.3.20)$$

and

$$\begin{aligned}
& \int_T \frac{dP}{d\lambda}(\lambda_k^{n+1}) \frac{d(dw_k^{n+1})}{dx} \frac{dw}{dx} \\
&= B^{-1} \int_{\hat{T}} \frac{dP}{d\lambda} \left( \widehat{\lambda_k^{n+1}} \right) \frac{d(\widehat{du_k^{n+1}})}{dx} \frac{d\hat{w}}{dx} \\
&= B^{-1} \int_{\hat{T}} \frac{dP}{d\lambda} \left( B^{-1} [\hat{D}\hat{P}] [\mathbf{u}_k^{n+1}] + 1 \right) [\hat{D}\hat{P}] [\mathbf{d}\mathbf{u}_k^{n+1}] [\hat{D}\hat{P}] [\mathbf{w}] \\
&= [\mathbf{w}]^\top \left( B^{-1} \int_{\hat{T}} \frac{dP}{d\lambda} \left( B^{-1} [\hat{D}\hat{P}] [\mathbf{u}_k^{n+1}] + 1 \right) [\hat{D}\hat{P}]^\top [\hat{D}\hat{P}] \right) [\mathbf{d}\mathbf{u}_k^{n+1}] \\
&=: [\mathbf{w}]^\top \mathbf{K}_T [\mathbf{d}\mathbf{u}_k^{n+1}]. \tag{4.3.21}
\end{aligned}$$

The terms  $\mathbf{M}_T$  and  $\mathbf{K}_T$  are local contributions to the global mass and stiffness matrices  $\mathbf{M}$  and  $\mathbf{K}$ , respectively. Following [91], we denote the assembly process by:

$$\mathbf{M} = \bigwedge_{T \in \mathcal{T}_h} \mathbf{M}_T, \quad \mathbf{K} = \bigwedge_{T \in \mathcal{T}_h} \mathbf{K}_T. \tag{4.3.22}$$

Next, we compute the terms on the right-hand side of (4.3.19):

$$\begin{aligned}
\rho_0 \int_T u_k^{n+1} w &= \rho_0 B \int_{\hat{T}} [\hat{P}] [\mathbf{u}_k^{n+1}] [\hat{P}] [\mathbf{w}] \\
&= [\mathbf{w}]^\top \left( \rho_0 B \int_{\hat{T}} [\hat{P}]^\top [\hat{P}] [\mathbf{u}_k^{n+1}] \right) \\
&=: [\mathbf{w}]^\top \mathbf{F}_T^{(1)}, \tag{4.3.23}
\end{aligned}$$

$$\begin{aligned}
\Delta t^2 \int_T P(\lambda_k^{n+1}) \frac{dw}{dx} &= \Delta t^2 \int_{\hat{T}} P \left( B^{-1} [\hat{D}\hat{P}] [\mathbf{u}_k^{n+1}] + 1 \right) [\hat{D}\hat{P}] [\mathbf{w}] \\
&= [\mathbf{w}]^\top \left( \Delta t^2 \int_{\hat{T}} P \left( B^{-1} [\hat{D}\hat{P}] [\mathbf{u}_k^{n+1}] + 1 \right) [\hat{D}\hat{P}]^\top \right) \tag{4.3.24}
\end{aligned}$$

$$=: [\mathbf{w}]^\top \mathbf{F}_T^{(2)}, \tag{4.3.25}$$

and

$$\begin{aligned}
\rho_0 \int_T (u^n + \Delta t v^n) w &= \rho_0 B \int_{\hat{T}} [\hat{P}] ([\mathbf{u}^n] + \Delta t [\mathbf{v}^n]) [\hat{P}] [\mathbf{w}] \\
&= [\mathbf{w}]^\top \left( \rho_0 B \int_{\hat{T}} [\hat{P}]^\top [\hat{P}] ([\mathbf{u}^n] + \Delta t [\mathbf{v}^n]) \right) \\
&=: [\mathbf{w}]^\top \mathbf{F}_T^{(3)}. \tag{4.3.26}
\end{aligned}$$

These are contributions to the load vector  $\mathbf{F}$  which can be computed as

$$\mathbf{F} = \bigwedge_{T \in \mathcal{T}_h} \mathbf{F}_T^{(1)} + \mathbf{F}_T^{(2)} + \mathbf{F}_T^{(3)}. \tag{4.3.27}$$

In conclusion, if we use Rothe's method, the fully discrete system that arises from the Galerkin formulation (4.3.9) for the increment  $\delta u_k^{n+1}$  is:

$$(\mathbf{M} + \Delta t^2 \mathbf{K}) \mathbf{d}\mathbf{u}_k^{n+1} = \mathbf{F}, \quad (4.3.28)$$

with  $\mathbf{M}$ ,  $\mathbf{K}$ , and  $\mathbf{F}$  as in (4.3.22) and (4.3.27).

### 4.3.2 Method of lines

In this case, we first discretize the problem in *space*. We construct a weak formulation for (4.2.1a) by multiplying the PDE by a test function  $w \in H_0^1(\Omega)$  and integrate by parts in space. This yields the problem: for each  $t > 0$ , find  $u(\cdot, t) \in H^1(\Omega)$  such that  $u(0, t) = 0$ ,  $u(L, t) = g(t)$ , and

$$\rho_0 \int_0^L u_{tt} w + \int_0^L P(\lambda) w_x = 0 \quad \forall w \in H_0^1(\Omega). \quad (4.3.29)$$

Then, the Galerkin scheme reads: for each  $t > 0$ , find  $u_h(\cdot, t) \in V_h$  such that  $u_h(0, t) = 0$ ,  $u_h(L, t) = g(t)$ , and

$$\rho_0 \int_0^L u_{h,tt} w_h + \int_0^L P(\lambda_h) w_{h,x} = 0 \quad \forall w_h \in V_{h,0}, \quad (4.3.30)$$

where  $V_{h,0} = V_h \cap H_0^1(\Omega)$ . As before, we consider  $V_h$  given by (4.3.10) and a discretization  $\mathcal{T}_h$  of the interval  $[0, L]$ , i.e.  $\mathcal{T}_h = \{[x_i, x_{i+1}]\}_{i=0}^N$ . In this case, for  $T \in \mathcal{T}_h$ , we can write

$$u_h(x, t) \Big|_T = \sum_{i=1}^3 p_i(x) u_i(t), \quad (4.3.31)$$

with  $p_i$  the shape functions given in (4.3.14). After computing the local contributions as in (4.3.19)-(4.3.26), the Galerkin scheme (4.3.30) reduces to the nonlinear system of equations:

$$\mathbf{M} \ddot{\mathbf{U}} + \mathbf{K}(\mathbf{U}) = \mathbf{0}, \quad (4.3.32)$$

where  $\mathbf{U} = (u_0(t), \dots, u_{2N+1}(t))^\top$  and  $\mathbf{M}$  is again the mass matrix:

$$\mathbf{M} = \bigwedge_{T \in \mathcal{T}_h} \mathbf{M}_T, \quad \mathbf{M}_T = \rho_0 B \int_{\hat{T}} [\hat{\mathbf{P}}]^\top [\hat{\mathbf{P}}], \quad (4.3.33)$$

but now  $\mathbf{K}(\mathbf{U})$  is the stiffness *vector*:

$$\mathbf{K} = \bigwedge_{T \in \mathcal{T}_h} \mathbf{K}(\mathbf{U})_T, \quad \mathbf{K}(\mathbf{U})_T = \int_{\hat{T}} P \left( B^{-1} [\hat{\mathbf{D}} \hat{\mathbf{P}}][\mathbf{u}(t)] + 1 \right) [\hat{\mathbf{D}} \hat{\mathbf{P}}]^\top. \quad (4.3.34)$$

At this juncture, we can use any appropriate ODE solver for the nonlinear system (4.3.32). Hence, let us consider first the same first order scheme as in (4.3.1):

$$\frac{\mathbf{U}^{n+1} - \mathbf{U}^n}{\Delta t} = \mathbf{V}^{n+1}, \quad (4.3.35a)$$

$$\mathbf{M} \left( \frac{\mathbf{V}^{n+1} - \mathbf{V}^n}{\Delta t} \right) + \mathbf{K}(\mathbf{U}^{n+1}) = \mathbf{0}. \quad (4.3.35b)$$

Combining these two equations yields:

$$\mathbf{M}\mathbf{U}^{n+1} + \Delta t^2 \mathbf{K}(\mathbf{U}^{n+1}) = \mathbf{M}(\mathbf{U}^n + \Delta t \mathbf{V}^n). \quad (4.3.36)$$

The equation above is a nonlinear system of equations that can be rewritten as:

$$\mathbf{R}(\mathbf{U}^{n+1}) := \mathbf{M}\mathbf{U}^{n+1} + \Delta t^2 \mathbf{K}(\mathbf{U}^{n+1}) - \mathbf{M}(\mathbf{U}^n + \Delta t \mathbf{V}^n) = \mathbf{0}. \quad (4.3.37)$$

Hence, a Taylor expansion reveals the Newton iteration to follow:

$$\mathbf{R}(\mathbf{U}_{k+1}^{n+1}) = \mathbf{R}(\mathbf{U}_k^{n+1}) + \frac{\partial \mathbf{R}}{\partial \mathbf{U}^{n+1}}(\mathbf{U}_k^{n+1}) \Delta \mathbf{U}_k^{n+1} + \dots = \mathbf{0}, \quad (4.3.38)$$

that is,

$$\frac{\partial \mathbf{R}}{\partial \mathbf{U}^{n+1}}(\mathbf{U}_k^{n+1}) \Delta \mathbf{U}_k^{n+1} = -\mathbf{R}(\mathbf{U}_k^{n+1}). \quad (4.3.39)$$

Therefore, the Newton iteration for the nonlinear problem (4.3.36) reads: find the increment vector  $\Delta \mathbf{U}_k^{n+1}$  such that:

$$\left[ \mathbf{M} + \Delta t^2 \frac{\partial \mathbf{K}}{\partial \mathbf{U}}(\mathbf{U}_k^{n+1}) \right] \Delta \mathbf{U}_k^{n+1} = -\mathbf{M}\mathbf{U}_k^{n+1} - \Delta t^2 \mathbf{K}(\mathbf{U}_k^{n+1}) + \mathbf{M}(\mathbf{U}^n + \Delta t \mathbf{V}^n). \quad (4.3.40)$$

Then, we can update the displacements  $\mathbf{U}_{k+1}^{n+1} = \mathbf{U}_k^{n+1} + \Delta \mathbf{U}_k^{n+1}$ . The new (matrix) term  $\frac{\partial \mathbf{K}}{\partial \mathbf{U}}$  can be computed from (4.3.34) as:

$$\frac{\partial \mathbf{K}}{\partial \mathbf{U}}(\mathbf{U}_k^{n+1}) = \bigwedge_{T \in \mathcal{T}_h} B^{-1} \int_{\widehat{T}} \frac{dP}{d\lambda} \left( B^{-1} [\widehat{\mathbf{D}} \widehat{\mathbf{P}}] [\mathbf{u}_k^{n+1}] + 1 \right) [\widehat{\mathbf{D}} \widehat{\mathbf{P}}]^{\top} [\widehat{\mathbf{D}} \widehat{\mathbf{P}}]. \quad (4.3.41)$$

In this case, the fully discrete linear system of equations (4.3.40) completely coincides with (4.3.28). However, the structure of the MOL allows for more vectorized operations, which can eventually reduce the computational time of solvers and reduce roundoff errors.

**Remark 4.1** (Implementation of boundary conditions). *Let us rewrite the system of equations (4.3.40) as:*

$$\mathcal{A}_k^{n+1} \Delta \mathbf{U}_k^{n+1} = \boldsymbol{\Upsilon}_k^{n+1}, \quad (4.3.42)$$

where

$$\mathbf{A}_k^{n+1} := \mathbf{M} + \Delta t^2 \frac{\partial \mathbf{K}}{\partial \mathbf{U}}(\mathbf{U}_k^{n+1}) \in \mathbb{R}^{2N+2 \times 2N+2}, \quad (4.3.43a)$$

$$\boldsymbol{\Upsilon}_k^{n+1} := -\mathbf{M}\mathbf{U}_k^{n+1} - \Delta t^2 \mathbf{K}(\mathbf{U}_k^{n+1}) + \mathbf{M}(\mathbf{U}^n + \Delta t \mathbf{V}^n) \in \mathbb{R}^{2N+2 \times 1}. \quad (4.3.43b)$$

Furthermore, let us reorder the nodes in the mesh so that the linear system (4.3.42) can be written as:

$$\begin{bmatrix} \mathbf{A}_{k,11}^{n+1} & \mathbf{A}_{k,12}^{n+1} \\ \mathbf{A}_{k,21}^{n+1} & \mathbf{A}_{k,22}^{n+1} \end{bmatrix} \begin{pmatrix} \Delta \mathbf{U}_{k,I}^{n+1} \\ \Delta \mathbf{U}_{k,D}^{n+1} \end{pmatrix} = \begin{pmatrix} \boldsymbol{\Upsilon}_{k,I}^{n+1} \\ \boldsymbol{\Upsilon}_{k,D}^{n+1} \end{pmatrix} \quad (4.3.44)$$

Here,  $\Delta \mathbf{U}_{k,I}^{n+1} \in \mathbb{R}^{2N \times 1}$  represents the increment at interior nodes (i.e. at nodes  $x_i$ ,  $i = 1, \dots, 2N$ ), while  $\boldsymbol{\Upsilon}_{k,D}^{n+1} \in \mathbb{R}^2$  represents the increment at Dirichlet points (i.e. at  $x_0 = 0$  and  $x_{2N+1} = L$ ). Since the increment at Dirichlet points is known at all Newton iterations and it is given by:

$$\Delta \mathbf{U}_{0,D}^{n+1} = \begin{pmatrix} 0 \\ g(t^{n+1}) - g(t^n) \end{pmatrix} \quad \text{and} \quad \Delta \mathbf{U}_{k,D}^{n+1} = \begin{pmatrix} 0 \\ 0 \end{pmatrix} \quad \text{for } k \geq 1, \quad (4.3.45)$$

it suffices to solve:

$$\mathbf{A}_{k,11}^{n+1} \Delta \mathbf{U}_{k,I}^{n+1} = \boldsymbol{\Upsilon}_{k,I}^{n+1} - \mathbf{A}_{k,12}^{n+1} \boldsymbol{\Upsilon}_{k,D}^{n+1}. \quad (4.3.46)$$

## 4.4 Newmark schemes

To introduce Newmark's method [136], we follow the presentation by Raviart & Thomas [161]. Let us consider the initial value problem:

$$y'' = \varphi(t, y, y'), \quad 0 \leq t \leq T \quad (4.4.1a)$$

$$y(0) = y_0, \quad y'(0) = z_0, \quad (4.4.1b)$$

where  $\varphi : [0, T] \times \mathbb{R} \times \mathbb{R} \rightarrow \mathbb{R}$  is a continuous function and  $y_0, z_0 \in \mathbb{R}$ . We also introduce a time step size  $\Delta t = T/N$  and time steps  $t_n = n\Delta t$ ,  $n = 0, \dots, N$ . For any smooth enough function  $y = y(t)$ , we have

$$y(t_{n+1}) = y(t_n) + \Delta t y'(t_n) + \frac{\Delta t^2}{2} [(1 - 2\beta)y''(t_n) + 2\beta y''(t_{n+1})] + \mathcal{O}(\Delta t^3), \quad (4.4.2a)$$

$$y'(t_{n+1}) = y'(t_n) + \Delta t [(1 - \gamma)y''(t_n) + \gamma y''(t_{n+1})] + \mathcal{O}(\Delta t^2), \quad (4.4.2b)$$

where  $\beta, \gamma \in \mathbb{R}$ . Hence, if  $y$  satisfies (4.4.1), then the equations above read:

$$\begin{aligned} y(t_{n+1}) &= y(t_n) + \Delta t y'(t_n) + \frac{\Delta t^2}{2} [(1 - 2\beta)\varphi(t_n, y(t_n), y'(t_n)) \\ &\quad + 2\beta\varphi(t_{n+1}, y(t_{n+1}), y'(t_{n+1}))] + \mathcal{O}(\Delta t^3), \end{aligned} \quad (4.4.3a)$$

$$\begin{aligned} y'(t_{n+1}) &= y'(t_n) + \Delta t [(1 - \gamma)\varphi(t_n, y(t_n), y'(t_n)) \\ &\quad + \gamma\varphi(t_{n+1}, y(t_{n+1}), y'(t_{n+1}))] + \mathcal{O}(\Delta t^2). \end{aligned} \quad (4.4.3b)$$

Newmark's method consists on finding pairs  $(y_n, z_n)$  such that

$$y_{n+1} = y_n + \Delta t z_n + \frac{\Delta t^2}{2} [(1 - 2\beta)\varphi_{n+1} + 2\beta\varphi_n], \quad (4.4.4a)$$

$$z_{n+1} = z_n + \Delta t [(1 - \gamma)\varphi_n + \gamma\varphi_{n+1}], \quad (4.4.4b)$$

where  $y_n \approx y(t_n)$ ,  $z_n \approx y'(t_n)$ , and  $\varphi_n = \varphi(t_n, y_n, z_n)$ . In terms of accuracy, the scheme is first order if  $\gamma \neq 1/2$  and second order if  $\gamma = 1/2$ . Furthermore, the scheme is unconditionally stable if  $1/2 \leq \gamma \leq 2\beta$  (cf. [91, 161]). In particular, we will consider  $\beta = 1/4$  and  $\gamma = 1/2$ , which corresponds to the *average acceleration* method<sup>1</sup>.

#### 4.4.1 Newmark in the context of Rothe's method

Let us define the velocity  $v = u_t$  and the acceleration  $a = u_{tt}$ , then discretize the nonlinear elasticity equation (4.2.1a) using the Newmark scheme (4.4.4):

$$u^{n+1} = u^n + \Delta t v^n + \frac{\Delta t^2}{2} [(1 - 2\beta)a^n + 2\beta a^{n+1}], \quad (4.4.5a)$$

$$v^{n+1} = v^n + \Delta t [(1 - \gamma)a^n + \gamma a^{n+1}], \quad (4.4.5b)$$

$$\rho_0 a^{n+1} = P(\lambda^{n+1})_x, \quad (4.4.5c)$$

where the stretch  $\lambda^{n+1} = \partial_x u^{n+1} + 1$ . Next, we define the following “predictors” which only require information from the previous time step:

$$\widetilde{u^{n+1}} = u^n + \Delta t v^n + \frac{\Delta t^2}{2}(1 - 2\beta)a^n, \quad (4.4.6a)$$

$$\widetilde{v^{n+1}} = v^n + \Delta t(1 - \gamma)a^n. \quad (4.4.6b)$$

<sup>1</sup>Some other well-known members of Newmark family of schemes are the *linear acceleration* method ( $\beta = 1/6, \gamma = 1/2$ ), the *Fox-Goodwin (royal road)* method ( $\beta = 1/12, \gamma = 1/2$ ), and the *central differences* method ( $\beta = 0, \gamma = 1/2$ ) [91]

Then, in the Rothe framework, a displacement-based method reads:

$$\rho_0 u^{n+1} - \beta \Delta t^2 P(\lambda^{n+1})_x = \rho_0 \widetilde{u^{n+1}}, \quad (4.4.7a)$$

$$a^{n+1} = \frac{u^{n+1} - \widetilde{u^{n+1}}}{\beta \Delta t^2} \quad (4.4.7b)$$

$$v^{n+1} = v^n + \Delta t \left[ (1 - \gamma) a^n + \gamma a^{n+1} \right]. \quad (4.4.7c)$$

Multiplying (4.4.7a) by a test function  $w \in H_0^1(\Omega)$  and integrating by parts yields the nonlinear weak problem: find  $u^{n+1} \in H^1(\Omega)$  such that  $u^{n+1}(0) = 0$ ,  $u^{n+1}(L) = g(t^{n+1})$ , and

$$\rho_0 \int_0^L u^{n+1} w + \beta \Delta t^2 \int_0^L P(\lambda^{n+1}) \frac{dw}{dx} = \rho_0 \int_0^L \widetilde{u^{n+1}} w. \quad (4.4.8)$$

Proceeding as before, the Newton increment  $\delta u_k^{n+1}$  can be found by solving the problem: find  $\delta u_k^{n+1}$  such that

$$\begin{aligned} \rho_0 \int_0^L \delta u_k^{n+1} w + \beta \Delta t^2 \int_0^L \frac{dP}{d\lambda}(\lambda_k^{n+1}) \frac{d(\delta u_k^{n+1})}{dx} \frac{dw}{dx} = \\ - \rho_0 \int_0^L u_k^{n+1} w - \beta \Delta t^2 \int_0^L P(\lambda_k^{n+1}) \frac{dw}{dx} + \rho_0 \int_0^L \widetilde{u^{n+1}} w. \end{aligned} \quad (4.4.9)$$

A fully discrete system can be obtained using the same steps as in Section 4.3.1, so we omit further details.

#### 4.4.2 Newmark in the context of the MOL

Going back to the nonlinear system of ODEs (4.3.32), Newmark's method translates into the following set of equations, where we define the velocity  $\mathbf{V} = \dot{\mathbf{U}}$  and the acceleration  $\mathbf{A} = \ddot{\mathbf{U}}$ :

$$\mathbf{U}^{n+1} = \mathbf{U}^n + \Delta t \mathbf{V}^n + \frac{\Delta t^2}{2} \left[ (1 - 2\beta) \mathbf{A}^n + 2\beta \mathbf{A}^{n+1} \right], \quad (4.4.10a)$$

$$\mathbf{V}^{n+1} = \mathbf{V}^n + \Delta t \left[ (1 - \gamma) \mathbf{A}^n + \gamma \mathbf{A}^{n+1} \right], \quad (4.4.10b)$$

$$\mathbf{M} \mathbf{A}^{n+1} + \mathbf{K}(\mathbf{U}^{n+1}) = \mathbf{0}. \quad (4.4.10c)$$

We note that this is typically how Newmark's method is introduced in the engineering literature (see, e.g., [91]). To obtain a displacement-based method, we first define the predictors:

$$\widetilde{\mathbf{U}^{n+1}} = \mathbf{U}^n + \Delta t \mathbf{V}^n + \frac{\Delta t^2}{2} (1 - 2\beta) \mathbf{A}^n, \quad (4.4.11a)$$

$$\widetilde{\mathbf{V}^{n+1}} = \mathbf{V}^n + \Delta t (1 - \gamma) \mathbf{A}^n. \quad (4.4.11b)$$

Thus, the expression for the displacements and velocities at time  $t_{n+1}$ , that is (4.4.10a) and (4.4.10b), read:

$$\mathbf{U}^{n+1} = \widetilde{\mathbf{U}^{n+1}} + \Delta t^2 \beta \mathbf{A}^{n+1}, \quad (4.4.12a)$$

$$\mathbf{V}^{n+1} = \widetilde{\mathbf{V}^{n+1}} + \Delta t \gamma \mathbf{A}^{n+1}. \quad (4.4.12b)$$

Furthermore, using these newly defined predictors, the system (4.4.10) now reads:

$$\mathbf{M}\mathbf{U}^{n+1} + \beta \Delta t^2 \mathbf{K}(\mathbf{U}^{n+1}) = \widetilde{\mathbf{M}\mathbf{U}^{n+1}}, \quad (4.4.13a)$$

$$\mathbf{A}^{n+1} = \frac{\mathbf{U}^{n+1} - \widetilde{\mathbf{U}^{n+1}}}{\Delta t^2}, \quad (4.4.13b)$$

$$\mathbf{V}^{n+1} = \mathbf{V}^n + \Delta t \left[ (1 - \gamma) \mathbf{A}^n + \gamma \mathbf{A}^{n+1} \right]. \quad (4.4.13c)$$

Equation (4.4.13a) is a nonlinear system of equations whose linearization is:

$$\left[ \mathbf{M} + \beta \Delta t^2 \frac{\partial \mathbf{K}}{\partial \mathbf{U}}(\mathbf{U}_k^{n+1}) \right] \Delta \mathbf{U}_{k+1}^{n+1} = -\mathbf{M}\mathbf{U}_k^{n+1} - \beta \Delta t^2 \mathbf{K}(\mathbf{U}_k^{n+1}) + \widetilde{\mathbf{M}\mathbf{U}^{n+1}}. \quad (4.4.14)$$

## 4.5 HHT- $\alpha$ method

To remove the spurious oscillations that Newmark's method could cause, Hilbert, Hughes & Taylor [84] proposed to introduce a lagging term in Newmark's equation (4.4.10c), which is controlled by a parameter  $\alpha \leq 0$ :

$$\mathbf{U}^{n+1} = \mathbf{U}^n + \Delta t \mathbf{V}^n + \frac{\Delta t}{2} \left[ (1 - 2\beta) \mathbf{A}^n + 2\beta \mathbf{A}^{n+1} \right], \quad (4.5.1a)$$

$$\mathbf{V}^{n+1} = \mathbf{V}^n + \Delta t \left[ (1 - \gamma) \mathbf{A}^n + \gamma \mathbf{A}^{n+1} \right], \quad (4.5.1b)$$

$$\mathbf{M}\mathbf{A}^{n+1} + (1 + \alpha) \mathbf{K}(\mathbf{U}^{n+1}) - \alpha \mathbf{K}(\mathbf{U}^n) = \mathbf{0}. \quad (4.5.1c)$$

To obtain an unconditionally stable, second order scheme,  $\beta$  and  $\gamma$  have to be taken as

$$\beta = \frac{(1 - \alpha)^2}{4}, \quad \gamma = \frac{1 - 2\alpha}{2},$$

and more importantly,  $-1/3 \leq \alpha \leq 0$ . The parameter  $\alpha$  controls the dissipation in the scheme, with  $\alpha = -1/3$  usually providing maximum dissipation and  $\alpha = 0$  being Newmark's average acceleration method.

### 4.5.1 HHT- $\alpha$ in the context of Rothe's method

Similar to (4.5.1), the HHT- $\alpha$  method in Rothe's framework for the PDE (4.2.1a) reads:

$$u^{n+1} = u^n + \Delta t v^n + \frac{\Delta t}{2} [(1 - 2\beta)a^n + 2\beta a^{n+1}] \quad (4.5.2a)$$

$$v^{n+1} = v^n + \Delta t [(1 - \gamma)a^n + \gamma a^{n+1}] \quad (4.5.2b)$$

$$\rho_0 a^{n+1} = (1 + \alpha)P(\lambda^{n+1})_x - \alpha P(\lambda^n)_x. \quad (4.5.2c)$$

Therefore, solving for  $u^{n+1}$  first and using the same predictors as in (4.4.6) we have

$$\rho_0 u^{n+1} = (1 + \alpha)\beta \Delta t^2 P(\lambda^{n+1})_x - \alpha \beta \Delta t^2 P(\lambda^n)_x + \rho_0 \widetilde{u^{n+1}}, \quad (4.5.3a)$$

$$a^{n+1} = \frac{u^{n+1} - \widetilde{u^{n+1}}}{\beta \Delta t^2}, \quad (4.5.3b)$$

$$v^{n+1} = v^n + \Delta t [(1 - \gamma)a^n + \gamma a^{n+1}]. \quad (4.5.3c)$$

In particular, the linearization of the equation for  $u^{n+1}$  reads: find increments  $\delta u_k^{n+1}$  such that:

$$\begin{aligned} \rho_0 \int_0^L \delta u_k^{n+1} w + (1 + \alpha)\beta \Delta t^2 \int_0^L \frac{dP}{d\lambda}(\lambda_k^{n+1}) \frac{d(\delta u_k^{n+1})}{dx} dw = \\ - \rho_0 \int_0^L u_k^{n+1} w - (1 + \alpha)\beta \Delta t^2 \int_0^L P(\lambda_k^{n+1}) \frac{dw}{dx} + \alpha \beta \Delta t^2 \int_0^L P(\lambda^n) \frac{dw}{dx} + \rho_0 \int_0^L \widetilde{u^{n+1}} w. \end{aligned} \quad (4.5.4)$$

As in Newmark's method, a fully discrete system can follow from the steps shown in Section 4.3.1.

### 4.5.2 HHT- $\alpha$ in the context of the MOL

After some algebraic manipulations, a displacement-based method for (4.5.1) reads:

$$\mathbf{M}\mathbf{U}^{n+1} + (1 + \alpha)\beta \Delta t^2 \mathbf{K}(\mathbf{U}^{n+1}) = \alpha \beta \Delta t^2 \mathbf{K}(\mathbf{U}^n) + \mathbf{M}\widetilde{\mathbf{U}^{n+1}}, \quad (4.5.5a)$$

$$\mathbf{A}^{n+1} = \frac{\mathbf{U}^{n+1} - \widetilde{\mathbf{U}^{n+1}}}{\Delta t^2}, \quad (4.5.5b)$$

$$\mathbf{V}^{n+1} = \mathbf{V}^n + \Delta t [(1 - \gamma)\mathbf{A}^n + \gamma \mathbf{A}^{n+1}]. \quad (4.5.5c)$$

Furthermore, the Newton increments  $\Delta \mathbf{U}_{k+1}^{n+1}$  can be computed as:

$$\begin{aligned} \left[ \mathbf{M} + (1 + \alpha)\beta \Delta t^2 \frac{\partial \mathbf{K}}{\partial \mathbf{U}}(\mathbf{U}_k^{n+1}) \right] \Delta \mathbf{U}_{k+1}^{n+1} \\ = -\mathbf{M}\mathbf{U}_k^{n+1} - (1 + \alpha)\beta \Delta t^2 \mathbf{K}(\mathbf{U}_k^{n+1}) + \alpha \beta \Delta t^2 \mathbf{K}(\mathbf{U}^n) + \mathbf{M}\widetilde{\mathbf{U}^{n+1}}. \end{aligned} \quad (4.5.6)$$

## 4.6 Convergence studies: linear elasticity

Since we will be interested in the different effects caused by the time discretization, as well as by the choice of Rothe's method vs. method of lines, let us first verify that each of our algorithms is converging in the way it is expected when applied to a linear problem with smooth boundary conditions. For simplicity, we consider the following names for these algorithms:

- *Rothe-First order*, for the scheme introduced in Section 4.3.1,
- *MOL-First order*, for the scheme introduced in Section 4.3.2,
- *Rothe-Newmark*, for the scheme introduced in Section 4.4.1,
- *MOL-Newmark*, for the scheme introduced in Section 4.4.2,
- *Rothe-HHT- $\alpha$* , for the scheme introduced in Section 4.5.1,
- *MOL-HHT- $\alpha$* , for the scheme introduced in Section 4.5.2.

We define the errors in time and space respectively by

$$e_t = \max_{0 \leq i \leq N+1} |u_h(x_i, T) - u(x_i, T)|, \quad e_x = \|u_h(\cdot, T) - u(\cdot, T)\|_{L^2(\Omega)}, \quad (4.6.1)$$

where  $u_h$  and  $u$  are the computed approximation and exact solutions to the initial boundary value problem (4.2.1). Furthermore, we define the rates of convergence in time and space respectively by

$$r_t = \frac{\log(e_t/e'_t)}{\log(\Delta t/\Delta t')}, \quad r_x = \frac{\log(e_x/e'_x)}{\log(\Delta x/\Delta x')}, \quad (4.6.2)$$

where  $e_t$  and  $e'_t$  ( $e_x$  and  $e'_x$ ) are the errors corresponding, respectively, to different time step (spatial mesh) sizes  $\Delta t$  and  $\Delta t'$  ( $\Delta x$  and  $\Delta x'$ ).

For this section, we consider the stress  $P$  given by a linear relationship (i.e., linear elasticity):

$$P(\lambda) = E(\lambda - 1), \quad E = 3\kappa(1 - 2\nu), \quad (4.6.3)$$

where  $E$ ,  $\kappa$ , and  $\nu$  are the Young's modulus, bulk modulus, and Poisson's ratio of the material, respectively. Thus, the initial boundary value problem (4.2.1) reduces to:

$$\rho_0 u_{tt} = Eu_{xx} \quad \text{in } \Omega \times (0, T), \quad (4.6.4a)$$

$$u(x, 0) = 0, \quad u_t(x, 0) = 0 \quad \text{in } \Omega \times \{t = 0\} \quad (4.6.4b)$$

$$u(0, t) = 0, \quad u(L, t) = g(t) \quad \text{in } (0, \infty), \quad (4.6.4c)$$

where  $T > 0$  and  $\Omega = (0, L)$ . Therefore, with the problem being linear, we expect to see convergence in time of order  $r_t = 1$  for the first order time stepping scheme, and order  $r_t = 2$

for the Newmark and HHT- $\alpha$  schemes. Moreover, for all three time stepping schemes, we expect convergence in space of order  $r_x = 3$  [61].

Let us consider  $\kappa = 1$  GPa,  $\nu = 0.499$ ,  $\rho_0 = 1060$  kg m $^{-3}$ ,  $L = 500$  mm,  $T = 500$ ms, and a boundary condition  $g(t) = 0.1t^3$ . The particular choice of these parameters is meant to resemble those found in skeletal muscle. In particular, the Poisson's ratio being close to 0.5 represents the quasi-incompressibility of skeletal muscle [19]. In this case, while the exact solution to (4.6.4) could be computed using Fourier series, we cannot reliably use this expression as any truncation of this series will lead to high oscillations at the ends of the interval (Gibbs phenomenon). Therefore, we decide to compute an "exact" solution by taking a sufficiently small  $\Delta t$  or  $\Delta x$ . We emphasize that both the exact solution and its approximations will be computed using the same solver (i.e. an *intrasolver* study). We avoid intersolver comparisons due to the choice of material, as it can potentially cause the solver to "lock", i.e. there will be a point where errors will stop decreasing regardless of how small  $\Delta x$  is taken [13].

With this in mind, we first, fix the space mesh size to  $\Delta x = L/8 = 62.5$  mm and decrease the time step size from 10 ms to 0.1 ms. In this case, for an exact solution computed with  $\Delta t = 0.01$  ms, we see from the third column in Table 4.1 that Rothe-First order and MOL-First order achieve a rate of convergence of 1, while the rest of the methods achieve a rate of convergence of 2, as expected. Next, we fix the time step size to  $\Delta t = 10$  ms and decrease the space mesh size from 125 mm to 7.8125 mm (or equivalently, increase the number of elements in the interval, from 4 to 64). In this case, for an exact solution computed with  $\Delta x = 1.953125$  mm (i.e. 256 elements), we observe from the sixth column in Table 4.1 that all methods converge with a rate equal to 3, as expected.

## 4.7 Neo-Hookean experiments, overshooting, and velocity approximations

We now turn to a nonlinear problem. Consider, for the 1D elasticity model (4.2.1), a stress  $P = P(\lambda)$  given by a Neo-Hookean relationship:

$$P(\lambda) = \mathcal{L}_\lambda \lambda + \frac{\mathcal{L}_\lambda \log \lambda - \mathcal{L}_\mu}{\lambda}, \quad (4.7.1)$$

where similar to (3.3.9),  $\mathcal{L}_\lambda$  and  $\mathcal{L}_\mu$  are the Lamé parameters of the material:

$$\mathcal{L}_\lambda = \frac{\kappa\nu}{(1-\nu)(1-2\nu)}, \quad \mathcal{L}_\mu = \frac{\kappa}{2(1+\nu)}, \quad (4.7.2)$$

$\kappa$  is the bulk modulus, and  $\nu$  the Poisson ratio. Furthermore, consider a rod with  $\rho_0 = 1060$  kg m $^{-3}$ ,  $\kappa = 1$  GPa,  $\nu = 0.4$ ,  $L = 100$  mm, and a simulation end time  $T = 2$  s. Note that we have chosen  $\rho_0$  and  $\kappa$  as in Section 4.6, but we have reduced the value of  $\nu$  to obtain more interpretable results.

Rothe-First order					
$\Delta t$ [s]	$e_t$ [m]	$r_t$	$\Delta x$ [m]	$e_x$ [m]	$r_x$
1.0e-02	3.5359e-05	-	1.2500e-01	1.1720e-06	-
5.0e-03	2.1775e-05	0.6994	6.2500e-02	1.4649e-07	3.0002
1.0e-03	5.3640e-06	0.8705	3.1250e-02	1.8315e-08	2.9997
5.0e-04	2.7656e-06	0.9557	1.5625e-02	2.2922e-09	2.9982
1.0e-04	5.2945e-07	1.0272	7.8125e-03	2.8785e-10	2.9933
Rothe-Newmark					
$\Delta t$ [s]	$e_t$ [m]	$r_t$	$\Delta x$ [m]	$e_x$ [m]	$r_x$
1.0e-02	1.0421e-06	-	1.2500e-01	1.3049e-06	-
5.0e-03	3.2229e-07	1.6931	6.2500e-02	1.5771e-07	3.0486
1.0e-03	1.3031e-08	1.9933	3.1250e-02	2.1257e-08	2.8912
5.0e-04	3.3822e-09	1.9459	1.5625e-02	2.7480e-09	2.9515
1.0e-04	1.8095e-10	1.8193	7.8125e-03	3.6347e-10	2.9185
Rothe-HHT $\alpha$					
$\Delta t$ [s]	$e_t$ [m]	$r_t$	$\Delta x$ [m]	$e_x$ [m]	$r_x$
1.0e-02	1.4903e-06	-	1.2500e-01	1.2667e-06	-
5.0e-03	4.8636e-07	1.6155	6.2500e-02	1.6072e-07	2.9784
1.0e-03	1.8973e-08	2.0156	3.1250e-02	1.9412e-08	3.0496
5.0e-04	4.9797e-09	1.9298	1.5625e-02	2.3875e-09	3.0233
1.0e-04	2.1426e-10	1.9547	7.8125e-03	2.9832e-10	3.0006
MOL-First order					
$\Delta t$ [s]	$e_t$ [m]	$r_t$	$\Delta x$ [m]	$e_x$ [m]	$r_x$
1.0e-02	3.5527e-05	-	1.2500e-01	5.8379e-07	-
5.0e-03	2.1637e-05	0.7155	6.2500e-02	7.2962e-08	3.0002
1.0e-03	5.3383e-06	0.8696	3.1250e-02	9.1223e-09	2.9997
5.0e-04	2.7535e-06	0.9551	1.5625e-02	1.1417e-09	2.9982
1.0e-04	5.2758e-07	1.0267	7.8125e-03	1.4337e-10	2.9933
MOL-Newmark					
$\Delta t$ [s]	$e_t$ [m]	$r_t$	$\Delta x$ [m]	$e_x$ [m]	$r_x$
1.0e-02	9.4285e-07	-	1.2500e-01	6.2004e-07	-
5.0e-03	3.3843e-07	1.4782	6.2500e-02	7.8989e-08	2.9726
1.0e-03	1.5963e-08	1.8976	3.1250e-02	1.0243e-08	2.9470
5.0e-04	3.9708e-09	2.0073	1.5625e-02	1.3705e-09	2.9019
1.0e-04	1.3462e-10	2.1028	7.8125e-03	1.9272e-10	2.8301
MOL-HHT $\alpha$					
$\Delta t$ [s]	$e_t$ [m]	$r_t$	$\Delta x$ [m]	$e_x$ [m]	$r_x$
1.0e-02	1.4745e-06	-	1.2500e-01	6.1040e-07	-
5.0e-03	4.4467e-07	1.7294	6.2500e-02	7.5935e-08	3.0069
1.0e-03	2.4003e-08	1.8138	3.1250e-02	9.4335e-09	3.0089
5.0e-04	6.0257e-09	1.9940	1.5625e-02	1.1774e-09	3.0022
1.0e-04	2.5532e-10	1.9642	7.8125e-03	1.4774e-10	2.9944

Table 4.1: Error behaviour for each of the proposed methods. Left three columns: convergence in time ( $L^\infty$  norm) with fixed space mesh size ( $\Delta x = L/8 = 62.5$  mm). Right three columns: convergence in space ( $L^2$  norm) with fixed time step size  $\Delta t = 10^{-5}$  s.

Our experiment consists in lengthening the rod from an initial length  $L$  to a length  $(1 + A)L$ , where  $A = 0.1$  (i.e. 10% strain), using three different strain profiles:

1. a function which transitions smoothly from  $\varepsilon_1(0) = 0$  to  $\varepsilon_1(T) = A$  with zero initial and end strain rate (i.e.  $\dot{\varepsilon}_1(0) = \dot{\varepsilon}_1(T) = 0$ ), as well as a maximum strain rate of  $\varepsilon_0 = 0.2 \text{ s}^{-1}$ :

$$\varepsilon_1(t) = A \phi\left(\frac{t}{T}\right), \quad (4.7.3)$$

where

$$\phi(t) = \frac{\psi(t)}{\psi(t) + \psi(1-t)}, \quad \psi(t) = \begin{cases} e^{-1/(c_0 t)}, & t > 0, \\ 0, & t \leq 0, \end{cases}$$

and  $c_0 = 2|A|/(\varepsilon_0 T)$ .

2. a profile in which the rod is held fixed until  $t_1 = 0.1 \text{ s}$ , then linearly lengthened until a strain  $A$  is reached at  $t_2 = 0.6 \text{ s}$ , then held fixed until  $t = T$ :

$$\varepsilon_2(t) = \begin{cases} 0 & \text{if } 0 \leq t < t_1, \\ A \frac{t - t_1}{t_2 - t_1} & \text{if } t_1 \leq t \leq t_2, \\ A & \text{if } t_2 < t \leq T; \end{cases} \quad (4.7.4)$$

3. a sinusoidal profile with  $f = 1 \text{ Hz}$ :

$$\varepsilon_3(t) = A \sin(2\pi f t), \quad 0 \leq t \leq T. \quad (4.7.5)$$

Therefore, the boundary condition for the elasticity model (4.2.1) is  $u(L, t) = L\varepsilon_k(t)$ ,  $k = 1, 2, 3$ . First, we discretize the PDE (4.2.1a) using the six methods mentioned in the previous section with  $\Delta x = L/8$ ,  $\Delta t = 10^{-4} \text{ s}$ , and tolerances for the nonlinear solver set to  $tol_u = 10^{-6}$  in displacement and  $tol_R = 10^{-8}$  in the residual (see (4.3.8)).

Because of the nonzero initial velocity when using (4.7.5) and the discontinuous velocity in (4.7.4), an elastic wave is expected to be generated (similar to the findings in the dynamical study by Tam [185]). This is also a situation where overshooting can happen, so it will be of interest to study how numerical methods deal with this issue.

## Smooth dynamics

First, we show in Figure 4.3 the results when the rod is lengthened using the smooth profile (4.7.3). Here, because the boundary conditions are  $C^\infty$  and the lengthening starts with zero velocity and acceleration, all methods compute the same displacement and velocity, both appearing to be smooth.

## Nonsmooth dynamics

Next, in Figure 4.4 and 4.5 we show the results for the case when the boundary condition is the linear profile (4.7.4) and the sinusoidal profile (4.7.5), respectively. In these cases, we observe a small wave that propagates through the rod and that is dissipated by the first order and HHT- $\alpha$  methods, in both Rothe and MOL implementations. These waves are caused by the sudden change in velocity at  $t = 0.1$  s and  $t = 0.6$  s for the linear boundary condition, and because of the nonzero initial velocity for the sinusoidal profile. Newmark's method, as suspected, did not dissipate this wave.

While not much of a difference is observed in terms of displacements, the picture changes completely when we look at the velocities that these methods compute. First, we show in Figure 4.6 the velocities for the linear boundary condition (4.7.4). In this case, the velocity is a step function, and therefore we would like our numerical methods to dissipate the wave that it generates as soon as possible. In general, we observe that MOL implementations dissipate this wave more quickly than Rothe implementations. However, the velocities computed by MOL-Newmark, as well as by Rothe-Newmark and Rothe-HHT- $\alpha$  are simply unusable. A closer look at the velocity jump in the bottom half of Figure 4.6 reveals high frequency oscillations that are well dissipated by Rothe-First order, MOL-First order, and MOL-HHT- $\alpha$  methods.

Similarly, when using the sinusoidal profile (4.7.5) as a boundary condition, we observe in Figure 4.7 some overshooting at the beginning of the simulation in all methods, but this is quickly fixed by the first order methods and the MOL-HHT- $\alpha$  method.

An IMEX scheme

We can also test an implicit-explicit (IMEX) scheme for the nonlinear system of equations (4.3.32). Observe from the definition of  $\mathbf{K}(\mathbf{U})$  in (4.3.34) that:

$$\begin{aligned} \mathbf{K}(\mathbf{U})_T &= \underbrace{\mathcal{L}_\mu \left( B^{-1} \int_{\widehat{T}} [\widehat{\mathbf{D}} \widehat{\mathbf{P}}]^\top [\widehat{\mathbf{D}} \widehat{\mathbf{P}}] \right)}_{=: \widetilde{\mathbf{K}}_T} [\mathbf{u}(t)] \\ &\quad + \underbrace{\int_{\widehat{T}} \frac{\mathcal{L}_\lambda \log(B^{-1}[\widehat{\mathbf{D}} \widehat{\mathbf{P}}][\mathbf{u}(t)] + 1) - \mathcal{L}_\mu [\widehat{\mathbf{D}} \widehat{\mathbf{P}}]^\top + \mathcal{L}_\mu \int_{\widehat{T}} [\widehat{\mathbf{D}} \widehat{\mathbf{P}}]^\top}{\mathcal{L}_\lambda}}_{=: \widetilde{\mathbf{F}}_1(\mathbf{U})_T} \quad (4.7.6) \\ &\quad = \underbrace{\widetilde{\mathbf{F}}_2 T}_{=: \widetilde{\mathbf{F}}_2 T} \end{aligned}$$

Thus, we can write:

$$\mathbf{K}(\mathbf{U}) = \mathcal{L}_\mu \tilde{\mathbf{K}}\mathbf{U} + \widetilde{\mathbf{F}_1}(\mathbf{U}) + \mathcal{L}_\mu \widetilde{\mathbf{F}_2}, \quad (4.7.7)$$

where

$$\tilde{\mathbf{K}} = \bigwedge_{T \in \mathcal{T}_h} \tilde{\mathbf{K}}_T, \quad \tilde{\mathbf{F}}_1(\mathbf{U}) = \bigwedge_{T \in \mathcal{T}_h} \tilde{\mathbf{F}}_1(\mathbf{U})_T, \quad \tilde{\mathbf{F}}_2 = \bigwedge_{T \in \mathcal{T}_h} \tilde{\mathbf{F}}_{2T}. \quad (4.7.8)$$

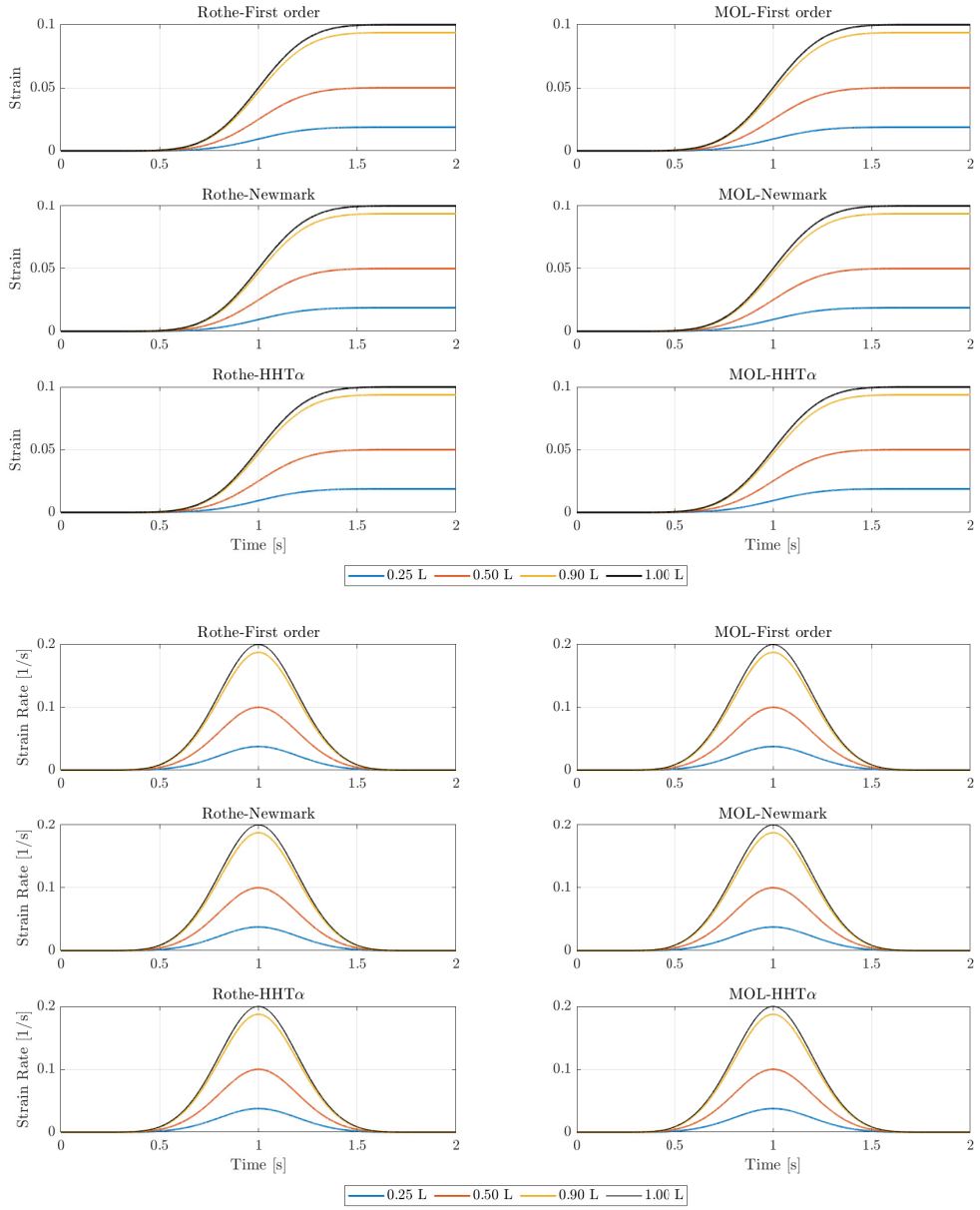


Figure 4.3: Strains (top half) and strain rates (bottom half) for the lengthening experiment using the  $C^\infty$  boundary condition (4.7.3) at four different locations:  $x = 0.25L$ ,  $x = 0.5L$ ,  $x = 0.9L$ , and  $x = L$ .

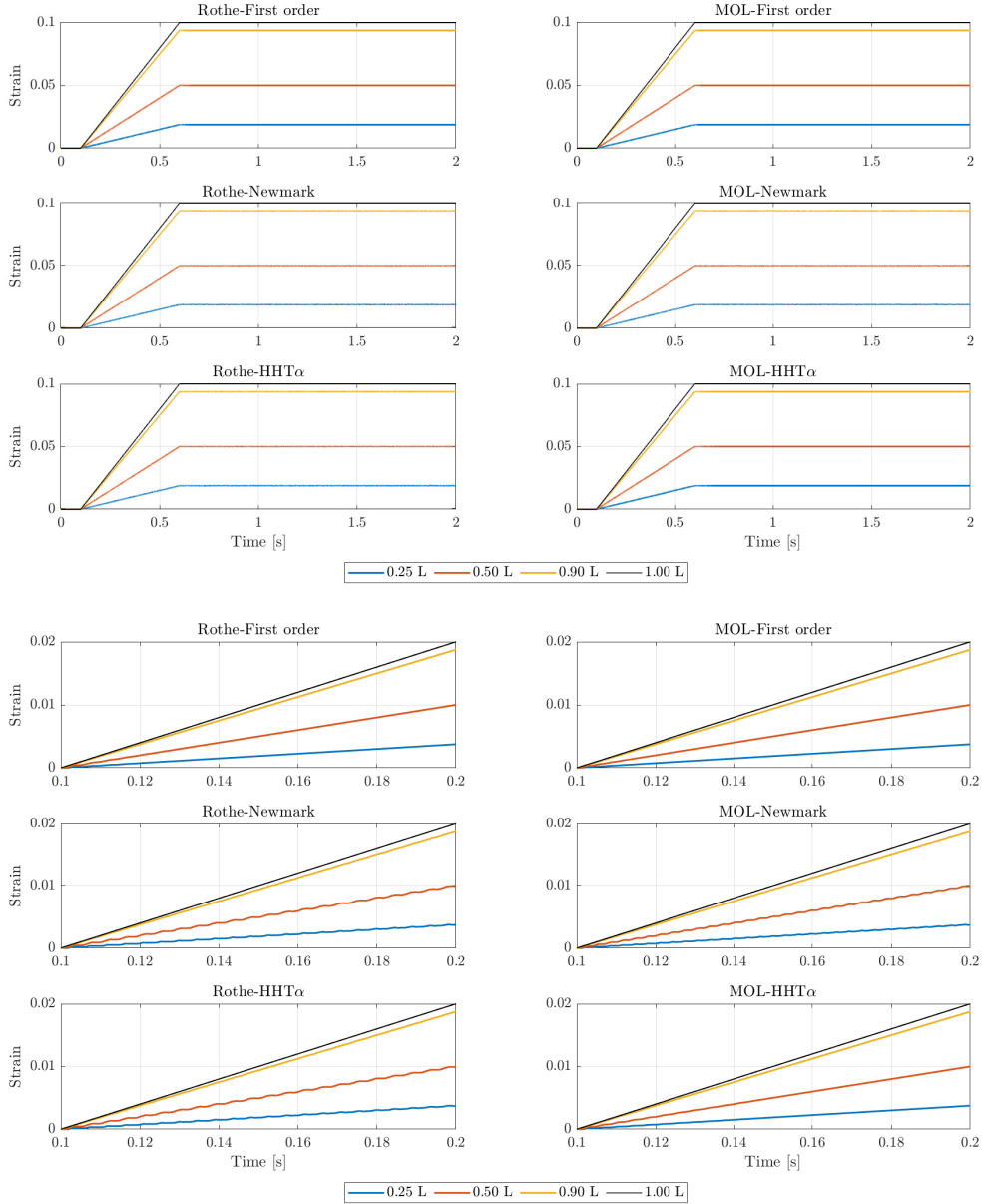


Figure 4.4: Strains over  $t \in [0, 2]$  (top half) and a zoomed version to  $t \in [0, 0.2]$  (bottom half) at four different locations:  $x = 0.25L$ ,  $x = 0.5L$ ,  $x = 0.9L$ , and  $x = L$ . Lengthening experiment performed using the linear profile (4.7.4).

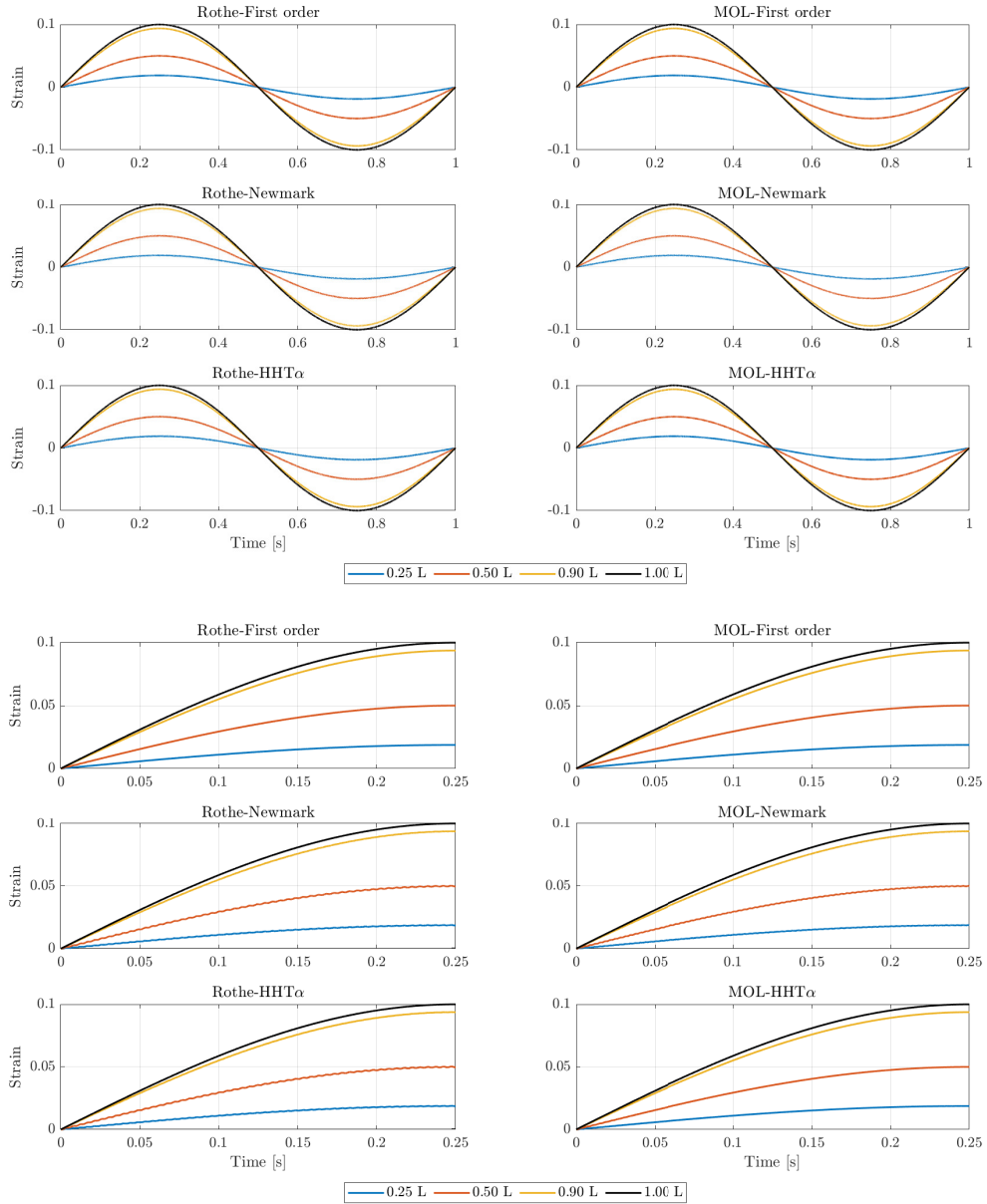


Figure 4.5: Strains over  $t \in [0, 1]$  (top half) and a zoomed version to  $t \in [0, 0.25]$  (bottom half) at four different locations:  $x = 0.25L$ ,  $x = 0.5L$ ,  $x = 0.9L$ , and  $x = L$ . Lengthening experiment performed using the sinusoidal profile (4.7.5).

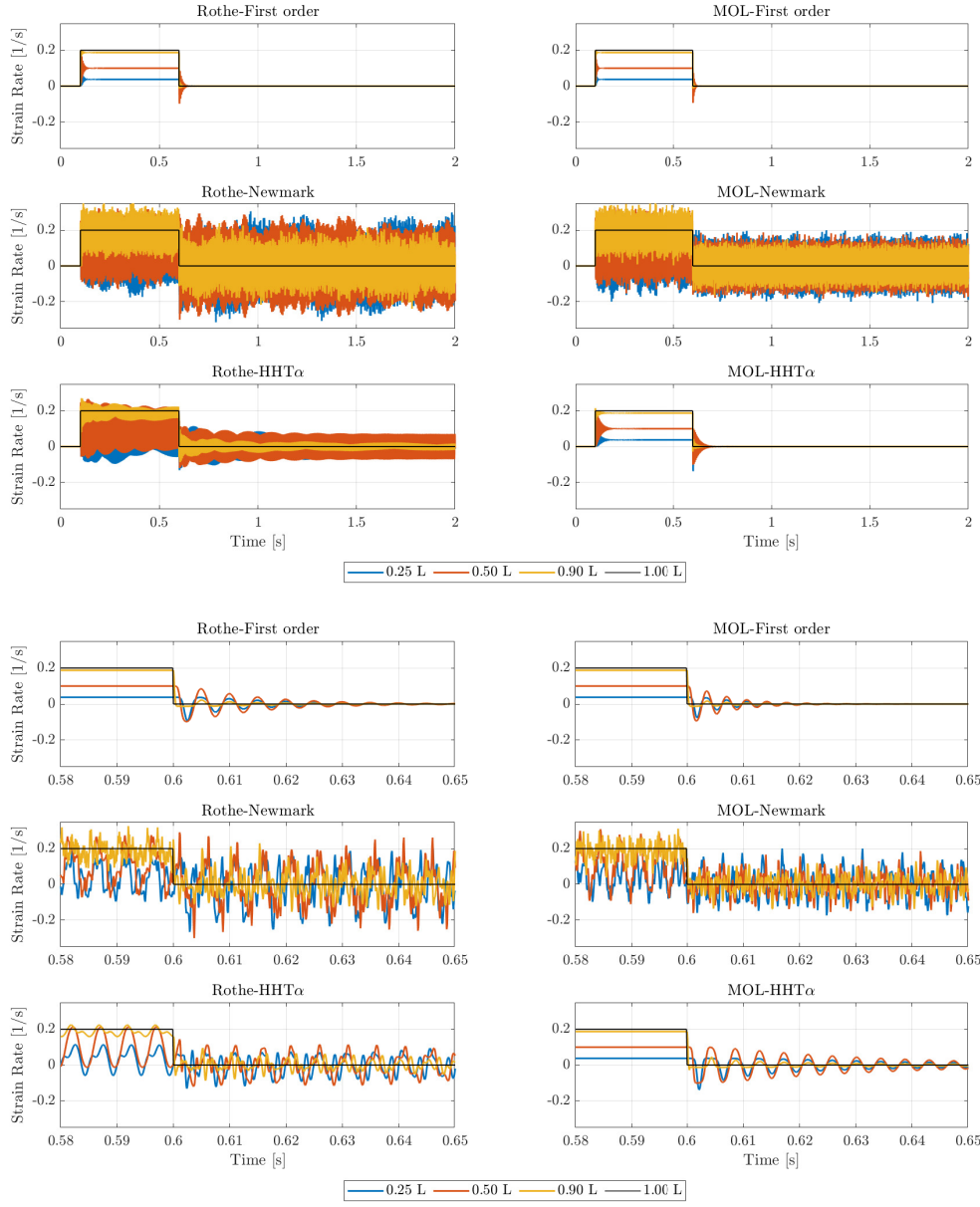


Figure 4.6: Strain rates over  $t \in [0, 2]$  (top half) and a zoomed version to  $t \in [0.58, 0.65]$  where the (prescribed) strain rate jumps from  $0.2 \text{ s}^{-1}$  to  $0 \text{ s}^{-1}$  (bottom half) at four different locations:  $x = 0.25L$ ,  $x = 0.5L$ ,  $x = 0.9L$ , and  $x = L$ . Lengthening experiment performed using the linear profile (4.7.4).

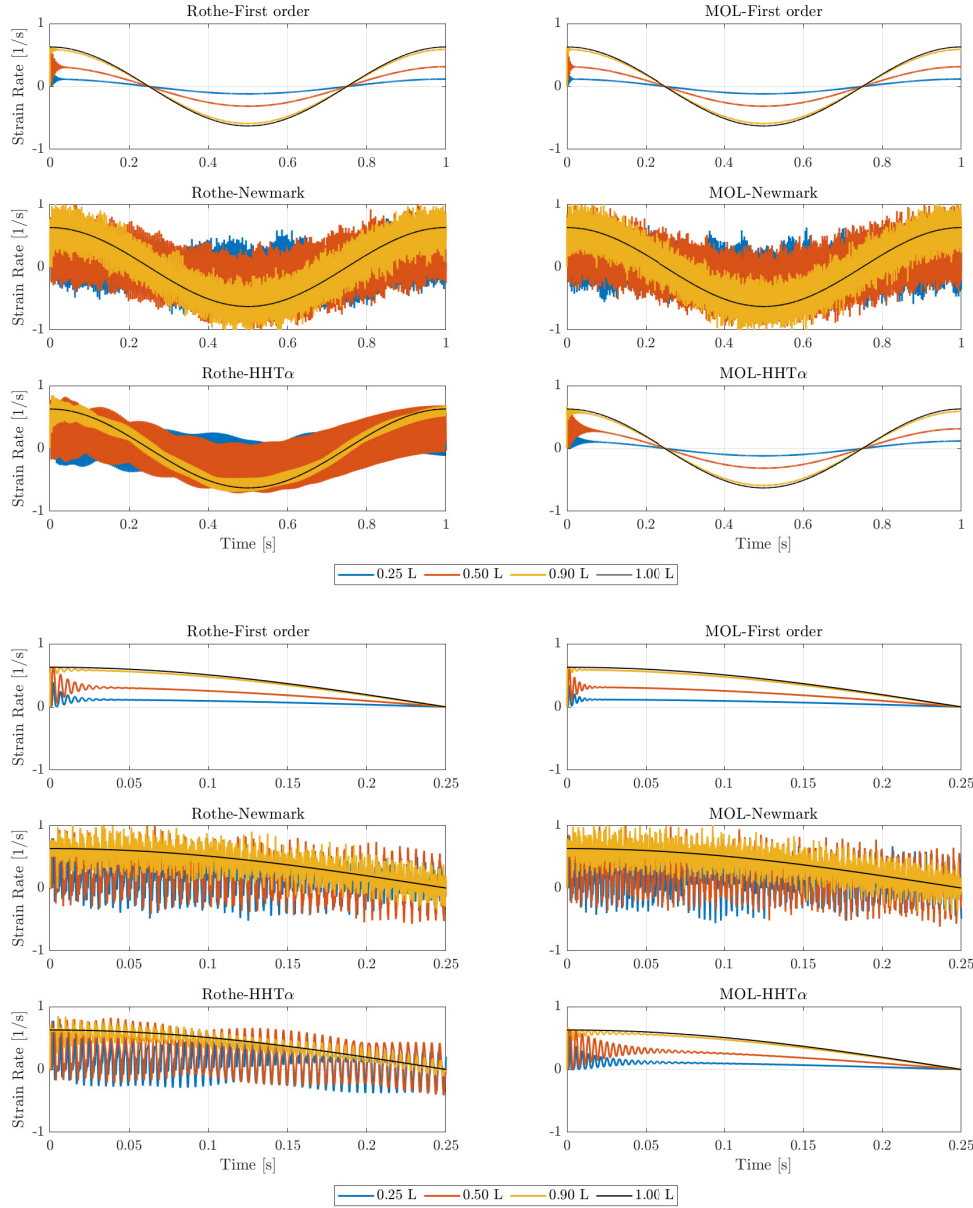


Figure 4.7: Strain rates over  $t \in [0, 1]$  (top half) and a zoomed version to  $t \in [0, 0.25]$  showcasing the nonzero velocity at the beginning (bottom half) at four different locations:  $x = 0.25L$ ,  $x = 0.5L$ ,  $x = 0.9L$ , and  $x = L$ . Lengthening experiment performed using the sinusoidal profile (4.7.4).

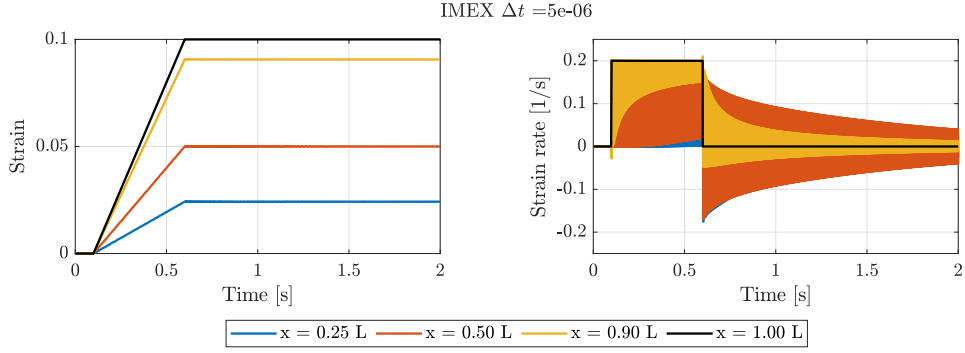


Figure 4.8: Strain (left) and strain rate (right) profiles at four different locations ( $x = 0.25L$ ,  $x = 0.50L$ ,  $x = 0.90L$ , and  $x = L$ ) for the lengthening experiment using the linear profile (4.7.4) and an IMEX time stepping scheme ( $\Delta x = L/64$ ,  $\Delta t = 0.5 \cdot 10^{-6}$ ).

Therefore, the MOL system (4.3.32) can be written as:

$$\mathbf{M}\ddot{\mathbf{U}} + \mathcal{L}_\mu \tilde{\mathbf{K}}\mathbf{U} + \tilde{\mathbf{F}}_1(\mathbf{U}) + \mathcal{L}_\mu \tilde{\mathbf{F}}_2 = \mathbf{0}.$$

Defining once again  $\mathbf{V} := \dot{\mathbf{U}}$  we can propose the following scheme:

$$\frac{\mathbf{U}^{n+1} - \mathbf{U}^n}{\Delta t} = \mathbf{V}^{n+1} \quad (4.7.9a)$$

$$\mathbf{M} \left( \frac{\mathbf{V}^{n+1} - \mathbf{V}^n}{\Delta t} \right) + \mathcal{L}_\mu \tilde{\mathbf{K}}\mathbf{U}^{n+1} = -\tilde{\mathbf{F}}_1(\mathbf{U}^n) - \mathcal{L}_\mu \tilde{\mathbf{F}}_2. \quad (4.7.9b)$$

This means that we treat the linear term *implicitly* and the nonlinear term *explicitly*. In this way, writing Equation (4.7.9b) in terms of displacements, we obtain:

$$(\mathbf{M} + \mu \Delta t^2 \tilde{\mathbf{K}}) \mathbf{U}^{n+1} = \mathbf{M}(\mathbf{U}^n + \Delta t \mathbf{V}^n) - \Delta t^2 \mathbf{F}_1(\mathbf{U}^n) - \mu \Delta t^2 \mathbf{F}_2. \quad (4.7.10)$$

No nonlinear solver is needed. However, numerical experiments for the linear boundary condition (4.7.4) show that this method does not compute better velocities than any of the previously presented methods (see Figure 4.8). Furthermore, this method behave more like an explicit method, since the largest time step size that was allowed was  $\Delta t = 5 \cdot 10^{-6}$  s (compare this to the rest of the experiments in which  $\Delta t = 10^{-4}$  s, of course with larger time step sizes being possible). This also shows that the stiffness in this problem comes from the nonlinear part of (4.7.1), rather than from the linear part.

### Matlab's built-in solvers

Once the MOL system (4.3.32) is constructed, many time-stepping schemes for ODE systems can be tested, including built-in Matlab solvers. For this set of experiments, we consider the sinusoidal pull (4.7.5) and no time step restrictions, thus letting Matlab choose the best

Solver	Finished?	Avg. $\Delta t$ [s]	CPU Time [s]
ode45	No	-	-
ode23	No	-	-
ode113	Yes	$1.46 \cdot 10^{-6}$	724
ode78	No	-	-
ode89	No	-	-
ode15s	No	-	-
ode23s	Yes	$5.69 \cdot 10^{-5}$	2,262
ode23t	Yes	$6.21 \cdot 10^{-7}$	1,301
ode23tb	Yes	$4.25 \cdot 10^{-5}$	29

Table 4.2: Performance of Matlab’s adaptive solvers for the MOL system (4.3.32) and the lengthening experiment using the sinusoidal profile (4.7.5) as boundary condition ( $\Delta x = L/64$ ). For `ode23s`, the Jacobian was (numerically) computed at each time step by the solver.

time step for the given tolerances (`RelTol` =  $10^{-2}$ , `AbsTol` =  $10^{-4}$ ). The MOL equations are solved as a square system of  $2 \times (\text{DOF}-2)$  equations ( $\text{DOF} = 2N - 1$ ).

We show in Table 4.2 a summary of the performance of each Matlab solver. As expected, most of the non-stiff solvers did not work (they would achieve  $\lambda = \partial_x u + 1 \leq 0$  at some iteration), with the exception being `ode113`. This is a variable-step, variable-order (VSVO) Adams-Bashforth-Moulton PECE (Predict-Evaluate-Correct-Evaluate) solver that uses orders up to 12 but applies a 13th-order formula for error estimation and local extrapolation. As a multistep solver, it relies on solutions from several previous time points to compute the current step. It can be more efficient than `ode45` for stringent tolerances or when evaluating the ODE function is particularly costly [178].

The solver `ode23tb` gave the best results. Not only it took the shortest time to compute a solution but also allowed for the largest time step of all Matlab solvers. However, the relatively crude tolerance chosen to run these experiments might have played a fundamental role. According to [178], `ode23tb` is an implicit Runge-Kutta solver based on the TR-BDF2 formula, combining a trapezoidal rule step with a second-stage backward differentiation formula. It reuses the same iteration matrix for both stages, improving efficiency. Like `ode23s` and `ode23t`, it can be more efficient than `ode15s` for problems with crude tolerances.

We show, in particular, the velocities and the time step sizes for the solvers that finished their computation (according to Table 4.2) in Figure 4.9. We observe that only `ode23s` and `ode23tb` computed velocities somewhat similar to those in Figure 4.7, but overshooting was still a problem in these solvers. Moreover, the time step size chosen by these solvers was in line with the one considered for Figure 4.7.

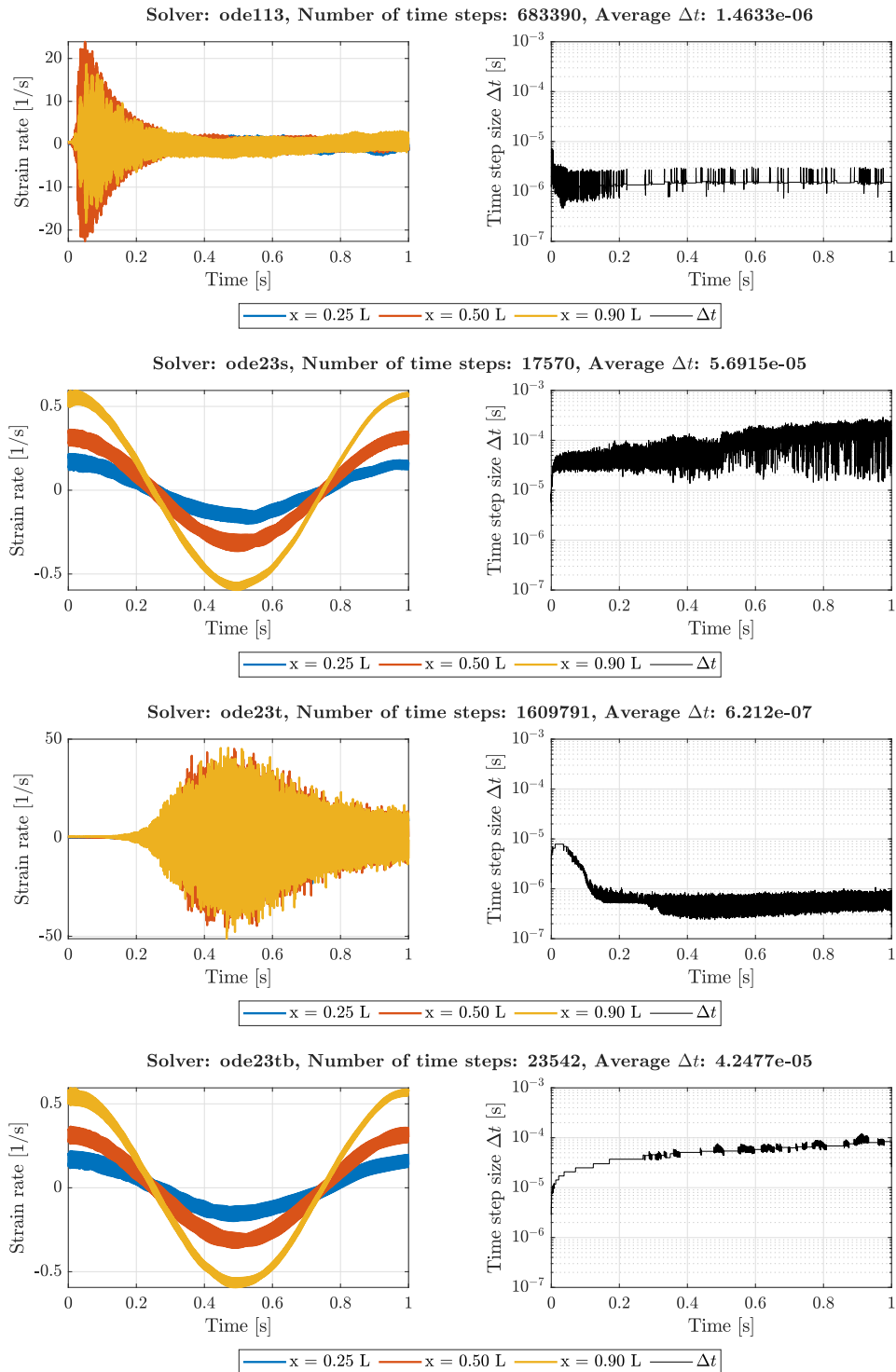


Figure 4.9: Strain rates (left column) and time step sizes (right column) for the Matlab solvers that finished solving the lengthening experiment (see Table 4.2).

## 4.8 Discussion

If studying Neo-Hookean dynamics was our ultimate goal, the conclusion would be that any of the six methods mentioned at the beginning of the previous section can be used as a time stepping scheme in a 1D or 3D elastic model. This primarily because the stress  $P$  only depends on the stretch  $\lambda$ , and therefore, only on the displacement field. However, since our main goal is to find a time stepping scheme suitable for skeletal muscle dynamics, our methods need to compute “good” displacements **and** velocities since, in this case, the stress will depend on both stretch and strain rates as a **multiplicative** term. By “good” we consider, for now, displacements and velocities free of unrealistic, high-frequency oscillations, and if they are present, they must get dissipated quickly. Thus, only three methods can become candidates for a 3D code: Rothe-First order, MOL-First order, and MOL-HHT- $\alpha$ .

Furthermore, from the experiments performed with the IMEX scheme (4.7.9), as well as with Matlab’s built in solvers, we expect that problems of this flavour will require rather small time step sizes. This does not contradict the unconditional stability of the fully implicit schemes presented here. While larger time step sizes are allowed for a linear problem, taking one that is too large in a nonlinear problem can lead to a loss of convergence in the nonlinear solver.

At this juncture, choosing which method to use becomes a software engineering decision. On the one hand, choosing the Rothe-First order method would allow us to reuse some of the computational developments by Dominguez [54] and implement them in a fully dynamic code. Thus, that code would only need to be *refactored* for our purposes. Moreover, this choice would allow for adaptive refinement to be added in the future. On the other hand, moving forward with a MOL approach would require us to almost completely *rewrite* the code developed in [54]. Therefore, we decide to discretize the 3D dynamic model using Rothe-First order method (4.3.1). The choice of a first-order over a second-order method is also justified by the fact that an alternative way to reduce the spurious oscillations in methods such as Newmark’s is precisely to take  $\gamma > 1/2$ , at the expense of losing second-order convergence [161, Section 8.6].

## 4.9 Conclusion

We studied the performance of several time stepping schemes for one-dimensional nonlinear elasticity, and in particular, for Neo-Hookean deformation. The first set of methods (first order method, Newmark’s method, and the HHT- $\alpha$  method, both in Rothe’s and MOL frameworks) gave mixed results for nonsmooth boundary conditions. Only the Rothe-First order, MOL-First order, and MOL-HHT- $\alpha$  methods dealt successfully with overshooting. Next, we tested an IMEX scheme which performed poorly compared to the previous methods. In fact, this method only ran with a very small time step size. Finally, we tested some of Matlab’s built-in solvers to assess the time step size they require to return a solution with

rather large tolerances. We found that almost all the solvers designed for non-stiff problems, as well as some stiff ones, did not finish their computation. Indeed, only the `ode113` and `ode23tb` computed results comparable to those from the MOL-Newmark method (i.e. without dissipation of high-frequency oscillations). These suggest a first-order implicit method is a good time stepping scheme candidate for the dynamic version of the full 3D model of skeletal muscle deformation.

## Part II

# Three-dimensional elastodynamics

# Chapter 5

## A Lagrangian framework for a model of skeletal muscle tissue

In this Chapter, we focus on the development of the theoretical background for a 3D finite element code base for dynamic skeletal muscle deformation, which we shall call *Flexodeal*. Some parts of this Chapter have been published in:

J. A. ALMONACID, S. A. DOMÍNGUEZ-RIVERA, R. N. KONNO, N. NIGAM, S. A. ROSS, C. TAM, AND J. M. WAKELING, *A three-dimensional model of skeletal muscle tissues*, SIAM Journal on Applied Mathematics, 84 (2024), pp. S538–S566

Compared to a quasi-static framework, the elastodynamics of striated tissues require careful consideration of the velocity variable, and in particular, of the along-fibre strain rate, both from an analytical and numerical standpoint. The treatment of this variable is crucial in developing a robust numerical scheme for fully dynamic, fully active muscle deformation.

First, we introduce some concepts of continuum mechanics that are required to understand problems of large deformation of transversely isotropic materials. Then, we describe a series of models for the different components of the muscle-tendon unit (MTU) that been introduced in works such as those by Rahemi et al. [156], Wakeling et al. [196], Konno et al. [102], and others. Next, we rewrite the dynamic model introduced by Dominguez [54] in a different frame of reference to obtain a more compact formulation with fully computable terms. Finally, we discretize the continuous problem using a first-order fully-implicit time stepping scheme and introduce a new nonlinear formulation, providing the linearization needed as part of a Newton iteration.

### 5.1 Elements of continuum mechanics

This section provides a review of concepts in continuum mechanics that will be used throughout this Chapter. The contents are based on the books by Bonet et al. [31] and Holzapfel

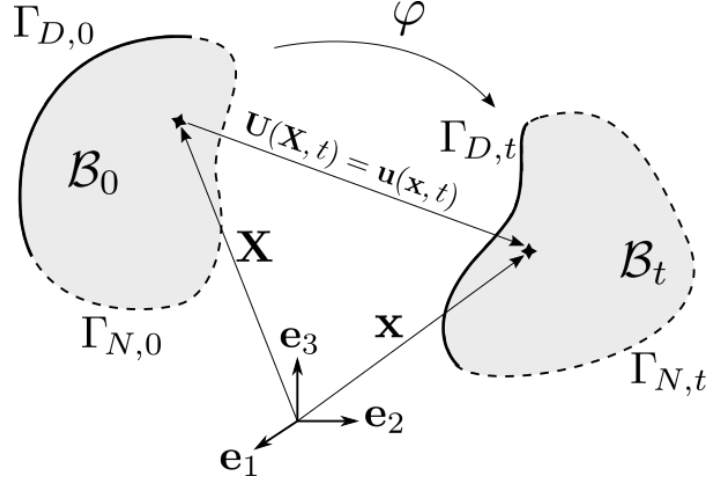


Figure 5.1: Deformation of a body from its reference configuration  $\mathcal{B}_0$  to a current configuration  $\mathcal{B}_t = \varphi(\mathcal{B}_0, t)$ , showing also the displacement  $\mathbf{U}(\mathbf{X}, t)$  of a typical particle from  $\mathbf{X} \in \mathcal{B}_0$  to  $\mathbf{x} \in \mathcal{B}_t$ . The motion  $\varphi$  also maps the Dirichlet boundary  $\Gamma_{D,0}$  to  $\Gamma_{D,t}$  (solid curves), as well as the Neumann boundary  $\Gamma_{N,0}$  to  $\Gamma_{N,t}$  (dashed curves).

[90], with some additional, newly-derived expressions to improve our understanding of the along-fibre dynamics.

### 5.1.1 Kinematics

Let  $\mathcal{B}_0 \subset \mathbb{R}^3$  denote the *reference* configuration of a deformable body with a smooth boundary  $\partial\mathcal{B}_0$ . For each time  $t > 0$ , we consider an invertible motion  $\varphi(\cdot, t) : \mathcal{B}_0 \rightarrow \mathbb{R}^3$  that maps *material* coordinates  $\mathbf{X} \in \mathcal{B}_0$  into *spatial* coordinates  $\mathbf{x} \in \mathcal{B}_t$  (see Figure 5.1), as follows:

$$\mathbf{x} = \varphi(\mathbf{X}, t), \quad \mathbf{X} = \varphi^{-1}(\mathbf{x}, t). \quad (5.1.1)$$

Note that, at time  $t = 0$ , we have the consistency condition  $\mathbf{x} = \mathbf{X}$ . The set  $\mathcal{B}_t$  is referred to as the *current* configuration of the body with reference configuration  $\mathcal{B}_0$ .

We also assume that the boundary  $\partial\mathcal{B}_0$  is divided as  $\partial\mathcal{B}_0 = \Gamma_{D,0} \cup \Gamma_{N,0}$ , with  $\Gamma_{N,0} \cap \Gamma_{D,0} = \emptyset$ . The first part,  $\Gamma_{D,0}$ , corresponds to the part of the boundary for which displacements are set (e.g. a clamped face or a face that moves with a prescribed displacement). We refer to this part of the boundary as the “Dirichlet” boundary. In turn,  $\Gamma_{N,0}$ , is the part of the boundary where tractions are set (e.g. faces with a predefined traction or traction-free faces). We refer to this part of the boundary as the “Neumann” boundary. Thus, it is natural to think that the motion  $\varphi$  extends to the boundary of  $\mathcal{B}_0$  and maps the Dirichlet and Neumann parts in the reference configuration to the current configuration (at time  $t > 0$ ) as  $\Gamma_{D,t} := \varphi(\Gamma_{D,0}, t)$  and  $\Gamma_{N,t} := \varphi(\Gamma_{N,0}, t)$  (see Figure 5.1).

We now define the *material* and *spatial displacements fields*  $\mathbf{U}$  and  $\mathbf{u}$  respectively as

$$\mathbf{U}(\mathbf{X}, t) := \mathbf{x} - \mathbf{X} = \varphi(\mathbf{X}, t) - \mathbf{X}, \quad \mathbf{u}(\mathbf{x}, t) := \mathbf{x} - \mathbf{X} = \mathbf{x} - \varphi^{-1}(\mathbf{x}, t), \quad t \geq 0. \quad (5.1.2)$$

Note that, magnitude-wise, these displacement fields coincide (i.e.  $|\mathbf{U}| = |\mathbf{u}|$ ). They are just observed in different reference frames (see Figure 5.1). We refer to a system described in  $\mathbf{X} \in \mathcal{B}_0$  coordinates as the material or *Lagrangian* description, whereas to one described in  $\mathbf{x} \in \mathcal{B}_t$  coordinates as the spatial or *Eulerian* description. In addition, we define the *material velocity* field  $\mathbf{V}$  and the *spatial velocity* field  $\mathbf{v}$  as

$$\mathbf{V}(\mathbf{X}, t) := \frac{\partial \varphi(\mathbf{X}, t)}{\partial t}, \quad \mathbf{v}(\mathbf{x}, t) := \mathbf{V}(\varphi^{-1}(\mathbf{x}, t), t). \quad (5.1.3)$$

**Remark 5.1.** *We can relate the material velocity and displacement fields using (5.1.2):*

$$\mathbf{V}(\mathbf{X}, t) = \frac{\partial \varphi(\mathbf{X}, t)}{\partial t} = \frac{\partial}{\partial t} (\mathbf{U}(\mathbf{X}, t) + \mathbf{X}) = \frac{\partial \mathbf{U}(\mathbf{X}, t)}{\partial t}. \quad (5.1.4)$$

*With an additional step, we can also relate the spatial velocity and displacement fields using (5.1.2) and (5.1.3):*

$$\begin{aligned} \mathbf{v}(\mathbf{x}, t) &= \mathbf{V}(\varphi^{-1}(\mathbf{x}, t), t) = \mathbf{V}(\mathbf{X}, t) = \frac{\partial \varphi(\mathbf{X}, t)}{\partial t} \\ &= \frac{\partial}{\partial t} (\varphi(\mathbf{X}, t) - \mathbf{X}) = \frac{\partial}{\partial t} (\mathbf{x} - \varphi^{-1}(\mathbf{x}, t)) = \frac{\partial \mathbf{u}(\mathbf{x}, t)}{\partial t}. \end{aligned} \quad (5.1.5)$$

*Therefore, it is consistent to define the material velocity using expression (5.1.4) and the spatial velocity using (5.1.5).*

### 5.1.2 Material and spatial derivatives

Because material coordinates  $\mathbf{X} \in \mathcal{B}_0$  and spatial coordinates  $\mathbf{x} \in \mathcal{B}_t$  are related through the motion  $\varphi$ , we can take derivatives of displacement and velocity fields with respect to any of these two variables. We call a smooth scalar field  $\mathcal{F} = \mathcal{F}(\cdot, t) : \mathcal{B}_0 \rightarrow \mathbb{R}$  a *material field* if it depends on material coordinates. Similarly, we call a smooth scalar field  $f(\cdot, t) : \mathcal{B}_t \rightarrow \mathbb{R}$  a *spatial field* if it depends on spatial coordinates. Whenever possible, we will write material and spatial fields using uppercase and lowercase letters respectively.

The *material time derivative of a material field* is defined by

$$\dot{\mathcal{F}}(\mathbf{X}, t) \equiv \frac{D\mathcal{F}(\mathbf{X}, t)}{Dt} := \left. \frac{\partial \mathcal{F}(\mathbf{X}, t)}{\partial t} \right|_{\mathbf{X}}, \quad (5.1.6)$$

that is, the partial derivative of  $\mathcal{F}$  with respect to  $t$  while holding  $\mathbf{X}$  constant (as usual). In particular,  $\mathbf{V} = \dot{\mathbf{U}}$  and we may define the *material acceleration field* as  $\mathbf{A} := \ddot{\mathbf{V}} = \ddot{\mathbf{U}}$ .

Furthermore, we denote the *material gradient* of a scalar field  $\mathcal{F}(\mathbf{X}, t)$  and the *material divergence* of a material vector field  $\mathbf{F}(\mathbf{X}, t) : \mathcal{B}_0 \rightarrow \mathbb{R}^3$  respectively as:

$$\nabla_0 \mathcal{F}(\mathbf{X}, t) := \frac{\partial \mathcal{F}(\mathbf{X}, t)}{\partial \mathbf{X}}, \quad \text{Div } \mathbf{F}(\mathbf{X}, t) := \frac{\partial \mathcal{F}_A(\mathbf{X}, t)}{\partial X_A}. \quad (5.1.7)$$

We denote the *spatial time derivative* of a spatial field  $f(\mathbf{x}, t)$  by  $\frac{\partial f(\mathbf{x}, t)}{\partial t}$ . We also define its *spatial gradient* and the *spatial divergence* of a vector field  $\mathbf{f}(\mathbf{x}, t) : \mathcal{B}_t \rightarrow \mathbb{R}^3$  by:

$$\nabla f(\mathbf{x}, t) := \frac{\partial f(\mathbf{x}, t)}{\partial \mathbf{x}}, \quad \text{div } \mathbf{f}(\mathbf{x}, t) := \frac{\partial f_a(\mathbf{x}, t)}{\partial x_a}. \quad (5.1.8)$$

**Remark 5.2** (Subscript notation). *In the previous expressions, and throughout the remainder of this document, we use the Einstein summation convention to express tensor operations in terms of its components. In particular, the divergence expressions in (5.1.7)<sub>2</sub> and (5.1.8)<sub>2</sub> should be understood as:*

$$\text{Div } \mathbf{F} = \sum_{A=1}^3 \frac{\partial \mathcal{F}_A}{\partial X_A}, \quad \text{div } \mathbf{f} = \sum_{a=1}^3 \frac{\partial f_a}{\partial x_a}.$$

Whenever possible, we will use uppercase subscripts to denote the components of a material quantity, and lowercase subscripts for a spatial quantity.

With these definitions in mind, we can now write an expression for the *material derivative of a spatial field*  $f(\mathbf{x}, t)$ . To do this, we first map  $f$  to the material description using the motion  $\varphi$ , then we take the material time derivative of this field, and then map back the result to the spatial description. Formally, we can write this as:

$$\dot{f}(\mathbf{x}, t) \equiv \frac{Df(\mathbf{x}, t)}{Dt} = \left. \frac{\partial f(\varphi(\mathbf{X}, t), t)}{\partial t} \right|_{\mathbf{X}=\varphi^{-1}(\mathbf{x}, t)}. \quad (5.1.9)$$

Using the chain rule in Equation (5.1.9), we obtain the more common expression:

$$\dot{f}(\mathbf{x}, t) \equiv \frac{Df(\mathbf{x}, t)}{Dt} = \frac{\partial f(\mathbf{x}, t)}{\partial t} + \nabla f(\mathbf{x}, t) \cdot \mathbf{v}. \quad (5.1.10)$$

In the case of a vector field  $\mathbf{f}(\mathbf{x}, t)$ , the previous expression takes the form

$$\dot{\mathbf{f}}(\mathbf{x}, t) \equiv \frac{D\mathbf{f}(\mathbf{x}, t)}{Dt} = \frac{\partial \mathbf{f}(\mathbf{x}, t)}{\partial t} + (\nabla \mathbf{f}(\mathbf{x}, t)) \mathbf{v}(\mathbf{x}, t) = \frac{\partial f_a}{\partial t} + \frac{\partial f_a}{\partial x_b} v_b. \quad (5.1.11)$$

In both (5.1.10) and (5.1.11), the terms  $\nabla f \cdot \mathbf{v}$  and  $(\nabla \mathbf{f}) \mathbf{v}$  are usually referred to as *convective* terms because they appear multiplied by the spatial velocity  $\mathbf{v}(\mathbf{x}, t)$ .

### 5.1.3 Deformation gradient

The primary measure of deformation in nonlinear continuum mechanics is given by the *deformation gradient tensor*  $\mathbf{F}$  (with components  $F_{aA}$ ,  $1 \leq a, A \leq 3$ ), which is defined as

$$\mathbf{F}(\mathbf{X}, t) := \frac{\partial \boldsymbol{\varphi}(\mathbf{X}, t)}{\partial \mathbf{X}} = \nabla_0 \mathbf{x}(\mathbf{X}, t), \quad \text{i.e. } F_{aA} := \frac{\partial x_a}{\partial X_A}, \quad (5.1.12)$$

with its inverse given by

$$\mathbf{F}^{-1}(\mathbf{x}, t) = \frac{\partial \boldsymbol{\varphi}^{-1}(\mathbf{x}, t)}{\partial \mathbf{x}} = \nabla \mathbf{X}(\mathbf{x}, t), \quad \text{i.e. } F_{Aa}^{-1} := \frac{\partial X_A}{\partial x_a}. \quad (5.1.13)$$

Moreover, we define the volume ratio  $J$  as:

$$J(\mathbf{X}, t) := \det \mathbf{F}(\mathbf{X}, t). \quad (5.1.14)$$

Note that as long as the motion  $\boldsymbol{\varphi}$  is invertible,  $\det \mathbf{F} \neq 0$ . Also, because volume elements cannot have negative volumes, we cannot have  $\det \mathbf{F} < 0$ . Hence, we will always have  $\det \mathbf{F} > 0$ .

Instead of referring to the deformation gradient by its definition (5.1.12), we will often use its expression in terms of the displacement gradient, i.e.,

$$\mathbf{F}(\mathbf{X}, t) = \mathbf{I} + \nabla_0 \mathbf{U}(\mathbf{X}, t), \quad \mathbf{F}^{-1}(\mathbf{x}, t) = \mathbf{I} - \nabla \mathbf{u}(\mathbf{x}, t), \quad (5.1.15)$$

where  $\mathbf{I}$  is the standard second-order identity tensor. In addition, the deformation gradient can be used to establish the following relationships between material and spatial gradients and divergences of smooth scalar, vector, and tensor fields  $\phi$ ,  $\mathbf{w}$ , and  $\mathbf{A}$ :

$$\nabla \phi = \mathbf{F}^{-T} \nabla_0 \phi = F_{Aa}^{-1} \frac{\partial \phi}{\partial X_A} \quad (5.1.16)$$

$$\nabla \mathbf{w} = \nabla_0 \mathbf{w} \mathbf{F}^{-1} = \frac{\partial w_a}{\partial X_A} F_{Ab}^{-1}, \quad (5.1.17)$$

$$\mathbf{div} \mathbf{A} = \nabla_0 \mathbf{A} : \mathbf{F}^{-T} = \frac{\partial A_{ab}}{\partial X_B} F_{Bb}^{-1}, \quad (5.1.18)$$

where the tensorial divergence is given by  $\mathbf{div} \mathbf{A} := \frac{\partial A_{ab}}{\partial x_b}$  (the notation here follows Remark 5.2).

Sometimes we refer to the volume ratio  $J$  as the *Jacobian determinant* because it provides a way to map infinitesimal elements in the reference configuration to the current configuration. Indeed, given infinitesimal elements  $dV$ ,  $dS$  in the interior and boundary of the reference configuration  $\mathcal{B}_0$  respectively; and  $dv$ ,  $ds$  in the interior and boundary of the

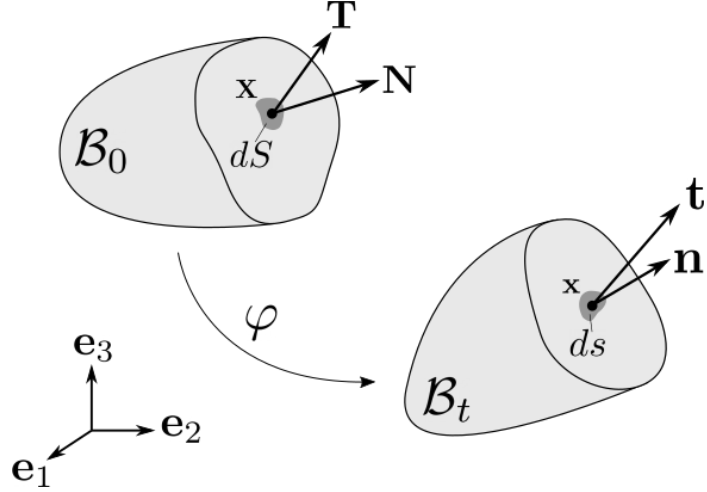


Figure 5.2: Transformation of surface elements. In the reference configuration  $\mathcal{B}_0$ , we observe a surface element  $dS$  (with unit normal  $\mathbf{N}$ ) and a traction vector  $\mathbf{T}$ . Similarly, in the current configuration  $\mathcal{B}_t$ , we have a surface element  $ds$  (with unit normal  $\mathbf{n}$ ) and a traction vector  $\mathbf{t}$ .

current configuration  $\mathcal{B}_t$ , we have

$$dv = J(\mathbf{X}, t) dV, \quad \mathbf{n} ds = J\mathbf{F}^{-T} \mathbf{N} dS, \quad (5.1.19)$$

where  $\mathbf{n}, \mathbf{N}$  denote the normal vectors on the surface of the current and reference configurations, respectively (see Figure 5.2). The last equality in this equation is the well-known *Nanson's formula*.

#### 5.1.4 Rates of deformation tensors

Now that we have defined the deformation tensor  $\mathbf{F}$ , we can describe velocity gradients. The *material velocity gradient* is given by

$$\dot{\mathbf{F}} = \frac{\partial}{\partial t} \left( \frac{\partial \varphi(\mathbf{X}, t)}{\partial \mathbf{X}} \right) = \frac{\partial}{\partial \mathbf{X}} \left( \frac{\partial \varphi(\mathbf{X}, t)}{\partial t} \right) = \frac{\partial \mathbf{V}(\mathbf{X}, t)}{\partial \mathbf{X}} \quad \text{or} \quad \dot{F}_{aA} = \frac{\partial V_a}{\partial X_A}. \quad (5.1.20)$$

In turn, the *spatial velocity gradient* is given by

$$\mathbf{l}(\mathbf{x}, t) = \frac{\partial \mathbf{v}(\mathbf{x}, t)}{\partial \mathbf{x}}. \quad (5.1.21)$$

We may relate these two quantities using the expression

$$\mathbf{l} = \dot{\mathbf{F}} \mathbf{F}^{-1}. \quad (5.1.22)$$

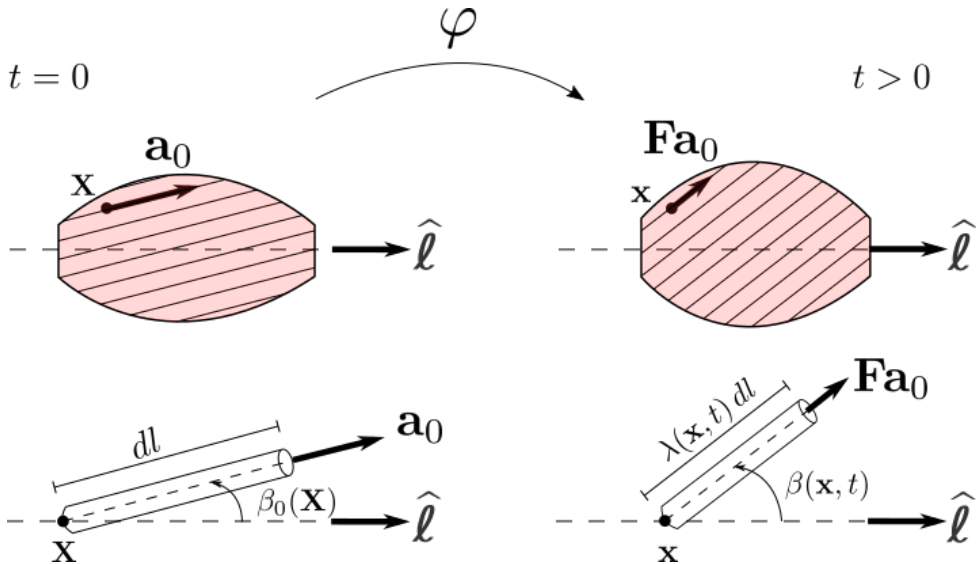


Figure 5.3: Fibre orientations fields  $\mathbf{a}_0$  in the reference configuration and  $\mathbf{a} = \mathbf{F}\mathbf{a}_0$  in the deformed configuration. A fibre can be represented as an infinitely small line element  $dl$  with orientation  $\mathbf{a}_0$  that passes through  $\mathbf{X} \in \mathcal{B}_0$  and deforms to an element of length  $\lambda dl$  with orientation  $\mathbf{a}$ , where  $\lambda$  is the fibre stretch field. The angle between the orientation  $\mathbf{a}$  and the line of action vector  $\hat{\ell}$  is called the *pennation angle* and is denoted by  $\beta$ . The initial pennation angle  $\beta_0$  is simply the angle between  $\mathbf{a}_0$  and  $\hat{\ell}$ .

Furthermore, we can additively decompose the spatial velocity gradient into its symmetric and skew-symmetric parts:

$$\mathbf{l}(\mathbf{x}, t) = \mathbf{d}(\mathbf{x}, t) + \mathbf{w}(\mathbf{x}, t), \quad (5.1.23)$$

where

$$\mathbf{d} = \frac{1}{2}(\mathbf{l} + \mathbf{l}^\top) \quad (5.1.24)$$

is the *rate of deformation tensor* (also called *rate of strain tensor*), and

$$\mathbf{w} = \frac{1}{2}(\mathbf{l} - \mathbf{l}^\top) \quad (5.1.25)$$

is the *rate of rotation tensor* or *vorticity tensor*.

### 5.1.5 Fundamental strain tensors, fibre stretch, and fibre strain rate

In elasticity, one of the primary focuses is determining the distribution of strains and stresses throughout the entire body. However, when analyzing skeletal muscle deformation, an additional key aspect is the deformation along the muscle fibres. This along-fibre deformation is critical for understanding muscle function, as it directly influences force transmission, tissue mechanics, and physiological behaviour.

Consider the *left* and *right Cauchy-Green strain tensors*, defined respectively:

$$\mathbf{C} = \mathbf{F}^\top \mathbf{F} \quad \text{or} \quad C_{AB} = F_{aA} F_{aB}, \quad (5.1.26)$$

and

$$\mathbf{b} = \mathbf{F} \mathbf{F}^\top \quad \text{or} \quad b_{ab} = F_{aA} F_{bA}. \quad (5.1.27)$$

Let  $d\ell \mathbf{a}_0$  be a line element in the reference configuration  $\mathcal{B}_0$  with unit orientation vector  $\mathbf{a}_0$ . Furthermore, let  $\lambda d\ell \mathbf{a}$  be the deformed version of  $d\ell \mathbf{a}_0$  in the current configuration  $\mathcal{B}_t$  with unit orientation vector  $\mathbf{a} = \mathbf{F} \mathbf{a}_0$  (see Figure 5.3). The quantity  $\lambda$ , known as the *stretch*, characterizes how a material line element changes in length from the reference to the current configuration:

$$\lambda(\mathbf{X}, t) := |\mathbf{F}(\mathbf{X}, t) \mathbf{a}_0| = \sqrt{\mathbf{a}_0^\top \mathbf{C} \mathbf{a}_0}, \quad (5.1.28)$$

Given that  $\mathbf{a}_0$  can be imagined as the orientation of a *fibre* passing through  $\mathbf{X} \in \mathcal{B}_0$ , we will refer to  $\lambda(\mathbf{X}, t)$  as the *fibre stretch*.

Consequently, we define the *fibre strain rate* as the time derivative of the fibre stretch, normalized by a factor  $\dot{\varepsilon}_0$ , typically representing the maximum strain rate at which a material element is allowed deform:

$$\dot{\varepsilon}(\mathbf{X}, t) := \frac{1}{\dot{\varepsilon}_0} \dot{\lambda}(\mathbf{X}, t) = \frac{1}{\dot{\varepsilon}_0} \frac{(\mathbf{F}(\mathbf{X}, t) \mathbf{a}_0)^\top \mathbf{d}(\mathbf{x}, t) \mathbf{F}(\mathbf{X}, t) \mathbf{a}_0}{\lambda(\mathbf{X}, t)}, \quad (5.1.29)$$

where the last equality arises from taking an implicit time derivative in (5.1.28) and the fact that  $\dot{\mathbf{C}} = 2\mathbf{F}^\top \mathbf{d}\mathbf{F}$  (cf. [90, Eq. (2.168)]). The normalization of this quantity is consistent with the definition of the one-dimensional strain rate in (2.2.1) and (3.2.4).

### 5.1.6 Stress tensors

Consider surface elements  $ds$  with normal  $\mathbf{n}$  in the current configuration and  $dS$  with normal  $\mathbf{N}$  in the reference configuration. Then, by Cauchy's stress theorem, for each pair of spatial and material tractions  $\mathbf{t}$  and  $\mathbf{T}$ , respectively, there exist tensors  $\boldsymbol{\sigma}$  and  $\mathbf{P}$  such that  $\mathbf{t} ds = \mathbf{T} dS$  and

$$\mathbf{t}(\mathbf{x}, t, \mathbf{n}) = \boldsymbol{\sigma}(\mathbf{x}, t) \mathbf{n} \quad \text{and} \quad \mathbf{T}(\mathbf{X}, t, \mathbf{N}) = \mathbf{P}(\mathbf{X}, t) \mathbf{N}. \quad (5.1.30)$$

We show these quantities in Figure 5.2. Here,  $\boldsymbol{\sigma}$  is called the *Cauchy stress tensor*, while  $\mathbf{P}$  is called the *first Piola-Kirchhoff tensor* (PK1). Notice that  $\boldsymbol{\sigma}$  describe the stresses in the body in the *current* configuration, while  $\mathbf{P}$  describes them in the *reference* configuration. Both measures of stress are related through the so-called *Piola transformation*:

$$\mathbf{P} = J \boldsymbol{\sigma} \mathbf{F}^{-\top}. \quad (5.1.31)$$

From this expression, it can be seen that, although  $\boldsymbol{\sigma}$  is a symmetric tensor, in general,  $\mathbf{P}$  is not.

Other stress tensors that will be used in this document are the (spatial) *Kirchhoff stress tensor* defined as:

$$\boldsymbol{\tau} = J\boldsymbol{\sigma}, \quad (5.1.32)$$

and the (material) *second Piola-Kirchhoff stress tensor* (PK2), which can be obtained as a pull-back operation on  $\boldsymbol{\tau}$ , that is:

$$\mathbf{S} = \mathbf{F}^{-1}\boldsymbol{\tau}\mathbf{F}^{-\top}. \quad (5.1.33)$$

Thus,  $\mathbf{S}$  is a symmetric tensor. Moreover, this last equation gives us another important relationship that will be used in this work:

$$\boldsymbol{\tau} = \mathbf{FSF}^{\top}. \quad (5.1.34)$$

Finally, the PK1 and PK2 tensors are related accordingly by the expression:

$$\mathbf{P} = \mathbf{FS}. \quad (5.1.35)$$

### 5.1.7 Volumetric-isochoric decomposition for compressible hyperelastic materials

In the case of compressible materials (even by very small amounts, as it is the case in skeletal muscle), it is customary to split the deformation tensor into volume-*changing* (volumetric) and volume-*preserving* (isochoric) parts, i.e.

$$\mathbf{F} = (J^{1/3}\mathbf{I})(J^{-1/3}\bar{\mathbf{F}}) = J^{1/3}\bar{\mathbf{F}}, \quad (5.1.36)$$

where

$$\bar{\mathbf{F}} := J^{-1/3}\mathbf{F} \quad (5.1.37)$$

is called the *modified deformation gradient*. Given that  $\det \bar{\mathbf{F}} = 1$ , the term  $\bar{\mathbf{F}}$  is associated with isochoric deformations of the material, whereas the term  $J^{1/3}\mathbf{I}$  is associated with volumetric deformations.

The volumetric-isochoric decomposition (5.1.36) yields modified versions of the right and left Cauchy-Green tensors:

$$\bar{\mathbf{C}} = \bar{\mathbf{F}}^{\top}\bar{\mathbf{F}} = J^{-2/3}\mathbf{C}, \quad \bar{\mathbf{b}} = \bar{\mathbf{F}}\bar{\mathbf{F}}^{\top} = J^{-2/3}\mathbf{b}. \quad (5.1.38)$$

In particular, the derivative of  $\bar{\mathbf{C}}$  with respect to  $\mathbf{C}$  is given by

$$\frac{\partial \bar{\mathbf{C}}}{\partial \mathbf{C}} = J^{-2/3} \left( \mathbb{I} - \frac{1}{3} \mathbf{C} \otimes \mathbf{C}^{-1} \right) = J^{-2/3} \mathbb{P}^\top, \quad (5.1.39)$$

where  $\mathbb{P}^\top$  is the transpose of the fourth-order *material projection tensor*  $\mathbb{P}$ , where

$$\mathbb{P} := \mathbb{I} - \frac{1}{3} \mathbf{C}^{-1} \otimes \mathbf{C}, \quad (5.1.40)$$

and  $\mathbb{I}_{ABCD} := \frac{1}{2} (\delta_{AC}\delta_{BD} + \delta_{AB}\delta_{BC})$  is the fourth-order symmetric identity tensor. Here, the transpose of  $\mathbb{P}$  is given by  $(\mathbb{P}^\top)_{IJKL} = \mathbb{P}_{KLIJ}$ .

**Remark 5.3.** *This multiplicative decomposition yields a modified fibre stretch  $\bar{\lambda}$ :*

$$\bar{\lambda} := \sqrt{\mathbf{a}_0^\top \bar{\mathbf{C}} \mathbf{a}_0} = J^{-1/3} \lambda, \quad (5.1.41)$$

as well as a modified fibre strain rate  $\bar{\varepsilon}$ , which we define as:

$$\bar{\varepsilon} := \frac{1}{\dot{\varepsilon}_0} \dot{\bar{\lambda}} = \frac{1}{\dot{\varepsilon}_0} \frac{(\bar{\mathbf{F}} \mathbf{a}_0)^\top (\mathbb{P} : \mathbf{d})(\bar{\mathbf{F}} \mathbf{a}_0)}{\bar{\lambda}}, \quad (5.1.42)$$

where  $\mathbb{P}$  is the fourth-order spatial projection tensor:

$$\mathbb{P} := \mathbb{I} - \frac{1}{3} \mathbf{I} \otimes \mathbf{I}. \quad (5.1.43)$$

Given that:

$$\mathbb{P} : \mathbf{d} = \mathbf{d} - \frac{1}{3} \text{tr}(\mathbf{d}) \mathbf{I}, \quad (5.1.44)$$

the tensor  $\mathbb{P}$  is also called the “deviatoric” tensor.

**Remark 5.4.** *The original strain rate  $\dot{\varepsilon}$  defined in (5.1.29) and the modified one  $\bar{\varepsilon}$  are related by the expression:*

$$\dot{\varepsilon} = J^{1/3} \left[ \bar{\varepsilon} + \frac{1}{3} \frac{\text{tr}(\mathbf{d})}{\dot{\varepsilon}_0} \bar{\lambda} \right], \quad (5.1.45)$$

which arises as a byproduct when deriving the expression for  $\bar{\varepsilon}$  in (5.1.42) using (5.1.29) and (5.1.41).

In general, we will refer to a material as being *hyperelastic* if there exists a function  $\Psi = \Psi(\mathbf{F})$  such that

$$\mathbf{P} = \frac{\partial \Psi(\mathbf{F})}{\partial \mathbf{F}}, \quad (5.1.46)$$

where  $\mathbf{P}$  is the PK1 tensor defined in (5.1.31). Here  $\Psi$  is called the *strain-energy function* (SEF) and provides a constitutive model for the material.

Furthermore, in the context of the volumetric-isochoric decomposition (5.1.36), we postulate that this SEF takes the particular form:

$$\Psi(\mathbf{C}) = \Psi_{vol}(J) + \Psi_{iso}(\bar{\mathbf{C}}), \quad (5.1.47)$$

where  $\Psi_{vol}$  and  $\Psi_{iso}$  are respectively SEFs describing the volumetric and isochoric responses of the material.

### Volumetric and isochoric components of stress and elasticity tensors

Considering a perfectly elastic material in isothermal conditions, the Clausius-Planck inequality requires that the internal dissipation  $\mathcal{D}_{int}$  vanishes, that is,

$$\mathcal{D}_{int} = w_{int} - \dot{\Psi} = 0, \quad (5.1.48)$$

where the internal power is given by  $w_{int} = \mathbf{S} : \dot{\mathbf{C}}/2$ . To compute the time derivative of the SEF, we use (5.1.39) and the fact that  $\dot{J} = J\mathbf{C}^{-1} : \dot{\mathbf{C}}/2$ :

$$\begin{aligned} \dot{\Psi} &= \frac{d\Psi_{vol}(J)}{dJ} \dot{J} + \frac{\partial\Psi_{iso}(\bar{\mathbf{C}})}{\partial\bar{\mathbf{C}}} : \dot{\bar{\mathbf{C}}} \\ &= J \frac{d\Psi_{vol}(J)}{dJ} \mathbf{C}^{-1} : \frac{\dot{\mathbf{C}}}{2} + \frac{\partial\Psi_{iso}(\bar{\mathbf{C}})}{\partial\bar{\mathbf{C}}} : 2J^{-2/3}\mathbb{P}^\top : \frac{\dot{\mathbf{C}}}{2}. \end{aligned} \quad (5.1.49)$$

Inserting this equation back into (5.1.48), we obtain

$$\mathcal{D}_{int} = \left( \mathbf{S} - J \frac{d\Psi_{vol}(J)}{dJ} \mathbf{C}^{-1} - J^{-2/3}\mathbb{P} : 2 \frac{\partial\Psi_{iso}(\bar{\mathbf{C}})}{\partial\bar{\mathbf{C}}} \right) : \frac{\dot{\mathbf{C}}}{2} = 0.$$

Therefore, the PK2 stress tensor can be described as

$$\mathbf{S} = \mathbf{S}_{vol} + \mathbf{S}_{iso}. \quad (5.1.50)$$

The volumetric part,  $\mathbf{S}_{vol}$ , is defined as:

$$\mathbf{S}_{vol} = pJ\mathbf{C}^{-1}, \quad (5.1.51)$$

where  $p$  is the *hydrostatic pressure*:

$$p := \frac{d\Psi_{vol}(J)}{dJ}. \quad (5.1.52)$$

In turn, the isochoric part,  $\mathbf{S}_{iso}$ , is given by

$$\mathbf{S}_{iso} = J^{-2/3}\mathbb{P} : \bar{\mathbf{S}}, \quad (5.1.53)$$

where  $\bar{\mathbf{S}}$  is the *fictitious PK2 stress tensor*:

$$\bar{\mathbf{S}} := 2 \frac{\partial \Psi_{iso}(\bar{\mathbf{C}})}{\partial \bar{\mathbf{C}}}, \quad (5.1.54)$$

and  $\mathbb{P}$  is the projection tensor defined in (5.1.40).

Pushing forward the equation describing  $\mathbf{S}$  (i.e., (5.1.50)) according to (5.1.34), we obtain that the Kirchhoff stress  $\boldsymbol{\tau}$  can be described as

$$\boldsymbol{\tau} = \boldsymbol{\tau}_{vol} + \boldsymbol{\tau}_{iso}, \quad (5.1.55)$$

where the volumetric part,  $\boldsymbol{\tau}_{vol}$ , is given by

$$\boldsymbol{\tau}_{vol} = p J \mathbf{I}, \quad (5.1.56)$$

and the isochoric part,  $\boldsymbol{\tau}_{iso}$  is given by

$$\boldsymbol{\tau}_{iso} = \bar{\mathbf{F}} (\mathbb{P} : \bar{\mathbf{S}}) \bar{\mathbf{F}}^\top = \mathbb{P} : \bar{\boldsymbol{\tau}}, \quad (5.1.57)$$

where  $\bar{\boldsymbol{\tau}}$  is the *fictitious Kirchhoff stress tensor*:

$$\bar{\boldsymbol{\tau}} = \bar{\mathbf{F}} \bar{\mathbf{S}} \bar{\mathbf{F}}^\top, \quad (5.1.58)$$

and  $\mathbb{P}$  is the projection tensor defined in (5.1.43).

## Elasticity tensors

Linearization techniques such as Newton's method require the computation of tensorial derivatives of stress tensors. In the material description, we define the fourth-order *material elasticity* tensor  $\mathbb{C}$  as:

$$\mathbb{C} = 2 \frac{\partial \mathbf{S}(\mathbf{C})}{\partial \mathbf{C}} \quad \text{or} \quad C_{ABCD} = 2 \frac{\partial S_{AB}}{\partial C_{CD}}. \quad (5.1.59)$$

In the spatial description, the elasticity tensor  $\mathbb{c}$  can be obtained by a push-forward of the material tensor  $\mathbb{C}$ , that is,

$$\mathbb{c} = J^{-1} \chi_*(\mathbb{C}) \quad \text{or} \quad c_{abcd} = J^{-1} F_a A F_b B F_c C F_d D C_{ABCD}. \quad (5.1.60)$$

Particularly for the volumetric-isochoric decomposition of the PK2 tensor in (5.1.50),  $\mathbb{C}$  can be split as:

$$\mathbb{C} = 2 \frac{\partial \mathbf{S}_{vol}}{\partial \mathbf{C}} + 2 \frac{\partial \mathbf{S}_{iso}}{\partial \mathbf{C}} =: \mathbb{C}_{vol} + \mathbb{C}_{iso}. \quad (5.1.61)$$

The volumetric part,  $\mathbb{C}_{vol}$ , is given by (cf. [90, Eq. (6.166)]):

$$\mathbb{C}_{vol} = J \left( p + J \frac{d^2 \Psi_{vol}(J)}{dJ^2} \right) \mathbf{C}^{-1} \otimes \mathbf{C}^{-1} - 2Jp \mathbf{C}^{-1} \odot \mathbf{C}^{-1}, \quad (5.1.62)$$

where

$$- (\mathbf{C}^{-1} \odot \mathbf{C}^{-1})_{ABCD} := -\frac{1}{2} (C_{AC}^{-1} C_{BD}^{-1} + C_{AD}^{-1} C_{BC}^{-1}). \quad (5.1.63)$$

The isochoric part,  $\mathbb{C}_{iso}$ , can be computed as (cf. [90, Example 6.8]):

$$\mathbb{C}_{iso} = \mathbb{P} \bar{\mathbb{C}} \mathbb{P}^\top + \frac{2}{3} (J^{-2/3} \bar{\mathbf{S}} : \mathbf{C}) \tilde{\mathbb{P}} - \frac{2}{3} (\mathbf{C}^{-1} \otimes \mathbf{S}_{iso} + \mathbf{S}_{iso} \otimes \mathbf{C}^{-1}), \quad (5.1.64)$$

where the *fictitious elasticity tensor in the material description*  $\bar{\mathbb{C}}$  is given by:

$$\bar{\mathbb{C}} = 2J^{-4/3} \frac{\partial \bar{\mathbf{S}}}{\partial \bar{\mathbf{C}}}, \quad (5.1.65)$$

and the *modified projection tensor*  $\tilde{\mathbb{P}}$  is:

$$\tilde{\mathbb{P}} = \mathbf{C}^{-1} \otimes \mathbf{C}^{-1} - \frac{1}{3} \mathbf{C}^{-1} \odot \mathbf{C}^{-1}. \quad (5.1.66)$$

In the spatial description, the picture is similar and fortunately, the expressions are much simpler. For the spatial elasticity tensor  $\mathbb{c}$ , we have:

$$\mathbb{c} = \mathbb{c}_{vol} + \mathbb{c}_{iso}, \quad (5.1.67)$$

where the volumetric and isochoric parts are respectively given by:

$$J\mathbb{c}_{vol} = pJ(\mathbf{I} \otimes \mathbf{I} - 2p\mathbb{I}) + J^2 \frac{d^2 \Psi_{vol}(J)}{dJ^2} \mathbf{I} \otimes \mathbf{I}, \quad (5.1.68)$$

and

$$J\mathbb{c}_{iso} = \mathbb{P} \bar{\mathbb{C}} \mathbb{P} + \frac{2}{3} \text{tr}(\bar{\boldsymbol{\tau}}) \mathbb{P} - \frac{2}{3} (\mathbf{I} \otimes \boldsymbol{\tau}_{iso} + \boldsymbol{\tau}_{iso} \otimes \mathbf{I}). \quad (5.1.69)$$

Note that we have multiplied these tensors by  $J$  as, ultimately, the weak formulations will require us compute  $J\mathbb{c}$ . In the previous expression,  $\mathbb{P}$  is the spatial projection tensor defined in (5.1.43) and  $\bar{\mathbb{C}}$  is the *fictitious elasticity tensor* in the spatial description defined as push-forward of  $\bar{\mathbb{C}}$ :

$$\bar{\mathbb{C}} = \chi_*(\bar{\mathbb{C}}) \quad \text{or} \quad \bar{c}_{abcd} = F_a A F_b B F_c C F_d D \bar{C}_{ABCD} = \bar{F}_a A \bar{F}_b B \bar{F}_c C \bar{F}_d D J^{4/3} \bar{C}_{ABCD}, \quad (5.1.70)$$

where  $\bar{C}_{ABCD}$  is computed according to (5.1.65). Note that the term  $\mathbb{P} \bar{\mathbb{C}} \mathbb{P}$  can be seen component wise as

$$(\mathbb{P} \bar{\mathbb{C}} \mathbb{P})_{klmn} = p_{klab} \bar{c}_{abcd} p_{cdmn}. \quad (5.1.71)$$

### 5.1.8 A strain-energy function for compressible, transversely isotropic materials

In compressible, transversely isotropic materials (i.e., materials that are reinforced by only one family of fibres and that have a single preferred direction of deformation), the following general strain-energy function (SEF) can be established [90, 199]:

$$\Psi = \Psi(\mathbf{C}, \mathbf{a}_0 \otimes \mathbf{a}_0) = \Psi_{vol}(J) + \Psi_{iso}(\bar{I}_1, \bar{I}_2, \bar{I}_4, \bar{I}_5). \quad (5.1.72)$$

Here,  $\Psi_{vol}$  and  $\Psi_{iso}$  respectively describe the volumetric and isochoric response of the material and  $\bar{I}_1, \dots, \bar{I}_5$  are the invariants ( $\bar{I}_4$  and  $\bar{I}_5$  are actually *pseudo-invariants* [90]) of the modified right Cauchy-Green tensor:

$$\begin{aligned} \bar{I}_1 &= \text{tr } \bar{\mathbf{C}}, & \bar{I}_2 &= \frac{1}{2} \left[ (\text{tr } \bar{\mathbf{C}})^2 - \text{tr } (\bar{\mathbf{C}}^2) \right], & \bar{I}_3 &= \det \bar{\mathbf{C}} \equiv 1, \\ \bar{I}_4 &= \mathbf{a}_0^\top \bar{\mathbf{C}} \mathbf{a}_0 = \lambda^2, & \bar{I}_5 &= \mathbf{a}_0^\top \bar{\mathbf{C}}^2 \mathbf{a}_0. \end{aligned} \quad (5.1.73)$$

Furthermore, their derivatives are given by:

$$\frac{\partial \bar{I}_1}{\partial \bar{\mathbf{C}}} = \mathbf{I}, \quad \frac{\partial \bar{I}_2}{\partial \bar{\mathbf{C}}} = \bar{I}_1 \mathbf{I} - \bar{\mathbf{C}}, \quad \frac{\partial \bar{I}_4}{\partial \bar{\mathbf{C}}} = \mathbf{a}_0 \otimes \mathbf{a}_0, \quad \frac{\partial \bar{I}_5}{\partial \bar{\mathbf{C}}} = \mathbf{a}_0 \otimes \bar{\mathbf{C}} \mathbf{a}_0 + \bar{\mathbf{C}} \mathbf{a}_0 \otimes \mathbf{a}_0. \quad (5.1.74)$$

For general expressions on the stress and elasticity tensors derived from the SEF (5.1.72), we refer the reader to [199]. Nevertheless, we will provide these expressions for the particular SEF that models skeletal muscle tissue in the following section.

## 5.2 Constitutive laws for skeletal muscle

Let us consider skeletal muscle tissue as a fibre-reinforced (i.e. transversely isotropic), composite, nearly incompressible hyperelastic material [54, 154, 196]. Furthermore, let us postulate the following strain-energy function (SEF) for skeletal muscle tissue:

$$\Psi_{mus} = \Psi_{vol}(J) + \Psi_{iso}(\bar{I}_1, \bar{I}_4, \dot{\bar{I}}_4). \quad (5.2.1)$$

The volumetric part of the SEF  $\Psi$  is given by:

$$\Psi_{vol}(J) = \frac{\kappa}{4} \left( J^2 - 2 \ln J - 1 \right), \quad (5.2.2)$$

where  $\kappa$  is the bulk modulus of muscle tissue. The bulk modulus may appear as a single constant or as a weighted combination of bulk moduli of the different tissue components (such as intramuscular fat, ECM, and cellular material; see below). The isochoric component

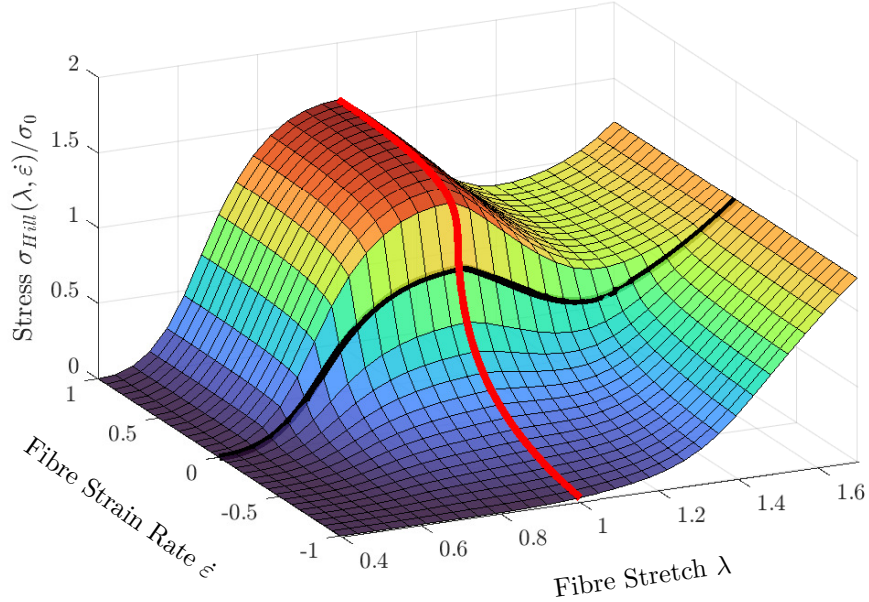


Figure 5.4: Hill’s model depicted as a manifold in which the fibre stretch  $\lambda$  and the fibre strain rate  $\dot{\varepsilon}$  can vary simultaneously according to (5.2.5). We also show the curves  $\sigma_{Hill}(\lambda, 0)/\sigma_0$  (red) and  $\sigma_{Hill}(0, \dot{\varepsilon})/\sigma_0$  (black), which correspond to the total force-length (FL) and force-velocity (FV) relationships in Figure 2.2.

of  $\Psi$  takes the form:

$$\Psi_{iso}(\bar{I}_1, \bar{I}_4, \dot{\bar{I}}_4) = (1 - \chi_{fat}) (\Psi_{fibre}(\bar{I}_4, \dot{\bar{I}}_4) + \Psi_{bm}(\bar{I}_1)) + \chi_{fat} \Psi_{fat}(\bar{I}_1). \quad (5.2.3)$$

We are assuming that muscle and other tissues are made of fibres embedded in a base material, with responses given by  $\Psi_{fibre}$  and  $\Psi_{bm}$ , respectively. Furthermore, their combined response is influenced by the fraction of intramuscular fat  $\chi_{fat}$  present in muscle tissue. In turn,  $\Psi_{fat}$  represents the response of intramuscular fat (adipose) tissue, which has been homogenized with the fibre and base material components following [156, Model M4].

In the next sections, we describe the SEF for each one of the components, as well as the stress tensors they induce. We will be particularly interested in the structure of the Kirchhoff stress  $\tau_{iso}$ , which in turn requires the knowledge of the fictitious Kirchhoff stress  $\bar{\tau}$  (see Equation (5.1.57)). We will compute this tensor as a push-forward of  $\bar{\mathbf{S}}$  (defined in (5.1.54)) according to the identity (5.1.58).

### 5.2.1 Muscle fibres

We assume that the SEF  $\Psi_{fibre}$  is given implicitly by the equation:

$$2\bar{I}_4 \frac{\partial \Psi_{fibre}}{\partial \bar{I}_4} = \sigma_{Hill}(\bar{\lambda}, \bar{\dot{\varepsilon}}), \quad (5.2.4)$$

where  $\sigma_{Hill}$  is Hill's muscle model written in terms of the maximum isometric stress  $\sigma_{0,mus}$ :

$$\sigma_{Hill}(\bar{\lambda}, \bar{\varepsilon}) = \sigma_{0,mus} \left( a(\mathbf{X}, t) \hat{\sigma}_A(\bar{\lambda}) \hat{\sigma}_V(\bar{\varepsilon}) + \hat{\sigma}_P(\bar{\lambda}) \right). \quad (5.2.5)$$

In this expression, the active stress-stretch relationship  $\hat{\sigma}_A$ , the stress-strain rate relationship  $\hat{\sigma}_V$ , and the passive stress-stretch relationship  $\hat{\sigma}_P$  can be respectively identified with the active force-length  $F_V$ , force-velocity  $F_V$ , and passive force-length  $F_P$  relationships in (2.2.3), respectively (all these quantities are dimensionless, see Appendix A, but we must recast them as stresses for this continuum mechanics framework). Furthermore, we now allow the activation function to also vary in space. For the special case when  $a \equiv 1$ , we portray this two-dimensional manifold in Figure 5.4.

Using Equation (5.1.54), the corresponding fictitious PK2 stress  $\bar{\mathbf{S}}_{fibre}$  can be computed as:

$$\bar{\mathbf{S}}_{fibre} = 2 \frac{\partial \Psi_{fibre}}{\partial \bar{\mathbf{C}}} = 2 \frac{\partial \Psi_{fibre}}{\partial \bar{I}_4} \frac{\partial \bar{I}_4}{\partial \bar{\mathbf{C}}}. \quad (5.2.6)$$

Thus, using (5.2.4) together with (5.1.74), we have:

$$\bar{\mathbf{S}}_{fibre} = \frac{1}{\bar{\lambda}^2} \sigma_{0,mus} \left( a(\mathbf{X}, t) \hat{\sigma}_A(\bar{\lambda}) \hat{\sigma}_V(\bar{\varepsilon}) + \hat{\sigma}_P(\bar{\lambda}) \right) \mathbf{a}_0(\mathbf{X}) \otimes \mathbf{a}_0(\mathbf{X}), \quad (5.2.7)$$

where  $\mathbf{a}_0$  is the initial orientation vector of a fibre crossing through the point  $\mathbf{X} \in \mathcal{B}_0$ . Moreover, according to (5.1.58), we obtain that:

$$\bar{\tau}_{fibre} = \frac{1}{\bar{\lambda}^2} \sigma_{0,mus} \left( a(\mathbf{X}, t) \hat{\sigma}_A(\bar{\lambda}) \hat{\sigma}_V(\bar{\varepsilon}) + \hat{\sigma}_P(\bar{\lambda}) \right) \bar{\mathbf{a}} \otimes \bar{\mathbf{a}}, \quad (5.2.8)$$

where  $\bar{\mathbf{a}} := \bar{\mathbf{F}} \mathbf{a}_0$ .

### 5.2.2 Base material

The base material component can be modelled using the following Yeoh SEF [164, 173, 196]:

$$\Psi_{bm}(\bar{I}_1) = s_{bm} \sigma_{0,bm} \sum_{k=1}^3 c_k (\bar{I}_1 - 3)^k, \quad (5.2.9)$$

where  $s_{bm}$  is a scaling factor,  $\sigma_{0,bm}$  a normalizing constant stress, and  $c_k \in \mathbb{R}$  are constants that were computed by Wakeling et al. [196] to fit the experimental data in Mohammadkhah et al. [130].

Similarly to the computation of  $\bar{\mathbf{S}}_{fibre}$  and  $\bar{\tau}_{fibre}$ , the fictitious PK2 and Kirchhoff stresses in this case are:

$$\bar{\mathbf{S}}_{bm} = 2s_{bm} \sigma_{0,bm} \left( 3c_3(\bar{I}_1 - 3)^2 + 2c_2(\bar{I}_1 - 3) + c_1 \right) \mathbf{I}, \quad (5.2.10)$$

and

$$\bar{\tau}_{bm} = 2s_{bm}\sigma_{0,bm} \left( 3c_3(\bar{I}_1 - 3)^2 + 2c_2(\bar{I}_1 - 3) + c_1 \right) \bar{\mathbf{b}}. \quad (5.2.11)$$

In the work by Konno et al. [102], the base material is considered as a weighted combination of ECM and cellular material contributions to study muscle affected by cerebral palsy. More precisely, the expression for the SEF  $\Psi_{bm}$  takes the form:

$$\Psi_{bm}(\bar{I}_1) = \chi_{ecm}\Psi_{ecm}(\bar{I}_1) + (1 - \chi_{ecm})\Psi_{cell}(\bar{I}_1), \quad (5.2.12)$$

where  $\chi_{ecm} > 0$  is the fraction of ECM content in muscle. The SEFs for ECM and cellular material are given respectively by:

$$\Psi_{ecm}(\bar{I}_1) = s_{ecm} \sum_{k=1}^3 c_k (\bar{I}_1 - 3)^k, \quad (5.2.13)$$

and

$$\Psi_{cell}(\bar{I}_1) = s_{cell} \sum_{k=1}^3 c_k (\bar{I}_1 - 3)^k. \quad (5.2.14)$$

The constants  $c_k \in \mathbb{R}$  in these models have been computed by Konno et al. [102] to fit the data in Gillies et al. [71] for the ECM and the data in Jin et al. [95] for the cellular material.

In this case, the fictitious stress tensors for each one of these SEFs are given by:

$$\bar{\mathbf{S}}_{ecm} = 2s_{ecm} \left( 3c_3(\bar{I}_1 - 3)^2 + 2c_2(\bar{I}_1 - 3) + c_1 \right) \mathbf{I}, \quad (5.2.15)$$

$$\bar{\tau}_{ecm} = 2s_{ecm} \left( 3c_3(\bar{I}_1 - 3)^2 + 2c_2(\bar{I}_1 - 3) + c_1 \right) \bar{\mathbf{b}}, \quad (5.2.16)$$

and

$$\bar{\mathbf{S}}_{cell} = 2s_{cell} \left( 3c_3(\bar{I}_1 - 3)^2 + 2c_2(\bar{I}_1 - 3) + c_1 \right) \mathbf{I}, \quad (5.2.17)$$

$$\bar{\tau}_{cell} = 2s_{cell} \left( 3c_3(\bar{I}_1 - 3)^2 + 2c_2(\bar{I}_1 - 3) + c_1 \right) \bar{\mathbf{b}}. \quad (5.2.18)$$

The constants  $\sigma_{0,base}$ ,  $s_{base}$ ,  $s_{ecm}$ ,  $s_{cell}$ , as well as  $c_k$  (which are local to each SEF), are given in Table 5.1. Note that the bulk modulus  $\kappa$  used to define the volumetric component  $\Psi_{vol}$  of the SEF  $\Psi$  now takes the form

$$\kappa = \chi_{ecm}\kappa_{ecm} + (1 - \chi_{ecm})\kappa_{cell}, \quad (5.2.19)$$

where  $\kappa_{ecm}$  and  $\kappa_{cell}$  are the bulk moduli for ECM and cellular material, respectively.

	Value in $\Psi_{bm}$ (5.2.9)		Value in $\Psi_{ecm}$ (5.2.13)		Value in $\Psi_{cell}$ (5.2.14)
$\sigma_{0,bm}$	200000 Pa	-	-	-	-
$s_{bm}$	1	$s_{ecm}$	200 Pa	$s_{cell}$	1 Pa
$c_1$	0.1990559575103343	$c_1$	1988.76435209844	$c_1$	3703.32723408173
$c_2$	0.3662334826469149	$c_2$	4917.02551347748	$c_2$	-707.76064007684
$c_3$	0.0	$c_3$	-591.533166457473	$c_3$	123.247643527575

Table 5.1: Constants in the SEFs defining the base material component of muscle tissue.

	Value in $\Psi_{fat}$ (5.2.20)
$s_{fat}$	1 Pa
$c_1$	323.91
$c_2$	5163.1
$c_3$	-3872.9

Table 5.2: Constants in the SEF defining intramuscular fat.

### 5.2.3 Intramuscular fat

Following [103], we consider the following SEF to model intramuscular fat:

$$\Psi_{fat}(\bar{I}_1) = s_{fat} \sum_{k=1}^3 c_k (\bar{I}_1 - 3)^k, \quad (5.2.20)$$

where  $s_{fat}$  is a scaling factor and the constants  $c_k$  are computed so that the expression above fits the data by Alkhouri et al. [2]. The values for these constants are listed in Table 5.2. Thus, the expressions for the fictitious stress tensors become:

$$\bar{\mathbf{S}}_{fat} = 2s_{fat} \left( 3c_3(\bar{I}_1 - 3)^2 + 2c_2(\bar{I}_1 - 3) + c_1 \right) \mathbf{I}, \quad (5.2.21)$$

and

$$\bar{\boldsymbol{\tau}}_{fat} = 2s_{fat} \left( 3c_3(\bar{I}_1 - 3)^2 + 2c_2(\bar{I}_1 - 3) + c_1 \right) \bar{\mathbf{b}}. \quad (5.2.22)$$

The bulk modulus for the volumetric SEF  $\Psi_{vol}$  now takes the form:

$$\kappa = (1 - \chi_{fat})\kappa_{bm} + \chi_{fat}\kappa_{fat}, \quad (5.2.23)$$

where  $\kappa_{bm}$  and  $\kappa_{fat}$  are the bulk moduli for the base material and fat components. In particular,  $\kappa_{bm}$  can be taken as a single constant or as the homogenized version in Equation (5.2.19).

## 5.3 Extending the SEF to the muscle-tendon unit

The expressions in the previous section are only applicable to geometries made entirely of muscle tissue, without internal or external tendons. To create a SEF for the whole muscle-

	Value in $\Psi_{tis}$ (5.3.8)
$s_{tis}$	1
$\sigma_{0,tis}$	200,000 Pa
$c_1$	4.6896264975
$c_2$	-3.45514101975
$c_3$	$4.8492055395 \cdot 10^2$

Table 5.3: Constants in the SEF defining tendon and aponeurosis.

tendon unit, let us consider a partition of the domain of interest into three parts  $\mathcal{B}_0 = \mathcal{B}_0^M \cup \mathcal{B}_0^A z \cup \mathcal{B}_0^T$ , where  $\mathcal{B}_0^M$ ,  $\mathcal{B}_0^A$ , and  $\mathcal{B}_0^T$  represent the parts of  $\mathcal{B}_0$  made of muscle tissue, aponeurosis, and tendon. Thus, a SEF for the MTU reads:

$$\Psi_{MTU}(\mathbf{X}, t) = \Psi_{mus}(\mathbf{X}, t)\iota_M(\mathbf{X}) + \Psi_{apo}(\mathbf{X}, t)\iota_A(\mathbf{X}) + \Psi_{ten}(\mathbf{X}, t)\iota_T(\mathbf{X}), \quad (5.3.1)$$

where  $\iota_M(\mathbf{X})$ ,  $\iota_A(\mathbf{X})$ , and  $\iota_T(\mathbf{X})$  are indicator functions on  $\mathcal{B}_0^M$ ,  $\mathcal{B}_0^A$ , and  $\mathcal{B}_0^T$ , respectively. Here, following Wakeling et al. [196], we consider an expression in common for the SEF of tendon and aponeurosis:

$$\Psi_{tis} = \Psi_{vol,tis}(J) + \Psi_{iso,tis}(\bar{I}_1, \bar{I}_4), \quad tis \in \{apo, ten\}. \quad (5.3.2)$$

Similar to muscle tissue, the volumetric part is given by

$$\Psi_{vol,tis} = \frac{\kappa_{tis}}{4} \left( J^2 - 2 \ln J - 1 \right), \quad tis \in \{apo, ten\}, \quad (5.3.3)$$

where  $\kappa_{apo}$  and  $\kappa_{ten}$  are the bulk moduli for aponeurosis and tendon, respectively. On the other hand, the isochoric component is given by:

$$\Psi_{iso,tis} = \Psi_{tis,fibre}(\bar{I}_4) + \Psi_{tis,bm}(\bar{I}_4), \quad tis \in \{apo, ten\}, \quad (5.3.4)$$

as tendon and aponeurosis are also transversely-isotropic materials.

Assuming that the fibre component  $\Psi_{tis,fibre}$  satisfies:

$$2\bar{I}_4 \frac{\partial \Psi_{tis,fibre}}{\partial \bar{I}_4} = \sigma_{0,tis} \hat{\sigma}_{tis}(\bar{\lambda}), \quad tis \in \{apo, ten\}, \quad (5.3.5)$$

for a given stress-stretch relationship  $\hat{\sigma}_{tis}$  (see Appendix A), we obtain the following stress tensors:

$$\bar{\mathbf{S}}_{tis,fibre} = \frac{1}{\bar{\lambda}^2} \sigma_{0,tis} \hat{\sigma}_{tis}(\bar{\lambda}) \mathbf{a}_0 \otimes \mathbf{a}_0, \quad (5.3.6)$$

$$\bar{\boldsymbol{\tau}}_{tis,fibre} = \frac{1}{\bar{\lambda}^2} \sigma_{0,tis} \hat{\sigma}_{tis}(\bar{\lambda}) \bar{\mathbf{a}} \otimes \bar{\mathbf{a}}. \quad (5.3.7)$$

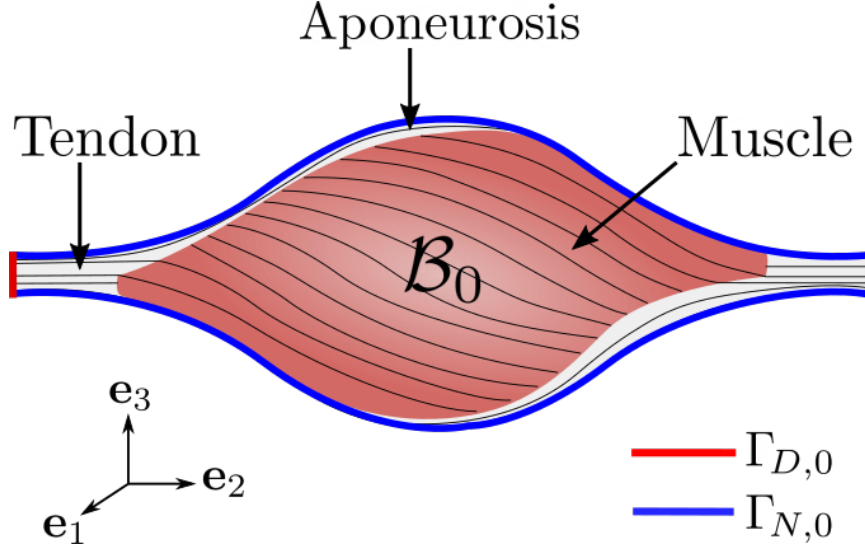


Figure 5.5: Three-dimensional continuum representation of the muscle-tendon unit showing its main three components: muscle tissue, aponeurosis, and tendon.

Moreover, assuming that SEF for the base material  $\Psi_{tis,bm}$  is given by a Yeoh SEF:

$$\Psi_{tis,bm} = s_{tis}\sigma_{0,tis} \sum_{k=1}^3 c_k(\bar{I}_1 - 3)^k, \quad (5.3.8)$$

we obtain the following stress tensors:

$$\bar{\mathbf{S}}_{tis,bm} = 2s_{tis}\sigma_{0,tis} \left( 3c_3(\bar{I}_1 - 3)^2 + 2c_2(\bar{I}_1 - 3) + c_1 \right) \mathbf{I}, \quad (5.3.9)$$

$$\bar{\tau}_{tis,bm} = 2s_{tis}\sigma_{0,tis} \left( 3c_3(\bar{I}_1 - 3)^2 + 2c_2(\bar{I}_1 - 3) + c_1 \right) \bar{\mathbf{b}}. \quad (5.3.10)$$

Following [54] we assume that the constants  $c_k$ ,  $k = 1, 2, 3$ , are identical for tendon and aponeurosis. These have been fitted in [54] from wild turkey gastrocnemii data [10] and are listed in Table 5.3.

## 5.4 Lagrangian formulation of the elastodynamic problem

Let  $\mathcal{B}_0 \subset \mathbb{R}^3$  be a region in three-dimensional space representing the undeformed muscle-tendon unit (MTU), potentially containing a combination of muscle, aponeurosis, and tendon, as described in Section 5.3. The boundary of this body,  $\partial\mathcal{B}_0$ , can be subdivided into two parts:  $\partial\mathcal{B}_0 = \Gamma_{0,D} \cup \Gamma_{0,N}$ , with  $\Gamma_{0,D} \cap \Gamma_{0,N} = \emptyset$ . They represent respectively the Dirichlet and Neumann parts of the boundary in the reference configuration (see Figure 5.5). Let also  $\mathcal{B}_t$  denote the deformed MTU at time  $t > 0$ .

The elastodynamic deformation of the MTU can be modelled using a system of PDEs in which, given an initial displacement  $\mathbf{U}_0 \in \mathbf{H}^1(\mathcal{B}_0)$ , an initial velocity  $\mathbf{V}_0 \in \mathbf{H}^1(\mathcal{B}_0)$ , an

initial pressure  $p_0 \in L^2(\mathcal{B}_0)$ , a body force  $\mathbf{f}_0(\cdot, t) \in \mathbf{L}^2(\mathcal{B}_0)$ , a prescribed traction  $\mathbf{T}(\cdot, t) \in \mathbf{H}^{-1/2}(\Gamma_{N,0})$ , and a prescribed displacement  $\mathbf{U}_D(\cdot, t) \in \mathbf{H}^{1/2}(\Gamma_{D,0})$ , we want to find large (material) displacements  $\mathbf{U}(\cdot, t) \in \mathbf{H}^1(\mathcal{B}_0)$ , a (material) velocity  $\mathbf{V} \in \mathbf{H}^1(\mathcal{B}_0)$ , a (material) internal pressure  $p(\cdot, t) \in L^2(\mathcal{B}_0)$ , and a (material) dilatation  $D(\cdot, t) \in L^2(\mathcal{B}_0)$  such that:

$$\frac{\partial \mathbf{U}}{\partial t} = \mathbf{V} \quad \text{in } \mathcal{B}_0 \times (0, \infty), \quad (5.4.1a)$$

$$\rho_0 \frac{\partial \mathbf{V}}{\partial t} - \mathbf{Div} \mathbf{P}(\mathbf{U}, \mathbf{V}, p, D) = \mathbf{f}_0 \quad \text{in } \mathcal{B}_0 \times (0, \infty), \quad (5.4.1b)$$

$$J(\mathbf{U}) - D = 0 \quad \text{in } \mathcal{B}_0 \times (0, \infty), \quad (5.4.1c)$$

$$p - \Psi'_{vol}(D) = 0 \quad \text{in } \mathcal{B}_0 \times (0, \infty), \quad (5.4.1d)$$

$$\mathbf{U} = \mathbf{U}_D \quad \text{on } \Gamma_{D,0} \times (0, \infty), \quad (5.4.1e)$$

$$\mathbf{P}(\mathbf{U}, \mathbf{V}, p, D) \mathbf{N} = \mathbf{T} \quad \text{on } \Gamma_{N,0} \times (0, \infty), \quad (5.4.1f)$$

$$\mathbf{U} = \mathbf{U}_0, \quad \mathbf{V} = \mathbf{V}_0, \quad p = p_0, \quad D = D_0 \quad \text{in } \mathcal{B}_0 \times \{t = 0\}. \quad (5.4.1g)$$

Here, the first expression corresponds to the definition of the material velocity (see Remark 5.1), whereas the second equation is just Cauchy's first equation of motion written in the Lagrangian description (see [90, Section 4.3]). The third equation is a constraint that relates  $D$  to its definition. Furthermore,  $\rho_0$  denotes the *reference density* of the MTU, and although it might depend on space coordinates  $\mathbf{X}$ , it does not depend on time.

**Remark 5.5.** *The set of equations (5.4.1) corresponds to a dynamic extension of the Euler-Lagrange equations that arise from the stationarity of the potential first proposed by Simo et al. [180]:*

$$\Pi(\mathbf{U}, p, D) = \int_{\mathcal{B}_0} \Psi_{vol}(D) + p(J(\mathbf{U}) - D) + \Psi_{iso}(\bar{\mathbf{C}}) - \int_{\mathcal{B}_0} \mathbf{f}_0 \cdot \mathbf{U}. \quad (5.4.2)$$

Therefore, we refer to (5.4.1) as the dynamic system. In turn, if we neglect the effect of the velocity on the system (i.e.  $\mathbf{V} \equiv 0$ ) as in (5.4.2), then we refer to (5.4.1) as the quasi-static system.

We also note that the system (5.4.1a)-(5.4.1d) is equivalent to the Eulerian formulation developed by Dominguez [54]:

$$\frac{\partial \mathbf{u}}{\partial t} = \mathbf{v} \quad \text{in } \mathcal{B}_t, \quad (5.4.3a)$$

$$\frac{\partial(\rho \mathbf{v})}{\partial t} + \mathbf{div}(\rho \mathbf{v} \otimes \mathbf{v}) - \mathbf{div} \boldsymbol{\sigma}(\mathbf{u}, \mathbf{v}, p, D) = \mathbf{f} \quad \text{in } \mathcal{B}_t, \quad (5.4.3b)$$

$$J(\mathbf{u}) - D = 0 \quad \text{in } \mathcal{B}_t, \quad (5.4.3c)$$

$$p - \Psi'_{vol}(D) = 0 \quad \text{in } \mathcal{B}_t, \quad (5.4.3d)$$

where the density in the current configuration  $\rho$  is given by

$$\rho = J(\mathbf{u})^{-1} \rho_0, \quad (5.4.4)$$

and the body force  $\mathbf{f}$  is:

$$\mathbf{f}(\mathbf{x}, t) = J(\mathbf{U})^{-1} \mathbf{f}_0(\varphi^{-1}(\mathbf{x}, t), t). \quad (5.4.5)$$

However, we have chosen to work with the Lagrangian formulation (5.4.1) because it leads to a simpler variational formulation, which consequently leads to a (significantly) simpler linearization of the problem (see below).

## 5.5 A first order, fully implicit time discretization

Based on the Neo-Hookean experiments we performed in Chapter 4, we discretize (5.4.1) using Rothe's method with a first-order, fully-implicit time stepping scheme. In this way, let us consider a time step size  $\Delta t = T/N$  and time steps  $t_n = n\Delta t$ , with  $n = 0, \dots, N$  and  $T > 0$  the simulation end time. For each  $n \geq 0$ , we seek approximations  $\mathbf{U}^{n+1}(\mathbf{X}) \approx \mathbf{U}(\mathbf{X}, t^{n+1})$ ,  $\mathbf{V}^{n+1}(\mathbf{X}) \approx \mathbf{V}(\mathbf{X}, t^{n+1})$ ,  $p^{n+1}(\mathbf{X}) \approx p(\mathbf{X}, t^{n+1})$ , and  $D^{n+1}(\mathbf{X}) \approx D(\mathbf{X}, t^{n+1})$  such that:

$$\frac{\mathbf{U}^{n+1} - \mathbf{U}^n}{\Delta t} = \mathbf{V}^{n+1} \quad \text{in } \mathcal{B}_0, \quad (5.5.1a)$$

$$\rho_0 \frac{\mathbf{V}^{n+1} - \mathbf{V}^n}{\Delta t} - \mathbf{Div} \mathbf{P}(\mathbf{U}^{n+1}, \mathbf{V}^{n+1}, p^{n+1}, D^{n+1}) = \mathbf{f}_0^{n+1} \quad \text{in } \mathcal{B}_0, \quad (5.5.1b)$$

$$J(\mathbf{U}^{n+1}) - D^{n+1} = 0 \quad \text{in } \mathcal{B}_0, \quad (5.5.1c)$$

$$p^{n+1} - \Psi'_{vol}(D^{n+1}) = 0 \quad \text{in } \mathcal{B}_0, \quad (5.5.1d)$$

$$\mathbf{U}^{n+1} = \mathbf{U}_D^{n+1} \quad \text{on } \Gamma_{D,0}, \quad (5.5.1e)$$

$$\mathbf{P}(\mathbf{U}^{n+1}, \mathbf{V}^n, p^{n+1}, D^{n+1}) \mathbf{N} = \mathbf{T}^{n+1} \quad \text{on } \Gamma_{N,0}. \quad (5.5.1f)$$

Combining the first two equations above we obtain the following displacement-pressure-dilatation system: for each  $n \geq 0$ , find  $\mathbf{U}^{n+1}$ ,  $p^{n+1}$ , and  $D^{n+1}$  such that:

$$\rho_0 \mathbf{U}^{n+1} - \Delta t^2 \mathbf{Div} \mathbf{P}(\mathbf{U}^{n+1}, \mathbf{V}^{n+1}, p^{n+1}, D^{n+1}) = \rho_0 \mathbf{U}^n + \Delta t \rho_0 \mathbf{V}^n + \Delta t^2 \mathbf{f}_0^{n+1}, \quad (5.5.2a)$$

$$D^{n+1} - J(\mathbf{u}^{n+1}) = 0, \quad (5.5.2b)$$

$$p^{n+1} - \Psi'_{vol}(D^{n+1}) = 0, \quad (5.5.2c)$$

and

$$\mathbf{V}^{n+1} = \frac{\mathbf{U}^{n+1} - \mathbf{U}^n}{\Delta t}, \quad (5.5.3)$$

with boundary conditions (5.5.1e) and (5.5.1f)

We now construct a variational formulation for the system (5.5.2). First, multiplying (5.5.2a) by  $\delta \mathbf{U} \in \mathbf{H}_0^1(\mathcal{B}_0)$  and integrating by parts, we obtain:

$$\begin{aligned} & \int_{\mathcal{B}_0} \rho_0 \mathbf{U}^{n+1} \cdot \delta \mathbf{U} + \Delta t^2 \int_{\mathcal{B}_0} \mathbf{P}(\mathbf{U}^{n+1}, \mathbf{V}^{n+1}) : \nabla_0(\delta \mathbf{U}) \\ &= \int_{\mathcal{B}_0} \rho_0 \mathbf{U}^n \cdot \delta \mathbf{U} + \Delta t \int_{\mathcal{B}_0} \rho_0 \mathbf{V}^n \cdot \delta \mathbf{U} + \Delta t^2 \int_{\mathcal{B}_0} \mathbf{f}_0^{n+1} \cdot \delta \mathbf{U} + \Delta t^2 \int_{\Gamma_{N,0}} \mathbf{T}^{n+1} \cdot \delta \mathbf{U}. \end{aligned} \quad (5.5.4)$$

Furthermore, we can use (5.1.31) to rewrite the second term in the previous expression as:

$$\begin{aligned} & \int_{\mathcal{B}_0} \mathbf{P}(\mathbf{U}^{n+1}, \mathbf{V}^{n+1}, p^{n+1}, D^{n+1}) : \nabla_0(\delta \mathbf{U}) \\ &= \int_{\mathcal{B}_0} J(\mathbf{U}^{n+1}) \boldsymbol{\sigma}(\mathbf{U}^{n+1}, \mathbf{V}^n, p^{n+1}, D^{n+1}) : \nabla_0(\delta \mathbf{U}) \mathbf{F}(\mathbf{U}^{n+1})^{-1} \\ &= \int_{\mathcal{B}_0} \boldsymbol{\tau}(\mathbf{U}^{n+1}, \mathbf{V}^n, p^{n+1}, D^{n+1}) : \nabla_0(\delta \mathbf{U}) \mathbf{F}(\mathbf{U}^{n+1})^{-1}. \end{aligned}$$

Thus, we can rewrite (5.5.4) as

$$\begin{aligned} & \int_{\mathcal{B}_0} \rho_0 \mathbf{U}^{n+1} \cdot \delta \mathbf{U} + \Delta t^2 \int_{\mathcal{B}_0} \boldsymbol{\tau}(\mathbf{U}^{n+1}, \mathbf{V}^{n+1}) : \nabla_0(\delta \mathbf{U}) \mathbf{F}(\mathbf{U}^{n+1})^{-1} \\ &= \int_{\mathcal{B}_0} \rho_0 \mathbf{U}^n \cdot \delta \mathbf{U} + \Delta t \int_{\mathcal{B}_0} \rho_0 \mathbf{V}^n \cdot \delta \mathbf{U} + \Delta t^2 \int_{\mathcal{B}_0} \mathbf{f}_0^{n+1} \cdot \delta \mathbf{U} + \Delta t^2 \int_{\Gamma_{N,0}} \mathbf{T}^{n+1} \cdot \delta \mathbf{U}. \end{aligned} \quad (5.5.5)$$

Similarly, for equations (5.5.2b) and (5.5.2c), we multiply them respectively by test functions  $\delta p \in L^2(\mathcal{B}_0)$  and  $\delta D \in L^2(\mathcal{B}_0)$  and integrate:

$$\int_{\mathcal{B}_0} \left\{ J(\mathbf{U}^{n+1}) - D^{n+1} \right\} \cdot \delta p = 0, \quad (5.5.6)$$

and

$$\int_{\mathcal{B}_0} \left\{ \psi'_{vol}(D^{n+1}) - p^{n+1} \right\} \cdot \delta D = 0. \quad (5.5.7)$$

Finally, multiplying (5.5.5) by  $\Delta t^{-2}$  and adding it to (5.5.6) and (5.5.7), we obtain the following nonlinear formulation of the semi-discrete problem (5.5.2): find  $\mathbf{U}^{n+1} \in \mathbf{H}^1(\mathcal{B}_0)$ ,  $p^{n+1} \in L^2(\mathcal{B}_0)$ , and  $D^{n+1} \in L^2(\mathcal{B}_0)$  such that

$$R(\mathbf{U}^{n+1}, p^{n+1}, D^{n+1}; \delta \mathbf{U}, \delta p, \delta D) = 0, \quad (5.5.8)$$

for any  $\delta\mathbf{U} \in \mathbf{H}_0^1(\mathcal{B}_0)$ ,  $\delta p \in L^2(\mathcal{B}_0)$ , and  $\delta D \in L^2(\mathcal{B}_0)$ , where

$$\begin{aligned}
R(\mathbf{U}^{n+1}, p^{n+1}, D^{n+1}; \delta\mathbf{U}, \delta p, \delta D) := & \\
& \Delta t^{-2} \int_{\mathcal{B}_0} \rho_0 \mathbf{U}^{n+1} \cdot \delta\mathbf{U} + \int_{\mathcal{B}_0} \boldsymbol{\tau}(\mathbf{U}^{n+1}, \mathbf{V}^{n+1}, p^{n+1}, D^{n+1}) : \nabla_0(\delta\mathbf{U}) \mathbf{F}(\mathbf{U}^{n+1})^{-1} \\
& + \int_{\mathcal{B}_0} \left\{ J(\mathbf{U}^{n+1}) - D^{n+1} \right\} \cdot \delta p + \int_{\mathcal{B}_0} \left\{ \psi'_{vol}(D^{n+1}) - p^{n+1} \right\} \cdot \delta D \\
& - \Delta t^{-1} \int_{\mathcal{B}_0} \rho_0 \mathbf{V}^n \cdot \delta\mathbf{U} - \Delta t^{-2} \int_{\mathcal{B}_0} \rho_0 \mathbf{U}^n \cdot \delta\mathbf{U} - \int_{\Gamma_{N,0}} \mathbf{T}^{n+1} \cdot \delta\mathbf{U} \\
& - \int_{\mathcal{B}_0} \mathbf{f}_0^{n+1} \cdot \delta\mathbf{U}.
\end{aligned} \tag{5.5.9}$$

We may also refer to (5.5.8) as the (semi-discretized) *principle of virtual work* [90]. In particular, we may split  $R$  into three components:

$$R = R_{ine} + R_{int} - R_{ext}, \tag{5.5.10}$$

where the (semi-discrete) work due to inertial, internal, and external forces are respectively given by:

$$\begin{aligned}
R_{ine}(\mathbf{U}^{n+1}; \delta\mathbf{U}) = & \Delta t^{-2} \int_{\mathcal{B}_0} \rho_0 \mathbf{U}^{n+1} \cdot \delta\mathbf{U} \\
& - \Delta t^{-2} \int_{\mathcal{B}_0} \rho_0 \mathbf{U}^n \cdot \delta\mathbf{U} \\
& - \Delta t^{-1} \int_{\mathcal{B}_0} \rho_0 \mathbf{V}^n \cdot \delta\mathbf{U},
\end{aligned} \tag{5.5.11}$$

$$\begin{aligned}
R_{int}(\mathbf{U}^{n+1}, p^{n+1}, D^{n+1}; \delta\mathbf{U}, \delta p, \delta D) = & \int_{\mathcal{B}_0} \boldsymbol{\tau}^{n+1} : \nabla_0(\delta\mathbf{U}) \mathbf{F}(\mathbf{U}^{n+1})^{-1} \\
& + \int_{\mathcal{B}_0} \left\{ J(\mathbf{U}^{n+1}) - D^{n+1} \right\} \cdot \delta p \\
& + \int_{\mathcal{B}_0} \left\{ \psi'_{vol}(D^{n+1}) - p^{n+1} \right\} \cdot \delta D,
\end{aligned} \tag{5.5.12}$$

and

$$R_{ext}(\delta\mathbf{U}) = \int_{\Gamma_{N,0}} \mathbf{T}^{n+1} \cdot \delta\mathbf{U} + \int_{\mathcal{B}_0} \mathbf{f}_0^{n+1} \cdot \delta\mathbf{U}. \tag{5.5.13}$$

In Equation (5.5.12), we have written  $\boldsymbol{\tau}^{n+1} = \boldsymbol{\tau}(\mathbf{U}^{n+1}, \mathbf{V}^{n+1}, p^{n+1}, D^{n+1})$ .

**Remark 5.6.** *Using this notation, a variational formulation for the quasi-static problem that arises from (5.4.1) (or equivalently, the stationarity of the potential (5.4.2)) reads: find  $\mathbf{U}^{n+1} \in \mathbf{H}^1(\mathcal{B}_0)$ ,  $p^{n+1} \in L^2(\mathcal{B}_0)$ , and  $D^{n+1} \in L^2(\mathcal{B}_0)$  such that*

$$R_{int}(\mathbf{U}^{n+1}, p^{n+1}, D^{n+1}; \delta\mathbf{U}, \delta p, \delta D) = R_{ext}(\delta\mathbf{U}), \tag{5.5.14}$$

for all virtual displacements  $\delta\mathbf{U} \in \mathbf{H}_0^1(\mathcal{B}_0)$ , virtual pressures  $\delta p \in L^2(\mathcal{B}_0)$ , and virtual dilatations  $\delta D \in L^2(\mathcal{B}_0)$ . Recall that, in this case, the equations do not involve

Before jumping into the linearization of the nonlinear problem (5.5.8), let us see how this formulation differs from the one introduced in [54].

**Remark 5.7.** Consider the variational formulation for the Eulerian system (5.4.3) as in [54, Equation 6.22] pulled back to the reference configuration: find  $\mathbf{U}^{n+1} \in \mathbf{H}^1(\mathcal{B}_0)$ ,  $p^{n+1} \in L^2(\mathcal{B}_0)$ , and  $D^{n+1} \in L^2(\mathcal{B}_0)$  such that

$$\tilde{R}(\mathbf{U}^{n+1}, p^{n+1}, D^{n+1}; \delta\mathbf{U}, \delta p, \delta D) = 0, \quad (5.5.15)$$

for any  $\delta\mathbf{U} \in \mathbf{H}_0^1(\mathcal{B}_0)$ ,  $\delta p \in L^2(\mathcal{B}_0)$ , and  $\delta D \in L^2(\mathcal{B}_0)$ , where

$$\begin{aligned} \tilde{R}(\mathbf{U}^{n+1}, p^{n+1}, D^{n+1}; \delta\mathbf{U}, \delta p, \delta D) := & \Delta t^{-2} \int_{\mathcal{B}_0} \rho_0 \mathbf{U}^{n+1} \cdot \delta\mathbf{U} + \int_{\mathcal{B}_0} \boldsymbol{\tau}(\mathbf{U}^{n+1}, \mathbf{V}^n, p^{n+1}, D^{n+1}) : \nabla_0^S(\delta\mathbf{U}) \mathbf{F}(\mathbf{U}^{n+1})^{-1} \\ & + \int_{\mathcal{B}_0} \left\{ J(\mathbf{U}^{n+1}) - D^{n+1} \right\} \cdot \delta p + \int_{\mathcal{B}_0} \left\{ \psi'_{vol}(D^{n+1}) - p^{n+1} \right\} \cdot \delta D \\ & - \Delta t^{-1} \int_{\mathcal{B}_0} \rho_0 \frac{J(\mathbf{U}^{n+1})}{J(\mathbf{U}^n)} \mathbf{V}^n \cdot \delta\mathbf{U} \\ & - \int_{\mathcal{B}_0} \left( \rho_0 \frac{J(\mathbf{U}^{n+1})}{J(\mathbf{U}^n)} \mathbf{V}^n \otimes \mathbf{V}^n \right) : \nabla_0^S(\delta\mathbf{U}) \mathbf{F}(\mathbf{U}^{n+1})^{-1} \\ & + \int_{\Gamma_{N,0}} \left( \rho_0 \frac{J(\mathbf{U}^{n+1})}{J(\mathbf{U}^n)} \mathbf{V}^n \otimes \mathbf{V}^n \right) \mathbf{F}(\mathbf{U}^{n+1})^{-T} \mathbf{N} \cdot \delta\mathbf{U} \\ & - \Delta t^{-2} \int_{\mathcal{B}_0} \rho_0 \mathbf{U}^n \cdot \delta\mathbf{U} - \int_{\Gamma_{N,0}} \mathbf{T}^{n+1} \cdot \delta\mathbf{U} - \int_{\mathcal{B}_0} \mathbf{f}_0^{n+1} \cdot \delta\mathbf{U}. \end{aligned} \quad (5.5.16)$$

Given that the Eulerian and the Lagrangian formulations model the exact same biological system but in difference frames of reference, it is clear that the nonlinear weak formulations (5.5.8) and (5.5.15) are completely equivalent. However, the linearization for these problems involves the computation of derivatives with respect to  $\mathbf{U}^{n+1}$ ,  $p^{n+1}$ , and  $D^{n+1}$  for the first four terms in (5.5.9), as opposed to the first seven in (5.5.16). Furthermore, the weak problem (5.5.8) represents a departure from (5.5.15) since we are now treating the velocity implicitly in the Kirchhoff stress  $\boldsymbol{\tau}$ , as opposed to the explicit treatment in (5.5.16) (as seen in the second term that defines  $\tilde{R}$ ).

## 5.6 Linearization

The linearization of the three-field formulation (5.5.8) is based on previous developments by Dominguez [54] and Pelteret [144], with additional terms appearing naturally from the inertia of the system. First, we give general details of Newton iteration, along with the

boundary conditions needed each for each iterate. Then, we provide computable versions of each one of the blocks that form the tangent operator  $\mathcal{D}R$ .

### 5.6.1 Newton's method

Given  $\mathbf{U}^n$ ,  $\mathbf{V}^n$ ,  $\mathbf{U}_k^{n+1}$ ,  $p_k^{n+1}$ , and  $D_k^{n+1}$ , we want to find updates  $\mathbf{dU}_k$ ,  $dp_k$ , and  $dD_k$  such that:

$$\begin{aligned}\mathcal{D}R(\mathbf{U}_k^{n+1}, p_k^{n+1}, D_k^{n+1}) & \left( d\mathbf{U}_k, dp_k, dD_k; \delta\mathbf{U}, \delta p, \delta D \right) \\ & = -R(\mathbf{U}_k^{n+1}, p_k^{n+1}, D_k^{n+1}; \delta\mathbf{U}, \delta p, \delta D),\end{aligned}\quad (5.6.1)$$

for all virtual increments  $\delta\mathbf{U}$ ,  $\delta p$ , and  $\delta D$ , then update the solution as

$$\mathbf{U}_{k+1}^{n+1} = \mathbf{U}_k^{n+1} + \mathbf{dU}_k, \quad p_{k+1}^{n+1} = p_k^{n+1} + dp_k, \quad D_{k+1}^{n+1} = D_k^{n+1} + dD_k, \quad (5.6.2)$$

until a convergence criterion is satisfied. Here,  $\mathcal{D}R$  denotes the Gâteaux derivative of the operator  $R$  ( $\mathcal{D}R$  is also known as the **tangent operator**). At the current time step, we set the initial solution as the converged one from the previous time step, i.e.,

$$\mathbf{U}_0^{n+1} = \mathbf{U}^n, \quad (5.6.3)$$

with analogous expressions for the pressure and dilatation. Therefore, the solution can be updated as:

$$\mathbf{U}_{k+1}^{n+1} = \mathbf{U}_k^{n+1} + \mathbf{dU}_k = \mathbf{U}_{k-1}^{n+1} + \mathbf{dU}_{k-1} + \mathbf{dU}_k = \cdots = \mathbf{U}_0^{n+1} + \Delta\mathbf{U}_k = \mathbf{U}^n + \Delta\mathbf{U}_k, \quad (5.6.4)$$

where we have defined the object:

$$\Delta\mathbf{U}_k = \sum_{l=0}^k \mathbf{dU}_k. \quad (5.6.5)$$

**Remark 5.8.** *Computationally speaking, at the beginning of every time step, one would set the object  $\Delta\mathbf{U}_k$  to zero and then start updating recursively this quantity with each Newton step  $\mathbf{dU}_k$ . Then, once convergence has been achieved, we can obtain the converged solution for the current time step as in the last equality of (5.6.4). This approach turns out to be less prone to numerical (round off) errors than updating the solution directly as in (5.6.2).*

**Remark 5.9** (Boundary conditions for the linearized system). *Consistent with the variational problem (5.5.8), the linearized problem (5.6.1) requires boundary conditions for the displacements  $\mathbf{dU}_k$  at each iteration  $k$ . To determine these, let us assume that for the time step  $t_{n+1}$ , the method converges in  $K + 1$  iterations. Thus, we can set  $\mathbf{U}^{n+1} := \mathbf{U}_{K+1}^{n+1}$  and*

therefore, according to (5.6.4),

$$\Delta \mathbf{U}_K = \mathbf{dU}_0 + \mathbf{dU}_1 + \cdots + \mathbf{dU}_K = \mathbf{U}^{n+1} - \mathbf{U}^n.$$

However, the displacements  $\mathbf{U}^{n+1}$  and  $\mathbf{U}^n$  are known along the Dirichlet part of the boundary. This suggests that, on  $\Gamma_{0,D}$ , we can set

$$\begin{aligned} \mathbf{dU}_0 &= \mathbf{U}^{n+1} - \mathbf{U}^n, \\ \mathbf{dU}_1 &= \mathbf{0}, \\ &\vdots \\ \mathbf{dU}_K &= \mathbf{0}, \end{aligned} \tag{5.6.6}$$

that is, the incremental displacement  $\mathbf{U}^{n+1} - \mathbf{U}^n$  is only implemented at the first Newton iteration and zero Dirichlet boundary conditions can be assumed for the rest.

### 5.6.2 Construction of the block-matrix system

We begin populating the elements forming the tangent operator  $\mathcal{D}R$  by computing the Gâteaux derivatives of each relevant term in (5.5.8). First, for the inertial contribution, only the first term in (5.5.11) depends on the current displacement, so the linearization of this term yields:

$$\mathbf{K}_{ine}^{\delta\mathbf{U},\mathbf{dU}} = \frac{d}{d\epsilon} R_{ine}(\mathbf{U}_k^{n+1} + \epsilon \mathbf{dU}_k; \delta\mathbf{U}) \Big|_{\epsilon=0} = \Delta t^{-2} \int_{\mathcal{B}_0} \rho_0 \mathbf{dU}_k \cdot \delta\mathbf{U}. \tag{5.6.7}$$

Next, for the internal contribution, the linearization of the first term in (5.5.12) is discussed in general terms in [90, Chapter 8]. This yields the term:

$$\mathbf{K}_{int}^{\delta\mathbf{U},\mathbf{dU}} = \int_{\mathcal{B}_0} \nabla(\delta\mathbf{U}) : J \mathbb{C}_k^{n+1} : \nabla(\mathbf{dU}_k) + \int_{\mathcal{B}_0} \nabla(\delta\mathbf{U}) : \nabla(\mathbf{dU}_k) \boldsymbol{\tau}^{n+1}, \tag{5.6.8}$$

where  $\mathbb{C}_k^{n+1} = \mathbb{c}(\mathbf{U}_k^{n+1}, \mathbf{V}_k^{n+1}, p_k^{n+1}, D_k^{n+1})$  is the fourth-order elasticity tensor defined in (5.1.60). The computation of this tensor will be the main focus of Section 5.7.

The rest of the contributions with respect to virtual displacements are easier to compute. Following (5.1.55), we use the decomposition

$$\boldsymbol{\tau} = \boldsymbol{\tau}_{vol}(p, J(\mathbf{U})) + \boldsymbol{\tau}_{iso}(\mathbf{U}, \mathbf{V}), \tag{5.6.9}$$

as the pressure only appears in the volumetric part of the Kirchhoff stress and there is no dependence on the approximate dilatation  $D$ :

$$\begin{aligned}\mathbf{K}^{\delta\mathbf{U},dp} &= \frac{d}{d\epsilon} R_{int}(\mathbf{U}_k^{n+1}, p_k^{n+1} + \epsilon dp_k, D_k^{n+1}; \delta\mathbf{U}) \Big|_{\epsilon=0} \\ &= \int_{\mathcal{B}_0} dp_k J \mathbf{I} : \nabla(\delta\mathbf{U}) \\ &= \int_{\mathcal{B}_0} dp_k J \mathbf{I} : \left\{ \nabla_0(\delta\mathbf{U}) \mathbf{F}(\mathbf{U}_k^{n+1})^{-1} \right\}\end{aligned}\quad (5.6.10)$$

and  $\mathbf{K}^{\delta\mathbf{U},dD} = 0$ . Next, for the contributions with respect to virtual pressures, we have

$$\begin{aligned}\mathbf{K}^{\delta p,\mathbf{dU}} &= \frac{d}{d\epsilon} R_{int}(\mathbf{U}_k^{n+1} + \epsilon \mathbf{dU}_k, p_k^{n+1}, D_k^{n+1}; \delta p) \Big|_{\epsilon=0} \\ &= \int_{\mathcal{B}_0} \delta p J \mathbf{I} : \nabla(\mathbf{dU}_k) \\ &= \int_{\mathcal{B}_0} \delta p J \mathbf{I} : \left\{ \nabla_0(\mathbf{dU}_k) \mathbf{F}(\mathbf{U}_k^{n+1})^{-1} \right\},\end{aligned}\quad (5.6.11)$$

$\mathbf{K}^{\delta p,dp} = 0$ , and

$$\begin{aligned}\mathbf{K}^{\delta p,dD} &= \frac{d}{d\epsilon} R_{int}(\mathbf{U}_k^{n+1}, p_k^{n+1}, D_k^{n+1} + \epsilon dD_k; \delta p) \Big|_{\epsilon=0} \\ &= - \int_{\mathcal{B}_0} dD \delta p.\end{aligned}\quad (5.6.12)$$

Finally, for the contributions with respect to virtual dilatations, we have  $\mathbf{K}^{\delta D,\mathbf{dU}} = 0$ ,

$$\begin{aligned}\mathbf{K}^{\delta D,dp} &= \frac{d}{d\epsilon} R_{int}(\mathbf{U}_k^{n+1}, p_k^{n+1} + \epsilon dp_k, D_k^{n+1}; \delta D) \Big|_{\epsilon=0} \\ &= - \int_{\mathcal{B}_0} dp \delta D,\end{aligned}\quad (5.6.13)$$

and

$$\begin{aligned}\mathbf{K}^{\delta D,dD} &= \frac{d}{d\epsilon} R_{int}(\mathbf{U}_k^{n+1}, p_k^{n+1}, D_k^{n+1} + \epsilon dD_k; \delta D) \Big|_{\epsilon=0} \\ &= \int_{\mathcal{B}_0} \Psi''_{vol}(D_k^{n+1}) dD \delta D.\end{aligned}\quad (5.6.14)$$

Therefore, the problem (5.6.1) can formally be written in matrix form as:

$$\begin{bmatrix} \mathbf{K}_{ine}^{\delta\mathbf{U},\mathbf{dU}} + \mathbf{K}_{int}^{\delta\mathbf{U},\mathbf{dU}} & \mathbf{K}^{\delta\mathbf{U},dp} & \mathbf{0} \\ \mathbf{K}^{\delta p,\mathbf{dU}} & \mathbf{0} & \mathbf{K}^{\delta p,dD} \\ \mathbf{0} & \mathbf{K}^{\delta D,dp} & \mathbf{K}^{\delta D,dD} \end{bmatrix} \begin{pmatrix} d\mathbf{U}_k \\ dp_k \\ dD_k \end{pmatrix} = - \begin{pmatrix} R_{ine}(\mathbf{U}_k^{n+1}) + R_{int}(\mathbf{U}_k^{n+1}) \\ R_{int}(p_k^{n+1}) \\ R_{int}(D_k^{n+1}) \end{pmatrix}. \quad (5.6.15)$$

## 5.7 Fourth-order elasticity tensors

To compute the fourth-order tensor  $\mathbb{C}^{n+1}$ , we first need to find the material tensor  $\bar{\mathbb{C}}$  (see Equations (5.1.67), (5.1.69), and (5.1.70)). In fact, each contribution to the isochoric SEF  $\Psi_{iso}$  yields a different contribution to the tensor  $\bar{\mathbb{C}}$ . For example, if we assume that  $\mathcal{B}_0$  contains muscle fibres, base material, and intramuscular fat as in (5.2.3), we will have:

$$\bar{\mathbb{C}} = (1 - \chi_{fat})(\bar{\mathbb{C}}_{fibre} + \bar{\mathbb{C}}_{bm}) + \chi_{fat}\bar{\mathbb{C}}_{fat}, \quad (5.7.1)$$

with analogous expressions if ECM, cell, tendon, or aponeurosis tissues are included.

The derivation of all parts that make the  $\bar{\mathbb{C}}$  tensor follows the same structure, so we focus mostly on the fibre contribution, as this is novel to the elastodynamics of skeletal muscle tissue.

### 5.7.1 Along-fibre contribution

Because of the implicit treatment of the velocity in the Kirchhoff stress, and because we are not considering the velocity and displacement as *independent* variables, the elasticity tensors needed for a Newton iteration take a more involved form (compared to the quasi-static case) that requires some particular approximations, specially regarding the modified fibre strain rate  $\bar{\varepsilon}$ . This will be one of the main contributions in this section.

According to Equation (5.1.65), we first have:

$$J^{4/3}\bar{\mathbb{C}}_{fibre}^{n+1} = 2 \frac{\partial \bar{\mathbf{S}}_{fibre}^{n+1}}{\partial \bar{\mathbb{C}}^{n+1}} = 2 \frac{\partial \bar{\mathbf{S}}_{fibre}^{n+1}}{\partial \bar{I}_4^{n+1}} \otimes \frac{\partial \bar{I}_4^{n+1}}{\partial \bar{\mathbb{C}}^{n+1}}. \quad (5.7.2)$$

Moreover, using (5.1.74) and the particular expression for  $\bar{\mathbf{S}}_{fibre}$  in (5.2.7), we obtain:

$$\begin{aligned} J^{4/3}\bar{\mathbb{C}}_{fibre}^{n+1} &= 2 \frac{\partial}{\partial \bar{I}_4^{n+1}} \left[ \frac{1}{\bar{I}_4^{n+1}} \sigma_{Hill}(\bar{I}_4^{n+1}) \right] \mathbf{a}_0 \otimes \mathbf{a}_0 \otimes \mathbf{a}_0 \otimes \mathbf{a}_0 \\ &= 2 \left[ -\frac{1}{(\bar{I}_4^{n+1})^2} \sigma_{Hill}(\bar{I}_4^{n+1}) + \frac{1}{\bar{I}_4^{n+1}} \frac{\partial \sigma_{Hill}(\bar{I}_4^{n+1})}{\partial \bar{I}_4^{n+1}} \right] \mathbf{a}_0 \otimes \mathbf{a}_0 \otimes \mathbf{a}_0 \otimes \mathbf{a}_0 \end{aligned} \quad (5.7.3)$$

At this juncture, we emphasize that these expressions are meant to be evaluated at the current Newton iteration  $k$  (see (5.6.8)). In particular, using the definition of Hill's fibre

stress in (5.2.5), we obtain the following expression for its derivative:

$$\begin{aligned} \frac{\partial \sigma_{Hill}(\bar{I}_4^{n+1})}{\partial \bar{I}_4^{n+1}} &= \frac{\partial \sigma_{Hill}(\bar{\lambda}_k^{n+1}, \bar{\varepsilon}_k^{n+1})}{\partial \bar{\lambda}_k^{n+1}} \frac{\partial \bar{\lambda}_k^{n+1}}{\partial \bar{I}_4^{n+1}} + \frac{\partial \sigma_{Hill}(\bar{\lambda}_k^{n+1}, \bar{\varepsilon}_k^{n+1})}{\partial \bar{\varepsilon}_k^{n+1}} \frac{\partial \bar{\varepsilon}_k^{n+1}}{\partial \bar{\lambda}_k^{n+1}} \frac{\partial \bar{\lambda}_k^{n+1}}{\partial \bar{I}_4^{n+1}} \\ &= \sigma_{0,mus} \left[ a^{n+1} \frac{d\hat{\sigma}_L(\bar{\lambda}_k^{n+1})}{d\bar{\lambda}_k^{n+1}} \hat{\sigma}_V(\bar{\varepsilon}_k^{n+1}) + \frac{d\hat{\sigma}_P(\bar{\lambda}_k^{n+1})}{d\bar{\lambda}_k^{n+1}} \right] \frac{1}{2\bar{\lambda}_k^{n+1}} \\ &\quad + \sigma_{0,mus} a^{n+1} \hat{\sigma}_L(\bar{\lambda}_k^{n+1}) \frac{d\sigma_V(\bar{\varepsilon}_k^{n+1})}{d\bar{\varepsilon}_k^{n+1}} \frac{\partial \bar{\varepsilon}_k^{n+1}}{\partial \bar{\lambda}_k^{n+1}} \frac{1}{2\bar{\lambda}_k^{n+1}}. \end{aligned} \quad (5.7.4)$$

In particular, following the definition of the modified strain rate  $\bar{\varepsilon}$  in (5.1.42)<sub>2</sub> we consider:

$$\bar{\varepsilon}_k^{n+1} = \frac{1}{\dot{\varepsilon}_0} \frac{(\bar{\mathbf{F}}_k^{n+1} \mathbf{a}_0)^\top (\mathbb{P} : \mathbf{d}_k^{n+1}) (\bar{\mathbf{F}}_k^{n+1} \mathbf{a}_0)}{\bar{\lambda}_k^{n+1}}, \quad (5.7.5)$$

where, according to (5.1.22),

$$\mathbf{d}_k^{n+1} = \text{symm} \left( \frac{\mathbf{F}_k^{n+1} - \mathbf{F}^n}{\Delta t} \left( \mathbf{F}_k^{n+1} \right)^{-1} \right). \quad (5.7.6)$$

However, for the term  $\frac{\partial \bar{\varepsilon}_k^{n+1}}{\partial \bar{\lambda}_k^{n+1}}$  (and only for this term), we approximate  $\bar{\varepsilon}_k^{n+1}$  as in (5.1.42)<sub>1</sub>:

$$\bar{\varepsilon}_k^{n+1} \approx \frac{1}{\dot{\varepsilon}_0} \frac{\bar{\lambda}_k^{n+1} - \bar{\lambda}^n}{\Delta t}, \quad (5.7.7)$$

and thus we set:

$$\frac{\partial \bar{\varepsilon}_k^{n+1}}{\partial \bar{\lambda}_k^{n+1}} = \frac{1}{\dot{\varepsilon}_0} \frac{1}{\Delta t}. \quad (5.7.8)$$

Therefore, the full expression for  $J^{4/3} \bar{\mathbb{C}}_{fibre}^{n+1}$  reads:

$$J^{4/3} \bar{\mathbb{C}}_{fibre}^{n+1} = \mathfrak{C} \left( \bar{\lambda}_k^{n+1}, \bar{\varepsilon}_k^{n+1} \right) \mathbf{a}_0 \otimes \mathbf{a}_0 \otimes \mathbf{a}_0 \otimes \mathbf{a}_0,$$

where

$$\begin{aligned} \mathfrak{C} \left( \bar{\lambda}_k^{n+1}, \bar{\varepsilon}_k^{n+1} \right) &= - \frac{2}{(\bar{\lambda}_k^{n+1})^4} \sigma_{0,mus} a^{n+1} \hat{\sigma}_L(\bar{\lambda}_k^{n+1}) \hat{\sigma}_V(\bar{\varepsilon}_k^{n+1}) \\ &\quad + \frac{1}{(\bar{\lambda}_k^{n+1})^3} \sigma_{0,mus} a^{n+1} \frac{d\hat{\sigma}_L}{d\bar{\lambda}} \left( \bar{\lambda}_k^{n+1} \right) \hat{\sigma}_V(\bar{\varepsilon}_k^{n+1}) \\ &\quad + \frac{1}{(\bar{\lambda}_k^{n+1})^3} \sigma_{0,mus} a^{n+1} \hat{\sigma}_L(\bar{\lambda}_k^{n+1}) \frac{d\hat{\sigma}_V}{d\bar{\varepsilon}} \left( \bar{\varepsilon}_k^{n+1} \right) \frac{1}{\dot{\varepsilon}_0 \Delta t} \\ &\quad - \frac{2}{(\bar{\lambda}_k^{n+1})^4} \sigma_{0,mus} \hat{\sigma}_P(\bar{\lambda}_k^{n+1}) + \frac{1}{(\bar{\lambda}_k^{n+1})^3} \sigma_{0,mus} \frac{d\hat{\sigma}_P}{d\bar{\lambda}} \left( \bar{\lambda}_k^{n+1} \right) \end{aligned} \quad (5.7.9)$$

In this way,

$$\bar{\mathbb{C}}_{fibre}^{n+1} = \mathfrak{C}\left(\bar{\lambda}_k^{n+1}, \bar{\varepsilon}_k^{n+1}\right) \bar{\mathbf{a}}_k^{n+1} \otimes \bar{\mathbf{a}}_k^{n+1} \otimes \bar{\mathbf{a}}_k^{n+1} \otimes \bar{\mathbf{a}}_k^{n+1}, \quad (5.7.10)$$

where  $\bar{\mathbf{a}}_k^{n+1} = \bar{\mathbf{F}}_k^{n+1} \mathbf{a}_0$ .

**Remark 5.10.** If the simulation is quasi-static, then Hill's stress does not depend on the fibre strain rate, and therefore

$$\bar{\mathbb{C}}_{fibre}^{n+1} = \tilde{\mathfrak{C}}\left(\bar{\lambda}_k^{n+1}\right) \bar{\mathbf{a}} \otimes \bar{\mathbf{a}} \otimes \bar{\mathbf{a}} \otimes \bar{\mathbf{a}}, \quad (5.7.11)$$

where

$$\begin{aligned} \tilde{\mathfrak{C}}\left(\bar{\lambda}_k^{n+1}\right) &= -\frac{2\sigma_{0,mus}}{(\bar{\lambda}_k^{n+1})^4} \left[ a^{n+1} \hat{\sigma}_A(\bar{\lambda}_k^{n+1}) + \hat{\sigma}_P(\bar{\lambda}_k^{n+1}) \right] \\ &\quad + \frac{\sigma_{0,mus}}{(\bar{\lambda}_k^{n+1})^3} \left[ a^{n+1} \frac{d\hat{\sigma}_A}{d\bar{\lambda}}(\bar{\lambda}_k^{n+1}) + \frac{d\hat{\sigma}_P}{d\bar{\lambda}}(\bar{\lambda}_k^{n+1}) \right] \end{aligned} \quad (5.7.12)$$

**Remark 5.11.** Although the expressions for the modified strain rate (5.7.5) and its derivative with respect to the modified stretch (5.7.8) may seem like a minor detail in the discretization of the Lagrangian formulation (5.4.1), they constitute elements of the numerical method that can "make or break" the code for fully active, fully dynamic simulations. Fibre strain rates are typically not included in finite element codes for skeletal muscle (see, for instance, [25, 140]), precisely because it is challenging to identify suitable approximations for them. The inclusion of this term in *Flexodeal* was preceded a series of developments. A very early iteration of the fibre-reinforced continuum mechanics approach was due to Rahemi [154], in which the fibre strain rate was always set to 0. This is the approximation made in most muscle codes. Next, Dominguez [54] suggested the following expression for the fibre strain rate:

$$\bar{\varepsilon}_k^{n+1} = \mathbf{V}^n \cdot (\bar{\mathbf{F}}_k^{n+1} \mathbf{a}_0), \quad (5.7.13)$$

with no information about what the expression for  $\partial_{\bar{\lambda}_k^{n+1}} \bar{\varepsilon}_k^{n+1}$  should look like. Later, in Ross et al. [164], the following expressions were used:

$$\bar{\varepsilon}_k^{n+1} = \frac{(\bar{\mathbf{F}}^n \mathbf{a}_0)^\top (\mathbb{P} : \mathbf{d}^n) (\bar{\mathbf{F}}^n \mathbf{a}_0)}{\bar{\lambda}_k^{n+1}}, \quad \frac{\partial \bar{\varepsilon}_k^{n+1}}{\partial \bar{\lambda}_k^{n+1}} = -\frac{\bar{\varepsilon}_k^{n+1}}{\bar{\lambda}_k^{n+1}}, \quad (5.7.14)$$

with the latter being an expression that implicitly assumes that the strain rate  $\bar{\varepsilon}_k^{n+1}$  does depend on the current deformation tensor  $\bar{\mathbf{F}}_k^{n+1}$  in the numerator, but keeps the deviatoric part of the rate of strain tensor (i.e.  $\mathbb{P} : \mathbf{d}^n$ ) constant for the current time step and the current Newton iteration. While this work does contain fully active, fully dynamic contractions,

*Tam [185] corrected (5.7.14) to:*

$$\bar{\varepsilon}_k^{n+1} = \frac{(\bar{\mathbf{F}}_k^{n+1} \mathbf{a}_0)^\top (\mathbb{P} : \mathbf{d}^n)(\bar{\mathbf{F}}_k^{n+1} \mathbf{a}_0)}{\bar{\lambda}_k^{n+1}}, \quad \frac{\partial \bar{\varepsilon}_k^{n+1}}{\partial \bar{\lambda}_k^{n+1}} = + \frac{\bar{\varepsilon}_k^{n+1}}{\bar{\lambda}_k^{n+1}}. \quad (5.7.15)$$

*This resulted in successful dynamic contractions but only to a maximum of 50% activation, provided the following time size restriction is met:*

$$\frac{c\Delta t}{h} < 1, \quad c := \sqrt{\frac{\kappa}{\rho_0}}. \quad (5.7.16)$$

### 5.7.2 Base material and other components of the MTU

Following the same procedure, we obtain the contributions to  $\bar{c}$  from the base material components:

$$\bar{c}_{bm}^{n+1} = 4s_{bm}\sigma_{0,bm} \left( 6c_3(\bar{I}_1 - 3) + 2c_2 \right) \bar{\mathbf{b}} \otimes \bar{\mathbf{b}} \quad (5.7.17)$$

$$\bar{c}_{ecm}^{n+1} = 4s_{ecm} \left( 6c_3(\bar{I}_1 - 3) + 2c_2 \right) \bar{\mathbf{b}} \otimes \bar{\mathbf{b}} \quad (5.7.18)$$

$$\bar{c}_{cell}^{n+1} = 4s_{cell} \left( 6c_3(\bar{I}_1 - 3) + 2c_2 \right) \bar{\mathbf{b}} \otimes \bar{\mathbf{b}} \quad (5.7.19)$$

(with the constants defined in Table 5.1) and from the intramuscular fat:

$$\bar{c}_{fat}^{n+1} = 4s_{fat} \left( 6c_3(\bar{I}_1 - 3) + 2c_2 \right) \bar{\mathbf{b}} \otimes \bar{\mathbf{b}}, \quad (5.7.20)$$

with the constants in this case defined in Table 5.2.

Finally, for tendon and aponeurosis tissue we have:

$$\begin{aligned} \bar{c}_{tis}^{n+1} = & \left[ -\frac{2\sigma_{0,tis}}{(\bar{\lambda}_k^{n+1})^4} \hat{\sigma}_{tis}(\bar{\lambda}_k^{n+1}) + \frac{\sigma_{0,tis}}{(\bar{\lambda}_k^{n+1})^3} \frac{d\hat{\sigma}_{tis}}{d\bar{\lambda}}(\bar{\lambda}_k^{n+1}) \right] \bar{\mathbf{a}} \otimes \bar{\mathbf{a}} \otimes \bar{\mathbf{a}} \otimes \bar{\mathbf{a}} \\ & + 4s_{tis}\sigma_{0,tis} \left( 6c_3(\bar{I}_1 - 3) + 2c_2 \right) \bar{\mathbf{b}} \otimes \bar{\mathbf{b}}, \end{aligned} \quad (5.7.21)$$

for  $tis \in \{apo, ten\}$ , where the constants for this expression are defined in Table 5.3.

## 5.8 Finite element approximation

Let  $\mathcal{T}_h$  be an unstructured mesh made of hexahedra  $T \in \mathcal{T}_h$ , each with diameter  $h_T$ . Furthermore, define the mesh size  $h := \max_{T \in \mathcal{T}_h} h_T$  and let  $P_k(T)$  be the space of polynomials of degree  $\leq k$  over  $T \in \mathcal{T}_h$ , with  $\mathbf{P}_k(T) := P_k(T) \times P_k(T) \times P_k(T)$ . Then, for  $k \geq 1$ , the displacement  $\mathbf{U}$ , the pressure  $p$ , and the dilatation  $D$  are respectively approximated using

the following finite element spaces:

$$\mathbf{H}_h^U = \left\{ \tilde{\mathbf{U}}_h \in \mathcal{C}(\mathcal{B}_0) : \tilde{\mathbf{U}}_h|_T \in \mathbf{P}_k(T) \quad \forall T \in \mathcal{T}_h \right\} \quad (5.8.1a)$$

$$H_h^p = \left\{ \tilde{p}_h \in L^2(\mathcal{B}_0) : \tilde{p}_h|_T \in P_{k-1}(T) \quad \forall T \in \mathcal{T}_h \right\} \quad (5.8.1b)$$

$$H_h^D = \left\{ \tilde{D}_h \in L^2(\mathcal{B}_0) : \tilde{D}_h|_T \in P_{k-1}(T) \quad \forall T \in \mathcal{T}_h \right\} \quad (5.8.1c)$$

The previous choice is commonly known as the  $Q_k/P_{k-1}$  family [27]. For  $k = 2$ , this implies that the displacements are approximated using quadratic 27-node Lagrange  $\mathbf{Q}_2$  elements, while pressures and dilatations are approximated with discontinuous elements  $P_1$  (based on monomials, 4 degrees of freedom per element).

### 5.8.1 Approximation properties

Given that at each time step, the nonlinear problem (5.5.8) is solved using a sequence of linear problems (5.6.1), the approximation properties for these types of problems are stated using results for the linear elasticity problem.

For  $k \geq 2$ , the  $Q_k/P_{k-1}$  family defined in (5.8.1) is known to satisfy the inf-sup condition for the linearized problem (5.6.1) [34], that is, there exists  $\beta > 0$ , independent of  $h$ , such that:

$$\inf_{\tilde{p}_h \in H_h^p} \sup_{\tilde{\mathbf{U}}_h \in \mathbf{H}_h^U} \sup_{\tilde{D}_h \in H_h^D} \frac{\int_{\mathcal{B}_0} \tilde{p}_h J(\tilde{\mathbf{U}}_h) \mathbf{I} : \nabla \tilde{\mathbf{U}}_h - \int_{\mathcal{B}_0} \tilde{p}_h \tilde{D}_h}{\|\tilde{p}_h\|_{0,\mathcal{B}_0} \left( \|\tilde{\mathbf{U}}_h\|_{1,\mathcal{B}_0} + \|\tilde{D}_h\|_{0,\mathcal{B}_0} \right)} \geq \beta. \quad (5.8.2)$$

For  $k = 1$ , the family  $Q_1/P_0$  does not satisfy this inf-sup condition, so it cannot be reliably used as an approximation space. Indeed, the pressure can exhibit so-called “checkerboard modes” (see, for instance, [99]).

On the other hand, the finite element spaces defined in (5.8.1) are known to have the following properties (cf. [27, 66]):

**(AP) <sub>$h$</sub> <sup>U</sup>**) There exists  $C > 0$ , independent of  $h$ , such that for each  $s \in (0, k]$  and for each  $\mathbf{U} \in \mathbf{H}^{s+1}(\mathcal{B}_0)$ , we have:

$$\text{dist}(\mathbf{U}, \mathbf{H}_h^U) \leq Ch^s \|\mathbf{U}\|_{s+1,\mathcal{B}_0}, \quad (5.8.3)$$

**(AP) <sub>$h$</sub> <sup>p</sup>**) there exists  $C > 0$ , independent of  $h$ , such that for each  $s \in (0, k-1]$  and for each  $p \in H^s(\mathcal{B}_0)$ , we have:

$$\text{dist}(p, H_h^p) \leq Ch^s \|p\|_{s,\mathcal{B}_0}, \quad (5.8.4)$$

**(AP) <sub>$h$</sub>  <sup>$D$</sup>** ) there exists  $C > 0$ , independent of  $h$ , such that for each  $s \in (0, k - 1]$  and for each  $D \in H^s(\mathcal{B}_0)$ , we have:

$$\text{dist}(D, \mathbf{H}_h^D) \leq Ch^s \|D\|_{s, \mathcal{B}_0}, \quad (5.8.5)$$

where, in general, for Banach spaces  $V, V_h$  with  $V_h \subset V$  and an element  $v \in V$ ,

$$\text{dist}(v, V_h) = \inf_{v_h \in V_h} \|v - v_h\|_V.$$

Therefore, assuming that the following Céa estimate holds, i.e., that there exist a constant  $C > 0$  independent of  $h$  (but possibly depending on the time step  $t_n$ ) such that

$$\begin{aligned} & \|\mathbf{dU}_k^{n+1} - \mathbf{dU}_{k,h}^{n+1}\|_{1,\mathcal{B}_0} + \|dp_{k,h}^{n+1} - dp_k^{n+1}\|_{0,\mathcal{B}_0} + \|dD_{k,h}^{n+1} - dD_k^{n+1}\|_{0,\mathcal{B}_0} \\ & \leq C \left( \text{dist}(\mathbf{dU}_k^{n+1}, \mathbf{H}_h^{\mathbf{U}}) + \text{dist}(dp_k^{n+1}, \mathbf{H}_h^p) + \text{dist}(dD_k^{n+1}, \mathbf{H}_h^D) \right), \end{aligned} \quad (5.8.6)$$

we conjecture that if  $\mathbf{dU}_k^{n+1} \in \mathbf{H}^{s+1}(\mathcal{B}_0)$ ,  $dp_k^{n+1} \in H^s(\mathcal{B}_0)$ , and  $dD_k^{n+1} \in H^s(\mathcal{B}_0)$  for some  $s > 0$ , then there exists  $\hat{C} > 0$ , at least independent of  $h$ , such that

$$\begin{aligned} & \|\mathbf{dU}_k^{n+1} - \mathbf{dU}_{k,h}^{n+1}\|_{1,\mathcal{B}_0} + \|dp_{k,h}^{n+1} - dp_k^{n+1}\|_{0,\mathcal{B}_0} + \|dD_{k,h}^{n+1} - dD_k^{n+1}\|_{0,\mathcal{B}_0} \\ & \leq \hat{C} h^{\min\{s,k\}} \left( \|\mathbf{dU}_k^{n+1}\|_{s+1,\mathcal{B}_0} + \|dp_k^{n+1}\|_{s,\mathcal{B}_0} + \|dD_k^{n+1}\|_{s,\mathcal{B}_0} \right). \end{aligned} \quad (5.8.7)$$

This result would follow straight from the Céa estimate (5.8.6) and the approximation properties **(AP) <sub>$h$</sub>  <sup>$\mathbf{U}$</sup>** , **(AP) <sub>$h$</sub>  <sup>$p$</sup>** , and **(AP) <sub>$h$</sub>  <sup>$D$</sup>**  (see, for instance, [5]). Furthermore, if the error in the increment of the displacement variable is measured in the  $\mathbf{L}^2(\mathcal{B}_0)$  norm, as opposed to the  $\mathbf{H}^1(\mathcal{B}_0)$  norm, then there holds [27]:

$$\|\mathbf{dU}_k^{n+1} - \mathbf{dU}_{k,h}^{n+1}\|_{1,\mathcal{B}_0} \leq \hat{C} h^{\min\{s,k+1\}} \|\mathbf{dU}_k^{n+1}\|_{s+1,\mathcal{B}_0} \quad (5.8.8)$$

Hence, if the  $Q_2/P_1$  family of elements is used to approximate each linear problem (5.6.1), then one would expect rates of convergence of 3 for the displacement (in the  $\mathbf{L}^2(\mathcal{B}_0)$  norm) and 2 for the pressure and dilatation, but only if *all* the Newton increments are sufficiently smooth (i.e., at every Newton iteration *and* at every time step).

### 5.8.2 On polyconvexity and well-posedness of the mixed formulation

Behind the rates of convergence one could obtain when solving the linear problem (5.6.1) is the question of existence and uniqueness of solutions for the nonlinear problem (5.4.1). This is an incredibly difficult field for which multiple open problems still exist [17, 43], so a full analysis is out of the scope of this dissertation. However, we must discuss some of the assumptions that lead to the existence of solutions, as they have a direct impact on the numerical analysis of the problem.

To simplify the discussion, let us focus on the quasi-static problem, which is equivalent to finding a minimizer of the potential energy described in (5.4.2). Furthermore, let us assume that the region in three-dimensional space  $\mathcal{B}_0$  contains only muscle tissue, that is, the strain-energy function (SEF) of the system takes the form:

$$\Psi = \Psi_{vol}(J) + \Psi_{iso}(\bar{I}_1, \bar{I}_4) = \Psi_{vol}(J) + \Psi_{bm}(\bar{I}_1) + \Psi_{fibre}(\bar{I}_4). \quad (5.8.9)$$

In particular, and also assuming that the muscle tissue is fully active (i.e.,  $a(\mathbf{X}, t) \equiv 1$ ), Hill's stress (5.2.5) takes the form:

$$\sigma_{Hill}(\bar{I}_4) = \sigma_0 \left( \hat{\sigma}_A(\bar{I}_4) + \hat{\sigma}_P(\bar{I}_4) \right), \quad (5.8.10)$$

which we have conveniently written in terms of the fourth modified invariant  $\bar{I}_4 = \bar{\lambda}^2$ . Recall that, Hill's stress (5.8.10) is related to the fibre SEF  $\Psi_{fibre}$  in (5.8.9) according to the assumption (5.2.4), which we rewrite here as

$$2\bar{I}_4 \frac{\partial \Psi_{fibre}}{\partial \bar{\mathbf{C}}} = \sigma_{Hill}(\bar{I}_4) \mathbf{a}_0 \otimes \mathbf{a}_0. \quad (5.8.11)$$

This equation is obtained by multiplying (5.2.4) by  $\frac{\partial \bar{I}_4}{\partial \bar{\mathbf{C}}} = \mathbf{a}_0 \otimes \mathbf{a}_0$ .

One of the most notable hypotheses to ensure the existence of a minimizer is known as the *polyconvexity* condition in the sense of Ball [16].

**Definition 5.1** (Polyconvexity). Let  $\mathbb{M}^{3 \times 3}$  denote the space of  $3 \times 3$  matrices and let  $W(\mathbf{F}) = \Psi(\mathbf{C}) \in C^2(\mathbb{M}^{3 \times 3}, \mathbb{R})$ . We say that  $W$  is *polyconvex* if and only if there exists a function  $\Sigma : \mathbb{M}^{3 \times 3} \times \mathbb{M}^{3 \times 3} \times \mathbb{R}$  (in general non-unique) such that

$$W(\mathbf{F}) = \Sigma(\mathbf{F}, \text{Adj } \mathbf{F}, \det \mathbf{F}), \quad (5.8.12)$$

and  $\Sigma$  is strictly convex in all its 19 components. Here,  $\mathbf{F}$  is the deformation tensor,  $\text{Adj } \mathbf{F}$  is the adjugate matrix of transposed cofactors of  $\mathbf{F}$  such that  $\text{Adj } \mathbf{F} = \det(\mathbf{F})\mathbf{F}^{-1}$  (whenever  $\det \mathbf{F} > 0$ , which ensures invertibility of  $\mathbf{F}$ ).

Given that the sum of convex functions is also convex, we can look at the polyconvexity of the SEF defined in (5.8.9) individually.

First, the volumetric SEF  $\Psi_{vol}$  as defined in (5.2.2), is a (scalar) convex function, hence polyconvex [53]. Furthermore, the base material SEF, being of Yeoh-type, is also polyconvex due to a result by Hartmann & Neff [77], and for the particular case of an equation like (5.2.9), by Funai et al. [64]. However,  $\Psi_{fibre}$  may not be polyconvex. To prove this, we need the following results (cf. Schröder & Neff [175]).

**Definition 5.2** (Ellipticity). The elastic free energy  $W(\mathbf{F}) = \Psi(\mathbf{C}) \in C^2(\mathbb{M}^{3 \times 3}, \mathbb{R})$  is *elliptic* if and only if the Legendre-Hadamard condition:

$$D_{\mathbf{F}}^2 W(\mathbf{F}).(\boldsymbol{\xi} \otimes \boldsymbol{\eta}, \boldsymbol{\xi} \otimes \boldsymbol{\eta}) \geq 0 \quad (5.8.13)$$

holds for any  $\mathbf{F} \in \mathbb{M}^{3 \times 3}$  and any  $\boldsymbol{\xi}, \boldsymbol{\eta} \in \mathbb{R}^3$ . Here  $D_{\mathbf{F}}^2 W(F)(\cdot, \cdot)$  is the second Fréchet derivative of  $W$ .

**Lemma 5.3** (Formal second derivative of  $W(\mathbf{F}) = \Psi(\mathbf{C})$ ). Let  $\mathbf{F} \in \mathbb{M}^{3 \times 3}$ . For  $\mathbf{H} \in \mathbb{M}^{3 \times 3}$  and  $W \in C^2(\mathbb{R}^{3 \times 3}, \mathbb{R})$ , there holds:

$$D_{\mathbf{F}}^2 W(\mathbf{F}).(\mathbf{H}, \mathbf{H}) = 2 \frac{\partial \Psi}{\partial \mathbf{C}} : \mathbf{H}^\top \mathbf{H} + (\mathbf{F}^\top \mathbf{H} + \mathbf{H}^\top \mathbf{F}) : \frac{\partial^2 \Psi}{\partial \mathbf{C} \partial \mathbf{C}} : (\mathbf{F}^\top \mathbf{H} + \mathbf{H}^\top \mathbf{F}). \quad (5.8.14)$$

**Lemma 5.4.** Let  $W(\mathbf{F}) = \Psi(\mathbf{C})$  be polyconvex. Then,  $W$  is elliptic (in the sense of Definition 5.2).

For the particular case of  $\Psi = \Psi_{fibre}$ , let us show that  $W$  is not always elliptic. From (5.8.11), we obtain that

$$\frac{\partial^2 \Psi_{fibre}}{\partial \bar{\mathbf{C}} \partial \bar{\mathbf{C}}} = \left( -\frac{1}{2\bar{I}_4^2} \sigma_{Hill}(\bar{I}_4) + \frac{1}{2\bar{I}_4} \frac{d\sigma_{Hill}(\bar{I}_4)}{d\bar{I}_4} \right) \mathbb{M}_0, \quad (5.8.15)$$

where  $\mathbb{M}_0 := \mathbf{a}_0 \otimes \mathbf{a}_0 \otimes \mathbf{a}_0 \otimes \mathbf{a}_0$ . Consequently, plugging this expression and (5.8.11) into (5.8.14), we obtain for arbitrary  $\mathbf{H} \in \mathbb{M}^{3 \times 3}$ :

$$\begin{aligned} D_{\mathbf{F}}^2 W(\mathbf{F}).(\mathbf{H}, \mathbf{H}) &= \frac{1}{\bar{I}_4} \sigma_{Hill}(\bar{I}_4) \mathbf{a}_0 \otimes \mathbf{a}_0 : \mathbf{H}^\top \mathbf{H} \\ &+ \left( -\frac{1}{2\bar{I}_4^2} \sigma_{Hill}(\bar{I}_4) + \frac{1}{2\bar{I}_4} \frac{d\sigma_{Hill}(\bar{I}_4)}{d\bar{I}_4} \right) (\mathbf{F}^\top \mathbf{H} + \mathbf{H}^\top \mathbf{F}) : \mathbb{M}_0 : (\mathbf{F}^\top \mathbf{H} + \mathbf{H}^\top \mathbf{F}). \end{aligned} \quad (5.8.16)$$

If in particular,  $\mathbf{H} = \mathbf{a}_0 \otimes \mathbf{a}_0$  (one of the many possible choices in Definition 5.2), we first have:

$$\mathbf{a}_0 \otimes \mathbf{a}_0 : \mathbf{H}^\top \mathbf{H} = \|\mathbf{a}_0\|^6. \quad (5.8.17)$$

Furthermore, assuming (for example) incompressible uniaxial stretch for  $\mathbf{F}$ , that is,

$$\mathbf{F} = \begin{bmatrix} \lambda_u & 0 & 0 \\ 0 & 1/\sqrt{\lambda_u} & 0 \\ 0 & 0 & 1/\sqrt{\lambda_u} \end{bmatrix}, \quad (5.8.18)$$

for a given stretch  $\lambda_u > 0$ , we have

$$\mathbf{F}^\top \mathbf{H} + \mathbf{H}^\top \mathbf{F} = \begin{bmatrix} 2\lambda_u a_{0,1}^2 & (\lambda_u + 1/\sqrt{\lambda_u}) a_{0,1} a_{0,2} & (\lambda_u + 1/\sqrt{\lambda_u}) a_{0,1} a_{0,3} \\ (\lambda_u + 1/\sqrt{\lambda_u}) a_{0,1} a_{0,2} & (2/\sqrt{\lambda_u}) a_{0,2}^2 & (2/\sqrt{\lambda_u}) a_{0,2} a_{0,3} \\ (\lambda_u + 1/\sqrt{\lambda_u}) & (2/\sqrt{\lambda_u}) a_{0,2} a_{0,3} & (2/\sqrt{\lambda_u}) a_{0,3}^2 \end{bmatrix}. \quad (5.8.19)$$

Defining  $\mathbf{Z} := \mathbf{F}^\top \mathbf{H} + \mathbf{H}^\top \mathbf{F}$ , we obtain for the contraction with the fourth order tensor in (5.8.16) that:

$$\mathbf{Z} : \mathbb{M}_0 : \mathbf{Z} = \mathbb{M}_0 : \mathbf{Z} \otimes \mathbf{Z} = a_{0,I} a_{0,J} a_{0,K} a_{0,L} Z_{IJ} Z_{KL} = 8\lambda_u^2 + 8\sqrt{\lambda_u} + \frac{20}{\lambda_u} =: v(\lambda_u), \quad (5.8.20)$$

assuming that muscle is (for example) of parallel architecture, i.e.  $\mathbf{a}_0 = \langle 1, 0, 0 \rangle$ . In this case,

$$D_{\mathbf{F}}^2 W(\mathbf{F}).(\mathbf{H}, \mathbf{H}) = \left( \frac{1}{\bar{I}_4} - \frac{v(\lambda_u)}{2\bar{I}_4^2} \right) \sigma_{Hill}(\bar{I}_4) + \frac{v(\lambda_u)}{2\bar{I}_4} \frac{d\sigma_{Hill}(\bar{I}_4)}{d\bar{I}_4}. \quad (5.8.21)$$

Because of the assumed muscle architecture, we may consider  $\bar{I}_4 \approx \lambda_u^2$ . In this case, the first term is negative for physiologically relevant values of  $\lambda_u$  (for instance,  $0 < \lambda_u < 2$ ), while the second term is negative along the descending limb of the total force-length curve (see Figure 3.1). By Lemma 5.4, we cannot guarantee the polyconvexity of  $\Psi_{fibre}$ .

This lack of polyconvexity can directly hinder the convergence of the algorithm at all for certain types of simulations. Indeed, not having the ellipticity condition (5.8.13) can be a sign that the bilinear form associated to the (1,1) block of the tangent matrix in (5.6.15) may not be coercive whenever the simulations take place along the descending limb of the force-length curve. In fact, ascending limb computations will not suffer from this lack of coercivity, as we will see in Section 6.4. A full numerical analysis which accounts for the lack of polyconvexity is outside the scope of this thesis.

### 5.8.3 Solution of the discretized linear system

When the linear system (5.6.15) is discretized using the finite element (5.8.1), the tangent matrix is symmetric, which allows us to use iterative methods such as conjugate gradient. However, for small problems, a direct solver such as UMFPACK can also be used.

We omit details of the discretization as this will be solved using the C++ finite element library *deal.II* [7]. In this case, the system as written in (5.6.15) is sufficient to begin a computational implementation. This will be the focus of the next chapter.

## Chapter 6

# Flexodeal: a new finite-element framework for studying musculoskeletal dynamics

**Flexodeal** is a new finite-element framework developed during this research project. It aims to be a research software for the study of 3D skeletal muscle deformation in a fully dynamic regime (with quasi-static deformations provided as an option as well). Some elements are based on previous codes developed by the Neuromuscular Mechanics Laboratory at Simon Fraser University, but they have been significantly restructured. **Flexodeal** is completely open-source and licensed under the same conditions as deal.II (GNU Lesser General Public License, version 2.1 [7]). It is freely available at:

[https://github.com/sfu-nml/flexodeal.](https://github.com/sfu-nml/flexodeal)

Using deal.II as a base library, **Flexodeal** implements an object-oriented C++ solver for the elastodynamic problem (5.4.1) based on user-defined material properties, boundary conditions, and other parameters of physiological relevance, such as activation profiles. It assumes that the muscle-tendon unit (MTU) can contain a combination of muscle, aponeurosis, and tendon tissues, each one of them admitting both a fibre and a base material contribution. In addition, muscle tissue is allowed to have a user-defined fraction of intramuscular fat, which is implemented according to Section 5.2.3. Given that the complexity of the tissue models can easily overtake many of the numerical aspects of this solver, we have also implemented a “lite” version of this software, which can be used as a tool to further develop the numerical methods used in of skeletal muscle deformation. We have called this code **Flexodeal Lite** and it is freely available at:

[https://github.com/sfu-nml/flexodeal-lite.](https://github.com/sfu-nml/flexodeal-lite)

**Flexodeal Lite** implements the same solver used in **Flexodeal** but in this case, the strain-energy function  $\Psi$  only models muscle tissue as a combination of fibres and base material

with no intramuscular fat (cf. (5.2.3)) or other extracellular tissues (tendinous or extracellular material).

In both cases, two particular challenges arise when implementing a solver for the elastodynamic system (5.4.1):

- (i) the problem is highly nonlinear and potentially non-convex, and
- (ii) the physiological quantities of interest—such as force on a boundary surface or fibre strain rates—are unconventional finite element methods.

In this Chapter, we present details about the computational implementation of **Flexodeal**, including documentation of input and output variables. Furthermore, we present a set of carefully-selected fundamental experiments that can be used as reference points for further modelling and computational developments. These include a combination of dynamic and quasi-static experiments.

We begin in Section 6.1 with some motivation behind these developments. Then, we describe some implementation aspects of **Flexodeal** in Section 6.2. Here, we focus on explaining how the different parameters in the solver are specified, the treatment of boundary conditions, and how to input the fibre activation function. We also discuss how some properties (such as tissue type, fibre orientation, and intramuscular fat fraction) can be prescribed in a space-dependent fashion thanks to the quadrature point logic surrounding deal.II and finite element methods in general. Next, in Section 6.3, we study the computational convergence of the numerical method for the nonlinear problem (5.5.8) in the particular case of the isometric contraction of a pennate block of muscle tissue. These results will be compared with the theoretical statements introduced in Section 5.8. In Section 6.4 we study the force-length relationship of *whole* muscle and discuss its implications on the numerical stability of the finite element method. Furthermore, in Section 6.5, we study the differences in key biomechanical quantities that arise from the consideration of dynamic simulations when compared to more classic quasi-static results. Finally, we show in Section 6.6 the applicability of **Flexodeal** to a more realistic situation in which the finite element mesh is derived from magnetic resonance imaging (MRI), while the activation and prescribed boundary conditions are obtained from an *in vivo* experiment of locomotion.

## 6.1 Motivation

Three-dimensional musculoskeletal simulations have been performed at the Neuromuscular Mechanics Laboratory (Simon Fraser University) for more than 10 years. Early works by Rahemi et al. focused on the effects of space-dependent activation [155] and the distribution of intramuscular fat [156]. Later, a series of articles on muscle energetics were published by Wakeling et al. [196], Ryan et al. [173], and Ross et al. [164]. More recently, Konno et al. studied the inclusion of the extracellular material (ECM) as part of the base material

properties of muscle [102] and the effect of this component in muscle affected by cerebral palsy [103]. Behind all these works, there was a single C++ file based on deal.II’s tutorial “step-44” [145] that was adapted to each research project, refactored to include new features, or simply rewritten. This resulted in a roughly 10,000-line C++ code that included many undocumented and untested features. Moreover, as deal.II continues to evolve, many parts of the original code simply became obsolete. Therefore, there was an urgent need to unify these code developments to ensure extensibility, reproducibility, and to facilitate dissemination of results.

Significant modifications to the original code were required to accommodate the Lagrangian model (5.4.1) used for the fully dynamic simulations. Therefore, we decided to take a more modern approach in terms of software engineering. This included the consideration of: simple but fundamental computational experiments that can be used for testing and debugging, version control (using GitHub), and enough documentation to support future code developments and make this software publicly available. Hence, **Flexodeal** was born. This constitutes the first open-source, 3D nonlinear musculoskeletal simulation tool that includes active anisotropy in a fully dynamic environment. Since this software was developed in a modular framework (facilitated by deal.II), researchers have the opportunity to adapt this code to other expressions of, for instance, force-length and force-velocity relationships, as well as different strain-energy functions for the tissue components.

## 6.2 Implementation details

**Flexodeal** and **Flexodeal Lite** have been implemented similarly to deal.II tutorials, which means they require CMake compilation and a version of deal.II which, in our case, must be at or above v9.3.0. As of the time of writing this document, **Flexodeal** also works with the newest version v9.6.2 [1]. The fibre and base material properties for all tissues are implemented as specified in Chapter 5 of this thesis. For reference, we show in Figure 6.1 the fibre properties implemented in this code.

We now proceed to describe the main inputs required to run **Flexodeal** and the output variables and results that the code produces.

### 6.2.1 Inputs

We use distinct input files to systematically prescribe important variables, such as the boundary strain and activation profiles, as well as the marker locations used for tracking point-valued displacements.

#### 6.2.1.1 Parameter file

Named by default `parameters.prm`, this file provides information about many scalar parameters used in the definition and finite element solution of (5.4.1), such as:

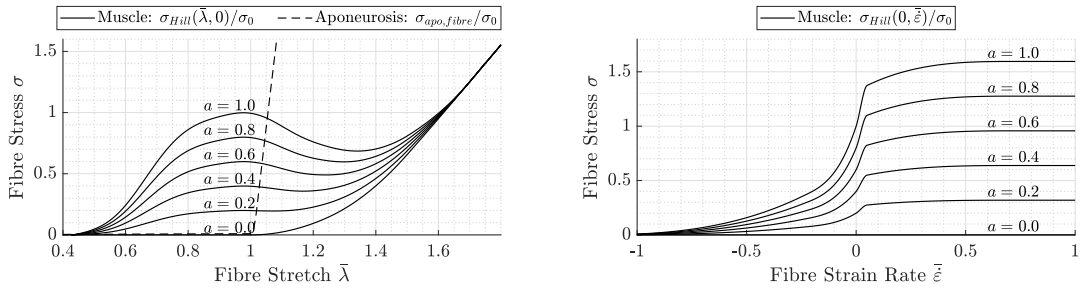


Figure 6.1: Fibre force relationships implemented in **Flexodeal** (muscle and aponeurosis) and **Flexodeal Lite** (muscle only). The code allows for continuously varying activation profiles, but for reference, we choose 6 different choices of activation level (from 0% to 100%) to represent the influence of the activation level on the fibre force.

- Polynomial degree  $k$  in the finite element  $\mathbf{Q}_k \times P_{k-1} \times P_{k-1}$  (5.8.1) used to approximate the solution to the three-field formulation (5.4.1).
- Rule order of the Gaussian quadrature formula used to approximate integrals in the computation of local mass and stiffness matrices, as well as local forcing terms.
- Type of simulation: **quasi-static** or **dynamic**, per Remark 5.5.
- Geometry and meshing parameters required to build the mesh.
- Linear solve information, such as preconditioners (**jacobi** or **ssor**) and solvers: **direct** (which uses the UMFPACK solver), **CG** (conjugate gradient), or **GMRES**.
- Material parameters, such as bulk moduli and the constants defining the Yeoh strain-energy functions (Tables 5.1-5.3) for muscle, tendon, aponeurosis, ECM material, cellular material, and fat tissue.
- Nonlinear solver information, such as the maximum number of nonlinear iterations and tolerances for displacement and force<sup>1</sup>, respectively denoted by **tol<sub>u</sub>** and **tol<sub>f</sub>**. At each time step, numerical convergence of the Newton method is assessed according to the criterion:

$$\|\mathbf{dU}_k^{n+1}\| \leq \mathbf{tol}_u \quad \text{and} \quad \|R(\mathbf{U}_k^{n+1}, p_k^{n+1}, D_k^{n+1})\| \leq \mathbf{tol}_f,$$

where  $\|\mathbf{dU}_k^{n+1}\|$  is the discrete  $\ell^2$  norm of the vector containing the evaluation of the Newton increment for displacement  $\mathbf{dU}_k^{n+1}$  (see Section 5.6.1) at the degrees of freedom (in the finite element sense) of the system and  $\|R(\mathbf{U}_k^{n+1}, p_k^{n+1}, D_k^{n+1})\|$  is the  $\ell^2$  norm of the right-hand side of the linear system of equations (5.6.15).

<sup>1</sup>In this context, force refers to the *forcing* term, i.e. the right-hand side of the linear system of equations (5.6.15).

- Time step size  $\Delta t$  simulation end time  $T$ .
- Label of the boundary surface (also known as “boundary ID”) on which the prescribed strain will be applied (see, for example, Figure 6.7).
- Location of file containing markers (see Section 6.2.1.2).
- Booleans that activate the output of binary files (see Section 6.2.2).

### 6.2.1.2 Prescribed strain and activation profiles

Named by default `control_points_strain.dat` and `control_points_activation.dat`, these files provide respectively information about the time-dependent boundary strain  $\varepsilon_M$  and activation  $a$  profiles. In particular, prescribing the boundary strain implements the following boundary condition for the system of PDEs (5.4.1):

$$\mathbf{u}_D = \begin{cases} \mathbf{0}, & \text{on } \mathcal{S}_{0, \text{fixed}}, \\ L_{\text{mus}} (\varepsilon_M(t) + 1) \hat{\ell}, & \text{on } \mathcal{S}_{0, \text{moving}}. \end{cases} \quad (6.2.1)$$

Here  $\mathcal{S}_{0, \text{fixed}}$ ,  $\mathcal{S}_{0, \text{moving}} \subseteq \Gamma_{D,0}$  are respectively the fixed and moving parts of the boundary  $\Gamma_{D,0}$ ,  $L_{\text{mus}}$  is the initial length of the muscle (as defined in the parameter file), and  $\hat{\ell}$  is the line of action vector, which is set by default to  $\langle 1, 0, 0 \rangle$ .

In these files, information is provided as a space-separated, two-column matrix containing the pairs  $(t_k, \varepsilon_M(t_k))$  (or  $(t_k, a(t_k))$  for activation). The continuous profiles  $\varepsilon_M(t)$  and  $a(t)$  are then constructed via linear interpolation between the provided control points. As shown in Figure 6.2, simple linear profiles can be constructed with a few control points. Since the code allows for an arbitrary number of control points, more involved profiles can be constructed as well (see Section 6.6).

### 6.2.1.3 Markers

Similar to a motion capture experiment, `Flexodeal` allows the user to mark a number of mesh vertices to track their displacement. They can be provided in a space-separated text file which, by default, is named `markers.dat` and their output can be found in the CSV file `displacements-3d.csv`.

### 6.2.1.4 Quadrature point data (not implemented in `Flexodeal Lite`)

In the context of finite element methods, many of the integrals involved in computing element stiffness matrices, mass matrices, and load vectors are not straightforward to evaluate analytically. Since exact integration may not be possible or practical for most element shapes, numerical integration is used to approximate these integrals.

`Flexodeal` uses a Gaussian quadrature rule. The order of this rule (which dictate the amount of QPs in each voxel) is specified in the `parameters.prm` file (see `set Quadrature`

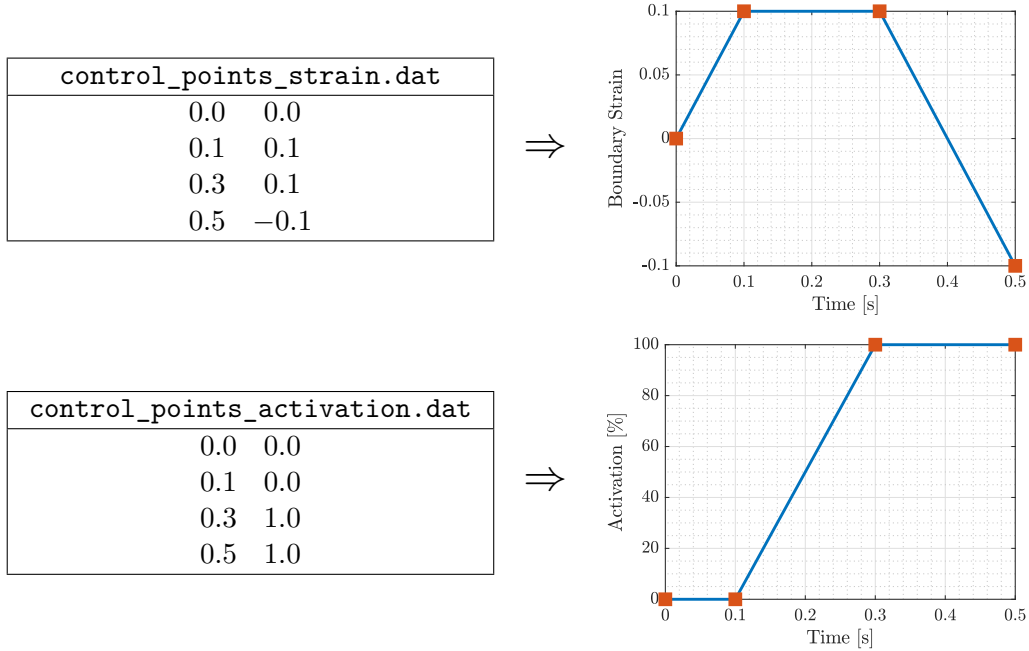


Figure 6.2: An example of the .dat files containing the necessary control points to define time-dependent curve. These particular boundary strain and activation profiles are part of the default experiment in **Flexodeal Lite v1.5.4**.

order in the `Finite element system` subsection). In Table 6.1 we provide a guideline to choose the correct quadrature rule order based on the chosen polynomial degree and whether the simulation is quasi-static or dynamic.

The QP file serves two main purposes: to list all the QPs associated to the current mesh and to attach material properties that might vary in space but not in time. Currently, the following properties are supported:

- Tissue ID (column name: `tissue_id`, SI units: none) which is set to 1 for muscle tissue, 2 for aponeurosis tissue, and 3 for tendon tissue. These IDs are set according to the material ID (also called “physical ID”) of each cell to which a QP belongs. Therefore, the material ID of each cell may be set at the time the mesh is constructed.
- Muscle maximum isometric stress  $\sigma_{0,mus}$  (column name: `max_iso_stress_muscle`, SI units: Pa). Although this quantity (see (5.2.5)) is usually constant throughout muscle tissue (equal to  $\sim 200$  kPa), some experiments might require this quantity to vary depending on fibre types [32].
- Muscle fibre orientation (specified in three columns, `muscle_fibre_orientation_x`, `muscle_fibre_orientation_y`, and `muscle_fibre_orientation_z`, SI units: none), a unit vector indicating the initial orientation of a fibre passing through the QP location.

Polynomial degree	Type of simulation	Quadrature order	QPs per voxel
1	quasi-static	2	8
1	dynamic	2	8
2	quasi-static	3	27
2	dynamic	4	64
3	quasi-static	4	64
3	dynamic	5	125

Table 6.1: Minimum quadrature order required depending on the type of simulation (dynamic or quasi-static) and finite element polynomial degree.

- Fat fraction  $\chi_{fat}$  (column name: `fat_fraction`, SI units: none), the fraction of fat (see (5.2.23)) at the QP location.

**Remark 6.1.** In *Flexodeal Lite*, these properties are implemented as constants throughout the domain and specified via the parameter file `parameters prm`.

## 6.2.2 Outputs

Several variables of physiological interest are readily available in Flexodeal.

### 6.2.2.1 Activation and muscle length

This CSV file (named `activation_muscle_length-3d.csv`) provides the time series  $a(t_k)$  and  $L_M(t_k)$  corresponding respectively to the activation level (in %) and muscle length (in m) at each time step  $t_k$ .

### 6.2.2.2 Displacements at predefined markers

This CSV file (named `displacements-3d.csv`) provides 3D displacement information at the mesh vertices listed in `markers.dat`.

### 6.2.2.3 Energies

This CSV file (named `energy_data-3d.csv`) provides time series for each one of the strain energies (in  $\text{J m}^{-3}$ ) in the system. In what follows,  $|\mathcal{B}_t|$  denotes the volume of the current configuration  $\mathcal{B}_t$ :

- Kinetic energy:

$$E_{kin}(t) = \frac{1}{|\mathcal{B}_t|} \int_{\mathcal{B}_0} \frac{1}{2} \rho_0 |\mathbf{V}|^2 d\mathbf{X}, \quad (6.2.2)$$

- Internal energy:

$$E_{int}(t) = \frac{1}{|\mathcal{B}_t|} \int_{\mathcal{B}_0} (\nabla_0 \mathbf{U}) \mathbf{F}^{-1} \boldsymbol{\tau} d\mathbf{X}, \quad (6.2.3)$$

with  $\boldsymbol{\tau}$  as defined in (5.1.55),

- Volumetric energy:

$$E_{vol}(t) = \frac{1}{|\mathcal{B}_t|} \int_{\mathcal{B}_0} (\nabla_0 \mathbf{U}) \mathbf{F}^{-1} \boldsymbol{\tau}_{vol} d\mathbf{X}, \quad (6.2.4)$$

with  $\boldsymbol{\tau}_{vol}$  as defined in (5.1.56),

- Isochoric energy:

$$E_{iso}(t) = \frac{1}{|\mathcal{B}_t|} \int_{\mathcal{B}_0} (\nabla_0 \mathbf{U}) \mathbf{F}^{-1} \boldsymbol{\tau}_{iso} d\mathbf{X}, \quad (6.2.5)$$

with  $\boldsymbol{\tau}_{iso}$  as defined in (5.1.57),

- Muscle active energy:

$$E_{mus,act}(t) = \frac{1}{|\mathcal{B}_t|} \int_{\mathcal{B}_0} (\nabla_0 \mathbf{U}) \mathbf{F}^{-1} \boldsymbol{\tau}_{mus,act} d\mathbf{X}, \quad (6.2.6)$$

where  $\boldsymbol{\tau}_{mus,act} = \mathbb{P} : \bar{\boldsymbol{\tau}}_{mus,act}$  and  $\bar{\boldsymbol{\tau}}_{mus,act}$  is the active part of the  $\bar{\boldsymbol{\tau}}_{fibre}$  tensor defined in (5.2.8), that is:

$$\bar{\boldsymbol{\tau}}_{mus,act} = \frac{1}{\lambda^2} \sigma_{0,mus} a(\mathbf{X}, t) \hat{\sigma}_A(\bar{\lambda}) \hat{\sigma}_V(\bar{\varepsilon}) \bar{\mathbf{a}} \otimes \bar{\mathbf{a}},$$

- Muscle passive energy:

$$E_{mus,pas}(t) = \frac{1}{|\mathcal{B}_t|} \int_{\mathcal{B}_0} (\nabla_0 \mathbf{U}) \mathbf{F}^{-1} \boldsymbol{\tau}_{mus,pas} d\mathbf{X}, \quad (6.2.7)$$

analogous to the muscle active energy,  $\boldsymbol{\tau}_{mus,pas} = \mathbb{P} : \bar{\boldsymbol{\tau}}_{mus,pas}$  and:

$$\bar{\boldsymbol{\tau}}_{mus,pas} = \frac{1}{\lambda^2} \sigma_{0,mus} \hat{\sigma}_P(\bar{\lambda}) \bar{\mathbf{a}} \otimes \bar{\mathbf{a}},$$

- Aponeurosis fibre energy:

$$E_{apo,fibre}(t) = \frac{1}{|\mathcal{B}_t|} \int_{\mathcal{B}_0} (\nabla_0 \mathbf{U}) \mathbf{F}^{-1} \boldsymbol{\tau}_{apo,fibre} d\mathbf{X}, \quad (6.2.8)$$

with  $\boldsymbol{\tau}_{apo,fibre} = \mathbb{P} : \bar{\boldsymbol{\tau}}_{apo,fibre}$  and  $\bar{\boldsymbol{\tau}}_{apo,fibre}$  as defined in (5.3.7),

- Aponeurosis base material energy:

$$E_{apo,bm}(t) = \frac{1}{|\mathcal{B}_t|} \int_{\mathcal{B}_0} (\nabla_0 \mathbf{U}) \mathbf{F}^{-1} \boldsymbol{\tau}_{apo,bm} d\mathbf{X}, \quad (6.2.9)$$

with  $\boldsymbol{\tau}_{apo,bm} = \mathbb{P} : \bar{\boldsymbol{\tau}}_{apo,bm}$  and  $\bar{\boldsymbol{\tau}}_{apo,bm}$  as defined in (5.3.10),

- Tendon fibre energy:

$$E_{ten,fibre}(t) = \frac{1}{|\mathcal{B}_t|} \int_{\mathcal{B}_0} (\nabla_0 \mathbf{U}) \mathbf{F}^{-1} \boldsymbol{\tau}_{ten,fibre} d\mathbf{X}, \quad (6.2.10)$$

with  $\boldsymbol{\tau}_{ten,fibre} = \mathbb{P} : \bar{\boldsymbol{\tau}}_{ten,fibre}$  and  $\bar{\boldsymbol{\tau}}_{ten,fibre}$  as defined in (5.3.7),

- Tendon base material energy:

$$E_{ten,bm}(t) = \frac{1}{|\mathcal{B}_t|} \int_{\mathcal{B}_0} (\nabla_0 \mathbf{U}) \mathbf{F}^{-1} \boldsymbol{\tau}_{ten,bm} d\mathbf{X}, \quad (6.2.11)$$

with  $\boldsymbol{\tau}_{ten,bm} = \mathbb{P} : \bar{\boldsymbol{\tau}}_{ten,bm}$  and  $\bar{\boldsymbol{\tau}}_{ten,bm}$  as defined in (5.3.10).

Therefore, the computed energies satisfy the additive relationships:

$$E_{int} = E_{vol} + E_{iso}, \quad (6.2.12)$$

and

$$E_{iso} = E_{mus,act} + E_{mus,pas} + E_{apo,fibre} + E_{apo,bm} + E_{ten,fibre} + E_{ten,bm}. \quad (6.2.13)$$

#### 6.2.2.4 Forces

Muscle forces are essential because they represent the active mechanical output generated by muscle fibres and transmitted to the tendon, ultimately enabling joint motion and force application to the skeleton. Therefore, it is of great physiological interest to compute these forces at particular surfaces of the muscle-tendon unit.

The general expression for the force exerted on a surface  $\mathcal{S}_t \subseteq \partial\mathcal{B}_t$  of the body whose current configuration is  $\mathcal{B}_t$  is given by:

$$\vec{F}(t) = \int_{\mathcal{S}_t} \boldsymbol{\sigma} \mathbf{n} ds = \int_{\mathcal{S}_0} J \boldsymbol{\sigma} \mathbf{F}^{-\top} \mathbf{N} dS = \int_{\mathcal{S}_0} \boldsymbol{\tau} \mathbf{F}^{-\top} \mathbf{N} dS. \quad (6.2.14)$$

Here, we have used Nanson's formula (5.1.19)<sub>2</sub> to transform the surface from its current configuration  $\mathcal{S}_t$  to the reference configuration  $\mathcal{S}_0$ . However,  $\boldsymbol{\tau}$  is a quantity that is only available at *interior* quadrature points, so the expression in (6.2.14) can only be *estimated*. In particular, the force at a surface  $\mathcal{S}_0$  is approximated in **Flexodeal** using the last equality in (6.2.14):

$$\vec{F}(t) \approx \sum_{T \in \mathcal{T}_h(\mathcal{S}_0)} \sum_{q=1}^{N_q^\partial} \boldsymbol{\tau}(\tilde{\mathbf{X}}_q, t) \mathbf{F}^{-\top}(\tilde{\mathbf{X}}_q, t) \mathbf{N}(\mathbf{X}_q, t) J_{T \rightarrow \square} w_q, \quad (6.2.15)$$

where  $\mathcal{T}_h(\mathcal{S}_0)$  is a tessellation (made of quadrilaterals) of the surface  $\mathcal{S}_0$ ,  $(\mathbf{X}_q, w_q)_{q=1}^{N_q^\partial}$  is a Gaussian quadrature on the unit square  $\square$  (of the same order as the one used in computing the volume integrals) with points  $\mathbf{X}_q$  and weights  $w_q$ ,  $J_{T \rightarrow \square}$  is the Jacobian of the affine transformation that maps  $T$  into  $\square$ , and  $\tilde{\mathbf{X}}_q$  is the closest interior quadrature point to the surface quadrature point  $\mathbf{X}_q$ .

These forces are written to disk in the files:

`force_data-3d-N.csv` and `force_data-3d.csv`.

The first file exports the force derived from the different Kirchhoff stresses that are computed in the code (e.g.  $\tau$ ,  $\tau_{vol}$ ,  $\tau_{iso}$ , etc.) at each part of the boundary  $\partial\mathcal{B}_0$ , where  $N$  is a suffix used to identify a particular time step. The second file exports the  $x$  component of the force vector  $\vec{F}$  at the boundary ID indicated in the parameter “`set Pulling face ID`” of the parameter file, since this is typically a quantity of interest in lengthening/shortening experiments.

The force  $\vec{F}$  computed in (6.2.14) corresponds to the total force arising from all the material components of the system, that is, using the stress tensor  $\tau$ . To compute individual contributions to this force, we modify the Kirchhoff stress to be used in (6.2.14) and proceed as in the computation of energies. This leads to the following quantities, which are available in all force-related CSV files:

- Volumetric force  $\vec{F}_{vol}$  computed using  $\tau_{vol}$ ,
- Isochoric force  $\vec{F}_{iso}$  computed using  $\tau_{iso}$ ,
- Muscle active force  $\vec{F}_{mus,act}$  computed using  $\tau_{mus,act}$ ,
- Muscle passive force  $\vec{F}_{mus,pas}$  computed using  $\tau_{mus,pas}$ ,
- Muscle base material  $\vec{F}_{mus,bm}$  computed using  $\tau_{mus,bm}$ ,
- Aponeurosis fibre force  $\vec{F}_{apo,fibre}$  computed using  $\tau_{apo,fibre}$ ,
- Aponeurosis base material  $\vec{F}_{apo,bm}$  computed using  $\tau_{bm,fibre}$ ,
- Tendon fibre force  $\vec{F}_{ten,fibre}$  computed using  $\tau_{ten,fibre}$ ,
- Tendon base material force  $\vec{F}_{ten,bm}$  computed using  $\tau_{ten,apo}$ .

Therefore, the following additive relationships hold:

$$\vec{F} = \vec{F}_{vol} + \vec{F}_{iso}, \quad (6.2.16)$$

and

$$\vec{F}_{iso} = \vec{F}_{mus,act} + \vec{F}_{mus,pas} + \vec{F}_{mus,bm} + \vec{F}_{apo,fibre} + \vec{F}_{apo,bm} + \vec{F}_{ten,fibre} + \vec{F}_{ten,bm}. \quad (6.2.17)$$

### 6.2.2.5 Gearing-related information

Gearing refers to the relationship between the muscle’s overall shortening (or lengthening) speed and the shortening (or lengthening) speed of its individual muscle fibres [8, 57]. This is a concept that we discuss in detail in Chapter 7. This file, named `gearing_info-3d.csv`, contains the following information:

- $x$ -component of the prescribed velocity at the moving end of the muscle, computed using the prescribed boundary strain  $\varepsilon_M$  (see Section 6.2.1.2) at each time step  $t_k$  as

$$V_M(t_k) = L_{mus} \frac{\varepsilon_M(t_k) - \varepsilon_M(t_{k-1})}{\Delta t}, \quad (6.2.18)$$

- Mean muscle velocity, computed as:

$$\text{avg}_S(\mathbf{V}_{mus})(t) = \frac{1}{|\text{slab}(\mathcal{B}_t)|} \int_{\text{slab}(\mathcal{B}_0)} \mathbf{V}(\mathbf{X}, t) J(\mathbf{X}, t) d\mathbf{X}, \quad (6.2.19)$$

where

$$\text{slab}(\mathcal{B}_0) := \left\{ \mathbf{X} = (x_1, x_2, x_3) \in \mathcal{B}_0 : \frac{3}{8}L_{mus} \leq x_1 \leq \frac{5}{8}L_{mus} \right\} \quad (6.2.20)$$

is a subregion of the reference configuration  $\mathcal{B}_0$  that removes the ends of the domain (assuming its length runs along the  $x$  direction) to leave out of consideration nonphysical effects that may happen at the Dirichlet boundaries. Naturally, we have  $\text{slab}(\mathcal{B}_t) = \varphi(\text{slab}(\mathcal{B}_0), t)$  where  $\varphi$  is the deformation that maps  $\mathcal{B}_0$  into  $\mathcal{B}_t$ .

- Mean fibre strain rate, computed as:

$$\text{avg}_S(\dot{\varepsilon})(t) = \frac{1}{|\text{slab}(\mathcal{B}_t)|} \int_{\text{slab}(\mathcal{B}_0)} \dot{\varepsilon}(\mathbf{X}, t) J(\mathbf{X}, t) d\mathbf{X}, \quad (6.2.21)$$

where  $\dot{\varepsilon}$  is the fibre strain rate defined in (5.1.45).

### 6.2.2.6 Mean fibre stretch and pennation

These time series are located in the `mean_stretch_pennation_data.csv` file. First, similar to the mean fibre strain rate in (6.2.21), the mean fibre stretch is computed on the region  $\text{slab}(\mathcal{B}_t)$  at each time  $t \geq 0$  according to (5.1.41), that is

$$\text{avg}_S(\lambda)(t) = \frac{1}{|\text{slab}(\mathcal{B}_t)|} \int_{\text{slab}(\mathcal{B}_0)} \lambda(\mathbf{X}, t) J(\mathbf{X}, t) d\mathbf{X}. \quad (6.2.22)$$

We define the pennation  $\beta(\mathbf{X}, t)$  of a muscle fibre passing through  $\mathbf{X}$  in the sense of Lieber & Fridén [113], that is, as the angle between its current orientation  $\mathbf{Fa}_0$  and the muscle's axis of force generation, which we assume to coincide with the line of action vector  $\hat{\ell}$ . Therefore,

$$\beta(\mathbf{X}, t) = \cos^{-1} \left( \frac{\mathbf{a}(\mathbf{X}, t) \cdot \hat{\ell}}{\lambda(\mathbf{X}, t)} \right), \quad \mathbf{a}(\mathbf{X}, t) := \mathbf{F}(\mathbf{X}, t) \mathbf{a}_0(\mathbf{X}). \quad (6.2.23)$$

Furthermore, since we are assuming that  $\hat{\ell} = \langle 1, 0, 0 \rangle$ , we have that the pennation can be computed from the first component of the current orientation vector  $\mathbf{a} = \langle a_1, a_2, a_3 \rangle$ , that

is:

$$\beta(\mathbf{X}, t) = \cos^{-1} \left( \frac{a_1}{\lambda} \right). \quad (6.2.24)$$

The initial pennation angle is denoted by  $\beta_0(\mathbf{X}) = \beta(\mathbf{X}, 0)$ . For  $t > 0$ , the mean pennation angle over the region slab( $\mathcal{B}_t$ ) is therefore given by:

$$\text{avg}_{\text{S}}(\beta)(t) = \frac{1}{|\text{slab}(\mathcal{B}_t)|} \int_{\text{slab}(\mathcal{B}_0)} \beta(\mathbf{X}, t) J(\mathbf{X}, t) d\mathbf{X}. \quad (6.2.25)$$

### 6.2.2.7 Mechanical variables at all QPs (binary files)

These set of files, named

`cell_data_main-3d-N.data` and `cell_data_tensors-3d-N.data`

provide detailed QP information about most of the variables computed in Flexodeal, where  $N$  is a suffix used to identify a particular time step. Each file contains an 2D array with a fixed number of columns and a fixed number of rows, the latter corresponding to the total number of quadrature points in the system. A description of the columns in each one of these files can be found respectively in Tables 6.2 and 6.3.

### 6.2.2.8 VTU files

To visualize the solutions in 3D space, we export several VTU files that can be opened in software such as Paraview or Visio. The main variables (displacement, pressure, and dilatation) are exported at each time step (denoted by the suffix  $N$ ) in the `solution-3d-N.vtu`. These are constructed directly from the DOFs of the finite element solution. In turn, variables that are stored only at quadrature points, such as stresses, fibre stretches, and fibre strain rates, are first projected onto an appropriate finite element space and then exported to VTU format. In particular, at each time step  $N$ , the following files are available:

- `strain_rate-3d-N.vtu` which contains the fibre strain rate field  $\dot{\epsilon}(\mathbf{X}, \cdot)$  computed via projection onto the `FE_DGQ` finite element of order  $k$  (same order as in the displacement finite element). This is a discontinuous element similar to  $P_k$  (see (5.8.1b)) but based on Lagrange polynomials rather than monomials.
- `stress-3d-N.vtu` which contains each of the 9 components<sup>2</sup> of the Kirchhoff stress  $\boldsymbol{\tau}$ , computed via projection onto the `FE_DGQ` finite element of order  $k - 1$ .
- `stretch-3d-N.vtu` which contains the fibre stretch  $\lambda(\mathbf{X}, \cdot)$  as well as the three components of the current orientation vector  $\mathbf{a} = \mathbf{F}\mathbf{a}_0$ , both of them projected componentwise onto `FE_DGQ` elements. In Paraview, this file can also be used to visualize bundles

<sup>2</sup>Technically, only 6 components are required since this is a symmetric tensor.

Column	Variable	Description
1	<code>qp_x</code>	X component of the QP in the reference configuration [m]
2	<code>qp_y</code>	Y component of the QP in the reference configuration [m]
3	<code>qp_z</code>	Z component of the QP in the reference configuration [m]
4	<code>JxW</code>	Dilatation multiplied by the quadrature rule weight at this point
5	<code>det_F</code>	Determinant of the deformation tensor $\mathbf{F}$
6	<code>u1</code>	First displacement component [m]
7	<code>u2</code>	Second displacement component [m]
8	<code>u3</code>	Third displacement component [m]
9	<code>v1</code>	First velocity component [ $\text{m s}^{-1}$ ]
10	<code>v2</code>	Second velocity component [ $\text{m s}^{-1}$ ]
11	<code>v3</code>	Third velocity component [ $\text{m s}^{-1}$ ]
12	<code>p</code>	Pressure $p$ [Pa]
13	<code>D</code>	Dilatation $D$ [nondim]
14	<code>stretch</code>	Fibre stretch $\lambda$ [nondim]
15	<code>stretch_bar</code>	Modified fibre stretch $\bar{\lambda}$ [nondim]
16	<code>strain_rate</code>	Fibre strain rate $\dot{\varepsilon}$ [nondim]
17	<code>strain_rate_bar</code>	Modified fibre strain rate $\bar{\dot{\varepsilon}}$ [nondim]
18	<code>orientation_x</code>	X component of current fibre orientation
19	<code>orientation_y</code>	Y component of current fibre orientation
20	<code>orientation_z</code>	Z component of current fibre orientation
21	<code>tissue_id</code>	Tissue ID

Table 6.2: Contents of the file `cell_data_main-3d-N.data`.

Column	Variable	Description
1	qp_x	X component of the QP in the reference configuration [m]
2	qp_y	Y component of the QP in the reference configuration [m]
3	qp_z	Z component of the QP in the reference configuration [m]
4	JxW	Dilatation multiplied by the quadrature rule weight at this point
5	det_F	Determinant of the deformation tensor $\mathbf{F}$
6-14	F_i_j	Components of the deformation tensor $\mathbf{F}$
15-23	tau_i_j	Components of the Kirchhoff stress $\boldsymbol{\tau}$
24-32	tau_vol_i_j	Components of the Kirchhoff stress $\boldsymbol{\tau}_{vol}$
33-41	tau_iso_i_j	Components of the Kirchhoff stress $\boldsymbol{\tau}_{iso}$
42-50	tau_muscle_active_i_j	Components of the Kirchhoff stress $\boldsymbol{\tau}_{mus,act}$
51-59	tau_muscle_passive_i_j	Components of the Kirchhoff stress $\boldsymbol{\tau}_{mus,pas}$
60-68	tau_muscle_base_i_j	Components of the Kirchhoff stress $\boldsymbol{\tau}_{bm}$
69	tissue_id	Tissue ID

Table 6.3: Contents of the file `cell_data_tensors-3d-N.data`. Each tensor is stored in row order, that is, the 9 columns contain information of the (1,1), (1,2), (1,3), (2,1), …, (3,2), and (3,3) components.

of individual fibres as streamlines of the vector field  $\mathbf{a}(\mathbf{X}, t)$ , as we do for instance in Figure 6.4.

- `velocity-3d-N.vtu` which contains the velocity field  $\mathbf{V}(\mathbf{X}, \cdot)$ , computed via projection from the stored quadrature-point information onto  $\mathbf{Q}_k$  elements (see (5.8.1a)).

#### 6.2.2.9 Other outputs

For reference, we also export the grid that was used in each experiment as `grid-3d.msh` and the parameters file as `parameters.prm`.

## 6.3 Convergence studies

In this section, we study the convergence of the finite element (FE) approximation of the nonlinear weak formulation (5.5.8) using the spaces described in (5.8.1). In general, we will consider sufficiently refined solutions as “exact” solutions for the error computation. To compare solutions computed using different meshes, we develop a separate code in which we reconstruct the solutions from their QP data using suitable projections. This helps preserve the structure of the core components of Flexodeal. We explain our choices next, before diving into the particulars of the convergence study.

### 6.3.1 Error computation

Let  $(\mathbf{U}_{h_f}, p_{h_f}, D_{h_f})$  and  $(\mathbf{U}_{h_c}, p_{h_c}, D_{h_c})$  be finite element (FE) solutions to the problem (5.4.1) using discretizations  $\mathcal{T}_{h_f}$  and  $\mathcal{T}_{h_c}$ , respectively. We assume that the mesh  $\mathcal{T}_{h_f}$  is finer than  $\mathcal{T}_{h_c}$ , so we may refer to them (and their associated FE solutions) as the “fine” and “coarse” meshes. We are interested in computing

$$\|\mathbf{U}_{h_f} - \mathbf{U}_{h_c}\|_{L^2(\mathcal{B}_0)}, \quad \|p_{h_f} - p_{h_c}\|_{L^2(\mathcal{B}_0)}, \quad \text{and} \quad \|D_{h_f} - D_{h_c}\|_{L^2(\mathcal{B}_0)},$$

at some time  $t > 0$ . Using the pressure field as an example, we notice that

$$\begin{aligned} \|p_{h_f} - p_{h_c}\|_{L^2(\mathcal{B}_0)}^2 &= \sum_{T \in \mathcal{T}_{h_c}} \int_T (p_{h_f}(\mathbf{X}, t) - p_{h_c}(\mathbf{X}, t))^2 d\mathbf{X} \\ &= \sum_{T \in \mathcal{T}_{h_c}} \int_{\square} (p_{h_f}(\mathbf{X}, t) - p_{h_c}(\mathbf{X}, t))^2 J_{T \rightarrow \square} d\mathbf{X} \\ &\approx \sum_{T \in \mathcal{T}_{h_c}} \sum_{q=1}^{N_q^c} (p_{h_f}(\mathbf{X}_q, t) - p_{h_c}(\mathbf{X}_q, t))^2 J_{T \rightarrow \square} w_q, \end{aligned} \quad (6.3.1)$$

where  $(\mathbf{X}_q, w_q)$  are the QPs and weights of the quadrature rule associated to the coarse mesh. Therefore, while the quantities  $p_{h_c}(\mathbf{X}_q, t)$  and  $J_{T \rightarrow \square}$ , and  $w_q$  are available in the binary files that **Flexodeal** exports (see Section 6.2.2.7), we must find a way to compute  $p_{h_f}(\mathbf{X}_q, t)$ , i.e. the *fine* solution at the QPs of the *coarse* mesh. This is performed in four steps:

1. Read the binary file corresponding to the fine solution and store the data in an appropriate structure,
2. Project the data into an evaluable FE solution, that is, solve the problem: find  $\widetilde{p_h} \in L^2(\mathcal{B}_0)$  such that

$$\int_{\mathcal{B}_0} \widetilde{p_h} q d\mathbf{X} = \int_{\mathcal{B}_0} p_{h_f} q_h d\mathbf{X}, \quad \forall q_h \in L^2(\mathcal{B}_0),$$

which is a solvable problem since we have the necessary QP information for  $p_{h_f}$  in the fine solution,

3. Evaluate  $\widetilde{p_h}$  at the QPs of the coarse mesh (using the `VectorTools::point_difference` function from deal.II),
4. Export the results to a CSV file and compute (6.3.1) externally.

In this way, solutions corresponding to different refinements can be computed independent of each other, allowing the user to perform convergence studies *without* modifying the core code of Flexodeal.

### 6.3.2 Isometric contractions

In what follows, we will consider the following definition of an isometric contraction.

**Definition 6.1** (Isometric contraction in the Flexodeal framework). Consider a muscle-tendon unit (MTU) whose current configuration occupies a region  $\mathcal{B}_t \subset \mathbb{R}^3$ . Furthermore, assume this region has a boundary  $\partial\mathcal{B}_t = \Gamma_D \cup \Gamma_N$ , where  $\Gamma_D \cap \Gamma_N = \emptyset$ , and  $\Gamma_D, \Gamma_N$  represent respectively the Dirichlet and Neumann boundaries of the domain. We say that a contraction is *isometric* if the MTU is activated from 0% to a pre-defined maximum activation level  $a_{max}$  over a timespan of  $T$  seconds, subject to the following boundary conditions:

$$\mathbf{u} = \mathbf{0} \quad \text{on } \Gamma_D, \quad \boldsymbol{\sigma} \mathbf{n} = \mathbf{0} \quad \text{on } \Gamma_N,$$

with equivalent Lagrangian boundary conditions when the contraction starts from its initial configuration  $\mathcal{B}_0$ .

Therefore, when  $\Gamma_D$  coincides with the ends of the muscle (as it is our case here), an isometric contraction maintains the (current) length of the MTU constant while allowing the fibres to deform. In this setup, isometric contractions are yet another example of a dynamic contraction for which force-velocity properties are perfectly applicable. After all, strains are nonuniform throughout the muscular structure [25], so velocity changes are expected to happen within. We will discuss these effects in more detail in Section 6.5.

### 6.3.3 Setup

We considered the domain and muscle architecture described in Figure 6.3, which we henceforth refer to as the “muscle block”. We also assumed that the block had dimensions  $L_{mus} = 3$  cm,  $W_{mus} = H_{mus} = 1$  cm and an initial pennation angle of  $\beta_0 = 30^\circ$ . Assuming a constant density of  $\rho_0 = 1,060$  kg m<sup>-3</sup>, the block therefore had a mass of 3.18 g.

We discretized the muscle block by subdividing its length, width, and height into  $2^n$  segments, where  $n \in \mathbb{N}$  is called *grid refinement level* (GRL), which resulted in a mesh with  $2^{3n}$  voxels and  $125 \times 2^{3n}$  quadrature points (a quadrature rule of order 5 was used). In this case, the mesh size is given by the diameter of each voxel, that is

$$h = 2^{-n} \sqrt{L_{mus}^2 + W_{mus}^2 + H_{mus}^2} = 2^{-n} \sqrt{11} \text{ cm.}$$

Therefore, to simplify the presentation, we refer to each mesh according to its GRL rather than to its mesh size  $h$ .

We performed an isometric contraction where the activation was linearly ramped up from 0% at  $t = 0$  s to 100% at  $t = T := 0.2$  s (i.e., over 200 ms). In particular, the fixed ends correspond to the +x and -x faces of the block. The other faces were traction free.

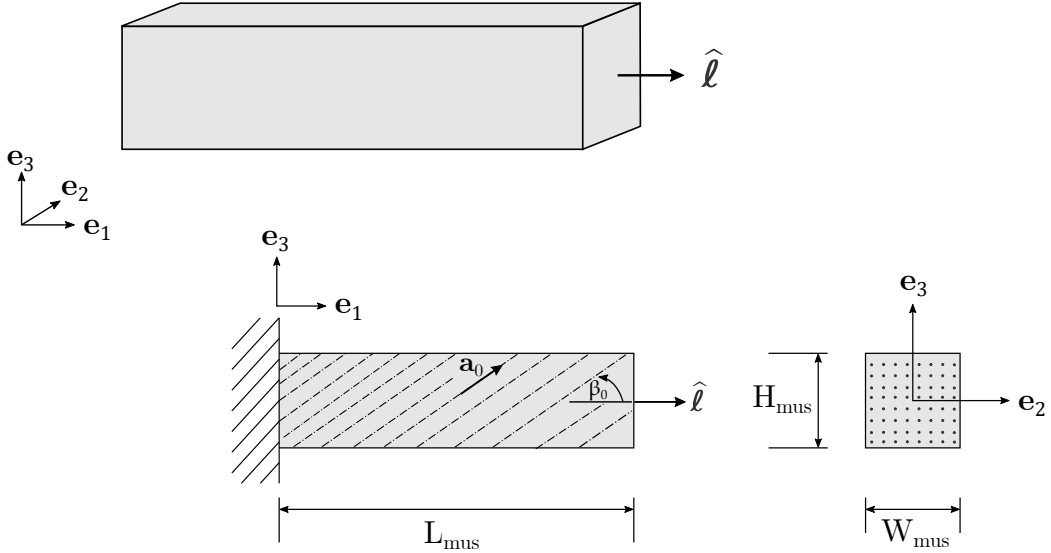


Figure 6.3: Muscle block geometry, including a 3D view (top) and the main quantities that describe the muscle architecture (bottom). In particular, the fibres are parallel to each other and oriented with an initial pennation angle  $\beta_0$  in the  $xz$  plane, which results in an initial orientation field  $\mathbf{a}_0(\mathbf{X}) = \langle \cos(\beta_0), 0, \sin(\beta_0) \rangle$  for any  $\mathbf{X} \in \mathcal{B}_0$ .

To study the convergence in time of the (nonlinear) finite element method, we compute the relative errors:

$$e_{\Delta t}^{\mathbf{U}} := \frac{\|\mathbf{U}_{\Delta t}(\cdot, T) - \mathbf{U}(\cdot, T)\|_{\mathbf{L}^2(\mathcal{B}_0)}}{\|\mathbf{U}(\cdot, T)\|_{\mathbf{L}^2(\mathcal{B}_0)}}, \quad (6.3.2a)$$

$$e_{\Delta t}^p := \frac{\|p_{\Delta t}(\cdot, T) - p(\cdot, T)\|_{L^2(\mathcal{B}_0)}}{\|p(\cdot, T)\|_{L^2(\mathcal{B}_0)}}, \quad (6.3.2b)$$

$$e_{\Delta t}^D := \frac{\|D_{\Delta t}(\cdot, T) - D(\cdot, T)\|_{L^2(\mathcal{B}_0)}}{\|D(\cdot, T)\|_{L^2(\mathcal{B}_0)}}, \quad (6.3.2c)$$

for a fixed GRL = 3 and time step sizes  $\Delta t = 1/(10 \cdot 2^{k+1})$  s,  $k = 1, \dots, 5$ . We compare these approximations  $(\mathbf{U}_{\Delta t}, p_{\Delta t}, D_{\Delta t})$  with a more refined solution  $(\mathbf{U}, p, D)$  computed with  $\Delta t = 1/(10 \cdot 2^8)$  s. For two different time step sizes  $\Delta t, \Delta t'$ , with  $\Delta t > \Delta t'$ , we also compute the rate of convergence as

$$r_t^\star := \frac{\log(e_{\Delta t}^\star / e_{\Delta t'}^\star)}{\log(\Delta t / \Delta t')}, \quad \star \in \{\mathbf{U}, p, D\}. \quad (6.3.3)$$

To study the convergence in space, we compute the relative errors:

$$e_h^{\mathbf{U}} := \frac{\|\mathbf{U}_h(\cdot, T) - \mathbf{U}(\cdot, T)\|_{\mathbf{L}^2(\mathcal{B}_0)}}{\|\mathbf{U}(\cdot, T)\|_{\mathbf{L}^2(\mathcal{B}_0)}}, \quad (6.3.4a)$$

$$e_h^p := \frac{\|p_h(\cdot, T) - p(\cdot, T)\|_{L^2(\mathcal{B}_0)}}{\|p(\cdot, T)\|_{L^2(\mathcal{B}_0)}}, \quad (6.3.4b)$$

$$e_h^D := \frac{\|D_h(\cdot, T) - D(\cdot, T)\|_{L^2(\mathcal{B}_0)}}{\|D(\cdot, T)\|_{L^2(\mathcal{B}_0)}}, \quad (6.3.4c)$$

for a fixed time step size  $\Delta t = 0.01$  s and GRL = 2, 3, 4, and 5. The approximations  $(\mathbf{U}_h, p_h, D_h)$  are compared to a refined solution  $(\mathbf{U}, p, D)$  computed using a GRL = 6. For two different mesh sizes  $h, h'$  (coming in particular from different GRLs), with  $h > h'$ , we compute the associated rates of convergence:

$$r_{\mathbf{x}}^* := \frac{\log(e_h^*/e_{h'}^*)}{\log(h/h')}, \quad * \in \{\mathbf{U}, p, D\}. \quad (6.3.5)$$

The solutions were computed using **Flexodeal Lite** v1.5.1 and a  $Q_2/P_1$  element. The linear systems were solved using a CG solver with a Jacobi preconditioner. Furthermore, the force and displacement tolerances for the nonlinear solver were set to  $10^{-4}$ . We set the quadrature order to 5, which was above the required number of quadrature points according to Table 6.1 to capture forces more accurately. This will be a constant choice throughout this thesis.

### 6.3.4 Main results

In Figure 6.4 we show the experiment performed for this convergence study according to the setup previously described. Furthermore, in Figure 6.5, we portray the corresponding error curves for the study of the dynamic problem. First, we observe from Figure 6.5 (left) that the numerical method converges with rate  $\mathcal{O}(\Delta t)$  (see also Table 6.4), which matches the fact that velocities and accelerations have been discretized using first-order difference formulas. Next, from Figure 6.5 (right), we observe that in the space variables, the displacement converges with rate  $\mathcal{O}(h)$  (in the  $\mathbf{L}^2(\mathcal{B}_0)$  norm), whereas the pressure and dilatation converge with rate  $\mathcal{O}(h^{3/2})$  (see also Table 6.5). These rates are certainly much lower than the  $\mathcal{O}(h^3)$  and  $\mathcal{O}(h^2)$  expected respectively for the linear iterations (see (5.8.7)). Multiple reasons contribute to this phenomenon. As mentioned in Section 5.8.1, the latter are rates that can only be expected for a single Newton iteration and only if the increments are sufficiently smooth (the fact that the muscle architecture is pennate and that the muscle is activated to 100% likely contribute to the lack of smoothness). However, this should not be understood as a failure of the implemented numerical method, but rather as a first (and honest) sign of the true complexity of three-dimensional, dynamic, fully active musculoskeletal simulation.

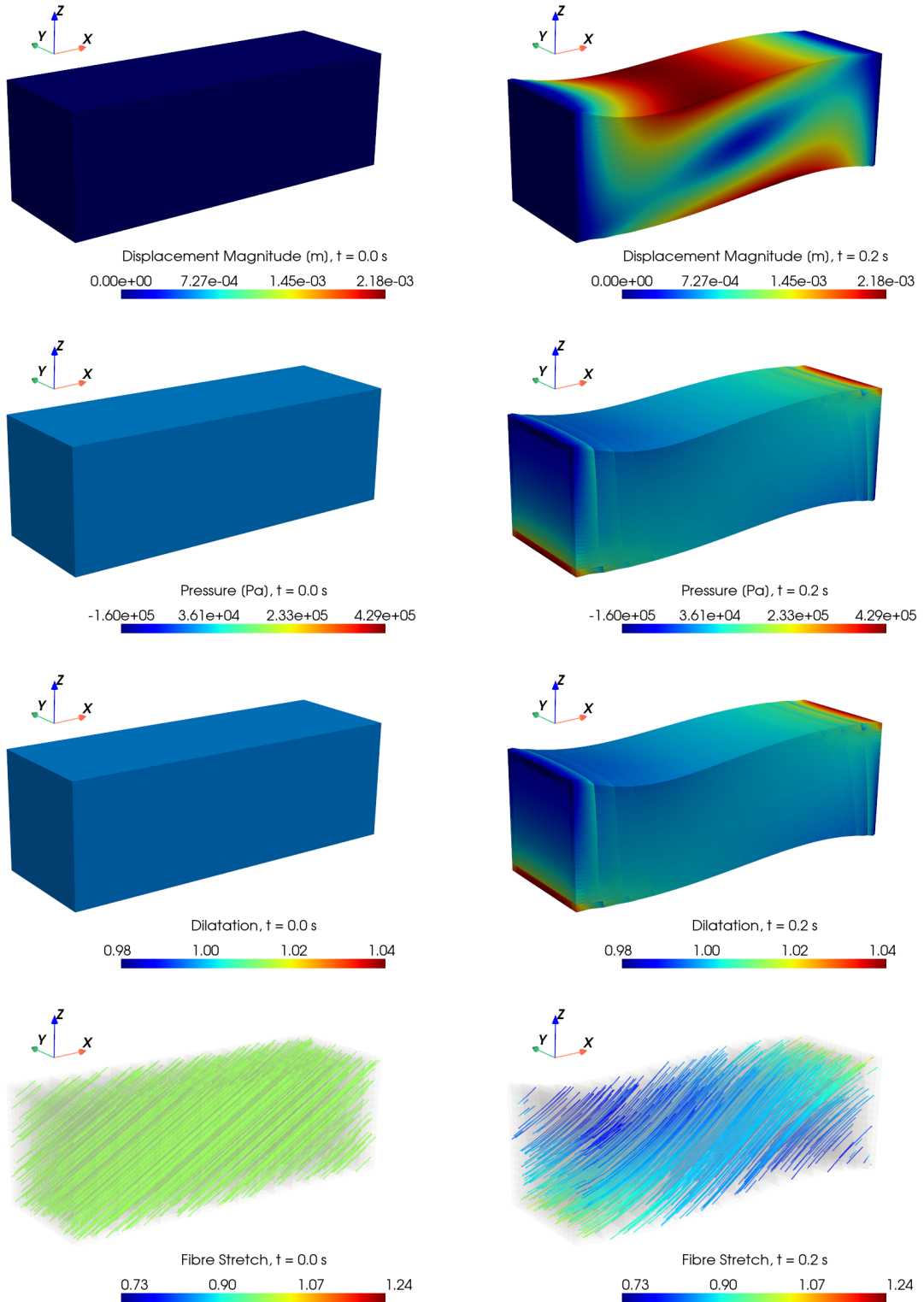


Figure 6.4: Visualization of the displacement  $\mathbf{U}$ , pressure  $p$ , dilatation  $D$ , and fibre stretch  $\lambda$  fields for the convergence study described in Section 6.3. Left column: initial state ( $t = 0.0\text{ s}$ ) showing  $(\mathbf{U}, p, D) = (\mathbf{0}, 0, 1)$  and  $\lambda = 1$ . Right column: end state ( $t = 0.2\text{ s}$ ).

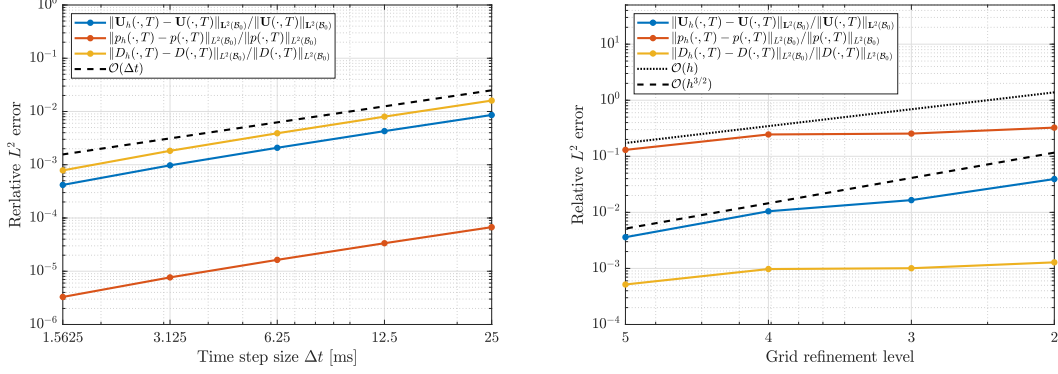


Figure 6.5: Relative  $L^2$  error in the displacement, pressure, and dilatation variables, measured at the end of the simulation time, using a dynamic computation. Left: error as  $\Delta t$  decreases while the grid refinement level is fixed to 3. Right: error as the grid refinement level increases while keeping  $\Delta t = 0.01\text{s}$ .

$\Delta t$ [ms]	$e_{\Delta t}^{\mathbf{U}}$	$r_t^{\mathbf{U}}$	$e_{\Delta t}^p$	$r_t^p$	$e_{\Delta t}^D$	$r_t^D$
25.0000	$8.5965 \times 10^{-3}$	-	$1.6034 \times 10^{-2}$	-	$6.7261 \times 10^{-5}$	-
12.5000	$4.2794 \times 10^{-3}$	1.0064	$8.0023 \times 10^{-3}$	1.0026	$3.3572 \times 10^{-5}$	1.0025
6.2500	$2.0821 \times 10^{-3}$	1.0393	$3.8993 \times 10^{-3}$	1.0372	$1.6359 \times 10^{-5}$	1.0371
3.1250	$9.7413 \times 10^{-4}$	1.0959	$1.8258 \times 10^{-3}$	1.0947	$7.6606 \times 10^{-6}$	1.0946
1.5625	$4.1786 \times 10^{-4}$	1.2211	$7.8361 \times 10^{-4}$	1.2203	$3.2883 \times 10^{-6}$	1.2201

Table 6.4: Errors and convergence rates for  $\mathbf{U}$ ,  $p$ , and  $D$  measured at time  $t = T$  for different time step sizes  $\Delta t$  using a dynamic simulation.

GRL	$h$ [cm]	$e_h^{\mathbf{U}}$	$r_{\mathbf{x}}^{\mathbf{U}}$	$e_h^p$	$r_{\mathbf{x}}^p$	$e_h^D$	$r_{\mathbf{x}}^D$
2	0.2764	$3.9284 \times 10^{-2}$	-	$3.2493 \times 10^{-1}$	-	$1.2835 \times 10^{-3}$	-
3	0.1382	$1.6537 \times 10^{-2}$	1.2482	$2.5413 \times 10^{-1}$	0.3546	$1.0080 \times 10^{-3}$	0.3486
4	0.0691	$1.0461 \times 10^{-2}$	0.6607	$2.4523 \times 10^{-1}$	0.0515	$9.7442 \times 10^{-4}$	0.0489
5	0.0345	$3.6063 \times 10^{-3}$	1.5364	$1.3026 \times 10^{-1}$	0.9128	$5.1693 \times 10^{-4}$	0.9146

Table 6.5: Errors and convergence rates for  $\mathbf{U}$ ,  $p$ , and  $D$  measured at time  $t = T$  for different grid refinement levels (GRL) using a dynamic simulation.

GRL	$h$ [cm]	$e_h^U$	$r_x^U$	$e_h^p$	$r_x^p$	$e_h^D$	$r_x^D$
2	0.2764	$6.3028 \times 10^{-2}$	-	$3.4312 \times 10^{-1}$	-	$1.9951 \times 10^{-3}$	-
3	0.1382	$2.3244 \times 10^{-2}$	1.4391	$2.0698 \times 10^{-1}$	0.7292	$1.2049 \times 10^{-3}$	0.7276
4	0.0691	$7.7435 \times 10^{-3}$	1.5858	$1.7361 \times 10^{-1}$	0.2536	$1.0106 \times 10^{-3}$	0.2537
5	0.0345	$1.9756 \times 10^{-3}$	1.9707	$9.5783 \times 10^{-2}$	0.8580	$5.5747 \times 10^{-4}$	0.8582

Table 6.6: Errors and convergence rates for  $\mathbf{U}$ ,  $p$ , and  $D$  at different grid refinement levels (GRL) using a quasi-static simulation.

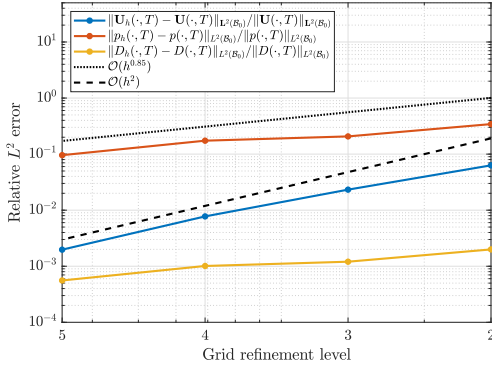


Figure 6.6: Relative  $L^2$  error in the displacement, pressure, and dilatation variables, measured at the end of the simulation time, using a quasi-static computation. Error computed using a fixed time step size  $\Delta t = 0.01$  s.

To complement these calculations, we also performed a convergence study on the quasi-static problem (see Figure 6.6 and Table 6.6), for which convergence rates were not significantly better. Indeed, while the rate of convergence for the displacement variable did improve to  $\mathcal{O}(h^2)$ , the rates for the pressure and dilatation variables decreased to  $\mathcal{O}(h^{0.85})$ .

## 6.4 The force-length relationship of whole muscle

The force-length (FL) relationship describes how the force a muscle can generate depends on its length at the time of contraction. While the overall pattern may remain similar from single fibres to whole muscles, there are important differences that arise due to structural and functional complexity at larger scales. At a single fibre level, the FL relationship is primarily determined by the overlap between actin and myosin filaments. However, at a whole muscle level, the FL relationship includes the effects of the muscle architecture overall (such as the pennation angle) and other components of muscle, such as connective tissues and intramuscular fat. Therefore, the shape of a fibre FL curve does not immediately translate into a whole muscle FL curve. For example, while fibre FL curves for cat soleus muscle do have a descending limb [176, 193], whole muscle FL curves for cat soleus do not [65].

In this section, we examine the FL relationship for whole muscle using **Flexodeal v1.0.1** and **Flexodeal Lite v1.5.1**. This will allow us to examine the force behaviour when multiple

material components of muscle tissue are combined. First, we describe a new domain under consideration and the protocol followed to compute these curves. Then, we describe the obtained results. Finally, we describe the implications of a different (but equally acceptable) protocol and how it relates to the (lack of) polyconvexity of the strain-energy function of the system.

#### 6.4.1 An idealized muscle

In addition to performing experiments using muscle tissue only, we would like to study the behaviour of the system when aponeurosis tissue is included. To accomplish this, we consider an idealized version of a human medial gastrocnemius (MG) previously considered in the work by Ross et al. [164] and others [54, 154]. We will refer to this domain as the “idealized MG”, which we show in Figure 6.7. This configuration in 3D space is characterized by the following parameters:

1. Muscle length  $L_{mus}$ , which is the measure of the muscle, from end to end, along the line of action  $\hat{\ell} = \langle 1, 0, 0 \rangle$ ,
2. Aponeurosis length  $L_{apo}$ , which is measured along the main direction of the aponeurosis layer,
3. Height of the aponeurosis layer  $H_{apo}$ , and
4. Initial pennation angle  $\beta_0$ .

Other parameters shown in Figure 6.7, such as the initial fibre length  $L_f$  and the angle between the aponeurosis layer and the fibres  $\alpha_0$  can be computed from trigonometric relations:

$$\gamma_0 := 180^\circ - \sin^{-1} \left( \frac{\sin(\beta_0)L_{mus}}{L_{apo}} \right), \quad L_f = L_{apo} \frac{\sin(\gamma_0 + \beta_0)}{\sin(\beta_0)}, \quad \alpha_0 = 180^\circ - \gamma_0. \quad (6.4.1)$$

#### 6.4.2 Setup

For this computational experiment, we considered two different geometries:

1. A muscle block geometry (as specified in Figure 6.3) with dimensions  $L_{mus} = 3$  cm,  $W_{mus} = H_{mus} = 1$  cm and an architecture based on parallel-fibred muscle (i.e.  $\beta_0 = 0$ ). In this case, the fibre length coincides with the muscle length  $L_{mus}$ , and therefore the average fibre stretch  $\text{avg}_S(\lambda)$  has magnitude close to the whole muscle stretch  $\lambda_M = L_{mus}(t)/L_{mus}(0)$ . The mesh considered for these experiments had a grid refinement level  $GRL = 4$ , yielding a total of 4,096 voxels (see Figure 6.8 left).

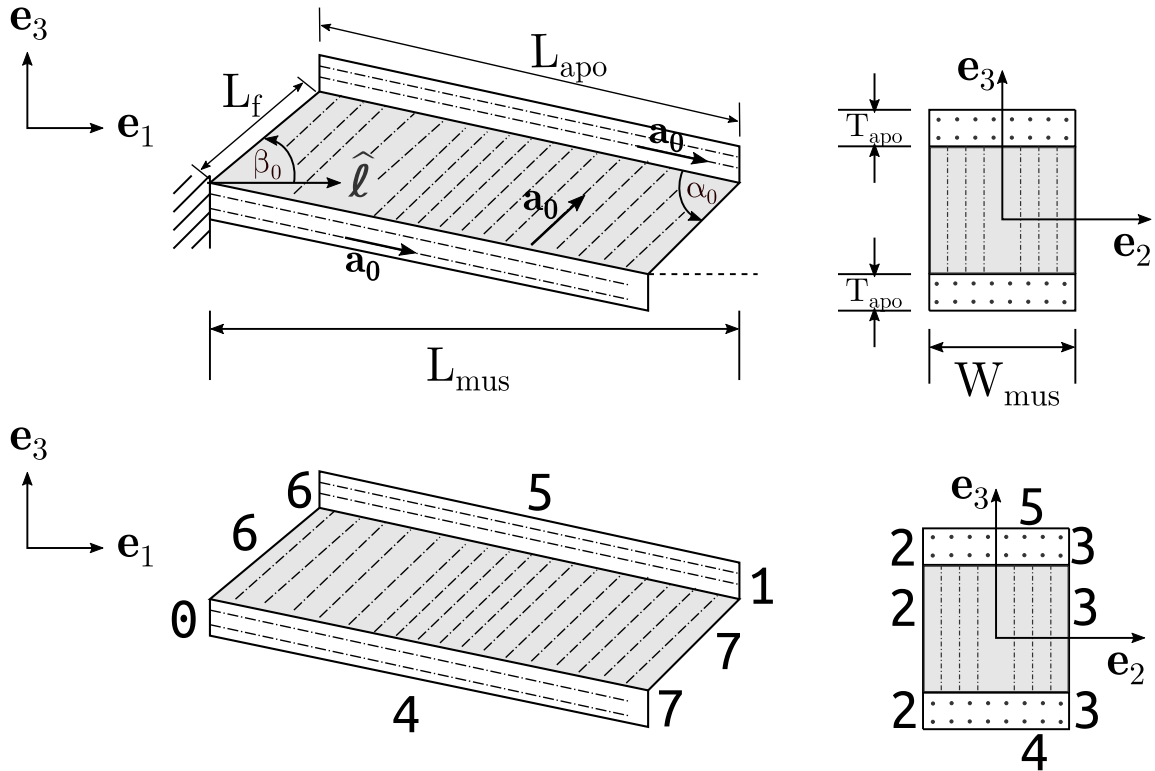


Figure 6.7: Idealization of a medial gastrocnemius muscle according to Ross et al. [164]. Top row: main dimensions describing the muscle architecture. Bottom row: (computational) boundary IDs for each face. The muscle fibres (grey region) run parallel to each other at an angle  $\beta_0$  with respect to the line of action  $\hat{\ell}$ . In turn, the aponeurosis fibres (white regions) run parallel to the longitudinal direction of the aponeurosis. The parameters that define this domain are the muscle length  $L_{mus}$ , aponeurosis length  $L_{apo}$ , aponeurosis height  $H_{apo}$ , muscle width  $W_{mus}$ , and the pennation angle  $\beta_0$ . The muscle fibre length  $L_f$  and angle  $\alpha_0$  can be computed as in Equation (6.4.1).

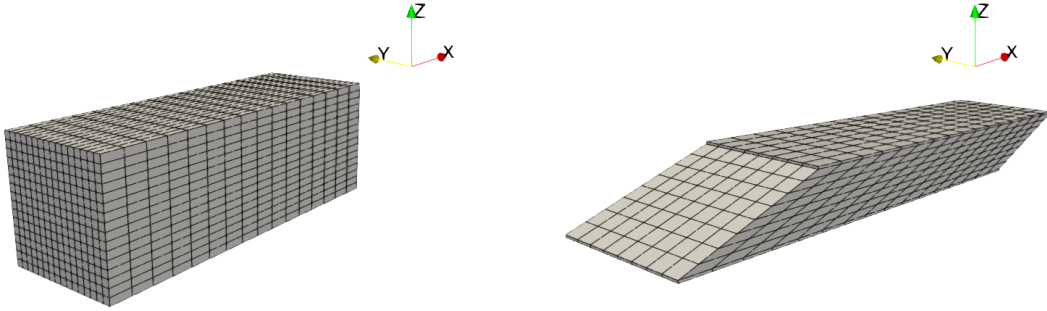


Figure 6.8: 3D view of the meshes used to compute the force-length curves in Figures 6.9 (left) and 6.10 (right). The mesh on the left only contains voxels with muscle tissue. In turn, the mesh on the right, contains voxels of muscle tissue, along with a pair of thin aponeurosis layers on the  $+z$  and  $-z$  faces of this domain.

2. An idealized MG with dimensions  $L_{mus} = 27$  cm,  $L_{apo} = 20.8$  cm,  $H_{apo} = 1$  cm, and an initial pennation angle  $\beta_0 = 15.3^\circ$ . The mesh in this case has 1,280 voxels and is shown in Figure 6.8 right.

For both domains, we set their bulk moduli to  $\kappa_{mus} = \kappa_{apo} = 10^7$  Pa. In the muscle block, the choice of increasing  $\kappa_{mus}$  from a previously used value of  $10^6$  (cf. [164, 173, 196]) was made to keep volume changes under 1%. Furthermore, the choice of reducing  $\kappa_{apo}$  from a previous value of  $10^8$  (cf. [102, 103]) was made to avoid excessive force generation by the aponeurosis. No agreement on the literature exists as to what these values should be (for example, Böll & Reese [30] consider  $\kappa_{mus} = 10^8$  Pa, whereas Blemker et al. [26] consider  $\kappa_{mus} = 10^7$  Pa and  $\kappa_{apo} = 10^8$  Pa), so further research in this area is needed.

In terms of boundary conditions, both geometries had a fixed end and a moving end. The fixed end corresponded to the  $-x$  face for the muscle block geometry and to the face with boundary ID 0 for the idealized MG. In turn, the moving end corresponded to the  $+x$  face in the muscle block and to the face with boundary ID 1 in the idealized MG. All other faces were traction free.

To find the force-length relationship of whole muscle, we first lengthened or shortened each domain from its resting length to a predefined stretch  $\lambda_M = L_{mus}(t)/L_{mus}(0)$  over 0.2 s. Then, we held the muscle in place and performed an isometric contraction in which we linearly increased the activation from 0% to 100% over 0.2 s (the total simulation time was therefore 0.4 s). In real life experiments, after the muscle (or fibre) has achieved its maximum activation level, there is usually a period of time in which the muscle (or fibre) is held at this state until all forces stabilize (see, for example, [65, 83]). In our computational setting, this translated into a series of quasi-static computations that were performed for each value of  $\lambda_M = 0.6, 0.65, 0.7, \dots, 1.6$  and for each one of the two domains. To obtain

quicker results, these experiments were run in the cluster *Cedar* at Simon Fraser University by linking **Flexodeal** (for the idealized MG) and **Flexodeal Lite** (for the muscle block) to deal.II v9.3.1. In all the experiments, the time step size was set to  $\Delta t = 0.01$  s. Experiments with the muscle block geometry were solved using a CG solver and a Jacobi preconditioner, while those with the idealized MG were simply solved using a direct solver (UMFPACK).

### 6.4.3 Results

In Figure 6.9 (top left), we observe the FL relationship for whole muscle when only muscle tissue is present and the scaling factor  $s_{base}$  (appearing as  $s_{bm}$  in (5.2.9)) is equal to 1. First, we notice that for  $\lambda_M > 1$ , the total force resembles the shape of the fibre FL relationship shown in, for example, Figure 6.1. However, this is not the case for  $\lambda_M < 1$  given the presence of compressive stresses, which 1D fibre FL curves do not account for.

The total force represents the aggregate of different components. First, we notice that about 35% of the maximum isometric force (i.e. when  $\lambda_M = 1$ ) comes from volumetric effects (i.e. the strain-energy function  $\Psi_{vol}$ , see (5.2.2)), while 65% comes from isochoric effects. The isochoric force, in this case, is made of the fibre active and passive components, as well as the base material (see Figure 6.9 top right). The proportions in these forces are in line with the results by Wakeling et al. [196], and therefore it is an indication that the material properties have been correctly implemented in Flexodeal.

One interesting fact that we observe from Figure 6.9 (top left) is that the total force still has a region where the slope is negative. Therefore, unlike in the 1D case where adding a base material component led to a FL relationship without a descending limb (see Section 3.3.3), the base material component does not completely convexify the total FL relationship. Naturally, if we artificially increase the contribution of the base material to the overall strain-energy of the system, then the total FL curve does not have a descending limb. We show this in Figure 6.9 (middle and bottom row) where we take  $s_{base}$  factors of 1.5 and 10.

Another way to convexify the FL relationship in 3D is the addition of aponeurosis, as we observe in Figure 6.10. In this case, the force does not have an active component since it has been measured at a face where there is only aponeurosis tissue. We observe from Figure 6.10 (left) that the total force in this domain resembles the force generated by a muscle block when  $s_{base} = 10$  (see Figure 6.9 bottom left). Furthermore, we observe from Figure 6.10 (right) that the aponeurosis base material is the primary contributor to the isochoric force. This could be explained because the base material component of the aponeurosis is significantly stiffer than the one corresponding to muscle tissue. We show the latter for the particular case of uniaxial extension (5.8.18) in Figure 6.11.

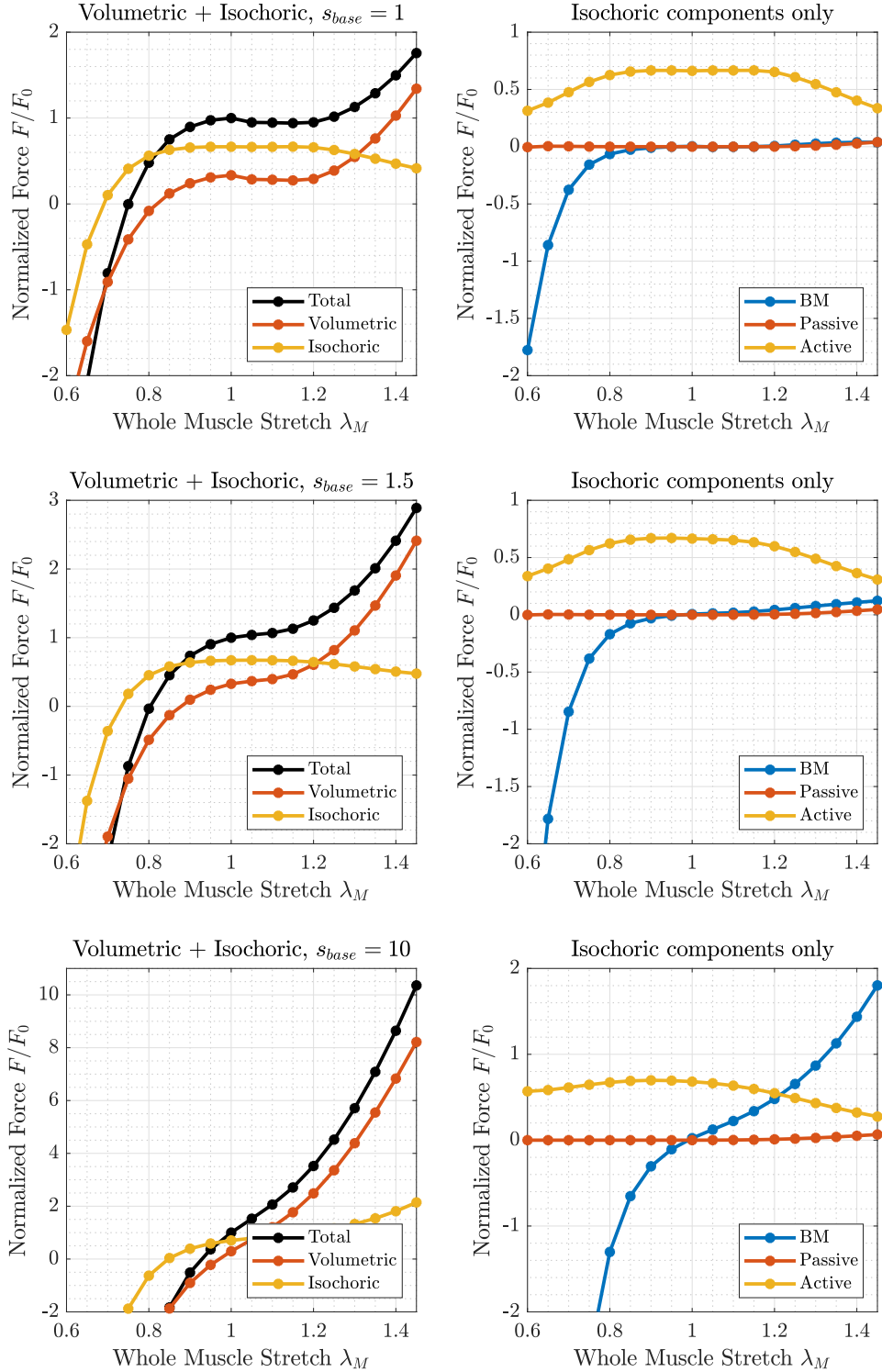


Figure 6.9: Force-length curves of whole muscle computed using **Flexodeal Lite** using a parallel-fibred muscle block geometry and different base material factors:  $s_{base} = 1$  (top row),  $s_{base} = 1.5$  (middle row),  $s_{base} = 10$  (bottom row). Force measured at the  $+x$  end of the domain.

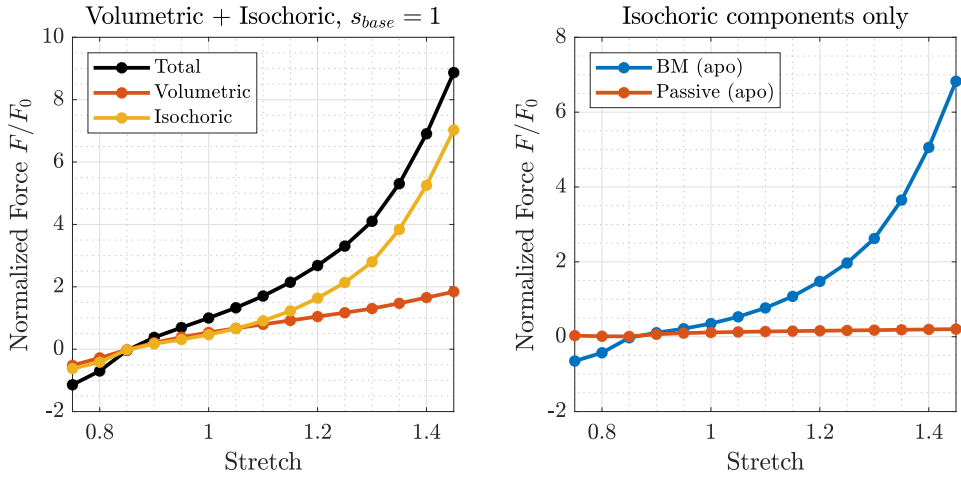


Figure 6.10: Force-length curve of whole muscle computed in **Flexodeal** using the idealized MG described in Figure 6.7 (initial pennation angle  $\beta_0 = 15.3^\circ$ ). Force measured at the face where the moving Dirichlet condition was applied, which also is a face where there is only aponeurosis tissue.

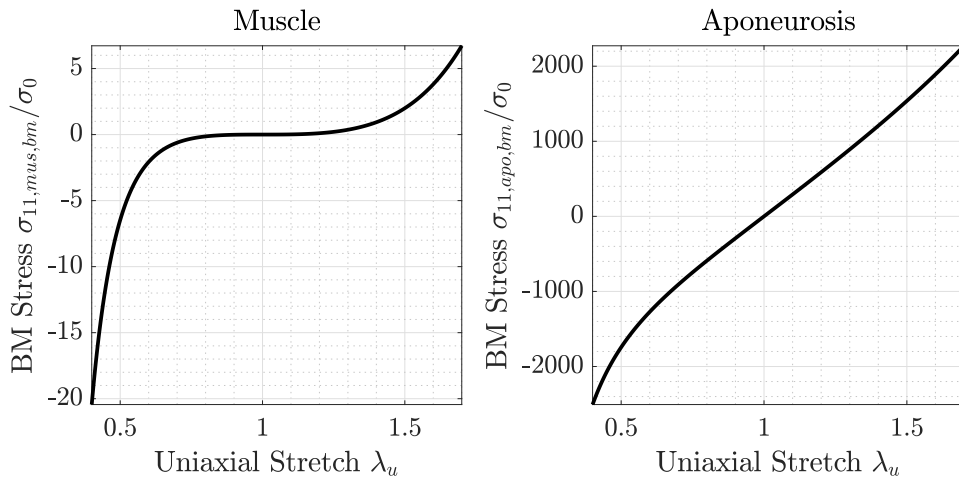


Figure 6.11: Stress-stretch relationships for the base material components of muscle (left) and aponeurosis (right), normalized by their maximum isometric stress  $\sigma_0$ , for the particular case of uniaxial extension.

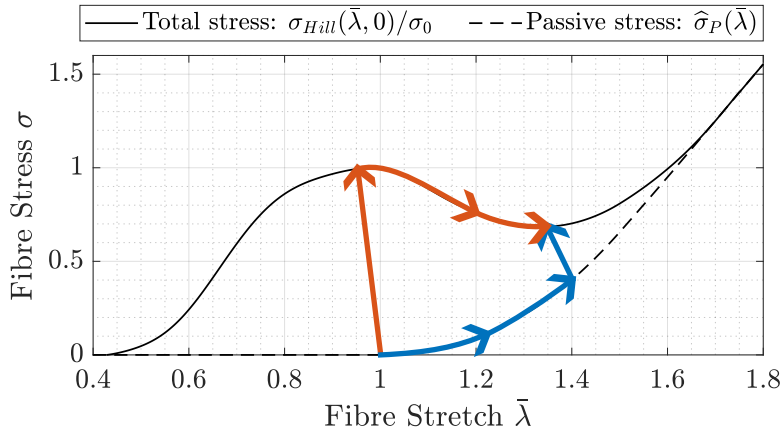


Figure 6.12: Evolution of the active fibre stress when the muscle is passively lengthened and then activated to 100% (blue path) and when the muscle is activated to 100% then lengthened (red path).

#### 6.4.4 Numerical implications of a different protocol involving active lengthening

As described in Section 6.4.2, the experiments in Figures 6.9 and 6.10 have been performed by lengthening or shortening the muscular structure to a predetermined stretch  $\lambda_M$ , then activating the muscle while keeping the ends fixed. Alternatively, one could think about activating the muscle first, and then lengthening or shortening to a desired stretch  $\lambda_M$ . In real muscle, these two protocols lead to different results, especially for  $\lambda_M > 1$ . Activating the muscle and then lengthening introduces residual force enhancement (RFE), commonly attributed to the action of titin (see the discussion in Section 3.3). Therefore, the total (unnormalized) force for  $\lambda_M > 1$  would be greater than the maximum isometric force (so no descending limb). However, in our 3D computational model, titin is not present, so activation and lengthening/shortening are processes whose order is interchangeable. We show these two protocols in Figure 6.12 for the particular case of lengthening.

The performance of the numerical methods along the ascending limb of the fibre FL curve ( $\lambda < 1$ ) is equivalent regardless on whether muscle is activated isometrically or passively shortened first. However, active lengthening along the descending limb (approximately  $1 < \lambda < 1.35$ ) was not possible and the solver would immediately break (with error  $\det(\mathbf{F}) < 0$ ) while solving the first time step after the muscle reached maximum activation. We conjecture that this is caused by the descending limb present in the *whole* muscle FL relationship (see Figure 6.9 top right), which according to the discussion in Section 5.8.2, could lead to a loss of polyconvexity in the strain-energy function of the system, and a consequent loss of coercivity in the finite element system. In fact, these simulations ran successfully when we increased the scaling factor in the base material component of muscle tissue  $s_{base}$  from 1 to 1.5. The latter leads to a completely convex (total) FL curve (see Figure 6.9 middle left).

Given that an alternative (and perhaps, more realistic) way of convexifying the FL curve is by adding aponeurosis to the domain (as seen in Figure 6.10), this also demonstrates the importance of aponeurosis in numerical stability.

The unsuccessful results discuss in this section here should not demotivate users of Flexodeal. For submaximal contractions, and especially for activations lower than 20%, the fibre FL curve *does not* have a descending limb (see Figure 6.1), so active lengthening should not pose a major difficulty. We will show in Section 6.6 a more realistic example in which we combine a domain derived from magnetic resonance imaging (MRI) and experimentally-obtained activation and whole muscle stretch profiles.

## 6.5 The effect of mass and the force-velocity relationship in isometric contractions

The title of this section might sound strange at first to many biomechanists. After all, in the traditional context of a single mass-spring system (i.e. Figure 2.3 Left), if there is no change in the length of the muscle (the isometric condition) then there is no change in velocity, and so force-velocity (FV) properties do not play a role. This idea would also apply to the three-dimensional case *if*, in Definition 6.1, we had included a “holding” step after  $t = T$  seconds, that is, a period of time in which the muscle is held at a fixed length and at a fixed activation until the quasi-static state is achieved (i.e. no accelerations and no velocities). Before reaching this state, however, muscle experiences local deformations with non-negligible velocity. Given that fibres rotate when they are activated [113], fibre strain rates are locally not zero, and therefore FV effects (represented by the term  $\hat{\sigma}_V$  in Equation (5.2.5)) are not necessarily negligible.

In this experiment, we will quantify the differences between quasi-static and dynamic simulations of isometric contractions (in the sense of Definition 6.1). In particular, we will analyze the behaviour of unipennate muscle tissue at different initial pennation angles. We will show that mass and FV effects have a significant impact in several biomechanical quantities, such as muscle force and fibre pennation, stretch, and strain rate, particularly during submaximal contractions.

### 6.5.1 Setup

We considered a block of muscle tissue of dimensions  $L_{mus} = 3$  cm,  $H_{mus} = W_{mus} = 1$  cm as described in Figure 6.3 with unipennate fibre architecture. In particular, we considered different initial pennation angles  $\beta_0 = 0^\circ, 5^\circ, \dots, 30^\circ$ , which correspond to the typical range of pennations found in mammalian muscle (measured at resting length) [113]. For this domain, we constructed a hexahedral mesh with grid refinement level  $GRL = 3$  and we chose a time step size  $\Delta t = 10$  ms. For each muscle architecture, we performed an isometric

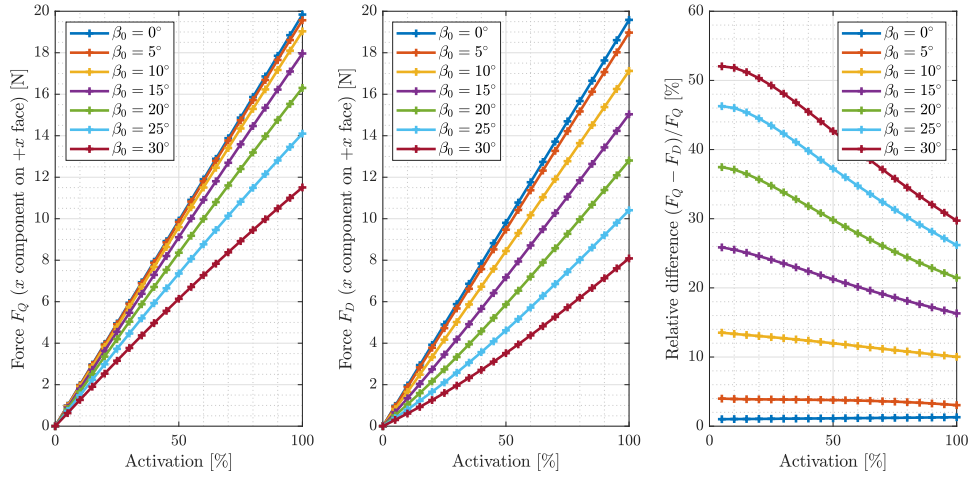


Figure 6.13: Computed force (+ $x$  component on the fixed + $x$  end) using the quasi-static code (left) and the dynamic code (middle) for different initial pennation angles  $\beta_0$ , and the relative difference between them (right).

contraction over 200 ms under fully dynamic conditions and another one under quasi-static conditions, both to a maximum activation level of 100%.

Similar to the convergence study, the solutions were computed using **Flexodeal Lite** v1.5.1 and a  $Q_2/P_1$  element. The linear systems were solved using a CG solver with a Jacobi preconditioner. Furthermore, the force and displacement tolerances for the nonlinear solver were set to  $10^{-4}$ , and the quadrature rule order was set to 5.

### 6.5.2 Main results

We focus our attention on the evolution of four key variables: force, pennation, fibre stretch, and fibre strain rate.

First, in Figure 6.13, we compare the muscle forces obtained from a quasi-static simulation vs. a dynamic one. These are computed according to Equation (6.2.15). The force reported in these figures correspond to the + $x$  component measured on the + $x$  face (which is fixed). In particular, we notice almost no difference between the outputs when muscle has zero pennation (i.e.  $\beta_0 = 0^\circ$ ), and between 30% and 52% relative difference when the muscle tissue has an initial pennation angle of  $\beta_0 = 30^\circ$ . The fact that the differences in force are the largest at low activation levels suggests that these effects arise from the consideration of mass in the system rather than from the FV relationship (according to Hill's stress equation (5.2.5)). These findings confirm that mass effects are more noticeable for submaximal contractions of highly-pennate muscle [196].

Next, in Figure 6.14, we show the evolution of the mean pennation angle over the middle slab of this muscle block, i.e.  $\text{avg}_S(\lambda)$  computed according to (6.2.25). When the muscle is activated, fibres rotate and increase in pennation angle, but these angles seem to be larger

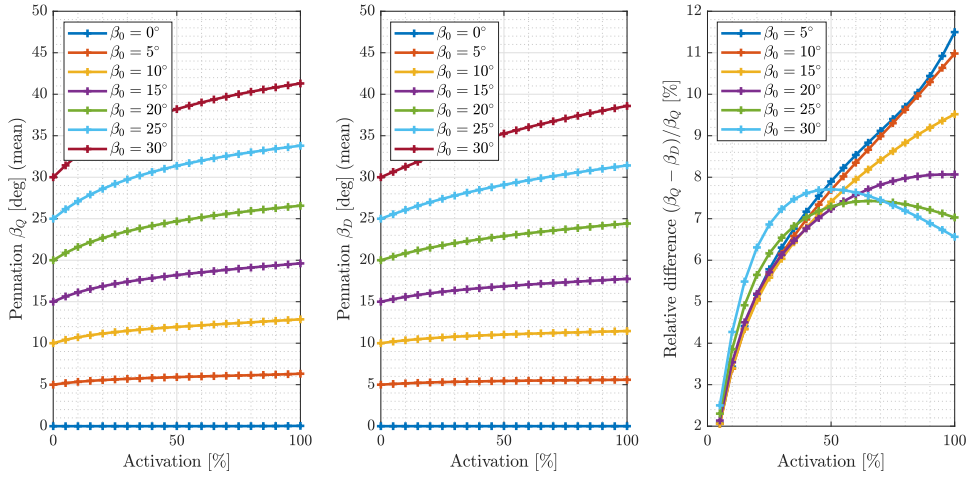


Figure 6.14: Computed mean pennation angle  $\text{avg}_S(\beta)$  using the quasi-static code (left) and the dynamic code (middle) for different initial pennation angles  $\beta_0$ , and the relative difference between them (right).

in the quasi-static simulations than dynamic ones. Nevertheless, up to  $\sim 11\%$  difference is observed when the activation is maximal. Similarly, in Figure 6.15 we show the computed mean fibre stretch  $\text{avg}_S(\lambda)$  according to (6.2.22), which also shows differences of up to 10% at maximal activation, with effects being larger as the initial pennation angle increases.

Finally, we look at the mean fibre strain rate  $\text{avg}_S(\dot{\varepsilon})$ . FV properties are not included in the quasi-static code, and therefore, no fibre strain rates are computed by default (because they are not needed). However, the fibre stretch field  $\lambda(\mathbf{X}, t)$  varies in space and time, so a fibre strain rate could still be computed using, for instance, a first order difference formula. This is how sometimes FV properties are included in quasi-static models (see, for instance, [52]). In particular, Figure 6.16 (left) shows the mean fibre strain rate  $\text{avg}_S(\dot{\varepsilon})$  estimated at each time step  $t_{n+1}$  as

$$\text{avg}_S(\dot{\varepsilon})(t_{n+1}) \approx \frac{\text{avg}_S(\lambda)(t_{n+1}) - \text{avg}_S(\lambda)(t_n)}{\dot{\varepsilon}_0 \Delta t}. \quad (6.5.1)$$

In turn, Figure 6.16 (middle) shows the mean fibre strain rate  $\text{avg}_S(\dot{\varepsilon})$  computed as in (6.2.21). From these results, we observe that fibre strain rate increases with larger pennation (so fibres rotate faster). However, fibre strain rates for an isometric contraction are, in general, expected to be small. Therefore, the fibre strain rates obtained from a quasi-static experiment do not seem to be physiologically reasonable, specially for low activation levels. Indeed, one can attribute this overestimation to the lack of mass in the model, since FV properties do not play a significant role in this case.

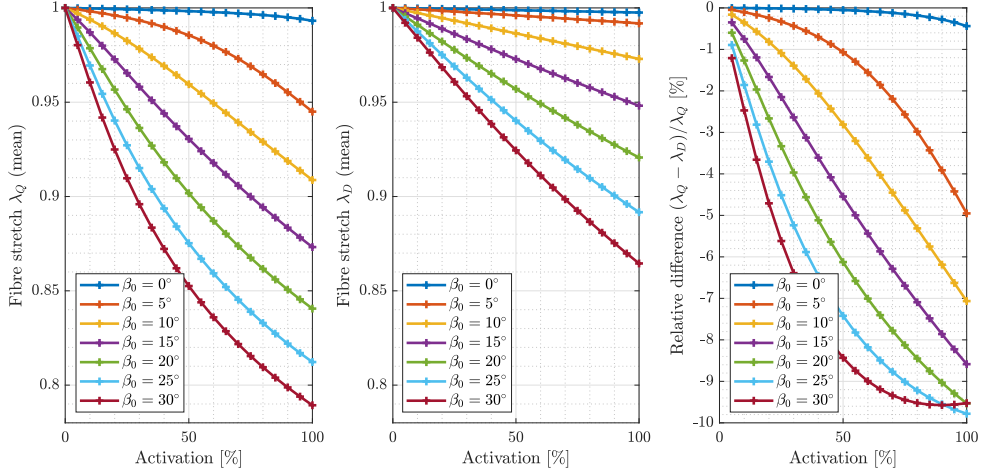


Figure 6.15: Computed mean fibre stretch  $\text{avg}_S(\lambda)$  using the quasi-static code (left) and the dynamic code (middle) for different initial pennation angles  $\beta_0$ , and the relative difference between them (right).

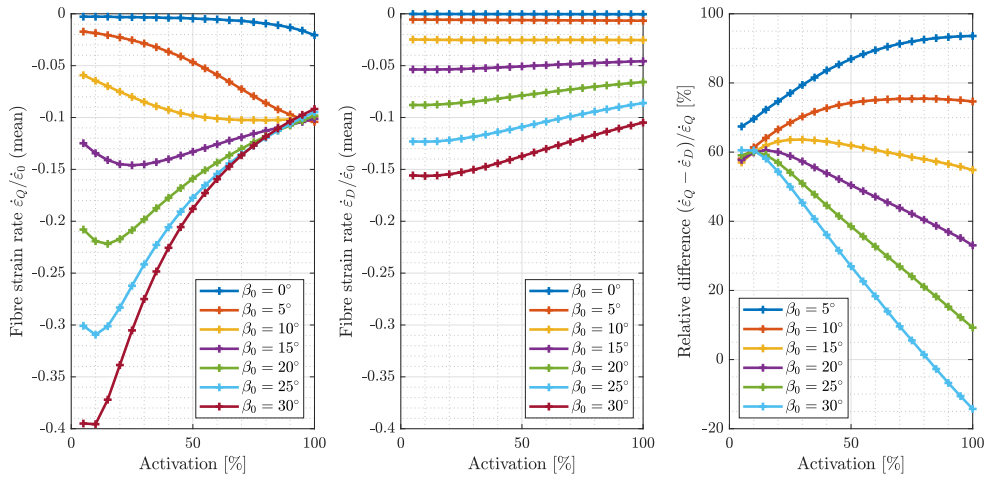


Figure 6.16: Post-processed mean fibre strain rate  $\text{avg}_S(\dot{\varepsilon})$  obtained from a quasi-static computation using mean fibre stretch data (left) and computed mean fibre strain rate using the dynamic code (middle) for different initial pennation angles  $\beta_0$ , and the relative difference between them (right).

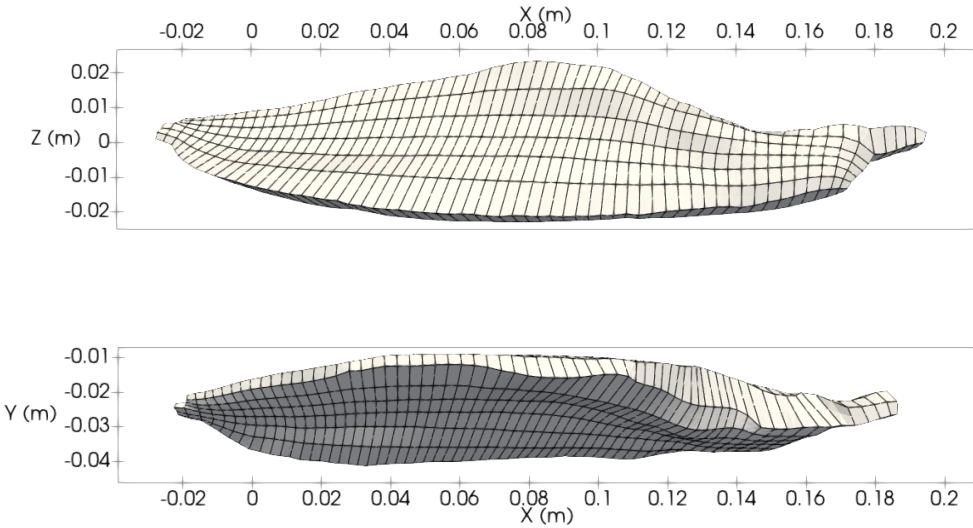


Figure 6.17: Computational representation of the human MG used in Section 6.6 derived from MRI shown in the XZ plane (top) and in the XY plane (bottom).

## 6.6 Deformation of a human medial gastrocnemius during locomotion

In this last experiment, we move one step closer towards the realistic simulation of skeletal muscle deformation. Here, we combined a computational domain based on magnetic resonance imaging (MRI) with motion capture and electromyography (EMG) data obtained from a locomotion study. This constitutes a “proof of concept” of the applicability of **Flexodeal** to subject-specific inputs, which could further lead into the development of digital twins of muscle. This is an active research area that has the potential to provide transformative solutions in healthcare and musculoskeletal simulation in general [51].

### 6.6.1 Setup

We considered a domain based on a human medial gastrocnemius (MG), collected as part of the study by D’Souza et al. [56]. The length of the muscle, as seen in Figure 6.17, was about 22 cm. Moreover, it had a volume of  $126.01 \text{ cm}^3$ , which resulted in a mass of  $133.57 \text{ g}$  (assuming a constant density of  $1,060 \text{ kg m}^{-3}$ ). Neither aponeurosis nor tendon were considered in this computational domain. We also assumed that the muscle had parallel fibres (i.e. zero initial pennation). This is in contrast to a muscle in which fibres do run between aponeurosis layers at a typical pennation of between  $15^\circ$  and  $20^\circ$  [135]. We aligned this domain with the X axis and set  $\hat{\ell} = \langle 1, 0, 0 \rangle$  as the line of action (see Figure 6.17). The hexahedral mesh contained 1,265 voxels.

The locomotion data used for this experiment corresponds to a particular set of traces used in Chapter 2 for the study of 1D mass-enhanced models. In particular, we considered the muscle-tendon unit length and EMG data from the MG of a subject while running. To construct a boundary strain profile, we first estimated the muscle length from the muscle-tendon unit (MTU) length data using the muscle-to-MTU length ratio in Table 2.1. This is equivalent to assuming that the tendon behaved like a strut. Then, we scaled this length so that at time  $t = 0.0$  s, the muscle length matches the one from the computational domain. This profile constituted the boundary condition prescribed on the  $+x$  end of this domain. The  $-x$  end was fixed at all times.

Similarly to the experiments in Chapter 2, we computed the activation profile using Zajac's transfer function (2.2.5) from the available EMG data. This resulted in submaximal activation that did not exceed 30%. For both strain and activation profiles, we selected a representative window of data (of 4.28 seconds) from the complete *in vivo* experiment (about 25 seconds).

The computational experiment was performed under fully dynamic conditions using **Flexodeal** v1.0.1 in a standard desktop computer (Intel i5-9600K, 3.70 GHz, 6 cores, 16 GB of RAM) with a Q2-P1 finite element, a CG linear solver, and a Jacobi preconditioner. Furthermore, we set the time step size  $\Delta t = 0.01$  s. Under these conditions, it took about 23 hours to compute 4.28 s of dynamic deformation.

### 6.6.2 Results

In Figure 6.18, we show the traces of some important quantities in the simulation. In particular, we notice that the muscle was strained at most 3%, purely along the ascending limb of the fibre FL curve. Furthermore, the fibre strain rate was at most 5% of the maximum fibre strain rate ( $5\text{ s}^{-1}$ ) and the pennation increased to at most  $4^\circ$ , consistent with the parallel-fibred nature of the domain we considered. The x-component of the force measured at the moving end never exceeded 15 N. We also examined the volume ratio  $V/V_0$ , which was computed as:

$$(V/V_0)(t) = \frac{|\mathcal{B}_t|}{|\mathcal{B}_0|}.$$

It can be seen from the last row of Figure 6.18 that the change in volume never exceeded 0.1%. This shows that, although compressibility has been introduced in the model (through the dilatation  $D$ ), **Flexodeal** is capable of reproducing essentially incompressible dynamics without the need of imposing  $D = 1$  in the system.

Finally, we show in Figure 6.19 snapshots of the displacement field at particular times: when the muscle is at rest ( $t = 0.0$  s), after a period of isometric contraction ( $t = 0.42$  s), when the muscle is at its shortest ( $t = 2.00$  s), when the muscle is at its longest and at its highest level of activation ( $t = 2.75$  s), and at the end of the simulation ( $t = 4.28$  s).

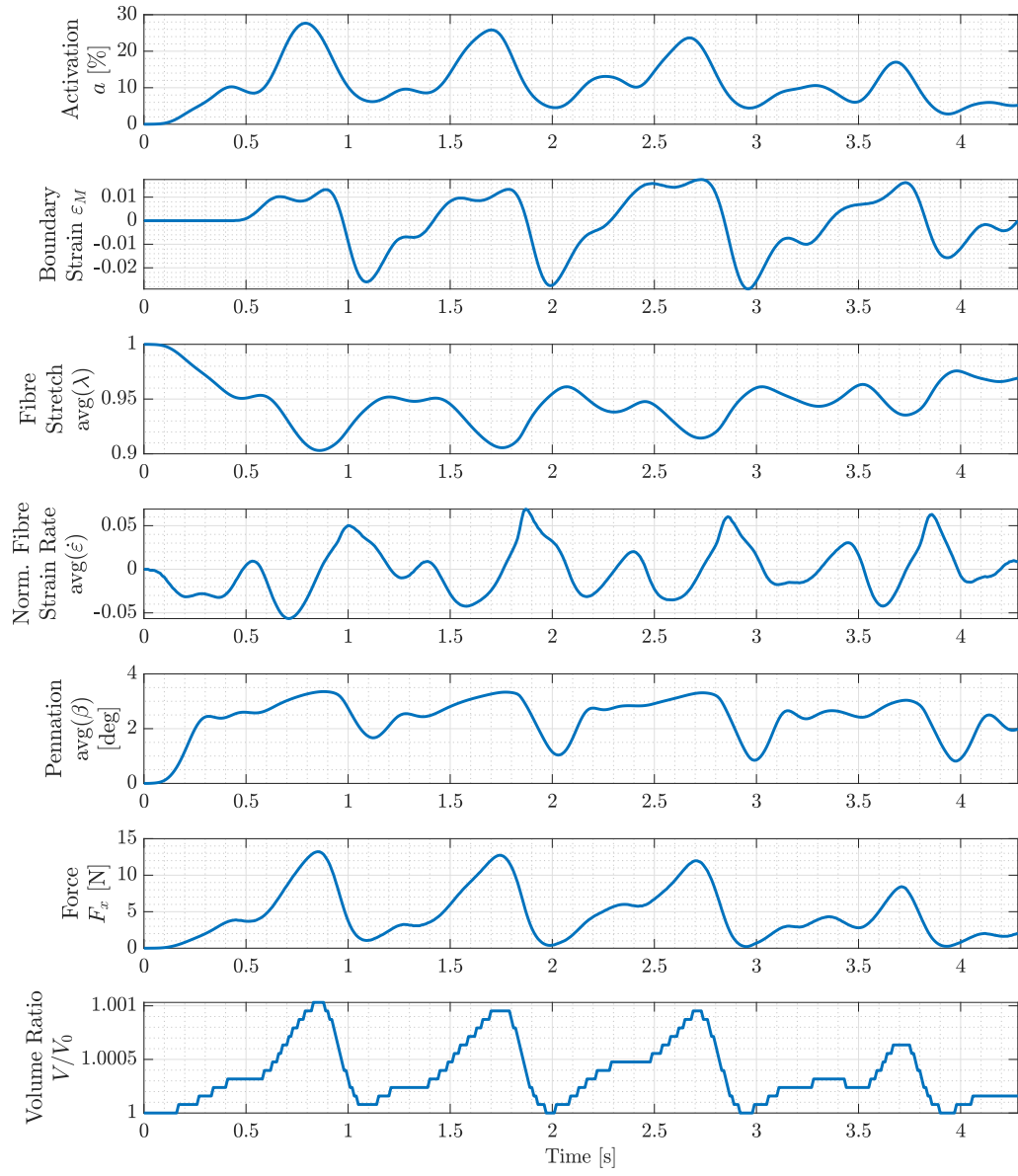


Figure 6.18: Top to bottom: traces of activation, boundary strain, average fibre stretch, average normalized fibre strain rate, average pennation angle, force (x component at the +x end of the domain) and volume ratio, for the experiment described in Section 6.6.

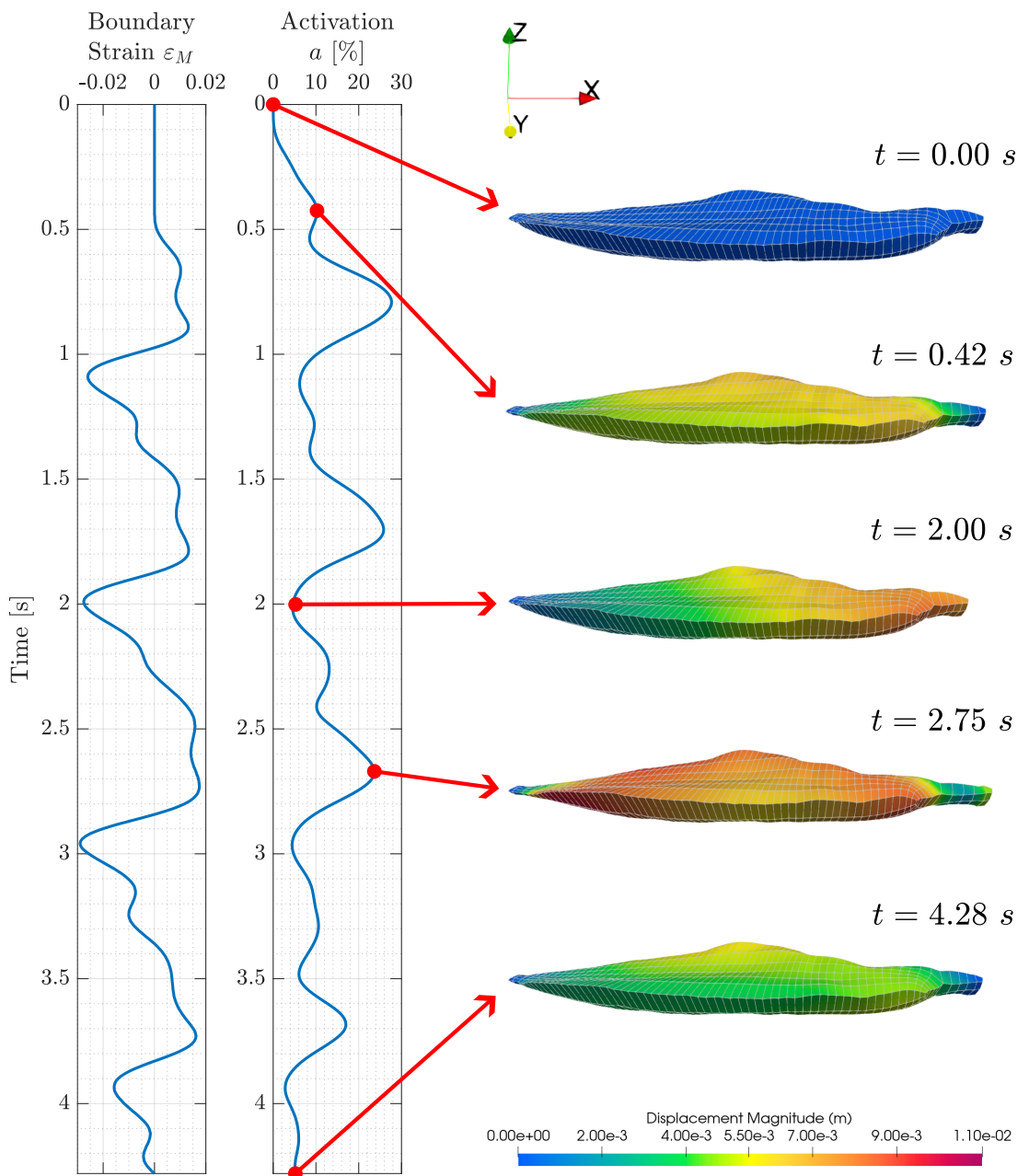


Figure 6.19: Snapshots of the displacement field (magnitude, in m) at five different points of the simulation described in Section 6.6.

# Chapter 7

## Gearing in muscle tissues: a first-of-its-kind computational study

In this chapter, we study *muscle gearing*: a particular mechanism by which fibres in pennate muscle modulate their performance upon contraction. This is an inherently dynamic, three-dimensional phenomenon [162] for which the computation of reliable fibre and muscle velocities is essential. However, there is neither a clear definition of what gearing is in 3D, nor are there robust 3D codes capable of computing it. The framework developed in Chapters 5 and 6 allows us to study this problem from a completely novel perspective that we hope inspires further research in this area.

We begin in Section 7.1 with an introduction to the concept of gearing from a historical perspective, including a discussion on different modelling approaches. Then, in Section 7.2, we explain the computational setup for this problem, which is inspired by an earlier study on rats. We provide a mathematical definition of gearing which captures main physiological ideas and is suitable for our 3D context. Finally, in Section 7.3 we present the results of this study (which have been computed using `Flexodeal Lite`) and discuss their validity and implications on the physiological elements that are necessary to describe gearing.

### 7.1 Introduction

Unlike static architectural descriptors that are typically derived from resting muscle morphology [113], gearing encapsulates the *dynamic* relationship between muscle and fibre velocities during contraction [8, 48]. Muscle gearing represents a fundamental mechanism by which muscles adapt their mechanical output under varying contractile demand [8]. It allows muscles to alter their functional output, shifting between force production and fibre shortening velocity (much like a transmission system in a car or the gears in a bicycle), by modulating fibre orientation and muscle shape [57, 194]. This capacity for variable gearing is particularly important in pennate muscles, since in this case muscle fibres tend to be

shorter and the space in which they can contract is limited by other musculoskeletal elements (such as bones, aponeurosis, or other muscles) [57]. As such, understanding muscle gearing is essential for explaining how muscles adapt their function *in vivo*, and for predicting performance in both healthy and pathological states, particularly during dynamic tasks involving non-isometric contractions.

The idea that fibre and muscle velocities are decoupled from one another has been around for 100 years. In 1925, Beritoff [20] observed from different frog muscles that, as muscle fibres contracted, their pennation angle rose significantly, meaning the fibres did not shorten as much as the overall muscle-tendon unit. These experimental findings were confirmed (and published in English) much later by Muhl [134] in 1982. It was also around this time in the work by Huijing & Woittiez [92] that geometrical arguments were used to explain the relationship between whole muscle length, fibre length, and pennation angle (see also Otten [141], Woittiez & Huijing [202], and Woittiez et al. [203]).

Experimental studies about gearing continue to be carried out in isolated muscle preparations [8, 12, 58, 89], *in vivo* for instance, using ultrasound [28, 48, 158, 194] or micro-computed tomography [106], and using bioinspired actuators, most commonly McKibben actuators [11, 115, 181, 198]. In particular, Wang [198] in 2022 studied the importance of pennation angle and number of contractile units in a Himisk actuator based on experimental testing and finite element simulations of the fluid dynamics within the actuators. To date, no studies in the literature have employed three-dimensional continuum mechanics models of skeletal muscle tissue to investigate muscle gearing.

The term “gearing” was introduced by Brainerd & Azizi [33] in 2005 as “architectural gear ratio” (AGR) and corresponded to the ratio of whole muscle strain to fibre strain. It was studied in aquatic salamanders using sonomicrometry and the results were compared to a geometrical model showing modest resemblance. However, the work of Azizi et al. [8] in 2008 defined gearing as the ratio of muscle *velocity* to fibre velocity, that is:

$$AGR = \frac{\text{muscle velocity}}{\text{fibre velocity}}. \quad (7.1.1)$$

This definition is now agreed upon in the literature due to its functional and physiological importance [150]. In this case, the muscle velocity is measured from a servomotor, whereas fibre velocity is measured independent of the muscle velocity using sonomicrometry. Therefore, the muscle velocity is only measured along the line of action and only corresponds to *whole-muscle* velocity, whereas the fibre velocity is only measured along the direction in which fibres shorten.

The primary goal of this study is to gain insights into gearing via 3D dynamic models, and that using **Flexodeal** is a trustworthy way of doing so by analyzing the qualitative agreement of the outputs with well-established literature results. Furthermore, we would like to explore gearing for a range of activation levels and muscle velocities that are not

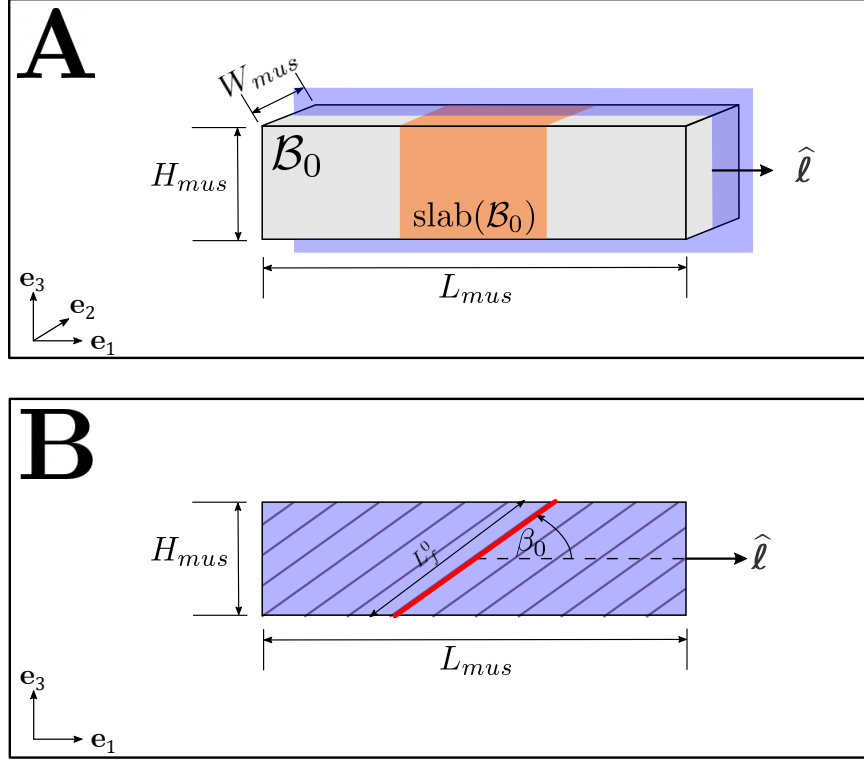


Figure 7.1: (A) Computational domain in its reference configuration  $\mathcal{B}_0$ , which corresponds to a muscle block of dimensions  $L_{mus} \times H_{mus} \times W_{mus}$ , including the line of action vector  $\hat{\ell} = \langle 1, 0, 0 \rangle$  and the region  $\text{slab}(\mathcal{B}_0) \subset \mathcal{B}_0$  (in orange) used to compute average quantities in Section 7.2.4. (B) Sagittal ( $xz$ ) plane showing a representative fibre (red line), and the initial pennation angle  $\beta_0$ .

feasible to perform *in vivo*, *in situ*, or *in vitro*. To do this, we must develop a computational setup that is simple (yet realistic) enough to capture the physics of gearing. This includes the description of an appropriate domain for the nonlinear elastodynamic system (5.4.1) and a testing protocol. Critically, we provide the first definition of gearing as a function of 3D spatio-temporal quantities. This is the main focus of the next Section.

## 7.2 Computational setup and main definitions

In this section, we develop a new setup to study gearing on the basis of the concepts and tools developed in Chapters 5 and 6 of this thesis. Let us first define a domain that captures the main physiological characteristics of a rat medial gastrocnemius.

### 7.2.1 Computational domain and architecture

We considered a block of muscle tissue (see Figure 7.1(A)) with dimensions and architecture that mimicked the average medial gastrocnemius (MG) from a young population of rats, as described by Holt et al. [89]. First, to define an appropriate height  $H_{mus}$ , we notice that the

pennation angle and initial fibre length for this population were  $\beta_0 = 26.1^\circ$  and  $L_f^0 = 15.8$  mm, respectively. Assuming the fibres are oriented parallel to the XZ plane and that  $L_f^0$  corresponds to the longest possible fibre length within the geometry, we set the height of the block to

$$H_{mus} = L_f^0 \sin(\beta_0) = 6.95 \text{ mm.} \quad (7.2.1)$$

This is shown in Figure 7.1(B). Next, Holt et al. [89] report a maximum isometric stress of  $\sigma_0 = 47.9 \text{ N cm}^{-2}$  and a maximum isometric force of  $F_0 = 24.4 \text{ N}$ . We estimate the physiological cross-sectional area (PCSA) at:

$$PCSA = \frac{F_0}{\sigma_0} = 0.509 \text{ cm}^2. \quad (7.2.2)$$

Having computed the height of the block and the PCSA, we compute the width of the muscle block as:

$$W_{mus} = \frac{PCSA \cdot \cos(\beta_0)}{H_{mus}} = 6.58 \text{ mm.} \quad (7.2.3)$$

The average MG in the young rat population had a mass of 0.9 g. Assuming a constant muscle tissue density of  $1,060 \mu\text{g mm}^{-3}$ , we estimate a volume  $V_0 = 849 \text{ mm}^3$ . Therefore, we set the length of the muscle block so that its volume (and therefore its mass) coincides with the average rat MG:

$$L_{mus} = \frac{V_0}{H_{mus} W_{mus}} = 18.6 \text{ mm.} \quad (7.2.4)$$

Finally, given that the initial pennation angle was measured at  $26.1^\circ$ , we set the initial orientation field to

$$\mathbf{a}_0 = \langle \cos(\beta_0), 0, \sin(\beta_0) \rangle = \langle 0.8980, 0, 0.4399 \rangle. \quad (7.2.5)$$

### 7.2.2 Muscle model

We chose the muscle model implemented in **Flexodeal Lite** as described at the beginning of Chapter 6. That is, we consider muscle tissue described as a fibre-reinforced composite material containing a Hill-type fibre contribution:

$$\mathbf{S}_{fibre}(\bar{\lambda}, \bar{\varepsilon}) = \frac{1}{\bar{\lambda}^2} \sigma_0 \left( a(t) \hat{\sigma}_A(\bar{\lambda}) \hat{\sigma}_V(\bar{\varepsilon}) + \hat{\sigma}_P(\bar{\lambda}) \right) \mathbf{a}_0 \otimes \mathbf{a}_0, \quad (7.2.6)$$

and a Yeoh base material contribution:

$$\bar{\mathbf{S}}_{bm} = s_{bm} \sigma_0 \left( 3c_3(\bar{I}_1 - 3)^2 + 2c_2(\bar{I}_1 - 3) + c_1 \right) \mathbf{I}, \quad (7.2.7)$$

where  $\bar{\mathbf{S}}_{fibre}$  and  $\bar{\mathbf{S}}_{bm}$  are the modified second Piola-Kirchhoff (PK2) tensors defined in (5.2.7) and (5.2.10), respectively. Differently from Holt et al. [89], we set the maximum

isometric stress to a more standard value of  $\sigma_0 = 20.0 \text{ N cm}^{-2}$ . Furthermore, we set the scaling factor  $s_{bm} = 1$  and we also assumed that the maximum unloaded fibre strain rate was  $\dot{\varepsilon}_0 = 5 \text{ s}^{-1}$ .

### 7.2.3 Testing protocol

Let  $\dot{\varepsilon}_M^* > 0$  and  $0 < a_{max} \leq 1$  be a prescribed whole-muscle shortening strain rate and a maximum activation level, respectively. The main experiment consisted of the following steps:

1. Starting from its rest state with the  $-x$  face fixed (clamped), passively lengthen the muscle at a speed of  $1 \text{ s}^{-1}$  until it reaches a whole-muscle strain of  $\varepsilon_M = 0.1$  (i.e. 110% of its resting length),
2. Perform an isometric contraction (in the sense of Definition 6.1) where the activation is linearly ramped up to  $a_{max}$  over 0.1 s,
3. Shorten the muscle block at a speed of  $\dot{\varepsilon}_M^*$  (prescribed at the  $+x$  face) until it reaches back its resting length.

The procedure above yields the following boundary condition:

$$\varepsilon_M(t) = \begin{cases} t, & 0 \leq t < 0.1, \\ 0.1, & 0.1 \leq t < 0.2, \\ -\dot{\varepsilon}_M^*(t - T), & 0.2 \leq t \leq T, \end{cases} \quad (7.2.8)$$

where  $T := 0.2 + 0.1/\dot{\varepsilon}_M^*$ , as well as the activation profile:

$$a(t) = \begin{cases} 0, & 0 \leq t < 0.1, \\ 10 a_{max} (t - 0.1), & 0.1 \leq t < 0.2, \\ a_{max}, & 0.2 \leq t \leq T. \end{cases} \quad (7.2.9)$$

Several quantities of interest were measured at the end of the simulation time, including values of mean muscle velocity, mean fibre velocity (necessary to compute gearing), muscle force (x component, at the  $+x$  end of the muscle block), and mean pennation angle, all of them computed as described in Section 6.2.2. We also measured the bulging in the midsection of the muscle block perpendicular to the x-axis by computing, in the current configuration, the distance between the midpoints that defined the width and height of the block in the reference configuration (see Figure 7.2), that is, if  $\mathbf{U} = \langle U_1, U_2, U_3 \rangle$  is the computed displacement vector field, the height  $H_{mus}^T$  and the width  $W_{mus}^T$  in the deformed configuration are given respectively by:

$$H_{mus}^T = H_{mus} + U_3(\mathbf{X}_T, T) - U_3(\mathbf{X}_B, T), \quad (7.2.10)$$

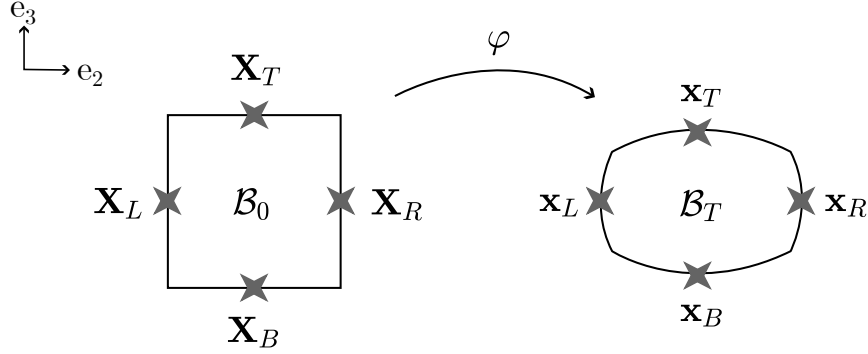


Figure 7.2: Midsection of the muscle block perpendicular to the  $x$ -axis (i.e. the plane that slices the domain at  $x_1 = L_{mus}/2$ ) in the reference configuration  $\mathcal{B}_0$  (left) and in the deformed configuration  $\mathcal{B}_T$  at time  $t = T$  (right). The figure also shows the location of the markers  $\mathbf{X}_L$ ,  $\mathbf{X}_R$ ,  $\mathbf{X}_T$ , and  $\mathbf{X}_B$  in the reference configuration (with their counterparts  $\mathbf{x}_L$ ,  $\mathbf{x}_R$ ,  $\mathbf{x}_T$ , and  $\mathbf{x}_B$  in the deformed configuration) used to compute the muscle thickness and width ( $H_{mus}^T$  and  $W_{mus}^T$ ) at the end of the simulation.

and

$$W_{mus}^T = W_{mus} + U_2(\mathbf{X}_R, T) - U_2(\mathbf{X}_L, T), \quad (7.2.11)$$

where  $\mathbf{X}_L$ ,  $\mathbf{X}_R$ ,  $\mathbf{X}_T$ , and  $\mathbf{X}_B$  are the left, right, top, and bottom midpoints of the muscle block's midsection in the reference configuration (see Figure 7.2).

We implemented this contraction in **Flexodeal Lite** for multiple whole-muscle shortening strain rates  $\dot{\varepsilon}_M^* = 0.5, 1, 2, 3, 4, \dots, 13 \text{ s}^{-1}$  and multiple maximum activation levels  $a_{max} = 0.1, 0.2, \dots, 1.0$ . This resulted in a total of 140 separate computational experiments. Any experiments that result in non-physiological dynamics will be removed. A sample of one of these experiments is portrayed in Figure 7.3 for  $\dot{\varepsilon}_M^* = 2 \text{ s}^{-1}$  and  $a_{max} = 1.0$ . The time step size  $\Delta t$  (in s) was set to:

$$\Delta t = \begin{cases} 0.025, & 0 \leq t < 0.1, \\ 0.0125, & 0.1 \leq t < 0.2, \\ \frac{0.1}{16\dot{\varepsilon}_M^*}, & 0.2 \leq t \leq T, \end{cases} \quad (7.2.12)$$

so that we compute 4 time steps of passive lengthening, 8 time steps of isometric activation, and 16 time steps of active shortening

#### 7.2.4 Gearing in the Flexodeal framework

In real muscle dynamics, neither the muscle velocity nor the fibre velocity are constant, scalar quantities. This is, of course, not the case for the definition given in (7.1.1), so we must define gearing suitably and construct an expression that accounts for 3D variations.

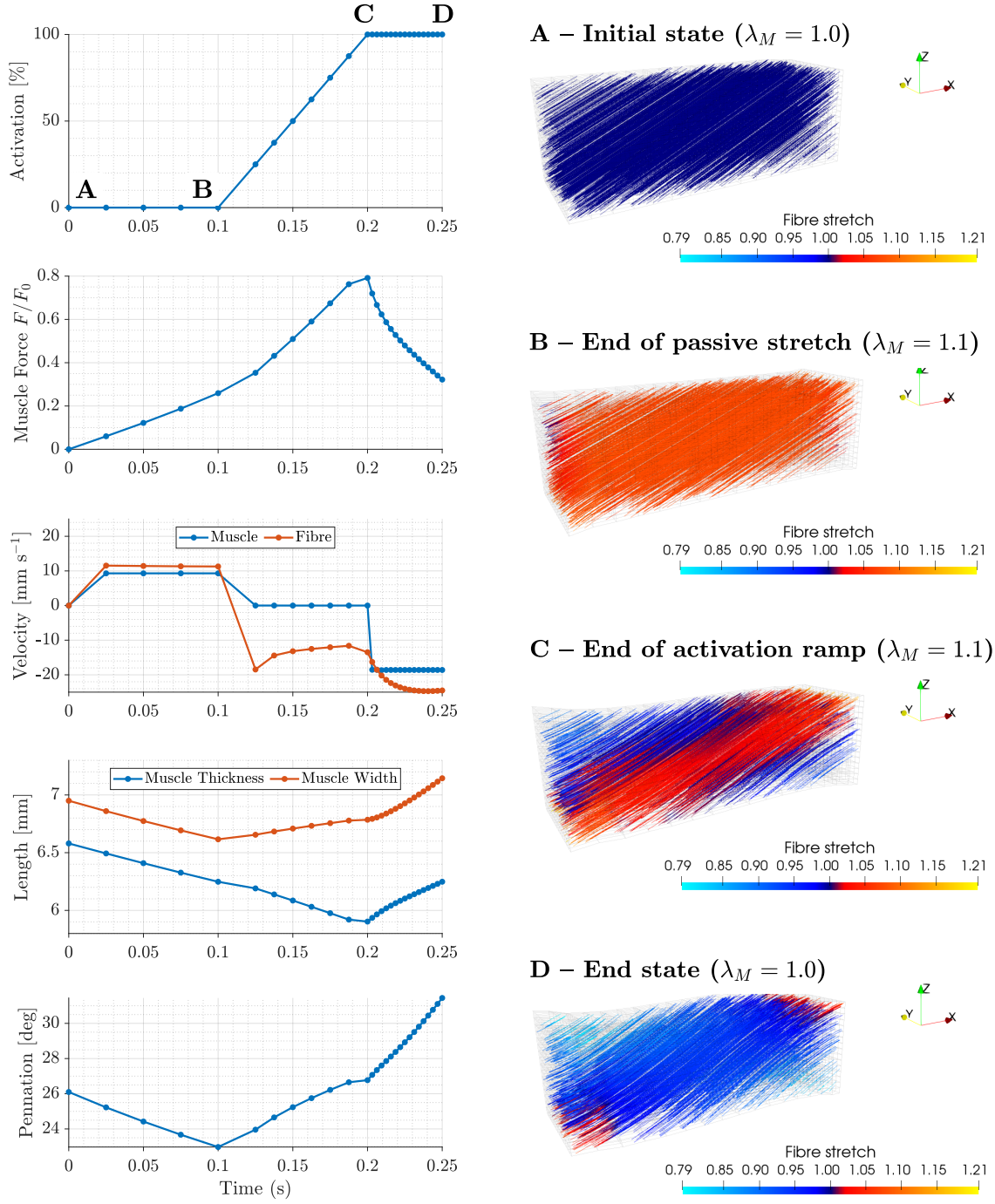


Figure 7.3: Representative computational experiment used to compute muscle gearing ( $\dot{\varepsilon}_M^* = 2 \text{ s}^{-1}$ ,  $a_{max} = 1.0$ ). Left column: Evolution of the activation, muscle force (x component, computed at the  $+x$  face), mean muscle and fibre velocities (averaged over slab( $\mathcal{B}_0$ )), muscle thickness and width, and pennation angle throughout the experiment. Right column: Evolution of the fibre stretch  $\lambda(\mathbf{X}, t)$  at four different times: initial state at  $t = 0 \text{ s}$  (A), end of the passive stretch phase at  $t = 0.1 \text{ s}$  (B), end of activation ramp at  $t = 0.2 \text{ s}$  (C), and end state at  $t = 0.2 + 0.1/\dot{\varepsilon}_M^*$ .

According to this, we define the muscle gearing  $G$  as:

$$G = \frac{\text{Mean Muscle Velocity (MMV)}}{\text{Mean Fibre Velocity (MFV)}} := \frac{-|\text{avg}_S(\mathbf{V})(t = T)|}{L_f^0 \dot{\varepsilon}_0 \text{avg}_S(\dot{\varepsilon})(t = T)}, \quad (7.2.13)$$

where  $|\cdot|$  is the Euclidean norm,  $T$  is the simulation end time (i.e. when the muscle reaches back its resting length according to the previously described protocol), and  $\text{avg}_S(\mathbf{V})(t)$  and  $\text{avg}_S(\dot{\varepsilon})$  are respectively the average (mean) muscle velocity and fibre strain rate in the middle section of the muscle block as described in Section 6.2.2.5, that is:

$$\text{avg}_S(\mathbf{V}_{\text{mus}})(t) = \frac{1}{|\text{slab}(\mathcal{B}_t)|} \int_{\text{slab}(\mathcal{B}_0)} \mathbf{V}(\mathbf{X}, t) J(\mathbf{X}, t) d\mathbf{X}, \quad (7.2.14)$$

and

$$\text{avg}_S(\dot{\varepsilon})(t) = \frac{1}{|\text{slab}(\mathcal{B}_t)|} \int_{\text{slab}(\mathcal{B}_0)} \dot{\varepsilon}(\mathbf{X}, t) J(\mathbf{X}, t) d\mathbf{X}, \quad (7.2.15)$$

where

$$\text{slab}(\mathcal{B}_0) := \left\{ \mathbf{X} = (x_1, x_2, x_3) \in \mathcal{B}_0 : \frac{3}{8} L_{\text{mus}} \leq x_1 \leq \frac{5}{8} L_{\text{mus}} \right\} \quad (7.2.16)$$

(see Figure 7.1(B)) and  $\text{slab}(\mathcal{B}_t) = \varphi(\text{slab}(\mathcal{B}_0), t)$ , with  $\varphi$  the deformation that maps  $\mathcal{B}_0$  into  $\mathcal{B}_t$ . Therefore,  $G > 1$  implies that the speed at which fibres shorten is smaller than the speed at which muscle does, and vice versa if  $G < 1$ . Note that the minus sign in (7.2.13) is to obtain a positive quantity since when the muscle actively shortens, so do the fibres, and therefore we expect that  $\dot{\varepsilon} < 0$ . We also note that, in (7.2.13), one could have alternatively considered the  $x$  component of the velocity field  $\mathbf{V}$ , or even the prescribed muscle velocity at the  $+x$  face as the numerator for  $G$ . However, computing gearing using  $|\mathbf{V}|$  rather than a single component gave better agreement with the values reported in [89], as we will see next.

### 7.3 Results

Of the 140 computational experiments performed, 37 of them were physiologically *not* reasonable since the mean fibre strain rate  $\text{avg}_S(\dot{\varepsilon})$  exceeded 1, that is, the (unnormalized) speed at which fibres were shortening was higher than their maximum unloaded strain rate  $\dot{\varepsilon}_0$ . These experiments were therefore discarded from the study and therefore not shown in any of the Figures presented below.

First, in Table 7.1, we show the full range of prescribed strain rates  $\dot{\varepsilon}_M^*$  (in  $\text{s}^{-1}$ ) and their equivalent in  $\text{mm s}^{-1}$ , which we call the “prescribed (shortening) velocity” and can be computed as  $L_{\text{mus}} \dot{\varepsilon}_M^*$ , where  $L_{\text{mus}}$  is the initial length of the muscle block. Furthermore, we compare these values with the mean muscle velocity (MMV)  $-|\text{avg}_S(\mathbf{V})|$ , where we observe that  $|\text{avg}_S(\mathbf{V})| \approx \frac{1}{2} L_{\text{mus}} \dot{\varepsilon}_M^*$ , which allows us to replace the prescribed strain rate by the MMV as one of the independent variables of the problem (the other one being activation).

Variable (Units)	Values						
PSR ( $\text{s}^{-1}$ )	0.50	1.00	2.00	3.00	4.00	5.00	6.00
PV ( $\text{mm s}^{-1}$ )	9.30	18.60	37.20	55.80	74.40	93.00	111.60
MMV ( $\text{mm s}^{-1}$ )	4.65	9.30	18.60	27.90	37.20	46.50	55.80

Variable (Units)	Values						
PSR ( $\text{s}^{-1}$ )	7.00	8.00	9.00	10.00	11.00	12.00	13.00
PV ( $\text{mm s}^{-1}$ )	130.20	148.80	167.40	186.00	204.60	223.20	241.80
MMV ( $\text{mm s}^{-1}$ )	65.10	74.40	83.70	93.00	102.29	111.58	120.88

Table 7.1: Range of prescribed strain rates (PSR)  $\dot{\varepsilon}_M^*$  at the  $+x$  end of the domain for the shortening phase of the experiment. Each PSR can be multiplied by the initial length of the muscle  $L_{\text{mus}}$  to obtain a prescribed (shortening) velocity (PV). Furthermore, we compare these values with the computed mean muscle velocity (MMV), where we observe  $\text{MMV} \approx \frac{1}{2}\text{PV}$ .

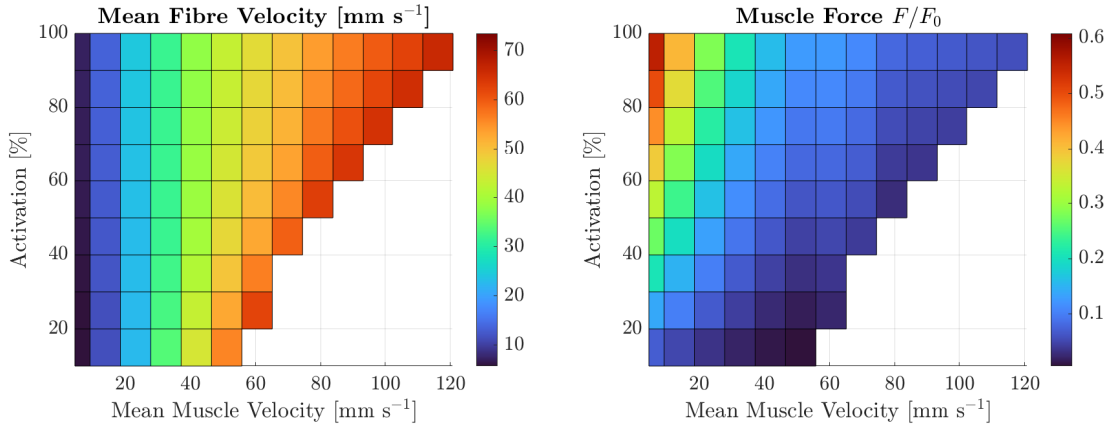


Figure 7.4: Mean fibre velocity (left) and normalized muscle force (right) as functions of MMV and maximum activation (measured at the end of each simulation, i.e. when the muscle block returned to its initial length).

In Figure 7.4, we show how the mean fibre velocity (MFV) and muscle force (x component, measured at the  $+x$  end of the muscle block) vary with activation and MMV. For a given maximum activation level, we observe how MFV increases with increasing MMV at a ratio that is not constant (Figure 7.4 (left)). This is the first indication of variable gearing. Then, in Figure 7.4 (right), we observe how muscle force increases with increasing activation but decreases with increasing MMV, which is expected given the force-velocity relationship of muscle fibres (see, for example, Figure 6.1).

Then, in Figure 7.5 we show the computed (mean) pennation angles and their rates of change, which have been computed from the mean pennation values using a first-order time difference formula. In particular, we observe how as fibres shorten they rotate to higher pennation angles, which is the expected behaviour in pennate muscle [57, 118, 134, 211]. Furthermore, the rate of pennation at which fibres rotate increases with increasing MMV.

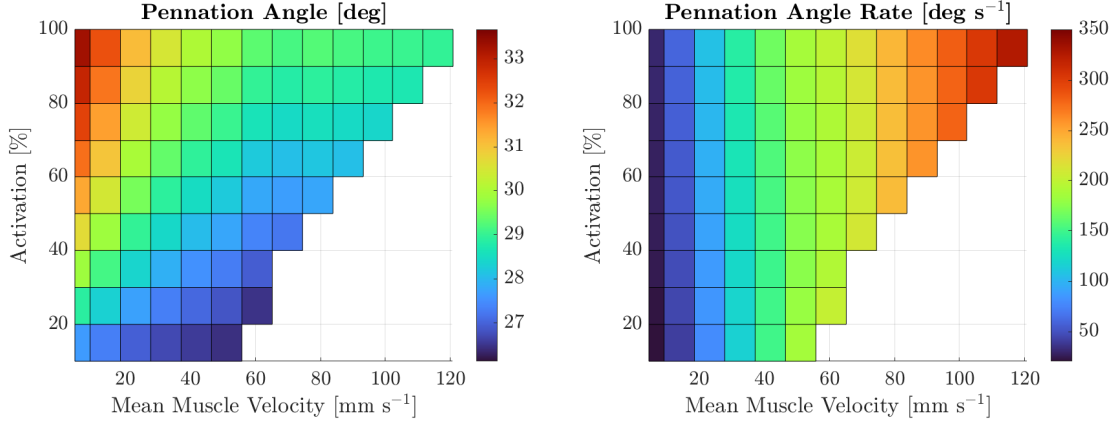


Figure 7.5: Mean pennation angle (left) and its rate of change (right) as functions of MMV and maximum activation (measured at the end of each simulation, i.e. when the muscle block returned to its initial length).

This behaviour, as well as the magnitudes of pennation angle rate for maximum activation levels below 50%, align with previous observations in cycling experiments [48].

Next, we compute muscle gearing as described in (7.2.13) and display first this quantity as a function of force and MMV in Figure 7.6, and as a function of force only for different maximum activation levels in Figure 7.7. We notice in particular how gearing decreases with increasing force, but increases with MMV and activation. The gearing values observed in this case align well with those observed by Holt et al. [89]. Finally, in Figure 7.8 we show how the muscle width and thickness vary in the midsection of the muscle block in an asymmetric fashion. For instance, when the MMV is small, the width of the midsection increases and its thickness decreases with increasing activation. Furthermore, there is a clear inverse relationship between muscle force (Figure 7.4) and muscle thickness (Figure 7.8), which is consistent with previous literature findings [8]. All simulation shown here had volume changes of < 1%, consistent with the (nearly) incompressible nature of skeletal muscle tissue [19].

The results above show how **Flexodeal** can reproduce the variable gearing observed experimentally in skeletal muscle tissue [8]. Moreover, not only we can perform experiments with maximal activation (as those performed in vitro or in situ) but also with lower levels of activation, similar to those seen in vivo. In particular, the results aligned with the well-established fact that muscle gearing decreases with increasing contractile force [57] and that in general, muscle gearing is higher during faster contractions and lower during forceful contractions [8, 57, 89, 162]. Furthermore, the fact that the gearing values are close to those reported by Holt et al. [89] suggest that the inclusion of mass (and therefore, inertia) in the system is necessary.

Muscle gearing is a multifactorial phenomenon and these results show how it emerges as an intrinsic property of active, fibre-reinforced composites, and that it is a truly 3D

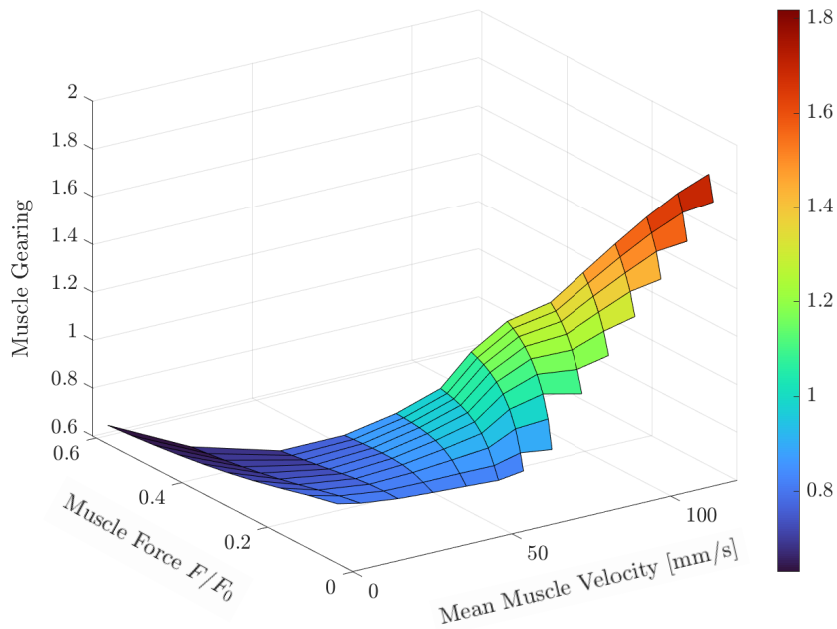


Figure 7.6: Muscle gearing as a function of (normalized) muscle force and MMV.

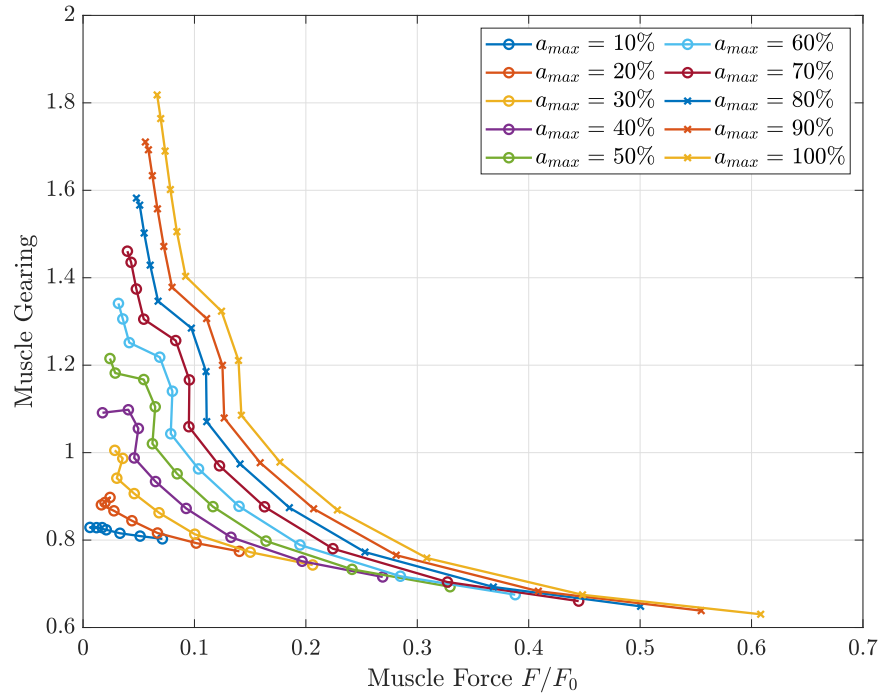


Figure 7.7: Muscle gearing as a function of (normalized) muscle force for different maximum activation levels.

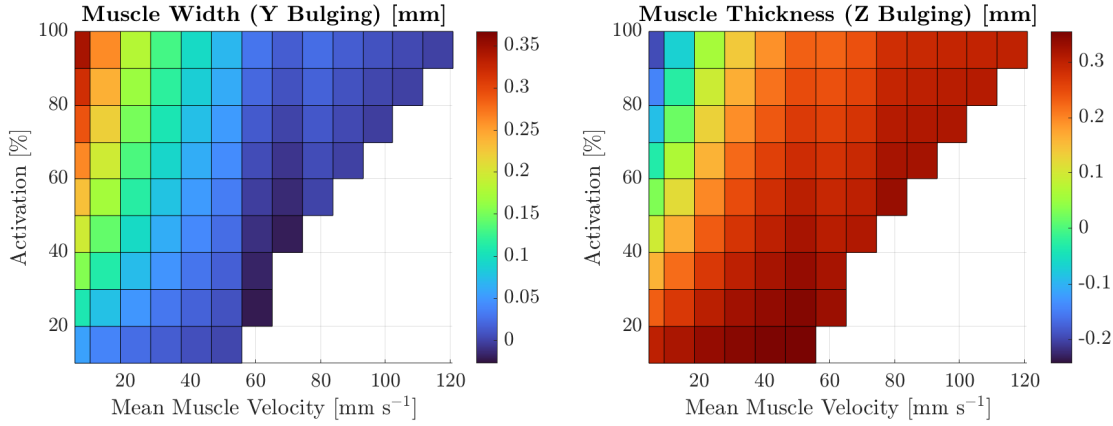


Figure 7.8: Muscle width and thickness at the end of the active shortening phase, shown here as a function of maximum activation level and MMV.

phenomenon (see Figure 7.3) that cannot be explained by 1D models. Extensive discussions exist in the literature as to what are the factors that influence muscle gearing the most [57]. Although it is out of the scope of this thesis to answer such question, we must emphasize that the muscle model used in these experiment does not have aponeurosis, intramuscular fat, or fluid contributions, which are factors typically thought to influence gearing [9, 33, 57, 89]. These factors are not necessary to explain why gearing occurs, but their consideration would certainly affect the overall material properties of muscle tissue, and may, therefore, modify the gearing characteristics of muscle. Further computational studies are needed in this area.

# Chapter 8

## Conclusions and future work

In this thesis, we studied mathematical, numerical, and physiological aspects of the elasto-dynamics of skeletal muscle tissue. We now present some conclusions of our work, as well as potential future directions.

### 8.1 Summary of contributions

In **Chapter 2**, we studied the inertial effects of mass in a set of simulations using a 1D multibody model of the muscle-tendon unit (MTU). We used motion capture and electromyography (EMG) data from three muscles of a human subject (medial gastrocnemius, vastus medialis, and semitendinosus) performing three different locomotion tasks (walking, cycling, and running). This data was collected by Chen [41] and was used in combination with our computations. We also considered the case when the muscle is scaled 10 times its size, given the fact that many times, human locomotion is explained using experiments performed in small animals, such as frogs and rats. In this case, we observed differences in force prediction between 2.1% (medial gastrocnemius, walking) and 14% (semitendinosus, running). These differences were computed using a 1D model with 64 masses, significantly more than the amount of masses used by Günter et al. [73] and Ross et al. [165]. With this number of masses, most (but not all) unphysical oscillations are avoided. We noticed it actually took 128 masses (and 42 hours of computational time) to compute the dynamics of the semitendinosus muscle while running (form scale  $s = 10$ ) without any unphysical oscillations. These computations point to the need for a continuum 1D model rather a system of 1D springs connected by dashpots.

In **Chapter 3**, we provided a mathematical description of the descending limb stability (DLI) in the multibody model used for Chapter 2. We noticed that this model can be viewed as a particular numerical discretization of a first-order wave equation that is a 1D version of the conservation of momentum equation in 3D for elasticity. We deduced from this fact that, to stabilize the model, one needs to add a secondary parallel elastic element (PEE) that is stiff enough to counteract the negative slope in the total force-length curve caused

by the DLI. This secondary PEE does *not* necessarily have to be titin. We homogenized the source term in this PDE to add a Neo-Hookean contribution, similar to the role of the base material in 3D models. We noticed that only 0.15% of Neo-Hookean material is needed to generate stable dynamics in the system. Furthermore, using a nondimensionalization argument, we proved that the stability of 1D Hill-type muscle models does not depend on the length, mass, scale, or fibre type in the model, where we defined a new nondimensional number called the neuromuscular Reynolds number  $\text{Re}_{MSK}$ .

In **Chapter 4**, we explored time stepping schemes for Neo-Hookean deformation in 1D. The nonlinearity in this model is crucial to visualize the difference between the order in which variables (space and time) are discretized. We noticed that, although second-order time stepping schemes (such as Newmark's or HHT- $\alpha$ ) are preferred in elastodynamics [91], first-order schemes were less prone to overshooting, especially in the velocity variable. This is an important consideration for 3D muscle models, since a more robust time discretization with respect to overshooting allows us to consider piecewise-linear lengthening or shortening profiles, similar to those reported in the literature [83]. Moreover, because of the multiplicative character of Hill's force, velocity oscillations, even if they are damped quickly, are not ideal. We also observed that, due to the stiffness in the system, an implicit-explicit scheme did not show better results since it behave similarly to an explicit scheme.

In **Chapter 5**, we introduced a new Lagrangian formulation for a 3D dynamic muscle model that was used previously [54, 103, 164, 173, 196]. Both are based on a three-field formulation by Simo et al. [180]. We first defined key physiological terms (such as fibre stretch and fibre strain rate) in terms of continuum mechanics. We also defined the strain-energy functions that constitute the muscle-tendon unit, depending on the choice of material components for the computational domain. Then, we introduced this Lagrangian formulation, equivalent to that used by Dominguez [54] but simpler to implement computationally. For the time discretization, and based on the results of Chapter 4, we chose a first-order fully implicit time stepping scheme. We did not introduce a new space discretization for this problem, which was based on  $Q_{k+1}/P_k$  finite elements on hexahedral meshes. Of particular importance was the linearization of this problem, especially in the fibre component. Here, we provided a complete expression of the fourth-order elasticity tensor that includes an appropriate treatment of the fibre strain rate variable. This is key to allow muscle to be completely activated in a dynamic setting. We also discussed how the strain-energy function for a system containing only base material and fibre properties may fail to be polyconvex due to the DLI (which was studied in Chapter 3).

In **Chapter 6**, we introduced a new, open-source, finite element framework for elastodynamics: **Flexodeal**. After providing documentation for this software, we performed a convergence study on the nonlinear problem of skeletal muscle deformation. Linear convergence was observed in the time variable, in line with the first-order time discretization employed. However, rates of convergence in the space variable were suboptimal (compared

to those found in a linear problem). In general, unless the solution to the variational formulation is sufficiently smooth (which is not necessarily the case in a muscle with complex architecture), it is not guaranteed that optimal rates of convergence will be achieved. We then proposed a series of fundamental experiments that can easily be reproduced with **Flexodeal**.

First, taking advantage of the efficiency of **Flexodeal**, we decided to perform some quasi-static experiments to obtain the force-length relationship of whole muscle. Here, we found that it is still possible for muscle to have a FL curve with a descending limb (which, in this case, *can* alter the numerical stability of the problem for active stretching), even when a base material component is present in the model. The results show that there are at least two alternatives to remove this descending limb: either by artificially increasing the base material contribution or by adding aponeurosis to the model. Then, we discussed the differences between quasi-static and dynamic simulations for isometric contractions in four physiological variables: force, fibre stretch, pennation angle, and fibre strain rate. Local variations in fibre strain rate cause the models to essentially give different responses, with differences of up to 50% in force. We demonstrated that dynamic models provide more reasonable results when compared to quasi-static ones (particularly when looking at quantities such as fibre strain rate), which highlights the crucial role of inertial in complex muscle models. Furthermore, we confirmed that mass and force-velocity effects are most noticeable during submaximal contractions of highly-pennate muscle [196]. Finally, we demonstrated the ability of **Flexodeal** to perform a forward dynamics simulation in a computational domain derived from magnetic resonance imaging (MRI) with boundary conditions and activation profiles obtained from a locomotion experiment.

In **Chapter 7**, we studied muscle gearing, which is a phenomenon that combines changes in muscle architecture with a decoupling of fibre and muscle velocities. This is the first time in the biomechanics literature that a continuum mechanics model is used to study gearing, which was possible thanks to the dynamic capabilities of **Flexodeal** and the Lagrangian framework introduced in **Chapter 5**. We performed 140 different experiments of muscle contraction, with varying levels of maximum activation and prescribed muscle velocities (implemented as a boundary condition), based on a previous experiment on rats by Holt et al. [89]. Our results showed that muscle gearing is an inherent property of fibre-reinforced active composites, that no fluid or aponeurosis contributions are necessary to observe this phenomenon, and that **Flexodeal** can compute gearing values (i.e. the ratio of muscle velocity to fibre velocity) similar to those observed experimentally, even in cases of submaximal activation that are observed *in vivo*.

## 8.2 Future work

The developments presented in this thesis open the door to multiple avenues of research that we, rather arbitrarily, group as follows.

### 8.2.1 Mass-enhanced muscle models in 1D

In Chapter 2, we noticed that converged results required to consider a large number of masses in the multibody model, which results in high computing times. To mitigate this, one could use the the 1D wave equation introduced in (3.3.6), that is:

$$\rho_{0,L} \frac{\partial^2 u(x,t)}{\partial t^2} = \frac{\partial F(\lambda(x,t), \dot{\varepsilon}(x,t))}{\partial x}, \quad 0 < x < L_{mus}^{opt}, \quad 0 < t < \infty, \quad (8.2.1)$$

to derive a new discretization. For instance, higher order finite difference formulas could be considered for the spatial discretization (for instance, using a leapfrog scheme [183]). However, it also remains to study whether the addition of a base material component in  $F$  would improve the numerical stability of the original discretization in (3.3.1) (used to compute the results in Chapter 2), so that fewer masses are required to obtained a converged result in space.

### 8.2.2 Hu-Washizu formulations for skeletal muscle

The physiological quantities of core interest: displacements, fibre stretch and strain rates, surface forces and pressures, are not all directly computed in our method. In particular forces on the boundary are of key interest, but so far they can only be estimated from the stress at interior points near the boundary (see (6.2.15)).

Currently, variational formulations for elasticity in the context of skeletal muscle are derived from engineering standards, namely Hu-Washizu type principles like the three-field formulation we used in the Lagrangian model (see Chapter 5). However, because there are no degrees of freedom in the boundary that allows us to compute muscle force exactly, new Hu-Washizu type principles should be derived that are suitable for problems of skeletal muscle deformation.

For example, Zdunek & Rachowicz [209] developed a new three-field formulation that reads for the quasi-static problem: Find  $(\mathbf{U}, \tilde{\varrho}, \tilde{\lambda})$  such that

$$\mathbf{Div} \mathbf{P} = \mathbf{0} \quad \text{in } \mathcal{B}_0 \times (0, \infty), \quad (8.2.2a)$$

$$\tilde{\lambda} - \lambda(\mathbf{U}) = 0 \quad \text{in } \mathcal{B}_0 \times (0, \infty), \quad (8.2.2b)$$

$$\tilde{\varrho} - \frac{\partial \Psi}{\partial \tilde{\lambda}} = 0 \quad \text{in } \mathcal{B}_0 \times (0, \infty), \quad (8.2.2c)$$

where  $\mathbf{U}$  is the material displacement,  $\tilde{\lambda}$  is a computed fibre stretch, and  $\tilde{\varrho}$  is the uniaxial tension. Although this formulation is used for compressible elasticity with inextensible fibres

(i.e. fibres that can bend but not stretch), this shows that alternative formulations to the commonly used displacement-pressure-dilatation are indeed possible.

Furthermore, Farrell et al. [62] introduced a Kirchhoff stress-displacement-pressure formulation for incompressible hyperelasticity, which could be extended to a four-field Kirchhoff stress-displacement-pressure-dilatation formulation. The advantage of this formulation is that, since now the Kirchhoff stress is a variable of the problem, its finite element space can be chosen to have degrees of freedom on the boundaries, so that exact forces can be computed.

### 8.2.3 A posteriori error estimator

Figure 1.2 shows that there are more complicated muscle architectures than the ones covered in this thesis. In particular, bipennate muscle architectures contain a thin layer of aponeurosis in the interior of the computational domain, whose deformation needs to be properly captured. This might require a more intricate mesh that needs to be adapted half way through the computation. Therefore, a posteriori error estimators can be used to refine the mesh in places where more resolution is needed (see, for instance, [6]). In particular, for large deformation problems, Brink & Stein [35] (see also [172]) proposed an a posteriori error estimator for Lagrangian formulations of quasi-static hyperelasticity, whose extension to the dynamic case could be studied.

### 8.2.4 Nonlinear solvers, preconditioners, and parallel computing

Although Newton's method is the gold standard in solving nonlinear problems [210], the high number of nonlinear iterations (especially for cases when muscle activation reaches 100%) can become a bottleneck in the solution of nonlinear problems. In this regard, Barnafi et al. studied several alternatives to Newton's method for problems of large deformation. The authors found that methods such as an inexact Newton-Krylov or BFGS methods can lead to a smaller number of nonlinear iterations while still retaining the quality of the solutions.

However, these types of solutions must be accompanied by an appropriate preconditioner. In the computational experiments discussed in this thesis, the majority of them required thousands of linear iterations per nonlinear iteration, which is a sign that a better preconditioner must be used. In particular, an Algebraic Multigrid (AMG) preconditioner could be used [18]. However, this requires us to parallelize the solution of the linear system using libraries such as PETSc [15] or Trilinos [189]. This parallelization effort would also require to handle the multiple inputs and outputs that are needed in **Flexodeal** using MPI-IO [42].

### 8.2.5 Validation, modifications, and further applications of Flexodeal

Although the results seen in this thesis confirm that **Flexodeal** can predict realistic dynamics of skeletal muscle tissue, a detailed study of the accuracy of the computed forces (with respect to actual muscle) is lacking. Further studies are required in this area to determine an appropriate combination of experimental protocols and modelling choices that can be contrasted with the outputs of **Flexodeal**. This might include particular choices of computational domains and force-length/force-velocity relationships that are closer to the experimental protocol.

The **Flexodeal** framework is flexible enough that more mechanical components can be considered and studied, such as titin [174], fatigue [29], or multiple fibre types [120]. Furthermore, **Flexodeal** could also be used to study active deformation of muscle affected by neuromuscular diseases, such as cerebral palsy or stroke [103, 114].

## 8.3 Conclusions

This thesis covered the nonlinear elastodynamics of skeletal muscle tissue, combining tried-and-tested approaches from mechanical engineering, sound mathematical and numerical analysis principles, well-recognized physiological results, and basic principles of software engineering. We hope that this interdisciplinary work further inspires researchers to team up and continue the progress of applied (and applicable) mathematics.

# Bibliography

- [1] P. C. AFRICA, D. ARNDT, W. BANGERTH, B. BLAIS, M. FEHLING, R. GASSMÖLLER, T. HEISTER, L. HELTAI, S. KINNEWIG, M. KRONBICHLER, M. MAIER, P. MUNCH, M. SCHRETER-FLEISCHHACKER, J. P. THIELE, B. TURCKSIN, D. WELLS, AND V. YUSHUTIN, *The deal.ii library, version 9.6*, Journal of Numerical Mathematics, 32 (2024), pp. 369–380.
- [2] N. ALKHOULI, J. MANSFIELD, E. GREEN, J. BELL, B. KNIGHT, N. LIVERSEDGE, J. C. THAM, R. WELBOURN, A. C. SHORE, K. KOS, ET AL., *The mechanical properties of human adipose tissues and their relationships to the structure and composition of the extracellular matrix*, American Journal of Physiology-Endocrinology and Metabolism, 305 (2013), pp. E1427–E1435.
- [3] T. L. ALLINGER, M. EPSTEIN, AND W. HERZOG, *Stability of muscle fibers on the descending limb of the force-length relation. a theoretical consideration*, Journal of biomechanics, 29 (1996), pp. 627–633.
- [4] J. A. ALMONACID, S. A. DOMÍNGUEZ-RIVERA, R. N. KONNO, N. NIGAM, S. A. ROSS, C. TAM, AND J. M. WAKELING, *A three-dimensional model of skeletal muscle tissues*, SIAM Journal on Applied Mathematics, 84 (2024), pp. S538–S566.
- [5] J. A. ALMONACID, G. N. GATICA, AND R. OYARZÚA, *A mixed-primal finite element method for the boussinesq problem with temperature-dependent viscosity*, Calcolo, 55 (2018), pp. 1–42.
- [6] ———, *A posteriori error analysis of a mixed-primal finite element method for the boussinesq problem with temperature-dependent viscosity*, Journal of Scientific Computing, 78 (2019), pp. 887–917.
- [7] D. ARNDT, W. BANGERTH, M. BERGBAUER, M. FEDER, M. FEHLING, J. HEINZ, T. HEISTER, L. HELTAI, M. KRONBICHLER, M. MAIER, P. MUNCH, J.-P. PELTERET, B. TURCKSIN, D. WELLS, AND S. ZAMPINI, *The deal.II library, version 9.5*, Journal of Numerical Mathematics, 31 (2023), pp. 231–246.
- [8] E. AZIZI, E. L. BRAINERD, AND T. J. ROBERTS, *Variable gearing in pennate muscles*, Proceedings of the National Academy of Sciences, 105 (2008), pp. 1745–1750.
- [9] E. AZIZI, G. B. GILLIS, AND E. L. BRAINERD, *Morphology and mechanics of myosepta in a swimming salamander (*siren lacertina*)*, Comparative Biochemistry and Physiology Part A: Molecular & Integrative Physiology, 133 (2002), pp. 967–978.

- [10] E. AZIZI, G. M. HALEND A, AND T. J. ROBERTS, *Mechanical properties of the gastrocnemius aponeurosis in wild turkeys*, Integrative and comparative biology, 49 (2009), pp. 51–58.
- [11] E. AZIZI AND T. J. ROBERTS, *Variable gearing in a biologically inspired pneumatic actuator array*, Bioinspiration & biomimetics, 8 (2013), p. 026002.
- [12] ——, *Geared up to stretch: pennate muscle behavior during active lengthening*, Journal of Experimental Biology, 217 (2014), pp. 376–381.
- [13] I. BABUŠKA AND M. SURI, *Locking effects in the finite element approximation of elasticity problems*, Numerische Mathematik, 62 (1992), pp. 439–463.
- [14] P. BAKENECKER, B. J. RAITERI, AND D. HAHN, *Force enhancement in the human vastus lateralis is muscle-length-dependent following stretch but not during stretch*, European Journal of Applied Physiology, 120 (2020), pp. 2597–2610.
- [15] S. BALAY, S. ABHYANKAR, M. F. ADAMS, J. BROWN, P. BRUNE, K. BUSCHELMAN, L. DALCIN, V. EIJKHOUT, W. D. GROPP, D. KAUSHIK, M. G. KNEPLEY, L. C. MCINNES, K. RUPP, B. F. SMITH, S. ZAMPINI, AND H. ZHANG, *PETSc Web page*. <http://www.mcs.anl.gov/petsc>, 2015.
- [16] J. M. BALL, *Convexity conditions and existence theorems in nonlinear elasticity*, Archive for rational mechanics and Analysis, 63 (1976), pp. 337–403.
- [17] ——, *Some open problems in elasticity*, in Geometry, mechanics, and dynamics, Springer, 2002, pp. 3–59.
- [18] N. A. BARNAFI, L. F. Pavarino, AND S. SCACCHI, *Parallel inexact newton-krylov and quasi-newton solvers for nonlinear elasticity*, Computer Methods in Applied Mechanics and Engineering, 400 (2022), p. 115557.
- [19] R. BASKIN AND P. PAOLINI, *Volume change and pressure development in muscle during contraction*, American Journal of Physiology-Legacy Content, 213 (1967), pp. 1025–1030.
- [20] J. BERITOFF, *Über die kontraktionsfähigkeit der skelettmuskeln: Iv. mitteilung. über die physiologische bedeutung des gefiederten baues der muskeln*, Pflüger's Archiv für die gesamte Physiologie des Menschen und der Tiere, 209 (1925), pp. 763–778.
- [21] J. G. BETTS, P. DESAIX, E. JOHNSON, J. E. JOHNSON, O. KOROL, D. KRUSE, B. POE, J. A. WISE, M. WOMBLE, AND K. A. YOUNG, *Anatomy and physiology 2e*. <https://openstax.org/details/books/anatomy-and-physiology-2e>. Accessed on 2025-06-18., 2022.
- [22] A. A. BIEWENER, R. BLICKHAN, A. K. PERRY, N. C. HEGLUND, AND C. R. TAYLOR, *Muscle forces during locomotion in kangaroo rats: force platform and tendon buckle measurements compared*, Journal of Experimental Biology, 137 (1988), pp. 191–205.
- [23] P. J. BISHOP, A. R. CUFF, AND J. R. HUTCHINSON, *How to build a dinosaur: Musculoskeletal modeling and simulation of locomotor biomechanics in extinct animals*, Paleobiology, 47 (2021), pp. 1–38.

- [24] S. S. BLEMKER, *Three-dimensional modeling of complex muscle architecture and geometry*, PhD thesis, Stanford University, 2004.
- [25] S. S. BLEMKER AND S. L. DELP, *Three-dimensional representation of complex muscle architectures and geometries*, Annals of biomedical engineering, 33 (2005), pp. 661–673.
- [26] S. S. BLEMKER, P. M. PINSKY, AND S. L. DELP, *A 3d model of muscle reveals the causes of nonuniform strains in the biceps brachii*, Journal of biomechanics, 38 (2005), pp. 657–665.
- [27] D. BOFFI, F. BREZZI, M. FORTIN, ET AL., *Mixed finite element methods and applications*, vol. 44, Springer, 2013.
- [28] S. BOHM, F. MERSMANN, A. SANTUZ, AND A. ARAMPATZIS, *The force-length-velocity potential of the human soleus muscle is related to the energetic cost of running*, Proceedings of the Royal Society B, 286 (2019), p. 20192560.
- [29] M. BÖL, A. PIPETZ, AND S. REESE, *Finite element model for the simulation of skeletal muscle fatigue*, Materialwissenschaft und Werkstofftechnik: Entwicklung, Fertigung, Prüfung, Eigenschaften und Anwendungen technischer Werkstoffe, 40 (2009), pp. 5–12.
- [30] M. BÖL AND S. REESE, *Micromechanical modelling of skeletal muscles based on the finite element method*, Computer methods in biomechanics and biomedical engineering, 11 (2008), pp. 489–504.
- [31] J. BONET, A. J. GIL, AND R. D. WOOD, *Nonlinear solid mechanics for finite element analysis: dynamics*, Cambridge University Press, 2021.
- [32] R. BOTTINELLI, M. A. PELLEGRINO, M. CANEPARI, R. ROSSI, AND C. REGGIANI, *Specific contributions of various muscle fibre types to human muscle performance: an in vitro study*, Journal of Electromyography and Kinesiology, 9 (1999), pp. 87–95.
- [33] E. L. BRAINERD AND E. AZIZI, *Muscle fiber angle, segment bulging and architectural gear ratio in segmented musculature*, Journal of Experimental Biology, 208 (2005), pp. 3249–3261.
- [34] U. BRINK AND E. STEIN, *On some mixed finite element methods for incompressible and nearly incompressible finite elasticity*, Computational Mechanics, 19 (1996), pp. 105–119.
- [35] ———, *A posteriori error estimation in large-strain elasticity using equilibrated local neumann problems*, Computer Methods in Applied Mechanics and Engineering, 161 (1998), pp. 77–101.
- [36] T. BRITANNICA, *skeletal muscle*. Encyclopedia Britannica. <https://www.britannica.com/science/skeletal-muscle>. Accessed on 2025-06-18.
- [37] T. J. BURKHOLDER AND R. L. LIEBER, *Sarcomere length operating range of vertebrate muscles during movement*, Journal of Experimental Biology, 204 (2001), pp. 1529–1536.

- [38] A. H. CAILLET, A. T. PHILLIPS, D. FARINA, AND L. MODENESE, *Motoneuron-driven computational muscle modelling with motor unit resolution and subject-specific musculoskeletal anatomy*, PLOS Computational Biology, 19 (2023), p. e1011606.
- [39] S.-Y. CHANG, *A new family of explicit methods for linear structural dynamics*, Computers & Structures, 88 (2010), pp. 755–772.
- [40] N. CHAPMAN, J. WHITTING, S. BROADBENT, Z. CROWLEY-MCHATTAN, AND R. MEIR, *Residual force enhancement in humans: a systematic review*, Journal of Applied Biomechanics, 34 (2018), pp. 240–248.
- [41] I.-J. CHEN, *Comparison of muscle predictions using mass-enhanced and massless hill-type muscle models in human locomotion*, MSc thesis, Department of Biomedical Physiology and Kinesiology, Simon Fraser University, 2024.
- [42] D. L. CHOPP, *Introduction to high performance scientific computing*, SIAM, 2019.
- [43] P. G. CIARLET, *Mathematical elasticity: Three-dimensional elasticity*, SIAM, 2021.
- [44] E. A. COAYLA-TERAN, S.-E. A. MOHAMMED, P. R. C. RUFFINO, ET AL., *Hartman-grobman theorems along hyperbolic stationary trajectories*, Discrete and Continuous Dynamical Systems, 17 (2007), p. 281.
- [45] S. L. DELP, F. C. ANDERSON, A. S. ARNOLD, P. LOAN, A. HABIB, C. T. JOHN, E. GUENDELMAN, AND D. G. THELEN, *OpenSim: open-source software to create and analyze dynamic simulations of movement*, IEEE transactions on biomedical engineering, 54 (2007), pp. 1940–1950.
- [46] T. J. DICK, A. S. ARNOLD, AND J. M. WAKELING, *Quantifying achilles tendon force in vivo from ultrasound images*, Journal of biomechanics, 49 (2016), pp. 3200–3207.
- [47] T. J. DICK, A. A. BIEWENER, AND J. M. WAKELING, *Comparison of human gastrocnemius forces predicted by hill-type muscle models and estimated from ultrasound images*, Journal of experimental biology, 220 (2017), pp. 1643–1653.
- [48] T. J. DICK AND J. M. WAKELING, *Shifting gears: dynamic muscle shape changes and force-velocity behavior in the medial gastrocnemius*, Journal of applied physiology, 123 (2017), pp. 1433–1442.
- [49] ———, *Geometric models to explore mechanisms of dynamic shape change in skeletal muscle*, Royal Society open science, 5 (2018), p. 172371.
- [50] T. J. M. DICK, *The mechanics of the gastrocnemii-Achilles tendon complex during human cycling: Experimental and modelling approaches to predict in vivo forces*, PhD thesis, Department of Biomedical Physiology and Kinesiology, Simon Fraser University, 2016.
- [51] P. DINIZ, B. GRIMM, F. GARCIA, J. FAYAD, C. LEY, C. MOUTON, J. F. OEDING, M. T. HIRSCHMANN, K. SAMUELSSON, AND R. SEIL, *Digital twin systems for musculoskeletal applications: A current concepts review*, Knee Surgery, Sports Traumatology, Arthroscopy, 33 (2025), pp. 1892–1910.

- [52] M. D. DiSALVO AND S. S. BLEMKER, *The need for speed—does the force–velocity property significantly alter strain distributions within skeletal muscle?*, Journal of Biomechanics, 167 (2024), p. 112089.
- [53] S. DOLL AND K. SCHWEIZERHOF, *On the development of volumetric strain energy functions*, J. Appl. Mech., 67 (2000), pp. 17–21.
- [54] S. DOMÍNGUEZ RIVERA, *From eigenbeauty to large-deformation horror*, PhD thesis, Department of Mathematics, Simon Fraser University, 2020.
- [55] J. R. DORMAND AND P. J. PRINCE, *A family of embedded runge-kutta formulae*, Journal of computational and applied mathematics, 6 (1980), pp. 19–26.
- [56] A. D’SOUZA, B. BOLSTERLEE, A. LANCASTER, AND R. D. HERBERT, *Muscle architecture in children with cerebral palsy and ankle contractures: an investigation using diffusion tensor imaging*, Clinical Biomechanics, 68 (2019), pp. 205–211.
- [57] C. M. ENG, E. AZIZI, AND T. J. ROBERTS, *Structural determinants of muscle gearing during dynamic contractions*, Integrative and comparative biology, 58 (2018), pp. 207–218.
- [58] C. M. ENG AND T. J. ROBERTS, *Aponeurosis influences the relationship between muscle gearing and force*, Journal of Applied Physiology, 125 (2018), pp. 513–519.
- [59] M. EPSTEIN AND W. HERZOG, *Aspects of skeletal muscle modelling*, Philosophical Transactions of the Royal Society of London. Series B: Biological Sciences, 358 (2003), pp. 1445–1452.
- [60] S. ERLICHER, L. BONAVENTURA, AND O. S. BURSI, *The analysis of the generalized- $\alpha$  method for non-linear dynamic problems*, Computational mechanics, 28 (2002), pp. 83–104.
- [61] A. ERN AND J.-L. GUERMOND, *Theory and practice of finite elements*, vol. 159, Springer, 2004.
- [62] P. E. FARRELL, L. F. GATICA, B. P. LAMICHHANE, R. OYARZÚA, AND R. RUIZ-BAIER, *Mixed kirchhoff stress–displacement–pressure formulations for incompressible hyperelasticity*, Computer Methods in Applied Mechanics and Engineering, 374 (2021), p. 113562.
- [63] J. FRIDÉN AND R. L. LIEBER, *Evidence for muscle attachment at relatively long lengths in tendon transfer surgery*, The Journal of hand surgery, 23 (1998), pp. 105–110.
- [64] T. FUNAI, H. KATAOKA, H. YOKOTA, AND T.-A. SUZUKI, *Proposal and validation of polyconvex strain-energy function for biological soft tissues*, Bio-Medical Materials and Engineering, 32 (2021), pp. 131–144.
- [65] H. GAREIS, S. MOSHE, R. BARATTA, R. BEST, AND R. D’AMBROSIA, *The isometric length-force models of nine different skeletal muscles*, Journal of Biomechanics, 25 (1992), pp. 903–916.

- [66] G. N. GATICA, *A simple introduction to the mixed finite element method, Theory and Applications*. Springer Briefs in Mathematics. Springer, London, (2014).
- [67] K. GAUTAM, M. S. HEFZY, A. A. MUSTAPHA, AND B. KYLE, *Comparison of open-sim and anybody modelling system™predictions in biomechanical modeling of upper extremities*, International Journal of Research in Orthopaedics, 10 (2024), p. 717.
- [68] G. GIANTESIO AND A. MUSESTI, *On the modeling of active deformation in biological transversely isotropic materials*, Journal of Elasticity, 157 (2024), pp. 1–17.
- [69] M. J. GILLESPIE, T. GORDON, AND P. R. MURPHY, *Motor units and histochemistry in rat lateral gastrocnemius and soleus muscles: evidence for dissociation of physiological and histochemical properties after reinnervation*, Journal of neurophysiology, 57 (1987), pp. 921–937.
- [70] A. R. GILLIES AND R. L. LIEBER, *Structure and function of the skeletal muscle extracellular matrix*, Muscle & nerve, 44 (2011), pp. 318–331.
- [71] A. R. GILLIES, L. R. SMITH, R. L. LIEBER, AND S. VARGHESE, *Method for decellularizing skeletal muscle without detergents or proteolytic enzymes*, Tissue engineering part C: Methods, 17 (2011), pp. 383–389.
- [72] A. GORDON, A. F. HUXLEY, AND F. JULIAN, *The variation in isometric tension with sarcomere length in vertebrate muscle fibres*, The Journal of physiology, 184 (1966), pp. 170–192.
- [73] M. GÜNTHER, O. RÖHRLE, D. F. HAEUFLE, AND S. SCHMITT, *Spreading out muscle mass within a hill-type model: A computer simulation study*, Computational and mathematical methods in medicine, 2012 (2012), p. 848630.
- [74] E. HAIRER, S. NORSETT, AND G. WANNER, *Solving Ordinary Differential Equations I: Nonstiff Problems*, Springer Series in Computational Mathematics, Springer Berlin Heidelberg, 2013.
- [75] G. G. HANDSFIELD, C. H. MEYER, J. M. HART, M. F. ABEL, AND S. S. BLEMKER, *Relationships of 35 lower limb muscles to height and body mass quantified using mri*, Journal of biomechanics, 47 (2014), pp. 631–638.
- [76] J. HANSON AND H. E. HUXLEY, *Structural basis of the cross-striations in muscle*, Nature, 172 (1953), pp. 530–532.
- [77] S. HARTMANN AND P. NEFF, *Polyconvexity of generalized polynomial-type hyperelastic strain energy functions for near-incompressibility*, International journal of solids and structures, 40 (2003), pp. 2767–2791.
- [78] T. HEIDLÄUF, T. KLOTZ, C. RODE, E. ALTAN, C. BLEILER, T. SIEBERT, AND O. RÖHRLE, *A multi-scale continuum model of skeletal muscle mechanics predicting force enhancement based on actin–titin interaction*, Biomechanics and modeling in mechanobiology, 15 (2016), pp. 1423–1437.

- [79] T. HEIDLAUF, T. KLOTZ, C. RODE, T. SIEBERT, AND O. RÖHRLE, *A continuum-mechanical skeletal muscle model including actin-titin interaction predicts stable contractions on the descending limb of the force-length relation*, PLoS computational biology, 13 (2017), p. e1005773.
- [80] T. HEIDLAUF AND O. RÖHRLE, *Modeling the chemoelectromechanical behavior of skeletal muscle using the parallel open-source software library openCMiss*, Computational and mathematical methods in medicine, 2013 (2013), p. 517287.
- [81] ———, *A multiscale chemo-electro-mechanical skeletal muscle model to analyze muscle contraction and force generation for different muscle fiber arrangements*, Frontiers in physiology, 5 (2014), p. 498.
- [82] W. HERZOG, *The role of titin in eccentric muscle contraction*, Journal of Experimental Biology, 217 (2014), pp. 2825–2833.
- [83] W. HERZOG AND T. R. LEONARD, *Force enhancement following stretching of skeletal muscle: a new mechanism*, Journal of Experimental Biology, 205 (2002), pp. 1275–1283.
- [84] H. M. HILBER, T. J. HUGHES, AND R. L. TAYLOR, *Improved numerical dissipation for time integration algorithms in structural dynamics*, Earthquake Engineering & Structural Dynamics, 5 (1977), pp. 283–292.
- [85] A. V. HILL, *The heat of shortening and the dynamic constants of muscle*, Proceedings of the Royal Society of London. Series B-Biological Sciences, 126 (1938), pp. 136–195.
- [86] ———, *First and last experiments in muscle mechanics*, Cambridge University Press, 1970.
- [87] A. HINKS, K. B. JACOB, M. A. PATTERSON, B. DALTON, AND G. A. POWER, *Residual force enhancement decreases when scaling from the single muscle fibre to joint level in humans*, bioRxiv, (2024), pp. 2024–06.
- [88] C. HOFF AND P. PAHL, *Development of an implicit method with numerical dissipation from a generalized single-step algorithm for structural dynamics*, Computer Methods in Applied Mechanics and Engineering, 67 (1988), pp. 367–385.
- [89] N. C. HOLT, N. DANOS, T. J. ROBERTS, AND E. AZIZI, *Stuck in gear: age-related loss of variable gearing in skeletal muscle*, Journal of Experimental Biology, 219 (2016), pp. 998–1003.
- [90] G. A. HOLZAPFEL, *Nonlinear Solid Mechanics: A Continuum Approach for Engineering*, Wiley, 2000.
- [91] T. HUGHES, *The Finite Element Method: Linear Static and Dynamic Finite Element Analysis*, Dover Civil and Mechanical Engineering, Dover Publications, 2012.
- [92] P. HUIJING AND R. WOITIEZ, *The effect of architecture on skeletal muscle performance: a simple planimetric model*, Netherlands Journal of Zoology, 34 (1983), pp. 21–32.

- [93] A. F. HUXLEY, *Muscle structure and theories of contraction*, Progress in biophysics and biophysical chemistry, 7 (1957), pp. 256–319.
- [94] A. F. HUXLEY AND R. NIEDERGERKE, *Structural changes in muscle during contraction: interference microscopy of living muscle fibres*, Nature, 173 (1954), pp. 971–973.
- [95] X. JIN, F. ZHU, H. MAO, M. SHEN, AND K. H. YANG, *A comprehensive experimental study on material properties of human brain tissue*, Journal of biomechanics, 46 (2013), pp. 2795–2801.
- [96] T. JOHANSSON, P. MEIER, AND R. BLICKHAN, *A finite-element model for the mechanical analysis of skeletal muscles*, Journal of theoretical biology, 206 (2000), pp. 131–149.
- [97] K. JOHNSTON, A. JINHA, AND W. HERZOG, *The role of sarcomere length non-uniformities in residual force enhancement of skeletal muscle myofibrils*, Royal Society Open Science, 3 (2016), p. 150657.
- [98] V. JOUMAA, T. LEONARD, AND W. HERZOG, *Residual force enhancement in myofibrils and sarcomeres*, Proceedings of the Royal Society B: Biological Sciences, 275 (2008), pp. 1411–1419.
- [99] C. KADAPA, *Mixed displacement-pressure formulations and suitable finite elements for multimaterial problems with compressible and incompressible models*, Computer methods in applied mechanics and engineering, 432 (2024), p. 117354.
- [100] C. KADAPA, W. DETTMER, AND D. PERIĆ, *On the advantages of using the first-order generalised-alpha scheme for structural dynamic problems*, Computers & Structures, 193 (2017), pp. 226–238.
- [101] P. V. KOMI, *Relevance of in vivo force measurements to human biomechanics*, Journal of biomechanics, 23 (1990), pp. 23–34.
- [102] R. N. KONNO, N. NIGAM, AND J. M. WAKELING, *Modelling extracellular matrix and cellular contributions to whole muscle mechanics*, Plos one, 16 (2021), p. e0249601.
- [103] R. N. KONNO, N. NIGAM, J. M. WAKELING, AND S. A. ROSS, *The contributions of extracellular matrix and sarcomere properties to passive muscle stiffness in cerebral palsy*, Frontiers in Physiology, 12 (2022), p. 2498.
- [104] B. KOVÁCS, I. KÓBOR, Z. GYIMES, Ö. SEBESTYÉN, AND J. TIHANYI, *Lower leg muscle-tendon unit characteristics are related to marathon running performance*, Scientific reports, 10 (2020), p. 17870.
- [105] C. D. KUTHE AND R. V. UDDANWADIKER, *Investigation of effect of fiber orientation on mechanical behavior of skeletal muscle*, Journal of Applied Biomaterials & Functional Materials, 14 (2016), pp. 154–162.
- [106] A. LEAVEY, C. T. RICHARDS, AND L. B. PORRO, *Frog fibres: What muscle architecture can tell us about anuran locomotor function*, Journal of Morphology, 286 (2025), p. e70016.

- [107] D. LEE, Z. LI, Q. Z. SOHAIL, K. JACKSON, E. FIUME, AND A. AGUR, *A three-dimensional approach to pennation angle estimation for human skeletal muscle*, Computer Methods in Biomechanics and Biomedical Engineering, 18 (2015), pp. 1474–1484.
- [108] S. S. LEE, A. S. ARNOLD, M. DE BOEF MIARA, A. A. BIEWENER, AND J. M. WAKELING, *Accuracy of gastrocnemius muscles forces in walking and running goats predicted by one-element and two-element hill-type models*, Journal of biomechanics, 46 (2013), pp. 2288–2295.
- [109] R. LEMOS, M. EPSTEIN, W. HERZOG, AND B. WYVILL, *Realistic skeletal muscle deformation using finite element analysis*, in Proceedings XIV Brazilian Symposium on Computer Graphics and Image Processing, IEEE, 2001, pp. 192–199.
- [110] R. J. LEVEQUE, *Finite Difference Methods for Ordinary and Partial Differential Equations*, Society for Industrial and Applied Mathematics, 2007.
- [111] R. L. LIEBER, *Skeletal muscle structure, function, and plasticity*, Lippincott Williams & Wilkins, 3rd ed., 2010.
- [112] ———, *Biomechanical response of skeletal muscle to eccentric contractions*, Journal of sport and health science, 7 (2018), pp. 294–309.
- [113] R. L. LIEBER AND J. FRIDÉN, *Functional and clinical significance of skeletal muscle architecture*, Muscle & Nerve: Official Journal of the American Association of Electromyographic and Clinical Neurophysiology, 23 (2000), pp. 1647–1666.
- [114] R. L. LIEBER, T. J. ROBERTS, S. S. BLEMKER, S. S. LEE, AND W. HERZOG, *Skeletal muscle mechanics, energetics and plasticity*, Journal of neuroengineering and rehabilitation, 14 (2017), pp. 1–16.
- [115] C. LIU, Y. WANG, Z. QIAN, K. WANG, F. ZHAO, P. DING, D. XU, G. WEI, L. REN, AND L. REN, *Bioinspired actuators with intrinsic muscle-like mechanical properties*, IScience, 24 (2021).
- [116] J. E. LLOYD, I. STAVNESS, AND S. FELS, *Artisynth: A fast interactive biomechanical modeling toolkit combining multibody and finite element simulation*, in Soft Tissue Biomechanical Modeling for Computer Assisted Surgery, Springer, 2012, pp. 355–394.
- [117] S. A. MAAS, B. J. ELLIS, G. A. ATESHIAN, AND J. A. WEISS, *Febio: finite elements for biomechanics*, Journal of Biomechanical Engineering, 134 (2012).
- [118] C. N. MAGANARIS, V. BALTZOPOULOS, AND A. J. SARGEANT, *In vivo measurements of the triceps surae complex architecture in man: implications for muscle function*, The Journal of physiology, 512 (1998), pp. 603–614.
- [119] M. A. MAHDY, *Skeletal muscle fibrosis: an overview*, Cell and tissue research, 375 (2019), pp. 575–588.
- [120] L. MARCUCCI, C. REGGIANI, A. N. NATALI, AND P. G. PAVAN, *From single muscle fiber to whole muscle mechanics: a finite element model of a muscle bundle with fast and slow fibers*, Biomechanics and modeling in mechanobiology, 16 (2017), pp. 1833–1843.

- [121] D. J. MAXAM AND K. K. TAMMA, *A re-evaluation of overshooting in time integration schemes: The neglected effect of physical damping in the starting procedure*, International Journal for Numerical Methods in Engineering, 123 (2022), pp. 2683–2704.
- [122] C. P. MCGOWAN, R. NEPTUNE, AND W. HERZOG, *A phenomenological muscle model to assess history dependent effects in human movement*, Journal of biomechanics, 46 (2013), pp. 151–157.
- [123] S. MEDLER, *Comparative trends in shortening velocity and force production in skeletal muscles*, American Journal of Physiology-Regulatory, Integrative and Comparative Physiology, 283 (2002), pp. R368–R378.
- [124] P. MEIER AND R. BLICKHAN, *FEM-simulation of skeletal muscle: the influence of inertia during activation and deactivation*, in *Skeletal Muscle Mechanics: From Mechanisms to Function*, W. Herzog, ed., John Wiley & Sons, 2000.
- [125] J. MÉNDEZ, *Density and composition of mammalian muscle.*, Metabolism, 9 (1960), pp. 184–188.
- [126] M. O. MENDOZA-GUTIÉRREZ, V. I. RAMÍREZ-VERA, I. BONILLA-GUTIÉRREZ, E. J. GONZÁLEZ-GALVÁN, AND A. LOREDO-FLORES, *Bounded human-robot interaction control using joint torque estimation from electromyographic signals*, IEEE Access, (2025).
- [127] B. MILIĆEVИĆ, M. IVANOVIĆ, B. STOJANOVИĆ, M. MILOŠEVИĆ, M. KOJIĆ, AND N. FILIPOVIĆ, *Huxley muscle model surrogates for high-speed multi-scale simulations of cardiac contraction*, Computers in Biology and Medicine, 149 (2022), p. 105963.
- [128] M. MILLARD, D. W. FRANKLIN, AND W. HERZOG, *A three filament mechanistic model of musculotendon force and impedance*, Elife, 12 (2024), p. RP88344.
- [129] M. MILLARD, T. UCHIDA, A. SETH, AND S. L. DELP, *Flexing computational muscle: modeling and simulation of musculotendon dynamics*, Journal of biomechanical engineering, 135 (2013).
- [130] M. MOHAMMADKHAH, P. MURPHY, AND C. K. SIMMS, *The in vitro passive elastic response of chicken pectoralis muscle to applied tensile and compressive deformation*, Journal of the mechanical behavior of biomedical materials, 62 (2016), pp. 468–480.
- [131] D. MORGAN, *New insights into the behavior of muscle during active lengthening*, Biophysical journal, 57 (1990), pp. 209–221.
- [132] D. L. MORGAN AND U. PROSKE, *Popping sarcomere hypothesis explains stretch induced muscle damage*, in Proceedings of the Australian Physiological and Pharmacological Society, vol. 34, 2004, pp. 19–23.
- [133] ———, *Sarcomere popping requires stretch over a range where total tension decreases with length*, The Journal of Physiology, 574 (2006), p. 627.
- [134] Z. F. MUHL, *Active length-tension relation and the effect of muscle pinnation on fiber lengthening*, Journal of Morphology, 173 (1982), pp. 285–292.

- [135] M. V. NARICI, T. BINZONI, E. HILTBRAND, J. FASEL, F. TERRIER, AND P. CERRETELLI, *In vivo human gastrocnemius architecture with changing joint angle at rest and during graded isometric contraction.*, The Journal of physiology, 496 (1996), pp. 287–297.
- [136] N. M. NEWMARK, *A method of computation for structural dynamics*, Journal of the engineering mechanics division, 85 (1959), pp. 67–94.
- [137] K. NISHIKAWA, *Titin: a tunable spring in active muscle*, Physiology, 35 (2020), pp. 209–217.
- [138] K. C. NISHIKAWA, J. A. MONROY, T. E. UYENO, S. H. YEO, D. K. PAI, AND S. L. LINDSTEDT, *Is titin a ‘winding filament’? a new twist on muscle contraction*, Proceedings of the royal society B: Biological sciences, 279 (2012), pp. 981–990.
- [139] G. ODEGARD, T. HAUT DONAHUE, D. MORROW, AND K. R. KAUFMAN, *Constitutive modeling of skeletal muscle tissue with an explicit strain-energy function*, Journal of biomechanical engineering, 130 (2008).
- [140] C. OOMENS, M. MAENHOUT, C. VAN OIJEN, M. DROST, AND F. BAAIJENS, *Finite element modelling of contracting skeletal muscle*, Philosophical Transactions of the Royal Society of London. Series B: Biological Sciences, 358 (2003), pp. 1453–1460.
- [141] E. OTTEN, *Some numerical reflections upon the simple planimetric muscle model of huijing & woittiez*, Netherlands journal of zoology, 35 (1984), pp. 517–520.
- [142] T. D. O'BRIEN, N. D. REEVES, V. BALTZOPOULOS, D. A. JONES, AND C. N. MAGANARIS, *Muscle-tendon structure and dimensions in adults and children*, Journal of anatomy, 216 (2010), pp. 631–642.
- [143] J. PASSIPIERI, H. BAKER, M. SIRIWARDANE, M. D. ELLENBURG, M. VADHAVKAR, J. M. SAUL, S. TOMBLYN, L. BURNETT, AND G. J. CHRIST, *Keratin hydrogel enhances in vivo skeletal muscle function in a rat model of volumetric muscle loss*, Tissue Engineering Part A, 23 (2017), pp. 556–571.
- [144] J.-P. PELTERET, *A computational neuromuscular model of the human upper airway*, PhD thesis, University of Cape Town, 2013.
- [145] J.-P. PELTERET AND A. MCBRIDE, *The deal.II tutorial step-44: Three-field formulation for non-linear solid mechanics*, Apr. 2012.
- [146] A. PEREIRA, M. SILVA, J. MARTINS, AND M. DE CARVALHO, *Implementation of an efficient muscle fatigue model in the framework of multibody systems dynamics for analysis of human movements*, Proceedings of the Institution of Mechanical Engineers, Part K: Journal of Multi-body Dynamics, 225 (2011), pp. 359–370.
- [147] E. J. PERREAULT, C. J. HECKMAN, AND T. G. SANDERCOCK, *Hill muscle model errors during movement are greatest within the physiologically relevant range of motor unit firing rates*, Journal of biomechanics, 36 (2003), pp. 211–218.
- [148] R. A. PINNELL, P. MASHOURI, N. MAZARA, E. WEERSINK, S. H. BROWN, AND G. A. POWER, *Residual force enhancement and force depression in human single muscle fibres*, Journal of Biomechanics, 91 (2019), pp. 164–169.

- [149] M. PINTO, J. WAKELING, J. ALMONACID, AND A. BLAZEVICH, *From muscle fibres to gears: How fibre rotation and shape change impact muscle function*, bioRxiv, (2025), pp. 2025–06.
- [150] M. D. PINTO, K. NOSAKA, J. M. WAKELING, AND A. J. BLAZEVICH, *Human in vivo medial gastrocnemius gear during active and passive muscle lengthening: effect of inconsistent methods and nomenclature on data interpretation*, Biology Open, 12 (2023).
- [151] S. PORSA, Y.-C. LIN, AND M. G. PANDY, *Direct methods for predicting movement biomechanics based upon optimal control theory with implementation in opensim*, Annals of biomedical engineering, 44 (2016), pp. 2542–2557.
- [152] P. L. POWELL, R. R. ROY, P. KANIM, M. A. BELLO, AND V. R. EDGERTON, *Predictability of skeletal muscle tension from architectural determinations in guinea pig hindlimbs*, Journal of applied physiology, 57 (1984), pp. 1715–1721.
- [153] P. M. RACK AND D. WESTBURY, *The effects of length and stimulus rate on tension in the isometric cat soleus muscle*, The Journal of physiology, 204 (1969), p. 443.
- [154] H. RAHEMI, *Structural mechanics of skeletal muscle contractions: Mechanistic findings using a finite element model*, PhD thesis, Department of Mathematics, Simon Fraser University, 2015.
- [155] H. RAHEMI, N. NIGAM, AND J. M. WAKELING, *Regionalizing muscle activity causes changes to the magnitude and direction of the force from whole muscles—a modeling study*, Frontiers in physiology, 5 (2014), p. 298.
- [156] ———, *The effect of intramuscular fat on skeletal muscle mechanics: implications for the elderly and obese*, Journal of The Royal Society Interface, 12 (2015), p. 20150365.
- [157] A. RAJAGOPAL, C. L. DEMBIA, M. S. DEMERS, D. D. DELP, J. L. HICKS, AND S. L. DELP, *Full-body musculoskeletal model for muscle-driven simulation of human gait*, IEEE transactions on biomedical engineering, 63 (2016), pp. 2068–2079.
- [158] A. RANDHAWA, M. E. JACKMAN, AND J. M. WAKELING, *Muscle gearing during isotonic and isokinetic movements in the ankle plantarflexors*, European journal of applied physiology, 113 (2013), pp. 437–447.
- [159] D. E. RASSIER, B. MACINTOSH, AND W. HERZOG, *Length dependence of active force production in skeletal muscle*, Journal of applied physiology, 86 (1999), pp. 1445–1457.
- [160] D. E. RASSIER AND I. PAVLOV, *Force produced by isolated sarcomeres and half-sarcomeres after an imposed stretch*, American Journal of Physiology-Cell Physiology, 302 (2012), pp. C240–C248.
- [161] P.-A. RAVIART AND J. M. THOMAS, *Introduction à l'analyse numérique des équations aux dérivées partielles*, Masson, Paris, 1983.
- [162] T. J. ROBERTS, C. M. ENG, D. A. SLEBODA, N. C. HOLT, E. L. BRAINERD, K. K. STOVER, R. L. MARSH, AND E. AZIZI, *The multi-scale, three-dimensional nature of skeletal muscle contraction*, Physiology, 34 (2019), pp. 402–408.

- [163] H. ROOTS, G. OFFER, AND K. RANATUNGA, *Comparison of the tension responses to ramp shortening and lengthening in intact mammalian muscle fibres: crossbridge and non-crossbridge contributions*, Journal of muscle research and cell motility, 28 (2007), pp. 123–139.
- [164] S. A. ROSS, S. DOMÍNGUEZ, N. NIGAM, AND J. M. WAKELING, *The energy of muscle contraction. III. Kinetic energy during cyclic contractions*, Frontiers in Physiology, 12 (2021), p. 628819.
- [165] S. A. ROSS, N. NIGAM, AND J. M. WAKELING, *A modelling approach for exploring muscle dynamics during cyclic contractions*, PLoS Computational Biology, 14 (2018).
- [166] S. A. ROSS, D. S. RYAN, S. DOMINGUEZ, N. NIGAM, AND J. M. WAKELING, *Size, history-dependent, activation and three-dimensional effects on the work and power produced during cyclic muscle contractions*, Integrative and Comparative Biology, 58 (2018), pp. 232–250.
- [167] S. A. ROSS AND J. M. WAKELING, *Muscle shortening velocity depends on tissue inertia and level of activation during submaximal contractions*, Biology letters, 12 (2016), p. 20151041.
- [168] ———, *The energy of muscle contraction. IV. Greater mass of larger muscles decreases contraction efficiency*, Journal of the Royal Society Interface, 18 (2021), p. 20210484.
- [169] D. F. ROSSI, W. G. FERREIRA, W. J. MANSUR, AND A. F. G. CALENZANI, *A review of automatic time-stepping strategies on numerical time integration for structural dynamics analysis*, Engineering structures, 80 (2014), pp. 118–136.
- [170] E. ROTHE, *Zweidimensionale parabolische randwertaufgaben als grenzfall eindimensionaler randwertaufgaben*, Mathematische Annalen, 102 (1930), pp. 650–670.
- [171] J. C. RÜEGG, *Calcium in muscle contraction: cellular and molecular physiology*, Springer Science & Business Media, 2012.
- [172] M. RÜTER AND E. STEIN, *Analysis, finite element computation and error estimation in transversely isotropic nearly incompressible finite elasticity*, Computer methods in applied mechanics and engineering, 190 (2000), pp. 519–541.
- [173] D. S. RYAN, S. DOMÍNGUEZ, S. A. ROSS, N. NIGAM, AND J. M. WAKELING, *The energy of muscle contraction. II. transverse compression and work*, Frontiers in Physiology, 11 (2020), p. 538522.
- [174] M. L. SAMPAIO DE OLIVEIRA AND T. K. UCHIDA, *Phenomenological muscle constitutive model with actin–titin binding for simulating active stretching*, Journal of Biomechanical Engineering, 147 (2025), p. 011002.
- [175] J. SCHRÖDER AND P. NEFF, *Invariant formulation of hyperelastic transverse isotropy based on polyconvex free energy functions*, International journal of solids and structures, 40 (2003), pp. 401–445.
- [176] S. H. SCOTT, I. E. BROWN, AND G. E. LOEB, *Mechanics of feline soleus: I. effect of fascicle length and velocity on force output*, Journal of Muscle Research & Cell Motility, 17 (1996), pp. 207–219.

- [177] L. F. SHAMPINE, *Solving  $0 = f(t, y(t), y'(t))$  in MATLAB*, Journal of Numerical Mathematics, 10 (2002), pp. 291–310.
- [178] L. F. SHAMPINE AND M. W. REICHELT, *The matlab ode suite*, SIAM journal on scientific computing, 18 (1997), pp. 1–22.
- [179] T. SIEBERT, M. GÜNTHER, AND R. BLICKHAN, *A 3d-geometric model for the deformation of a transversally loaded muscle*, Journal of theoretical biology, 298 (2012), pp. 116–121.
- [180] J. SIMO, R. L. TAYLOR, AND K. PISTER, *Variational and projection methods for the volume constraint in finite deformation elasto-plasticity*, Computer methods in applied mechanics and engineering, 51 (1985), pp. 177–208.
- [181] D. A. SLEBODA, T. J. ROBERTS, AND E. AZIZI, *Architectural gear ratio depends on actuator spacing in a physical model of pennate muscle*, Bioinspiration & Biomimetics, 19 (2024), p. 026007.
- [182] H. STARK, M. S. FISCHER, A. HUNT, F. YOUNG, R. QUINN, AND E. ANDRADA, *A three-dimensional musculoskeletal model of the dog*, Scientific reports, 11 (2021), pp. 1–13.
- [183] J. C. STRIKWERDA, *Finite difference schemes and partial differential equations*, Society for Industrial and Applied Mathematics, 2004.
- [184] S. STROGATZ, *Nonlinear Dynamics and Chaos: With Applications to Physics, Biology, Chemistry, and Engineering*, CRC Press, 2018.
- [185] C. TAM, *The dynamics of skeletal muscle: a computational study*, MSc thesis, Department of Mathematics, Simon Fraser University, 2022.
- [186] C. Y. TANG, C. P. TSUI, B. STOJANOVIC, AND M. KOJIC, *Finite element modelling of skeletal muscles coupled with fatigue*, International Journal of Mechanical Sciences, 49 (2007), pp. 1179–1191.
- [187] C. Y. TANG, G. ZHANG, AND C. P. TSUI, *A 3d skeletal muscle model coupled with active contraction of muscle fibres and hyperelastic behaviour*, Journal of biomechanics, 42 (2009), pp. 865–872.
- [188] J. A. TIGUE, W. B. ROCKWELL, K. B. FOREMAN, AND S. A. MASCARO, *Investigating the effects of flexor tendon shortening on active range of motion after finger tendon repair*, The Anatomical Record, 305 (2022), pp. 1231–1244.
- [189] T. TRILINOS PROJECT TEAM, *The Trilinos Project Website*.
- [190] C. TRUESDELL, W. NOLL, C. TRUESDELL, AND W. NOLL, *The non-linear field theories of mechanics*, Springer, 2004.
- [191] F. J. VALERO-CUEVAS, H. HOFFMANN, M. U. KURSE, J. J. KUTCH, AND E. A. THEODOROU, *Computational models for neuromuscular function*, IEEE reviews in biomedical engineering, 2 (2009), pp. 110–135.

- [192] V. VAVOURAKIS, A. KAZAKIDI, D. TSAKIRIS, AND J. A. EKATERINARIS, *A nonlinear dynamic finite element approach for simulating muscular hydrostats*, Computer Methods in Biomechanics and Biomedical Engineering, 17 (2014), pp. 917–931.
- [193] M. A. VAZ, C. DE LA ROCHA FREITAS, T. LEONARD, AND W. HERZOG, *The force-length relationship of the cat soleus muscle*, Muscles, ligaments and tendons journal, 2 (2012), p. 79.
- [194] J. M. WAKELING, O. M. BLAKE, I. WONG, M. RANA, AND S. S. LEE, *Movement mechanics as a determinate of muscle structure, recruitment and coordination*, Philosophical Transactions of the Royal Society B: Biological Sciences, 366 (2011), pp. 1554–1564.
- [195] J. M. WAKELING, S. S. LEE, A. S. ARNOLD, M. DE BOEF MIARA, AND A. A. BIEWENER, *A muscle's force depends on the recruitment patterns of its fibers*, Annals of biomedical engineering, 40 (2012), pp. 1708–1720.
- [196] J. M. WAKELING, S. A. ROSS, D. S. RYAN, B. BOLSTERLEE, R. KONNO, S. DOMÍNGUEZ, AND N. NIGAM, *The energy of muscle contraction. I. Tissue force and deformation during fixed-end contractions*, Frontiers in Physiology, 11 (2020), p. 813.
- [197] J. P. WALTER, A. L. KINNEY, S. A. BANKS, D. D. D'LIMA, T. F. BESIER, D. G. LLOYD, AND B. J. FREGLY, *Muscle synergies may improve optimization prediction of knee contact forces during walking*, Journal of biomechanical engineering, 136 (2014), p. 021031.
- [198] Y. WANG, C. LIU, L. REN, AND L. REN, *Load-dependent variable gearing mechanism of muscle-like soft actuator*, Journal of Bionic Engineering, (2022), pp. 1–15.
- [199] J. A. WEISS, B. N. MAKER, AND S. GOVINDJEE, *Finite element implementation of incompressible, transversely isotropic hyperelasticity*, Computer methods in applied mechanics and engineering, 135 (1996), pp. 107–128.
- [200] E. L. WILSON, *A computer program for the dynamic stress analysis of underground structures*, Tech. Rep. SESM Report No. 68-1, Berkeley, CA: Division of Structural Engineering and Structural Mechanics, University of California, 1968.
- [201] T. M. WINTERS, M. TAKAHASHI, R. L. LIEBER, AND S. R. WARD, *Whole muscle length-tension relationships are accurately modeled as scaled sarcomeres in rabbit hindlimb muscles*, Journal of biomechanics, 44 (2011), pp. 109–115.
- [202] R. WOITTIEZ AND P. HUIJING, *Notes on planimetric and three-dimensional muscle models*, Netherlands journal of zoology, 35 (1984), pp. 521–525.
- [203] R. WOITTIEZ, P. HUIJING, H. BOOM, AND R. ROZENDAL, *A three-dimensional muscle model: a quantified relation between form and function of skeletal muscles*, Journal of Morphology, 182 (1984), pp. 95–113.
- [204] W. WOOD, M. BOSSAK, AND O. ZIENKIEWICZ, *An alpha modification of newmark's method*, International journal for numerical methods in engineering, 15 (1980), pp. 1562–1566.

- [205] X. WU, B. T. CORONA, X. CHEN, AND T. J. WALTERS, *A standardized rat model of volumetric muscle loss injury for the development of tissue engineering therapies*, BioResearch open access, 1 (2012), pp. 280–290.
- [206] S.-H. YEO, J. VERHEUL, W. HERZOG, AND S. SUEDA, *Numerical instability of hill-type muscle models*, Journal of the Royal Society Interface, 20 (2023), p. 20220430.
- [207] G. I. ZAHALAK, *Can muscle fibers be stable on the descending limbs of their sarcomere length-tension relations?*, Journal of Biomechanics, 30 (1997), pp. 1179–1182.
- [208] F. E. ZAJAC, *Muscle and tendon: properties, models, scaling, and application to biomechanics and motor control.*, Critical reviews in biomedical engineering, 17 (1989), pp. 359–411.
- [209] A. ZDUNEK AND W. RACHOWICZ, *A 3-field formulation for strongly transversely isotropic compressible finite hyperelasticity*, Computer Methods in Applied Mechanics and Engineering, 315 (2017), pp. 478–500.
- [210] O. C. ZIENKIEWICZ AND R. L. TAYLOR, *The finite element method: solid mechanics*, vol. 2, Butterworth-heinemann, 2000.
- [211] C. J. ZUURBIER AND P. A. HUIJING, *Influence of muscle geometry on shortening speed of fibre, aponeurosis and muscle*, Journal of biomechanics, 25 (1992), pp. 1017–1026.

# Appendix A

## Force relationships

In this Appendix, we describe the mathematical expressions used for the force relationships in this study. A GitHub repository with Matlab implementations of these curves is available at:

<https://github.com/sfu-nml/force-relationships>.

### A.1 Forces used in 1D experiments

For these experiments, we fitted the force relationships originally given by Bézier curves in [167] to cubic splines. Thus, the forces take the a piecewise form. For  $k = 1, 2, \dots, N$ , a force  $\hat{F}$  can take the form:

$$\hat{F}(t) = a_3^{(k)}(t - t_{k-1})^3 + a_2^{(k)}(t - t_{k-1})^2 + a_1^{(k)}(t - t_{k-1}) + a_0^{(k)}, \quad t_{k-1} \leq t < t_k. \quad (\text{A.1.1})$$

We thus have  $N$  pieces and  $N+1$  knots  $\{t_0, t_1, \dots, t_N\}$ . We show the coefficients and knots that define the active force-length, passive force-length, force-velocity, and tendon force relationships in Tables A.1-A.4.

### A.2 Forces used in 3D experiments

In this case, we decide to keep the stress relationships used in previous studies [54, 102, 164, 173, 196].

The active stress-stretch relationship for muscle was reported by Konno [102] as:

$$\hat{\sigma}_A(\bar{\lambda}) = \begin{cases} \sum_{k=1}^7 c_k \sin(a_k \bar{\lambda} + b_k), & 0.4 \leq \bar{\lambda} \leq 1.75 \\ 0.0, & \text{otherwise,} \end{cases} \quad (\text{A.2.1})$$

Coefficients in descending polynomial order				Interval
16.259504	2.735529	0.000000	0.000000	$0.4 \leq \lambda_M < 0.6$
-71.836426	12.491232	3.045352	0.239497	$0.6 \leq \lambda_M < 0.7$
7.352394	-9.059696	3.388506	0.597108	$0.7 \leq \lambda_M < 0.9$
11.676119	-4.648260	0.646915	0.971241	$0.9 \leq \lambda_M < 0.95$
2.669948	-2.896842	0.269660	0.993425	$0.95 \leq \lambda_M < 1.0$
185.407729	-30.069106	0.000000	1.000000	$1.0 \leq \lambda_M < 1.05$
2.958338	-2.257947	-1.616353	0.948003	$1.05 \leq \lambda_M < 1.1$
7.333359	-1.814196	-1.819960	0.861910	$1.1 \leq \lambda_M < 1.2$
1.162833	0.385812	-1.962798	0.669106	$1.2 \leq \lambda_M < 1.4$
3.773432	1.083512	-1.668934	0.301281	$1.4 \leq \lambda_M \leq 1.7$

Table A.1: Cubic spline coefficients for the active force-length relationship  $\hat{F}_A$  used for 1D experiments.

Coefficients in descending polynomial order				Interval
0.637061	0.073924	0.000706	0.000000	$0.7 \leq \lambda_M < 1.0$
1.239310	0.647279	0.217067	0.024066	$1.0 \leq \lambda_M < 1.12$
7.439238	1.093430	0.425952	0.061576	$1.12 \leq \lambda_M < 1.35$
-18.101816	6.226505	2.109537	0.307901	$1.35 \leq \lambda_M < 1.47$
-3.080909	-0.290149	2.821900	0.619427	$1.47 \leq \lambda_M \leq 1.65$

Table A.2: Cubic spline coefficients for the passive force-length relationship  $\hat{F}_P$  used for 1D experiments.

with  $a_k, b_k, c_k \in \mathbb{R}$ . This corresponds to a fit from experimental data in [201]. The constants that define this function are listed in Table A.5.

The passive stress-stretch relationship for muscle was reported by Konno [102] as:

$$\hat{\sigma}_P(\bar{\lambda}) = \begin{cases} 0, & \bar{\lambda} \leq 1, \\ c_1(\bar{\lambda} - 1)^2 + c_2(\bar{\lambda} - 1) + c_3, & 1 < \bar{\lambda} \leq 1.25, \\ c_4(\bar{\lambda} - 1.25)^2 + c_5(\bar{\lambda} - 1.25) + c_6, & 1.25 < \bar{\lambda} \leq 1.5, \\ c_7(\bar{\lambda} - 1.5)^2 + c_8(\bar{\lambda} - 1.5) + c_9, & 1.5 < \bar{\lambda} \leq 1.65, \\ c_{10}(\bar{\lambda} - 1.65) + c_{11}, & \bar{\lambda} > 1.65, \end{cases} \quad (\text{A.2.2})$$

with  $c_k \in \mathbb{R}$ . This corresponds to a fit from experimental data in [201]. The constants that define this function are listed in Table A.6.

Coefficients in descending polynomial order				Interval
0.220624	0.180895	0.169799	0.000000	$-1.0 \leq \dot{\varepsilon}_M < -0.6$
0.809642	0.445644	0.420414	0.110983	$-0.6 \leq \dot{\varepsilon}_M < -0.4$
1.352406	0.931429	0.695829	0.219368	$-0.4 \leq \dot{\varepsilon}_M < -0.3$
5.649771	1.337151	0.922687	0.299618	$-0.3 \leq \dot{\varepsilon}_M < -0.15$
33.819416	3.879548	1.705192	0.487175	$-0.15 \leq \dot{\varepsilon}_M < -0.1$
29.535258	8.952460	2.346792	0.586361	$-0.1 \leq \dot{\varepsilon}_M < -0.05$
508.735536	13.382749	3.463553	0.729774	$-0.05 \leq \dot{\varepsilon}_M < 0.00$
143713.368503	-204.615076	8.745168	1.000000	$0.00 \leq \dot{\varepsilon}_M < 0.007$
-705905.249709	2813.365662	27.006422	1.100484	$0.007 \leq \dot{\varepsilon}_M < 0.01$
234818.856704	-3539.781585	24.827174	1.187764	$0.01 \leq \dot{\varepsilon}_M < 0.015$
-14695.733995	-17.498735	7.040773	1.252758	$0.015 \leq \dot{\varepsilon}_M < 0.02$
6806.732497	-237.934745	5.763605	1.285687	$0.02 \leq \dot{\varepsilon}_M < 0.03$
117.239184	-33.732770	3.046930	1.326336	$0.03 \leq \dot{\varepsilon}_M < 0.04$
257.061419	-30.215594	2.407447	1.353550	$0.04 \leq \dot{\varepsilon}_M < 0.07$
26.551643	-7.080067	1.288577	1.405520	$0.07 \leq \dot{\varepsilon}_M < 0.12$
8.331011	-3.097320	0.779708	1.455567	$0.12 \leq \dot{\varepsilon}_M < 0.2$
1.699155	-1.097878	0.444092	1.502386	$0.2 \leq \dot{\varepsilon}_M < 0.3$
0.842130	-0.588131	0.275491	1.537516	$0.3 \leq \dot{\varepsilon}_M < 0.4$
0.299331	-0.335492	0.183129	1.560026	$0.4 \leq \dot{\varepsilon}_M < 0.6$
0.083998	-0.155894	0.084851	1.585627	$0.6 \leq \dot{\varepsilon}_M \leq 1.0$

Table A.3: Cubic spline coefficients for the force-velocity  $\hat{F}_V$  relationship used for 1D experiments.

Coefficients in descending polynomial order				Interval
0.000000	0.000000	0.009717	0.000000	$0.0 \leq \lambda_T < 1.00472$
-32632.569799	961.712634	5.666232	0.009763	$1.00472 \leq \lambda_T < 1.01$
-12072.697295	444.812728	13.092686	0.061688	$1.01 \leq \lambda_T < 1.02$
-770.792801	82.631809	18.367131	0.225024	$1.02 \leq \lambda_T < 1.058$
0.000000	0.000000	21.308074	1.000000	$1.058 \leq \lambda_T$

Table A.4: Cubic spline coefficients for the tendon force-length relationship  $\hat{F}_T$  used for 1D experiments.

$c_k$	Value	$a_k$	Value	$b_k$	Value
$c_1$	0.642587	$a_1$	1.290128	$b_1$	0.629168
$c_2$	0.325980	$a_2$	5.308970	$b_2$	-4.520102
$c_3$	0.328204	$a_3$	6.744187	$b_3$	1.689156
$c_4$	0.015389	$a_4$	19.823677	$b_4$	-7.386155
$c_5$	0.139240	$a_5$	8.038287	$b_5$	2.543022
$c_6$	0.001802	$a_6$	32.237736	$b_6$	-6.454098
$c_7$	0.012561	$a_7$	23.117614	$b_7$	-2.643347

Table A.5: Parameters describing the muscle active stress-stretch relationship  $\hat{\sigma}_A$  used for 3D experiments.

The stress-strain-rate relationship for muscle was reported by Ross et al. [165] as:

$$\hat{\sigma}_V(\bar{\varepsilon}) = \begin{cases} 0.0, & \bar{\varepsilon} < -1.2, \\ c_1 (\bar{\varepsilon} + 1.2)^3 + c_2 (\bar{\varepsilon} + 1.2)^2 + c_3 (\bar{\varepsilon} + 1.2) + c_4, & -1.2 \leq \bar{\varepsilon} \leq -0.25, \\ c_5 (\bar{\varepsilon} + 0.25)^3 + c_6 (\bar{\varepsilon} + 0.25)^2 + c_7 (\bar{\varepsilon} + 0.25) + c_8, & -0.25 \leq \bar{\varepsilon} < 0.0 \\ c_9 (\bar{\varepsilon} - 0.0)^3 + c_{10} (\bar{\varepsilon} - 0.0)^2 + c_{11} (\bar{\varepsilon} - 0.0) + c_{12}, & 0.0 \leq \bar{\varepsilon} \leq 0.05 \\ c_{13} (\bar{\varepsilon} - 0.05)^3 + c_{14} (\bar{\varepsilon} - 0.05)^2 + c_{15} (\bar{\varepsilon} - 0.05) + c_{16}, & 0.05 \leq \bar{\varepsilon} < 0.75 \\ c_{17}, & \bar{\varepsilon} \geq 0.75, \end{cases} \quad (\text{A.2.3})$$

with  $c_k \in \mathbb{R}$ . This corresponds to a fit from experimental data in [163]. The constants that define this function are listed in Table A.7.

The stress-stretch relationship for aponeurosis was fit from experimental data by Dick [50]:

$$\hat{\sigma}_{apo}(\bar{\lambda}) = \begin{cases} c_0 \bar{\lambda}, & 0 < \bar{\lambda} < 1.00, \\ c_1 (\bar{\lambda} - 1.00)^2 + c_2 (\bar{\lambda} - 1.00) + c_3, & 1.00 \leq \bar{\lambda} < 1.01, \\ c_4 (\bar{\lambda} - 1.01)^2 + c_5 (\bar{\lambda} - 1.01) + c_6, & 1.01 \leq \bar{\lambda} < 1.02, \\ c_7 (\bar{\lambda} - 1.02)^2 + c_8 (\bar{\lambda} - 1.02) + c_9, & 1.02 \leq \bar{\lambda} < 1.15, \\ c_{10} (\bar{\lambda} - 1.15) + c_{11}, & \bar{\lambda} \geq 1.15, \end{cases} \quad (\text{A.2.4})$$

with  $c_k \in \mathbb{R}$ . The constants that define this function are listed in Table A.8.

Parameter	Value	Parameter	Value
$\sigma_{0,M}$	200 kPa	$c_6$	0.147115
$c_1$	2.353845	$c_7$	0.427408
$c_2$	0.000000	$c_8$	2.895101
$c_3$	0.000000	$c_9$	0.656118
$c_4$	3.436357	$c_{10}$	3.023323
$c_5$	1.176922	$c_{11}$	1.100000

Table A.6: Parameters describing the muscle passive stress-stretch relationship  $\hat{\sigma}_P$  used for 3D experiments.

$c_k$	Value	$c_k$	Value	$c_k$	Value
$c_1$	0.257927	$c_7$	0.970369	$c_{13}$	0.688221
$c_2$	0.143175	$c_8$	0.350355	$c_{14}$	-1.413963
$c_3$	0.000000	$c_9$	-3165.684798	$c_{15}$	0.967864
$c_4$	0.000000	$c_{10}$	186.196125	$c_{16}$	1.374324
$c_5$	29.825565	$c_{11}$	6.090887	$c_{17}$	1.595047
$c_6$	-0.943550	$c_{12}$	1.000000	-	-

Table A.7: Parameters describing the muscle passive stress-strain-rate relationship  $\hat{\sigma}_V$  used for 3D experiments.

$c_k$	Value	$c_k$	Value	$c_k$	Value
$c_0$	0.010000	$c_4$	600.590242	$c_8$	22.339446
$c_1$	515.882034	$c_5$	10.327641	$c_9$	0.225024
$c_2$	0.010000	$c_6$	0.061688	$c_{10}$	19.745862
$c_3$	0.010000	$c_7$	-9.975322	$c_{11}$	2.960569

Table A.8: Parameters describing the aponeurosis stress-stretch relationship  $\hat{\sigma}_{apo}$  used for 3D experiments.